Contact Lens Platforms for Ocular Health Monitoring

By

Rosalia Moreddu

A thesis submitted to the University of Birmingham for the degree of Doctor of Philosophy

School of Chemical Engineering

University of Birmingham

April 2021

Innovation begins with myths

Abstract

As of today, the World Health Organization (WHO) counts millions of cases of preventable blindness every year in high income countries, attributed to the lack of early-stage ophthalmic screening technologies. Contemporary methods rely on bulky and costly equipment exclusively operated by specialized clinicians, resulting in a medical approach based on reaction over prevention. A possible approach results from a literature survey on the tear fluid properties, which revealed its potential to be used as a diagnostic medium. However, existing tear sampling technologies lack practicality, and introduce a high contamination risk of tear samples.

In this context, the work of this thesis builds up on the belief that contact lenses may represent a suitable platform to monitor tear fluid composition and ocular physical parameters (temperature, pressure) directly on-eye. With this objective, commercial contact lenses were surface-functionalized with microstructures and microfluidic networks by laser ablation, and with nanostructures by replica molding.

The development of a customized 7-axis femtosecond laser writing system allowed to obtain geometrically-consistent microfeatures with the highest resolution observed so far in contact lenses (80 μm) and to modulate the flow velocity across the channels via microfluidic elements. Flow velocity drops of the 8.3%, 20.8%, and 29% were observed in microfluidic valves with enlargements of the 100%, 200% and 300% compared to the base channel, respectively. Microfluidic resistors yielded flow rate drops of 20.8% 33% and 50% in the small, medium, and large configurations, respectively. Contact lens-embedding microsplitters and micromixers were also demonstrated. Laser ablation process and flow velocity profiles were computed and visualized using the finite element method (FEM). Such systems were further employed in the detection of tear fluid analytes from artificial tears and on ex-vivo eye models.

Colorimetric chemical sensors for the detection of uric acid (Limit of detection (LOD) = 16 nm/mgL^{-1}), pH (LOD = 0.2 units), glucose (LOD = 1.1 nm/mmolL^{-1}), proteins (LOD = 1.1 nm/gL^{-1}), L-ascorbic acid (LOD = 0.05 nm/mgL^{-1}) and nitrites (LOD = 0.53 nm/µmolL^{-1}) were integrated in microfluidic contact lenses by drop casting, irreversible chemical bonding (O_2 plasma followed by APTES/GPTES), or paper deposition. Digital readouts were implemented in MATLAB and further translated in the Visual Studio smartphone interface, based on the Nearest Neighbor Model. The algorithm allowed to read discrete concentration values for each analyte, as set by the calibration points given as inputs.

The same technological approach was implemented to obtain microcavities in contact lenses, where temperature-sensitive liquid crystals were embedded to map the ocular surface temperature by direct contact with the cornea. They yielded a time response of 490 ms and a reflection peak shift from 738 ± 4 nm to 474 ± 4 nm in the physiological temperature range (29.0-40.0 °C). Colorimetric smartphone readouts were compared with infrared thermal measurements, resulting in an average error of 0.3 °C.

Nanostructured contact lenses were implemented as strain-tunable diffraction gratings for ocular pressure monitoring. Nano-holes were patterned on silicon by e-beam lithography and further incorporated as nano-buttons into contact lenses by replica molding and O_2 plasma bonding. Strain sensors were characterized under monochromatic laser sources, yielding a LOD <2 mmHg and a linear response in the range of interest (15-35 mmHg). A smartphone readout method based on preferentially reflected colors was proposed to pave the way towards smartphone-based ocular health monitoring.

Such devices may help overcoming the hurdles encountered with traditional ophthalmic technologies, reducing the costs and easing the operation. In addition, they could be employed as continuous ocular health monitoring platforms at point-of-care settings.

Table of contents

Preface 9
List of figures 11
List of tables 16
Chapter 1 17
Contact Lens Technology: From Fundamentals to Applications 17
1.1. Introduction 17
1.1.1. History of contact lenses 21
1.1.2. Evolution of the human eye 22
1.1.3. The tear fluid 23
1.1.4. The eye microbiota 29
1.2. Polymers in contact lenses 30
1.2.1. Rigid lenses 30
1.2.2. Soft lenses 31
1.2.3. Hybrid lenses 36
1.3. Properties of contact lens materials 37
1.3.1. Chemical properties 37
1.3.2. Mechanical properties 39
1.3.3. Optical properties 39
1.4. Contact lens manufacture 40
1.4.1. Molding 41
1.4.2. Lathe cutting 41
1.4.3. Quality control and packaging 44
1.5. Applications 45
1.5.1. Refractive disorders 46
1.5.2. Prosthetics 49
1.5.3. Therapeutics 50
1.5.4. Contact lens sensors 52

1.5.5. Contact lenses as drug delivery systems 54
1.6. Contamination in contact lenses 57
1.6.1. Contamination of contact lens cases 60
1.6.2. Contact lens care 62
1.7. Regulations of contact lenses 63
1.7.1. In vitro toxicological test 64
1.7.2. In vivo animal test 64
1.8. Contact lens market 65
1.9. Conclusions 68
1.10. References 69
Chapter 2 76
Design of the sensing platforms 76
2.1 Contact lens patterning 76
2.1.1. Laser inscription of contact lenses 77
2.1.2. Replica molding 98
2.2. Multiphysics simulations 98
2.3. Chemical sensing 98
2.4. Readout methods 99
2.5. References 101
Chapter 3 103
Ocular Temperature Monitoring 103
3.1. Introduction 103
3.2. Materials and Methods 106
3.3. Results 107
3.4. Discussion 119
3.5. Conclusions 120
3.6. References 121
Chapter 4 124
Ocular Pressure Monitoring 124
4.1. Introduction 124

4.2. Materials and Methods 128
4.3. Results 131
4.3. Discussion 141
4.4. Conclusions 142
Chapter 5 146
Sensing Tears Analytes 146
5.1. Introduction 146
5.2. Materials and methods 149
5.3. Results and Discussion 151
5.3.1. Capillary flow along microfluidic channels 151
5.3.2. Paper-assisted flow 162
5.4. Conclusions 173
5.5. References 175
Chapter 6 177
Conclusions and future work 177
Appendix I 181
MATLAB Code for Computational Femtosecond Laser Ablation 181
Appendix II 184
Supplementary Information on Femtosecond Laser Ablation of Contact Lenses 184
Appendix III 191
Nanobuttons Design 191
Appendix IV 194
Colorimetric Sensors Readout 194
Appendix V 204
Additional Applications: Tattoo Sensors 204
Appendix VI 215
Additional Methods: Soaking 215
Appendix VII 217
Supplementary Information on Ocular Pressure Monitoring 217
Appendix VIII 222

Supplementary Information on Paper-assisted Microfluidics 222

Preface

The scope of this thesis is to unravel the potential of contact lens devices to be functionalized as sensing platforms for ocular health monitoring.

Chapter 1 of the thesis discusses the tear fluid and state of the art methods and applications of contact lenses, including materials, fabrication processes, contaminations and contact lens care, with a final section dedicated to contact lens global market and novel research applications, such as sensing and drug delivery.

Chapter 2 presents general materials and methods used throughout this work. Experimental methods include laser ablation and nanopatterning. Direct laser inscription was tested on commercial rigid contact lenses to obtain micro-patterns and microfluidic networks to analyze the tear fluid directly on-eye. Surface nanopatterning was achieved by replica molding of nano-structured silicon wafers, with applications in pressure sensing. Computational modeling based on the finite element method has been employed to predict, confirm, or visualize experimental outcomes of laser inscription, tear fluid flow within microchannels, and stress/strain behavior of polymeric nanostructures. Sensors readouts were based on the nearest neighbor model, performed using MATLAB (computer-based), Visual Studio and Android Studio (smartphone-based).

The application of these technologies is addressed in *Chapter 3*, devolved to the monitoring of the ocular surface temperature (OST). This was achieved by incorporating temperature-sensitive liquid crystals into microcavities etched in contact lenses.

Ocular pressure monitoring is discussed in *Chapter 4*. Stretchable nanostructures were integrated into soft contact lenses and used as tunable diffraction gratings.

Chapter 5 looks at another field of application of these devices, particularly the use of microfluidic networks in contact lenses for the *in situ* analysis of the tear film. This concept results from a literature

survey on the tear fluid composition, where several biomarkers and proxies were identified as potential candidates in the early-stage diagnosis and in the monitoring of multiple ocular and systemic health conditions. Two approaches were investigated for the integration of biosensors within microfluidic networks in contact lenses, namely capillary flow through the inscribed contact lens matrix, and paper-assisted capillary flow. Glucose, pH, proteins, L-ascorbic acid, uric acid and nitrites colorimetric sensing was demonstrated.

Chapter 6 draws the final conclusions and potential expansions of this work.

List of figures

Figure 1. Timeline of contact lens evolution.

Figure 2. The tear fluid.

Figure 3. Contact lens polymers.

Figure 4. Properties of contact lens materials.

Figure 5. Contact lens manufacture.

Figure 6. Contact lens design, inspection, and measurement.

Figure 7. Classification of contact lenses based on the geometrical features.

Figure 8. The most frequent refractive errors in the human visual system.

Figure 9. Eye disorders and therapeutic contact lenses.

Figure 10. Selected contact lens sensors.

Figure 11. Selected contact lenses as drug delivery systems.

Figure 12. Contact lens complications.

Figure 13. Trends on contact lens usage.

Figure 14. Femtosecond laser ablation.

Figure 15. Computational evaluation of the laser ablation process by time-resolved FEM modelling.

Figure 16. Flow valves engraved in contact lenses.

Figure 17. Flow resistors engraved in contact lenses.

Figure 18. Multi-inlet flow geometries and flow splitters engraved in contact lenses.

Figure 19. Microfluidic tear volume sensor.

Figure 20. Microfluidic contact lens as a tear uric acid sensor.

Figure 21. Contact lens temperature sensor.

Figure 22. Characterization of liquid crystal (COC/CN/CB wt%, 0.40:0.58:0.10) in the temperature range 29.0-40.0 °C.

Figure 23. Readouts, hysteresis, and time response of contact lens temperature sensors.

Figure 24. Optical characterization of a contact lens temperature sensor with four active areas.

Figure 25. Readout process tested on an *ex-vivo* porcine eye.

Figure 26. Tunable diffraction gratings as ocular pressure sensors.

Figure 27. Fabrication of PDMS nanobuttons.

Figure 28. Optical characterization setup and characterization of pattern 1 (spacing 500 nm).

Figure 29. Optical characterization of pattern 2 (spacing 1 μm).

Figure 30. Optical characterization of pattern 3 (spacing 2 μm).

Figure 31. Computation of PDMS nanostructures.

Figure 32. Color characterization of the diffraction gratings in reflection mode.

Figure 33. Microfluidic contact lenses for the colorimetric sensing of tear metabolites.

Figure 34. Characterization of the tear pH sensor.

Figure 35. Characterization of the tear glucose sensor.

Figure 36. Characterization of the tear protein sensor.

Figure 37. Characterization of the tear nitrite sensor.

Figure 38. Characterization of microfluidic contact lenses.

Figure 39. Microfluidic contact lens sensor based on paper-assisted flow.

Figure 40. Characterization of the paper tear pH sensor over the range between 5.0 and 8.0.

Figure 41. Characterization of the paper tear glucose sensor in the range between 0 and 10 $mmolL^{-1}$.

Figure 42. Characterization of the paper tear protein sensor in the range between 0 and 8.0 $mg\ mL^{-1}$.

Figure 43. Characterization of the paper tear L-ascorbic acid sensor in the range between 0 and 1.0 $g\ L^{-1}$

Figure 44. Characterization of the paper tear nitrite sensor in the range between 0 and 160 $\mu molL^{-1}$.

Figure 45. Capillary flow within the paper based microfluidic device and characterization of the tear fluid sensors embedded in the contact lenses.

Figure 46. Smartphone readouts of contact lens sensors.

Figure A1. 2D schematic of the laser setup with components.

Figure A2. Valve geometries.

Figure A3. PMMA contact angle before and after oxygen plasma treatment.

Figure A4. Resistors geometries.

Figure A5. Multi-inlet geometries.

Figure A6. Splitter geometries.

Figure A7. Contact lens sensor geometries.

Figure A8. Design of nanobuttons.

Figure A9. SEM micrographs of the 16 sets of nanostructures contained in each array.

Figure A10. Injection of colorimetric biosensors within the dermis.

Figure A11. Dermal pH sensors.

Figure A12. Dermal glucose sensors.

Figure A13. Dermal albumin sensors.

Figure A14. Multiplex dermal sensors.

Figure A15. Anthocyanin-functionalized soft contact lenses for ocular pH sensing.

Figure A16. Setup for stress/strain characterization of diffraction gratings.

Figure A17. Pressure-dependent individual angular shifts in Pattern 1.

Figure A18. Pressure-dependent individual angular shifts in Pattern 2.

Figure A19. Pressure-dependent individual angular shifts in Pattern 3.

Figure A20. Cross section of a PDMS lab-made contact lens imaged with an ooptical microscope.

Figure A21. Screenshots of the smartphone apps.

Figure A22. Percentage of RGB color at different concentration of analytes.

Figure A23. UV-dependent reflection peak trend when exposing the sensors to UV light.

Figure A24. Time response of the pH sensor at different pH values.

Figure A25. Time response of the glucose sensor at different glucose concentrations.

Figure A26. Time response of the protein sensor at different protein concentrations.

Figure A27. Time response of the L-ascorbic acid sensor at different concentrations.

Figure A28. Time response of the nitrite sensor at different concentrations.

List of tables

Table 1. Scientific collocation of this work.

Table 2. Composition of the pre-ocular tear film.

Table 3. Tear fluid biomarkers.

Table 4. Selected rigid contact lenses on the market

Table 5. Comparison between Boston RGP materials.

Table 6. Selected commercial hydrogel contact lenses.

Table 7. Some commercial silicone hydrogel soft contact lenses.

Table 8. Advantages and disadvantages of hybrid contact lenses compared to other designs.

Table 9. Applications of prosthetic contact lenses based on defective eye site.

Table 10. The microbiota in conjunctiva, lids and tears of a healthy eye, and in contact lenses of asymptomatic patients.

Table 11. Contact lens complications based on eye site.

Table 12. Key future improvements for the proposed devices.

Chapter 1

Contact Lens Technology: From Fundamentals to Applications

Contact lenses are ocular prosthetic devices used by over 150 million people worldwide. Primary applications of contact lenses include vision correction, therapeutics, and cosmetics. Contact lens materials have significantly evolved over time to minimize adverse effects associated to contact lens wear, to maintain a regular corneal metabolism, and to preserve tear film stability. This chapter encompasses contact lens technologies, including materials, chemical and physical properties, manufacturing processes, microbial contamination, and ocular complications. The function and the composition of the tear fluid are discussed, to assess its potential as a diagnostic medium. An outlook toward contact lens platforms for medical applications is provided. The regulatory standards of contact lens devices with regards to biocompatibility and contact lens market are presented. Prospects in contact lens technology are evaluated, with particular interest given to theranostic applications for *in situ* ocular health monitoring.

1.1. Introduction

The human eye is one of the most complex organs of the animal kingdom, and its retina one of the most complex tissues. The human eye can be capable of detecting a single photon.[1] However, eye dysfunctions affect a significant percentage of the modern population. According to the World Health Organization, 1.3 billion people worldwide experience visual deficiency. Among them, 189 million people have mild distance vision impairment,[2] 217 million have moderate to severe distance vision impairment,[2] 826 million people live with a near vision impairment,[3] and 36 million people are blind.[3] The majority of vision impaired individuals are over the age of 50 years, and the leading causes include uncorrected refractive errors, cataracts, glaucoma, and diabetic retinopathy. Approximately the 80% of all vision

impairment is considered avoidable.[2, 3] Eye surgery technologies to restore vision have gained popularity in the last three decades, particularly Laser Assisted In-Situ Keratomileusis (LASIK), to re-shape the cornea and restore its ability to properly focus light on the retina. However, post-LASIK ocular complications have been extensively reported,[4-7] and the most common methods currently used for vision correction remain spectacles and contact lenses.

Contact lenses are optical devices regulated by the US Food and Drug Administration (FDA).[8] Approximately 140 million people worldwide and 40.9 million people in the US use contact lenses to correct refractive errors in myopia, hyperopia, and astigmatism cases.[9] The contact lens global market is predicted to reach over 19 billion US dollars by 2024.[10] Therapeutic contact lenses are used to treat eye dysfunctions, particularly corneal irregularities, and for post-refractive surgery rehabilitation. Cosmetic contact lenses, such as colored lenses and limbal-ring lenses, are also popular, especially in Asian countries, and they are now classified as medical devices in the UK, US, China, Singapore, Malaysia, and Korea.[11-14] Contact lenses were used as smart delivery systems to achieve extended drug releasing times, and as wearable bio-sensing platforms.[12, 15-19] On the other hand, contact lens wear was found to induce adverse effects,[20] the most frequent being discomfort,[21, 22] microbial keratitis,[23, 24] allergies,[25, 26] and corneal complications.[27]

As further discussed in detail throughout this thesis, enabling contact lenses with novel functionalities presents several advantages over currently employed methods in ophthalmology, the most important of which being the possibility to target early-stage ocular diseases diagnosis, and continuous monitoring of the ocular health. In addition, contact lenses significantly reduce contamination risks associated to tear fluid analysis, currently performed with time consuming and error-prone procedures.

Table 1 summarizes the scientific collocation of this thesis within the contemporary landscape of contact lens sensing technologies. In particular, the work addresses the limitations of existing devices reported in the literature with regards to:

- **Materials**: the use of soft or rigid commercial contact lenses over lab-made devices;
- **Technology**: developing fast and efficient processes that can be standardized, to minimize inter-device variability and envision a future route to commercialization;
- **Applications**: addressing unmet needs and expand the potential use of the technology;
- **Usability**: designing readout methods that can be widely employed by non-specialists.

This work focuses on the functionalization of commercial contact lenses with 1-2 steps processes, where the core technologies are laser writing and replica molding. Despite the use of these methods having been previously reported, the unpleasant combination of materials/technology produced unpracticable results (e.g. laser writing of microfluidic structures in hydrophilic polymers).[18] The purpose of this work is further investigated in practical applications, namely tear fluid screening (composition and volume), and ocular surface monitoring (temperature, pressure). The next paragraphs present a detailed overview of the origin of contact lenses, materials, processes, market, and applications, that provides the reader with the fundamental knowledge to navigating through the result chapters.

Table 1. Scientific collocation of this thesis. The table highlights the disadvantages associated to existing technologies employed in the development of contact lens sensors.[18, 25-26, 35]

Application	Surface Modification Technology	Working principle	Lens type	Commercial contact lens material	Technological disadvantages	Reference
Tear fluid screening	Laser ablation	Microfluidics	Soft	Yes	• Microfluidics on a hydrophilic material • Low resolution	[18]
Tear fluid screening	Replica molding	Microfluidics	Soft	No (Poly-HEMA)	• Microfluidics on a hydrophilic material	[25]
Tear glucose monitoring	Replica molding	Contact sensing	Soft	No (PDMS)	• Multi-step processing • Inter-device variability	[26]
Ocular pressure monitoring	Replica molding	Microfluidics	Soft	No (PDMS)	• Multi-step processing • Lab-made contact lens • Additional materials	[27]
Ocular pressure monitoring	Replica molding	Contact sensing	Soft	Yes	• Multi-step processing (could be avoided)	Chapter 4
Tear volume sensing	Laser ablation	Microfluidics	Rigid	Yes	N/A	Chapter 2
Ocular temperature monitoring	Laser ablation	Contact sensing	Rigid	Yes	N/A	Chapter 3
Tear fluid screening	Laser ablation	Microfluidics	Rigid	Yes	• Additional materials	Chapters 5
Tear fluid screening	Laser ablation	Microfluidics	Rigid	Yes	N/A	Chapters 2, 5

Legend. Red: disadvantages; Yellow: minor disadvantages; Green: advantages; Gray: neutral; Blue: this work.

1.1.1. History of contact lenses

Leonardo da Vinci introduced the concept of contact lenses in 1508,[8] followed by René Descartes in 1636. However, both Da Vinci's and Descartes' ideas were impracticable.[28] The first pair of contact lenses was manufactured by Thomas Young in 1801.[29] John Herschel conceived the possibility to obtain molds of the cornea by impression on a transparent material.[30] In 1888, Adolf Fick successfully constructed and fitted scleral lenses for the first time. They were made of heavy blown glass, with diameters ranging from 18 to 21 mm. Fick's lenses were fitted on rabbit and human volunteers using a dextrose solution, and they allowed a maximum wearing time of two hours.[31] The development of Plexiglas in the '30s allowed to manufacture plastic contact lenses. Contact lenses made of fully plastic materials were produced by István Györffy in 1939.[28] Corneal lenses were developed in 1949, and they could be worn for 16 consecutive hours. Polymethyl methacrylate (PMMA) corneal lenses gained popularity in the 1960s.[28] However, upon realizing that the low oxygen permeability of PMMA was the cause of several adverse effects, from the 1970s Rigid Gas Permeable (RGP) materials were introduced. In 1965, Bausch & Lomb started to manufacture hydrogel contact lenses in the US,[28] which were previously invented by Wichterle and Lím in 1959.[32] The first hydrogel contact lenses appeared in the 1960s, and in 1971 the Soflens material received the first FDA approval. In 1972, disposable soft contact lenses were produced. Silicone hydrogels combined high oxygen permeability and comfort. Diverse commercial materials with similar properties followed shortly after. Nowadays, silicone hydrogels and RGP materials lead the market of soft and rigid lenses, respectively. A timeline on the history of contact lenses is illustrated in **Figure 1**.

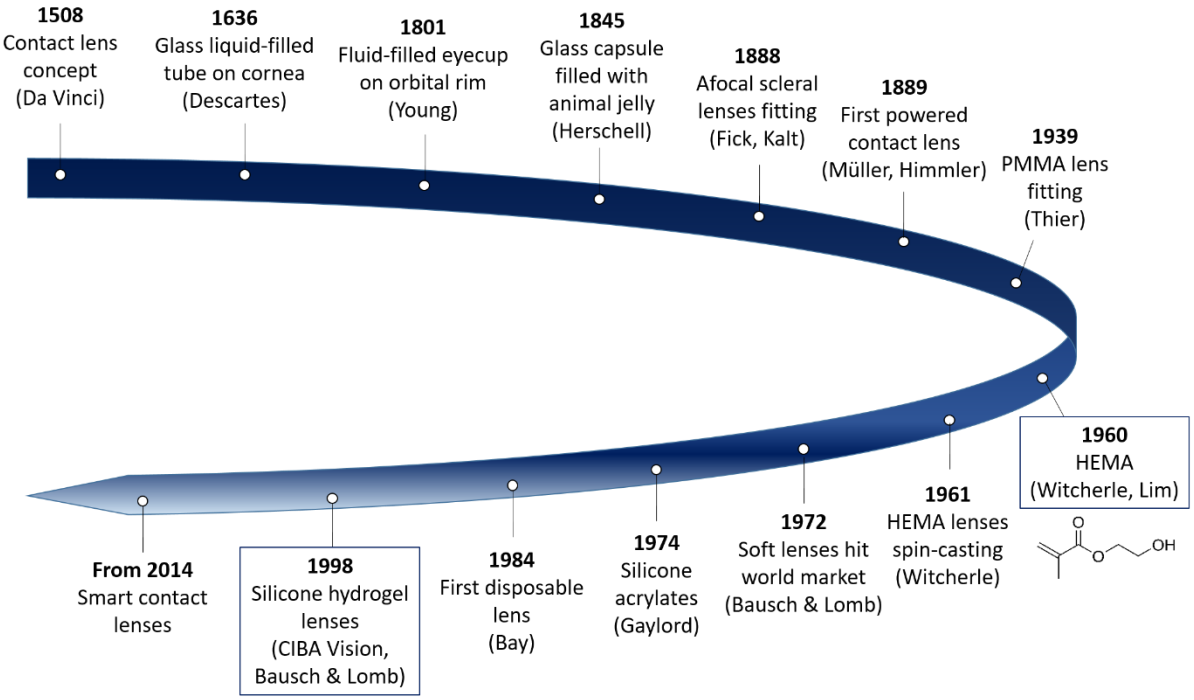

Figure 1. Timeline of contact lens evolution. The highlighted inventions of HEMA in 1960 and silicone hydrogel contact lenses in 1998 are defined as the most ground-breaking developments in contact lens history.

1.1.2. Evolution of the human eye

The first reported eye-like structure dates back to 521 million years ago, during the Cambrian explosion, in which earth has seen the first optical devices in animals in the form of eyes with lenses, followed by the first reflector around 13 years later.[33, 34] In the same period, a variety of life forms started differentiating from the worm-like animals that inhabited earth until then to most of the phyla known today, and visual systems quickly became a dominant arm in the survival game. Optical structures found in animals have been identified as multilayer reflectors, diffraction gratings, liquid crystals, light scattering structures, and natural photonic crystals.[35-37] Despite soft tissues rarely fossilize whilst maintaining the full original information, different eye structures were found in fossils,[38, 39] adding pieces to the evolution of the human eye puzzle.[39]

The human eye can be divided into two main chambers, namely the anterior and the posterior segments.[40] The anterior chamber hosts cornea, iris and lens. Vitreous, retina, choroid, optic nerve and sclera are located in the posterior chamber. The cornea acts as a protection for the front-eye side, and it focuses light into the retina. The sclera is the outer white shell, connected to the cornea via the limbus. The iris is a pigmented circular structure surrounding the pupil and adjusting its dilation together with the sphincter muscles to regulate the amount of light entering the eye. The ciliary body produces the aqueous humor, located between lens and cornea, with immunological and nourishment functions, which drains from the posterior to the anterior chamber via the pupil, maintaining an intraocular pressure (IoP) of 12 to 22 mmHg in healthy conditions.[40] The most relevant eye structures in the framework of this thesis are cornea and sclera. All contact lenses are used in direct contact to the cornea and/or the sclera.

The human vision process starts in the eye, where the optical input is received. Light enters the eye through cornea, pupil, and lens. Photons reaching the inner retina are converted into electrical signals by rods and cones, photoreceptive cells that respond to different intensities and wavelengths of light. Intrinsically photosensitive retinal ganglion cells project to the lateral geniculate nucleus, where the electrical signals travel to three sites of the visual cortex. The visual center of the eye, i.e. the line of sight, is not centered within the pupil, it can rather be found dislodged towards the left hand side.[40]

1.1.3. The tear fluid

Tears are bio-fluids that may reflect ocular and systemic physiological health.[41-45] The tear fluid nourishes the ocular surface tissues and flushes away the waste products of corneal metabolism. Tears can be divided in three main layers: the outer lipid layer, secreted by the meibomian glands, the aqueous layer, secreted by the lacrimal glands, and the mucin layer, produced by the conjunctival goblet cells.[40] The tear fluid is often referred to as the proximal fluid, which is the outer layer of the lacrimal function unit (LFU). Tear fluid can be collected with minimally-invasive procedures **(Figure 2a)**.[46] This is an advantage over body fluids such as plasma, serum and blood that need a specialized operator, and

cerebrospinal fluid or biopsy that require hospitalization.[8] The Schirmer's test is the gold standard for tear fluid collection. However, the collected fluid may be contaminated by proteins from epithelial cells. The Schirmer's test consists of placing a paper strip, known as Schirmer's strip, inside the lower eyelid for 5 minutes. The strip is further stored at -70 to -80 °C to deactivate enzymes and hydrolases found in tears. The sample can be frozen either before or after extraction, both methods showing advantages and drawbacks.[47, 48] Alternatively, tear samples may be collected with capillary tubes, made either of glass or plastics, and inserted horizontally in the lower eyelid.[46] The physical properties of the pre-ocular tear film are summarized in **Figure 2b**. The tear fluid composition can be analyzed with different techniques. The best methods for mass screening of tear proteins are considered to be SELDI-TOF-MS and LC-MALDI.[44, 45, 49] The most sensitive technique to study lipidome in tears is LC-MS,[47] to address the limitations of NMR and GC-MS. Low-weight substances are studied by MALDI-TOF-MS and LC-MS/MS techniques.[50]

The tear fluid is composed of a mixture of lipids, electrolytes, proteins, peptides, glucose, amino-acids, and O-linked carbohydrates with a protein core.[47-49] The typical protein concentration in tears is 5-7 μg μL^{-1}, given by over 1500 different proteins, the 90% of which include lysozyme, lipocalin, lacritin, and lactoferrin.[50, 51] The most complete human tears lipidome has individuated over than 600 lipid species.[48, 52] Tear lipids are involved in anti-inflammatory processes, they maintain tear film stability, reduce surface free energy, act as a barrier to the aqueous layer, and control water evaporation from the ocular surface.[52] Very low concentrations of hydrophilic metabolites were also found in the tear fluid,[48, 49] as well as vitamin A, E and of the B family (B1, B2, B3).[53-55] Different expressions of micro RNAs and mucins (MUC1, MUC5AC, MUC4, MUC16) have also been targeted as potential biomarkers to be found in tears.[47] The composition of the human pre-ocular tear film is summarized in **Table 2**. Multiple studies are currently working towards the identification of biomarkers in the tear fluid.[48] Potential tear fluid biomarkers associated with ocular and systemic disorders are summarized in **Table 3**.

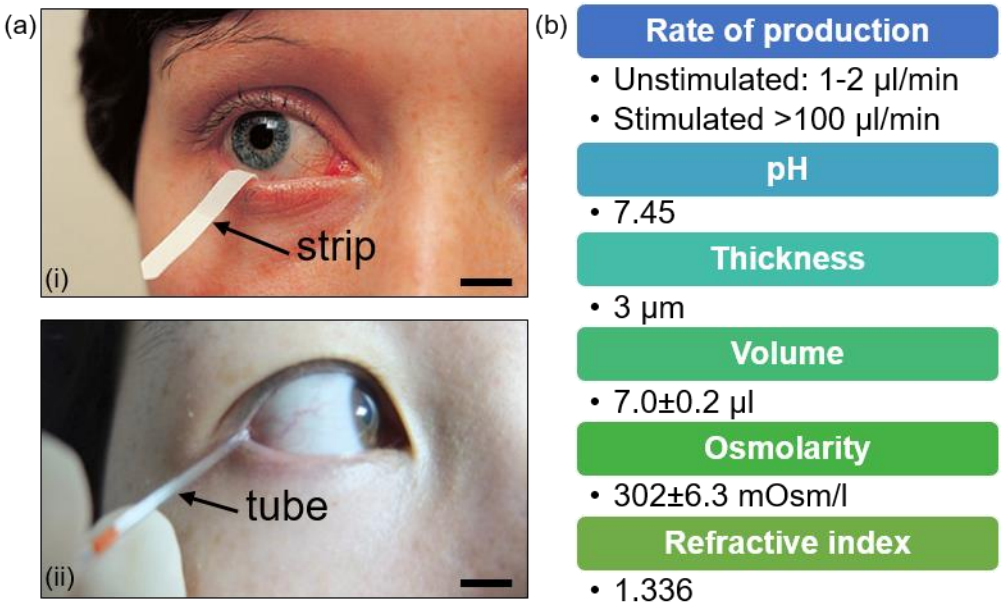

Figure 2. The tear fluid. (a) Tears collection methods. (i) Shirmer's test. Reproduced with permission.[56] Copyrights 2016, Springer Nature. Scale bar: 1.5 cm. (ii) Capillary tube. Reproduced with permission.[57] Copyrights 2017, Elsevier. Scale bar: 1.5 cm. (b) Physical properties of the pre-ocular tear film.

Table 2. Composition of the pre-ocular tear film (mEq=milliequivalent).

Components	Concentration	Ref.
Electrolytes		
Na^+	135 mEq L^{-1}	[49, 58]
Cl^-	131 mEq L^{-1}	[60]
K^-	36 mEq L^{-1}	[60]
HCO^{3-}	26 mEq L^{-1}	[49, 60]
Ca^{2+}	0.46 mEq L^{-1}	[60]
Mg^{2+}	0.36 mEq L^{-1}	[60]
Proteins	*5-7 µg µL^{-1}*	[51]
Lysozyme	2.07 g L^{-1}	[60]
Secretory IgA	3.69 g L^{-1}	[60]
Lactoferrin	1.65 g L^{-1}	[49, 60]
Lipocalin	1.55 g L^{-1}	[60]
Albumin	0.04 g L^{-1}	[49, 60]
IgG	0.004 g L^{-1}	[60]
Aquaporin 5	31.1±23.9 µg L^{-1}	[49]
EGF	5.09±3.74 µg L^{-1}	[49]
Lipids		
Wax esters	41%, 44%	[49, 59]
Cholesteryl esters	27.3%	[61]
Polar lipids	14.8%	[60]
Hydrocarbons	7.5%, 2%	[60]
Diesters	7.7%	[60]

Triacylglycerides	3.7%, 5%	[49, 61]
Fatty acids	2.0%	[60]
Free steroids	1.6%	[49, 61]

Table 3. Tear fluid biomarkers.

Complication	Biomarkers	Ref.
Dry Eye Disease (DED)	Proteins	[50,60, 61]
	Lysozyme, S100 A9/calgranulin B, Mammaglobin B, lactoferrin, LPRR3-4, Calgranulin A/S100 A8, S100 A4, lipophilin A, S100 A11, Transferrin, lactotransferrin.	
	Mucin	[62]
	(MUC)5AC	
	Neuromediators	[50, 63]
	NGF, CGRP, NPY	
	Serotonin	
	Cytokines/chemokines	[50, 65]
	Interleukins, CXCL11/I-TAC, RANTES/CCL5, EGF, TNF-α, INF-γ, MMP-9.	
	Lipids	[50, 65]
	Lysophospholipids, HEL, HNE, MDA	
	Metabolites	[50, 65]
	Cholesterol, creatine, acetylcholine, arginine, glucose, phenylalanine	
Ocular allergies	Cytokines/Chemochines	[50]
	Interleukins, eotaxin-1/CCL11, eotaxin-2/CCL24, RANTES/CCL5, TNF-α, IFN-γ.	
	Proteins	[50]
	Histamine, MMP-1, TIMP-2, Haemopexin, Transferrin, mammaglobin B, IgE.	
	Neuromediators	[50]
Keratoconus	GCDFP-15/PIP, RANTES/CCL5, MMP-13, MMP-9, IL-6, IFN-γ, Prolidase, galectin-1, galectin-3	50, [64-66]
Ocular GVHD	Cytokines/chemokines	[50, 65]

Trachoma	Immunoglobulins, EGF, TGF-β1, TNF-α	[50, 65]
Graves' orbitopathy	Interleukins, TNF-α, RANTES/CCL5	[50]
Aniridia	Zinc-α2-glycoprotein, lactoferrin, VEGF, Ap4A, Ap5A	[50]
Glaucoma	Immunoglobulins, lysozyme C, protein S100, lactotransferrin, cystatin S, MUC5AC.	[50]
Diabetic retinopathy	NGF, LCN-1, lactotransferrin, lysozyme C, lacritin, lipophilin A, TNF-α	[67-71], [72-74]
Systemic sclerosis	CFD, EGF, MCP-1, MMP-9, VDBP	[75-77]
Cystic fibrosis	IL-8, IFN-γ, MIP-1α, MIP-1β	[78, 79]
Breast cancer	Lacryglobin, cystatin SA, malate dehydrogenase, immunoglobulins, protein S100-A4, keratin II, pericentrin.	[48, 80-83]
Multiple sclerosis	IgG	[84-86]
Alzheimer's disease	Lipocalin-1, dermcidin, lysozyme-C, lacritin	[86, 87]
Parkinson's disease	α-Antichymotrypsin, TNF-α	[88-90]

1.1.4. The eye microbiota

The ocular surface is exposed to the external environment, hence to different types of microbes. Bacteria are naturally present in the ocular environment, and they act as a protection against colonization of pathogens in the eye. Three main types of bacteria populate the ocular environment in normal conditions, and they are coagulase negative *Staphylococci, Corynebacterium sp. And Propionibacterium sp.,* also known as skin-like bacteria.[91] Coagulase-negative *Staphylococci* are the most represented bacteria in the conjunctiva, lids and tears (over 50%).[92-95] Other bacteria isolated from the ocular surface in a lower percentage include *Propionibacterium sp.* and *Diphteroid* bacteria, the most common of which is *Corynebacterium sp.*[91] The broth used to culture bacteria may induce the growth of preferential strains.[96] Thioglycolate broth grows coagulase-negative *Staphylococci*, whereas blood agar plates increases the growth rate of *Corynebacterium sp.*[96] Other factors can affect the resulting dominant strain, such as growth in aerobic or anaerobic conditions,[96] culturing the conjunctiva before or after sleep,[97]

and the use of eye drops.[98] By using sequencing methods, other bacteria have been found to compose the eye microbiota.[99]

1.2. Polymers in contact lenses

Contact lenses interact with the ocular surface via the tear film, the corneal epithelium, and the conjunctival epithelium. A contact lens must allow sufficient oxygen flow to maintain aerobic metabolism, corneal homeostasis, and tear film stability. Contact lenses can be grouped in three main categories based on their composition: rigid, soft, and hybrid contact lenses.

1.2.1. Rigid lenses

Rigid lenses were the first to be introduced in the form of glass lenses.[28] Rigid contact lenses are used to address astigmatism and corneal irregularities with a variety of designs, including front-toric, back-toric, and bi-toric.[100-102] The first rigid lens was made of glass, further replaced by PMMA, obtained by MMA polymerization (**Figure 3a**). PMMA in turn exhibited substantial limitations in terms of corneal respiration, which increased the risk of undergoing ocular complications.[28] Several flexible thermoplastics were proposed to replace PMMA, including poly (4-methyl-1-pentene) (**Figure 3b**), and cellulose acetate butyrate (CAB) (**Figure 3c**).[103] Both exhibited an oxygen permeability 20 times higher than that of PMMA, and they could be fabricated by molding techniques. However, they lacked dimensional stability.[103] The oxygen permeability of silicone rubber may be up to 1000 times higher than that of PMMA, due to its silicon-oxygen atoms backbone (**Figure 3d**), but its low hydrophilicity never made it suitable to be used in contact lenses.[103]

The development of RGP materials started with the introduction of silicone acrylates, which combined the oxygen permeability of silicone with the accessible manufacture of PMMA. Examples were siloxy-methacrylate monomer (**Figure 3e**), tris (trimethyl-siloxy)–methacryloxy-propylsilane (TRIS) (**Figure 3f**), and the incorporation of fluoroalkyl methacrylates to enhance oxygen permeability.[103] Siloxy-methacrylate-based materials with enhanced wettability laid the foundations to the development of Boston

RPG materials. Among them, the additional use of methacrylic acid, and the incorporation of an itaconate ester on the traditional TRIS structure (**Figure 3g**).[103] Menicon is credited with introducing the first contact lenses with hyperoxygen transmissibility (*Dk* = 175), composed of tris (trimethylsiloxy) silyl styrene and fluoromethacrylate (**Figure 3h, i**). As of 2019, Menicon Z contact lenses were the only rigid lenses that received FDA approval for 30 days of continuous wear. Current RGP lenses on the market and their composition are summarized in **Table 4**. **Table 5** presents a comparison between commercial Boston RGP materials.[104] Rigid lenses were initially fabricated as corneal lenses or scleral lenses, with diameters ranging from 7.0 to 12.0 mm, and above 18.0 mm, respectively. Over the past decade, therapeutics drove the market towards manufacturing rigid lenses with intermediate dimensions. Nowadays, rigid lenses are used in the form of corneo-scleral lenses, with diameters ranging from 12.0 to 15.0 mm, and mini-scleral lenses, having diameters of 15.0 to 18.0 mm.

1.2.2. Soft lenses

Soft lenses are made of hydrogels, i.e. water-containing polymers, allowing better comfort and flexibility than rigid lenses. Soft lenses are 2-3 mm larger than the cornea, with a diameter of 14.5 mm. They are produced solely in the form of corneal lenses, and they lay on the cornea. Soft lens materials may be hydrogels (low-*Dk* materials) or silicone hydrogels (high-*Dk* materials).[105] Hydrogel lenses were firstly produced by polymerization of HEMA (**Figure 3j**), leading to a 40% water content.[32]

Table 4. Selected rigid contact lenses on the market.[105-108]

Manufacturer	Commercial name	Polymer	Dk
Bausch & Lomb	Boston II, IV	Silicone acrylate	12, 19
	Boston Equalens, II	Fluorosilicone acrylate	47, 85
	Boston ES, EO, XO, XO_2	Fluorosilicone acrylate	18, 58, 100, 141
GT laboratories	Fluorex 300, 500, 700	Fluorosilicate acrylic	30, 50, 70
InnoVision	Accu-Con, $HydrO_2$	Fluorosilicone acrylate	25, 50
Lagado Corporation	SA 18, 32	Silicone acrylate	18, 32
	FLOSI, ONSI-56	Fluorosilicone acrylate	26, 56
	TYRO-97	Fluorosilicone acrylate	97
The LifeStyle Company	SGP, SGP II	Siloxane acrylate	22, 43.5
	SGP 3	Fluorosiloxane acrylate	43.5
Menicon	Menicon Z	Fluorosiloxanyl stirene	163
Stellar	OP-2, OP-3, OP-6	Fluorosilicone acrylate	15, 30, 60

Table 5. Comparison between Boston RGP materials.[104]

Property	Boston Material			
	ES	EO	XO	XO_2
Refractive index	1.441	1.429	1.415	1.424
Oxygen permeability (Dk)	18	58	100	141
Oxygen transmissibility (Dk/t)	15	48	67	94
Silicone content (%)	5-7	5-6	8-9	12-13
Wetting angle (°)	52	49	49	38
Dynamic contact angle (advancing/receiving) (°)	52/50	62/60	59/58	50/40

However, hydrogel materials transport oxygen via the water channels, which limits their water content. This limitation was addressed with the introduction of HEMA copolymers, including *N*-vinyl pyrrolidone (NVP) (**Figure 3k**), the copolymerization of MMA and NVP. Nevertheless, the addition of MAA also resulted in an ultra-sensitivity to changes in tonicity, pH, and heat. A material with high wettability was produced utilizing Glyceryl methacrylate (GMA) (**Figure 3l**) with HEMA. The resulting bio-inspired material mimicked the hydrophilicity of mucins, and it was insensitive to pH variations. Commercial contact lenses based on this technology are the hioxifilcon A (Clear 1 Day lenses by Clearlab), and Proclear lens (Coopervision). Disposable soft lenses were also produced using poly vinyl alcohol (PVA) (**Figure 3m**).[105] FDA classifies soft lenses in four groups, based on their equilibrium water content (EWC) and ionic content (IC). Selected commercial hydrogel lenses are listed in **Table 6**. Silicone hydrogels were firstly introduced in 1998.[105] First generation silicone hydrogel lenses include balafilcon A, and lotrafilicon A. Reduction of surface hydrophobicity was reduced using gas surface plasma treatments. However, limitations in wettability were reported. Further generations of silicone hydrogel lenses exhibited increased water content and lower modulus, reporting a lower incidence of papillary conjunctivitis associated to contact lens wear.[105] The use of internal wetting agents eliminated the need of surface treatments.[109] Selected silicone hydrogel contact lenses on the market are grouped in **Table 7**.

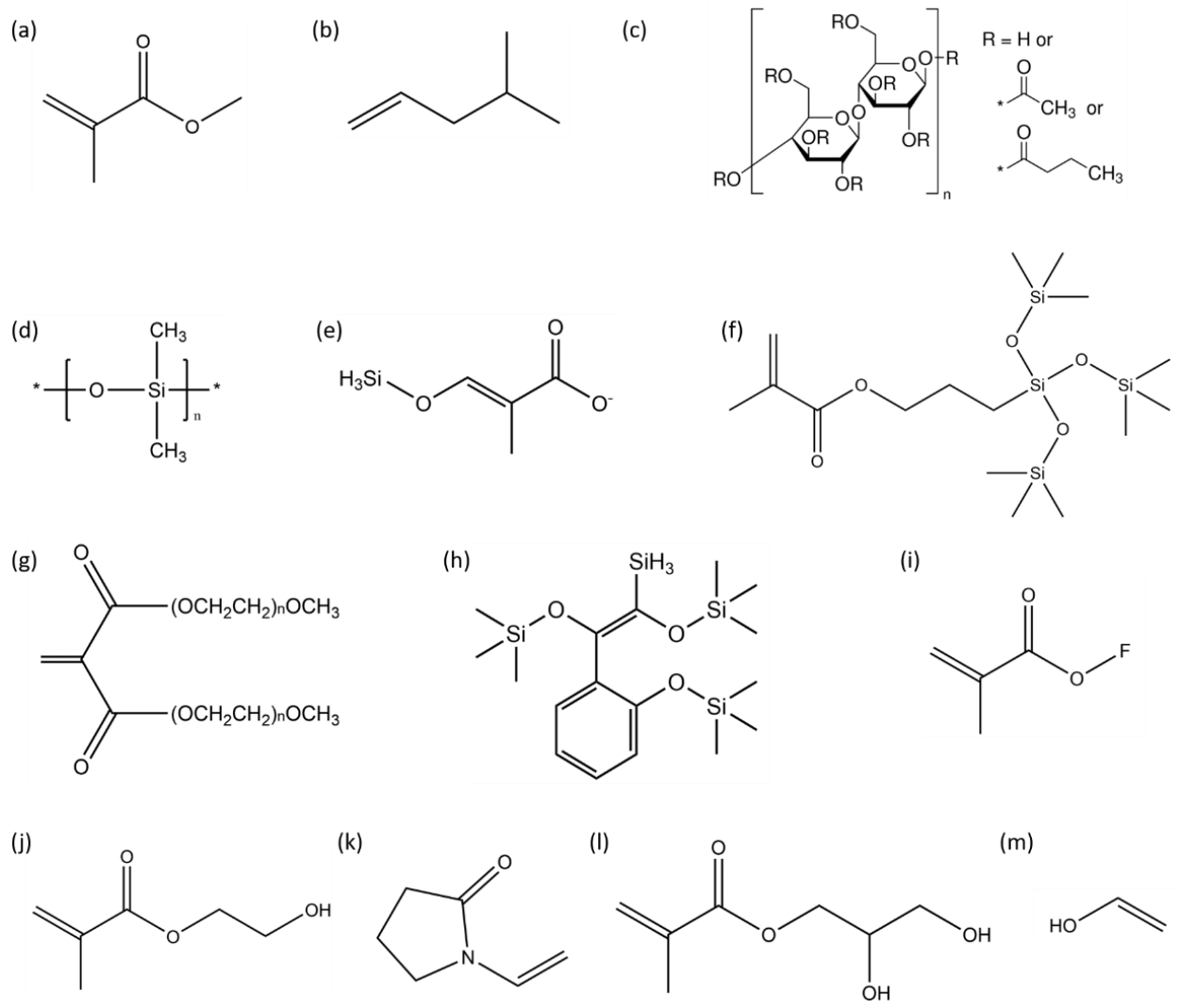

Figure 3. Contact lens polymers. a–i) Chemical structures of rigid lens polymers. (a) Methyl methacrylate. (b) 4-methyl-1-pentene. (c) Cellulose acetate butyrate (CAB). (d) Silicone rubber. (e) Siloxy methacrylate. (f) Tris(trimethyl-siloxy)-methacryloxy-propylsilane. (g) Itaconate ester. (h) Tris(trimethylsiloxy) silyl styrene. (i) Fluoro methacrylate. j–m) Chemical structures of soft lens polymers. (j) Hydroxyethyl methacrylate. (k) N-Vinyl pyrrolidone. (l) Glyceryl methacrylate. (m) Vinyl alcohol.

Table 6. Selected commercial hydrogel contact lenses.[105, 106, 108-110]

Commercial name	Supplier	Polymer Type	EWC (%)	USAN name
FDA Group I				
Durawave	UltraVision CLPL	HEMA, GMA	49	Hioxifilcon B
Menicon soft	Menicon	HEMA, VA, PMA	30	Mafilcon A
SOfLens 38	Bausch & Lomb	HEMA	38	Polymacon
FDA Group II				
Biotrue one day	Bausch & Lomb	HEMA, VP	78	Nesofilcon A
Dailies AquaComfort plus	Alcon	PVA	69	Nefilcon A
SofLens daily disposable	Bausch & Lomb	HEMA, VP	59	Hilafilcon B
FDA Group III				
Accusoft	Ophthalmos	HEMA, PVP, MAA	47	Droxifilcon A
Comfort Flex	Capital Contact Lens	HEMA, BMA, MAA	43	Deltafilcon A
Soft Mate II	CIBA Vision	HEMA, DAA, MAA	45	Bufilcon A
FDA Group IV				
1-day Acuvue moist	Johnson & Johnson	HEMA, MAA	58	Etafilcon A
Frequency 55	Coopervision	HEMA, MAA	55	MethafilconA
Permalens	CIBA Vision	HEMA, VP, MAA	71	Perfilcon A

Table 7. Some commercial silicone hydrogel soft contact lenses.[105, 106, 108, 111]

Name (USAN name)	Supplier	EWC (%)	Oxygen permeability (Barrers)	Surface treatment	Polymers
Pure Vision (Balafilcon A)	Bausch & Lomb	36	91	Oxygen plasma	NVP, TPVC, NCVE, PBVC
Dailies Total 1 (Delefilcon A)	Alcon	33 core >80 surface	140	Water surface gradient	DMA, TRIS-Am, siloxane, polyamidoamine and poly(acrylamide-acrylic acid) copolymers
Biofinity (Comfilcon A)	Coopervision	48	128	N/A	NVP, VMA, IBM, TAIC, M3U, FM0411M, HOB
Acuvue Oasys (Senofilcon A)	Johnson & Johnson	38	103	N/A	MPDMS, DMA, HEMA, siloxane macromer, TEGDMA, PVP
Premi O (Asmofilcon A)	Menicon	40	172	Plasma treatment	SIMA, SIA, DMA, pyrolidone derivative
Clarity 1 day (Somofilcon A)	Sauflon	56	60	N/A	Alkyl methacrylates, siloxane monomers, NVP

1.2.3. Hybrid lenses

Hybrid contact lenses have a central optical zone made of RGP material, surrounded by a peripheral fitting zone of a silicone hydrogel. They have a diameter of 14.5 mm and they combine the wearing comfort of soft lenses with the clearer optics of RGP lenses.[112] As of 2019, only a few companies provided hybrid lenses and they did not gain high popularity. Advantages and disadvantages of hybrid lenses over other designs are highlighted in **Table 8**.

Table 8. Advantages and disadvantages of hybrid contact lenses compared to other designs.

	Hybrid/GP	Hybrid/Soft	Hybrid/Scleral
Advantages	More comfortable. Quicker adaptation. Easier to center. More stable vision. Vaulting. Firm positioning. Lower negative power. Unilateral wear.	Higher visual quality. Astigmatism correction without stabilization. Better for high order aberrations. Better for presbyopia correction in astigmatic patients.	Soft skirt conforms to scleral shape. Less chance of seal-off. Lower clearance. Higher oxygen permeability. Reduced fogging.
Disadvantages	More difficult to apply and remove. Longer time to settle. More frequent replacement.	Higher costs. Difficult to fit. More difficult to apply and remove.	Longer time to settle. More difficult to fit in irregular corneas. More frequent replacement

1.3. Properties of contact lens materials

Ideal properties for a contact lens material are durability, stability, clarity of vision, and the ability to preserve corneal metabolism by allowing a sufficient oxygen flow to the cornea.[112, 113] Properties of contact lenses may be grouped in mechanical, optical, and chemical. Contact lenses are also defined and designed considering a range of geometrical properties, extensively described elsewhere-[110, 114-117]

1.3.1. Chemical properties

Chemical properties with the highest significance with regards to contact lens polymers are wettability, water content, oxygen permeability, and swell factor. The surface properties of a polymer determine the way it interacts with the tear fluid.[118] *In vivo* wettability is evaluated by tear film break-up time and interferometry tests, and it reflects the ability of the contact lens to keep a stable tear film within the ocular

surface. *In vitro* wettability is assessed by evaluating the contact angle at the solid-liquid-air interface, and measuring the hysteresis, i.e. the difference between advanced and receding contact angle. **Figure 4a** displays a contact angle measurement on a hydrophobic contact lens surface.

The equilibrium water content (EWC) of a hydrogel lens is described by:[105]

$$EWC = \frac{weight\ of\ water\ in\ polymer}{total\ weight\ of\ hydrated\ polymer} * 100 \qquad \text{(Eq. 1)}$$

The EWC of a hydrogel is influenced by environmental conditions, pH, tonicity, and temperature. The International Organization for Standardization (ISO) defines the regulatory standards for EWC measurements in contact lens hydrogels. Both thermogravimetry and back-calculation by refractive index measurements are considered valid techniques for EWC assessment.[111]

The oxygen permeability is indicated as *Dk*, where *D* is the diffusivity and *k* is the solubility of the material.[103, 105] Hydrogels transport oxygen *via* water channels and their oxygen permeability is closely related to temperature and to the EWC, according to the following equation:[105]

$$Dk = 1.67e^{0.0397EWC} \qquad \text{(Eq. 2)}$$

The amount of oxygen transported from the anterior to the posterior surface $O_{2,\,A\,\rightarrow P}$ of a lens can be calculated dividing the oxygen permeability *Dk* by the lens thickness *t*:[105]

$$O_{2,A\,\rightarrow P} = \frac{Dk}{t} \qquad \text{(Eq. 3)}$$

Oxygen permeability and EWC are closely dependent on each other. **Figure 4b** presents the variation of *Dk* as a function of EWC in silicone hydrogels and hydrogels.

Another important parameter of a contact lens is the swell factor, which is a measure of the dimensional stability of a hydrogel lens.[105] The swell factor is influenced by temperature, pH and tonicity, and it is described by the following relationship:[108]

$$SF = \frac{wet\ dimension}{dry\ dimension} \qquad \text{(Eq. 4)}$$

Hydrogels swell anisotropically. Their radial swell factor can be obtained by:[105]

$$SF_{rad} = 2 * \frac{SF_{dia}}{SF_{ax}} \quad \text{(Eq. 5)}$$

where SF_{rad} is the radial swell factor, SF_{dia} is the diametral swell factor, and SF_{ax} is the axial swell factor.

1.3.2. Mechanical properties

The mechanical properties of contact lenses determine their comfort, visual performance, fitting methods, and durability. Soft lenses are obtained with wettable polymers which properties change with water content.[103, 105] Mechanical testing involves applying a stress (compression, tensile or shear) and observing the resulting strain. Contact lens polymers are mechanically characterized by their stress–strain curve, and their Young's modulus is defined by the formula $E = \sigma * \varepsilon^{-1}$, where σ is the applied stress, and ε is the corresponding strain.[120] The modulus of rigid lens materials amounts to 10 GPa,[103] whereas hydrated soft lenses have modulus of 0.2 to 1.5 MPa.[105] The increased content of siloxy-methacrylates in RGP materials confers them a higher oxygen permeability, but it reduces their dimensional stability.[103] Another parameter to be evaluated in contact lenses is the friction exerted between eyelid and contact lens. The coefficient of friction (CoF) of a contact lens is defined as the ratio of the sliding force to the normal force that keeps the two surfaces together. There is no standard reference value due to the difficulties in replicating an eye environment, and the optimization of this parameter is currently under investigation.[103, 105]

1.3.3. Optical properties

Optical properties of contact lenses are crucial characteristics to provide a good visual performance. The most important optical parameters of a contact lens are optical transparency and refractive index of the polymer. Hydrogels have a light transmission >90%.[105] Sometimes micro-phase separation of water occurs, negatively affecting hydrogels transparency by creating zones with different refractive indexes. Ideally, the refractive index of a contact lens matches the one of the cornea (1.37).[103] The refractive index is measured using an Abbé refractometer.[111] Fluorosilicone acrylate lenses have a refractive index of

1.42-1.46, and silicone acrylates have a refractive index above 1.460.[103] The refractive index of PMMA is 1.49.[105] Commercial contact lenses with higher refractive indexes (1.51-1.54) include Optimum HR (Contamac) and Paragon HDS HI (Paragon Vision Science), being advantageous in aspheric multifocal designs.[109]

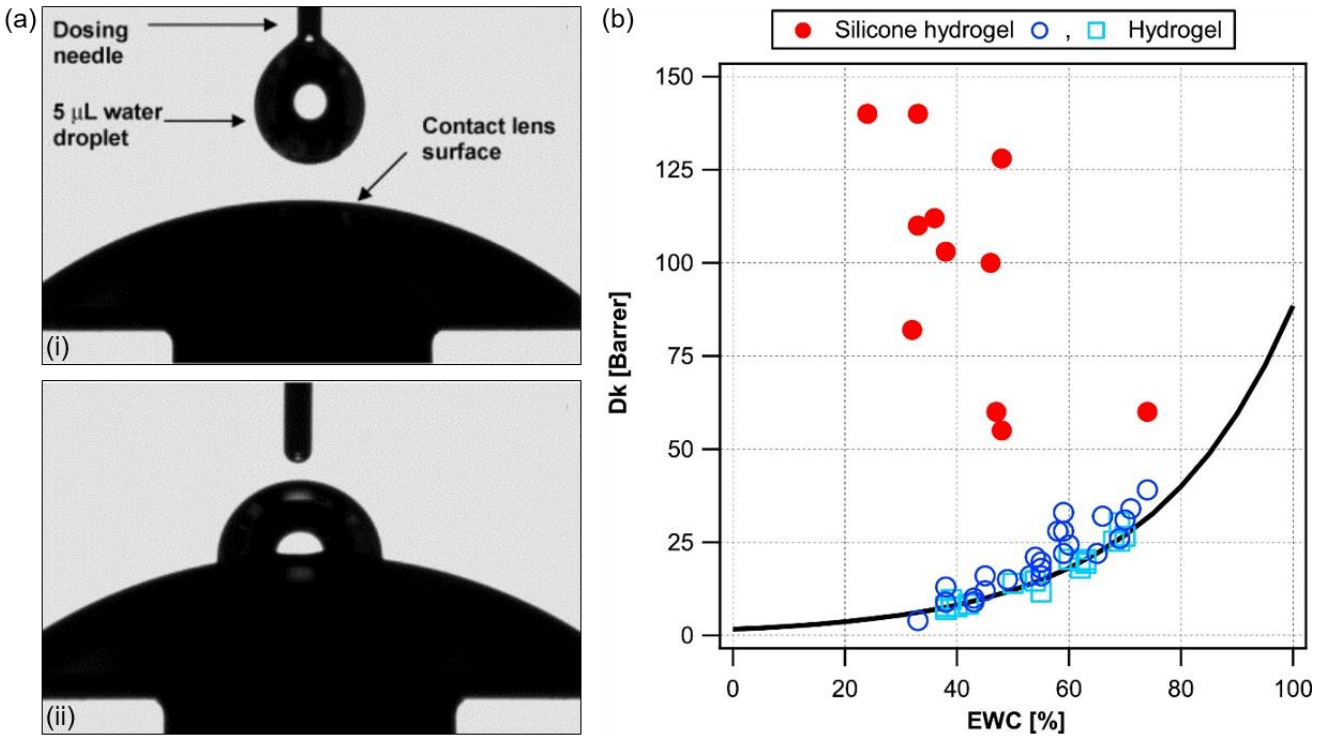

Figure 4. Properties of contact lens materials. (a) Wettability evaluated by contact angle measurement. Reproduced with permission.[119] Copyright 2014, Elsevier. Scale bars: 2.0 mm. (b) Equilibrium Water content and oxygen permeability. Reproduced with permission.[120] Copyrights 2017, Elsevier.

1.4. Contact lens manufacture

Contact lenses are manufactured by shaping a plastic material into specific curvatures, namely the central anterior curve (CAC) and the central posterior curve (CPC). Contact lenses may be manufactured by either molding or lathe cutting. Molding is an additive process that consists of curing a solution inside a lens-shaped mold, and it is used for mass-production in general prescriptions. Lathe cutting is a subtractive process where a blank of material is modelled to the desired shape for individual prescriptions.[106, 121]

1.4.1. Molding

The molding process is primarily dedicated to soft lenses fabrication. It can be done by spin casting, compression, or injection.[106] The first soft lenses were obtained by spin casting. Compression molding was used in the past for PMMA lenses fabrication, but it has now fallen out of fashion.[121] Nowadays, individually packaged, disposable soft contact lenses are mass-produced by spin casting and injection molding. The spin casting process is illustrated in **Figure 5a**. The contact lens solution is spun at a controlled speed inside a mold, resulting in the liquid being uniformly spread all over the mold, followed by UV curing. The resulting lens is peeled off, edged, and hydrated. Lenses are then autoclaved and packaged. The injection molding process (**Figure 5b**) is equivalent to spin casting, but the lens is shaped by using a two-pieces mold. In injection molding, the molten plastic is injected into the mold under pressure and cured under UV irradiation. The lens is peeled off, cooled, and finished on a lathe. Contact lenses are finally softened by hydration prior to undergoing quality assurance tests.

1.4.2. Lathe cutting

Lathe cutting is primarily adopted in customized rigid lenses production, but soft lenses can be also fabricated by lathe cutting in a similar manner. The fabrication of rigid lenses by lathe cutting is illustrated in **Figure 5c**. In a first step, back and front surfaces are etched and polished. The blank is centrally mounted on a micro-lathe where the diameter is reduced to 0.10-0.15 mm above the final diameter of the lens. The back-optic zone radius (BOZR) is cut using a diamond tool and further polished using a double rotation technique. Subsequently, fine diamond-coated tools are used to generate secondary and peripheral curves. BOZD and peripheral diameters are measured using a band measuring magnifier. Peripheral curves are left unpolished until the very last stage of production, to avoid damaging the blank. The blank is removed from the button, it is cleaned and mounted by its back surface on a chuck, where the front optic radius is cut with a diamond tool. At this stage, the lenticulation of positive powered lenses takes place. In positive lenses, the lenticulation is polished before the front optic, whereas in negative lenses the optics is polished before the lenticulation to control power adjustments more accurately. The hard lens

is ready for the next steps, whereas the soft lens needs to be hydrated and cleaned. Subsequently, edge and peripheral curves are shaped and polished. The dry lens is mounted on a hot chuck with the concave surface facing up and centered on a rotating vertical spindle. A razor blade is used to reduce the diameter and to shape the lens, from the back surface to the lower front surface. Peripheral curves are polished and blended, and the edges of the lens are then polished. The lens is removed from the chuck, rinsed, dried, and inspected. The lens is now fully fabricated. When dealing with soft lenses, any error will be increased by a multiple of the linear expansion ratio when the lens will be hydrated, thus special measures to avoid hydrate before completion need to be taken. The polish material used must be water-free. The dehydrated lens must be cleaned in an ultrasonic bath of solvent prior to hydration, and the lens needs to be sterilized in an autoclaving process. After the front and back surfaces are shaped with automated cutting tools, the lens is hydrated. Hybrid lenses in a very similar fashion to lathe cutting of soft contact lenses, but the blanks feature a GP center bonded to the surrounding non-hydrated soft material. Peculiar shapes, such as toric and bifocals, are addressed with similar machinery after preparation of a suitable blank.

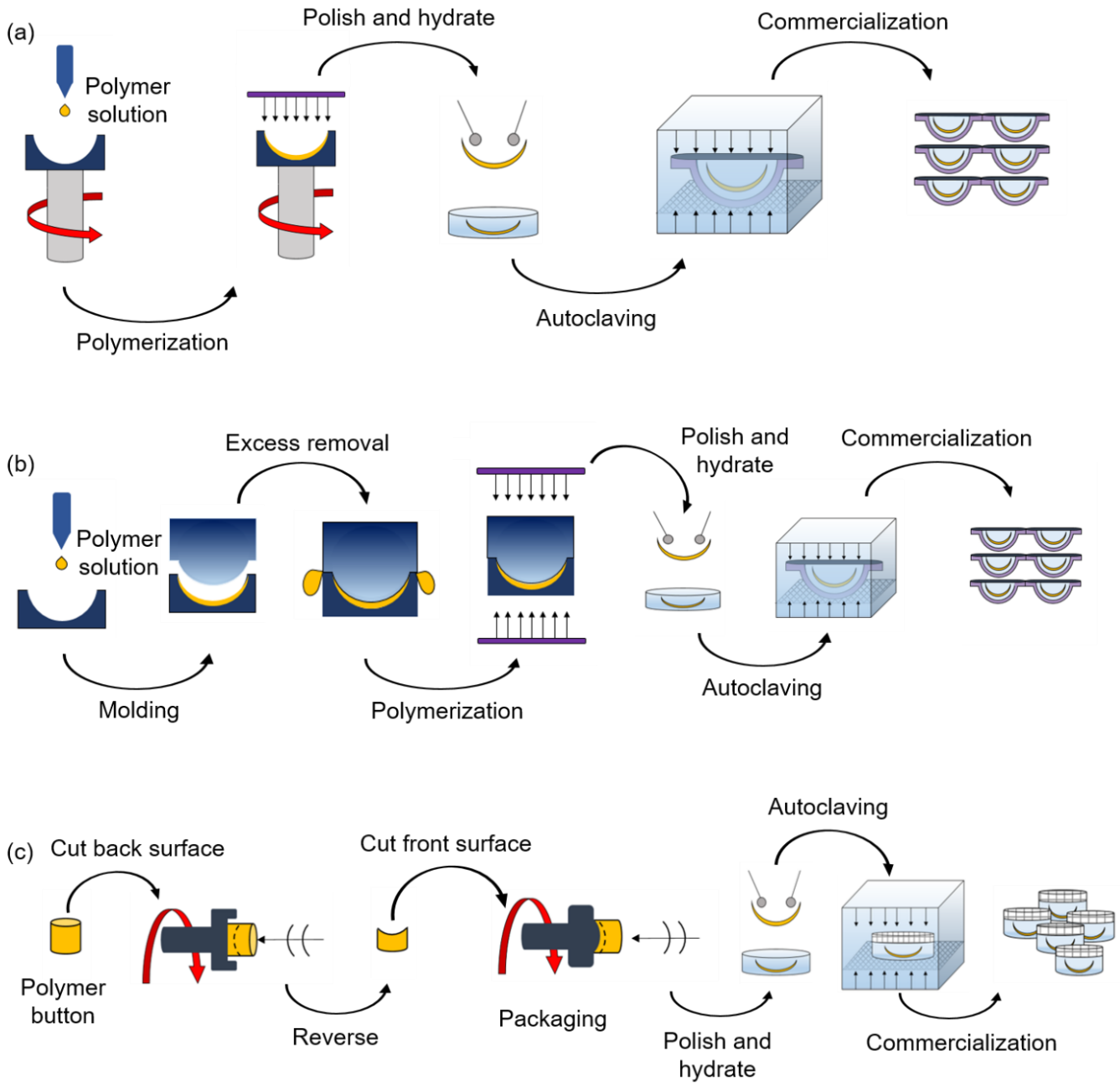

Figure 5. Contact lens manufacture. (a) Mass production of soft contact lenses by spin-casting. The mold is mounted on a spinning cylinder, where the contact lens solution is poured. The solution is further polymerized via UV light exposure, resulting in a lens-shaped piece. The lens is peeled off and refined, and the edges are polished. The contact lens is hydrated in a saline solution, inspected, packaged in a blister, sealed, and autoclaved. Contact lenses are ready to be dispatched. (b) Production of individually packaged contact lenses via injection molding process. The contact lens solution is poured on the concave piece of the mold, and the complementary convex mold is pressed over the concave mold until reaching full contact. The excess polymer is squeezed out, followed by polymerization under UV light. The resulting contact lens is peeled off, the edges are polished, and the lens is hydrated in a saline solution. The lens is placed in a sealed blister, and autoclaved. Contact lenses are ready to be dispatched. (c) Contact lens manufacture by lathe cutting. A button-shaped dry polymer is inserted in a

spinning, where back and front surface are cut using a diamond tool. The lens is removed from the lathe, inspected, edge-polished, and hydrated in a saline solution. The lens is transferred into a glass vial containing a saline water solution, sealed, and autoclaved. Contact lenses are ready to be individually dispatched inside the same glass vials, right after autoclaving.

1.4.3. Quality control and packaging

Finished lenses undergo quality assurance tests prior to be introduced in the market.[106, 121] Diameter and curvature are measured with automated tools. After inspection and measurement, the lens is sterilized. **Figure 6a** displays the measurement of the contact lens diameter using a v-gauge. Commercial contact lenses are packaged in glass or plastic vials containing a saline solution. When defects are found in the lens during quality control, the lens cannot be commercialized. Examples of defects include the presence of excess material, notches, tears (intended as the name of a particular type of defects), edge roughness, splits, blemishes, and the more evident lens breakage into multiple pieces (**Figure 6b-e**). Defects may also be intentionally produced within a contact lens, for customized applications. An example is the notching of scleral lenses, which consists of etching an additional part of the lens in a specific area, to avoid physical contact between the lens and the injured scleral area of the patient's eye. Lab-made contact lenses for diverse research purposes have been fabricated with multiple customized methods, mostly inspired to spin casting and injection molding techniques. Hydrogel contact lenses were recently fabricated using eyeball molds immersed in a petri dish containing a hydrogel, followed by polymerization and cutting.[122] In the majority of cases, injection molding is used to fabricate contact lenses based on novel solutions incorporating sensing properties.[123-125]

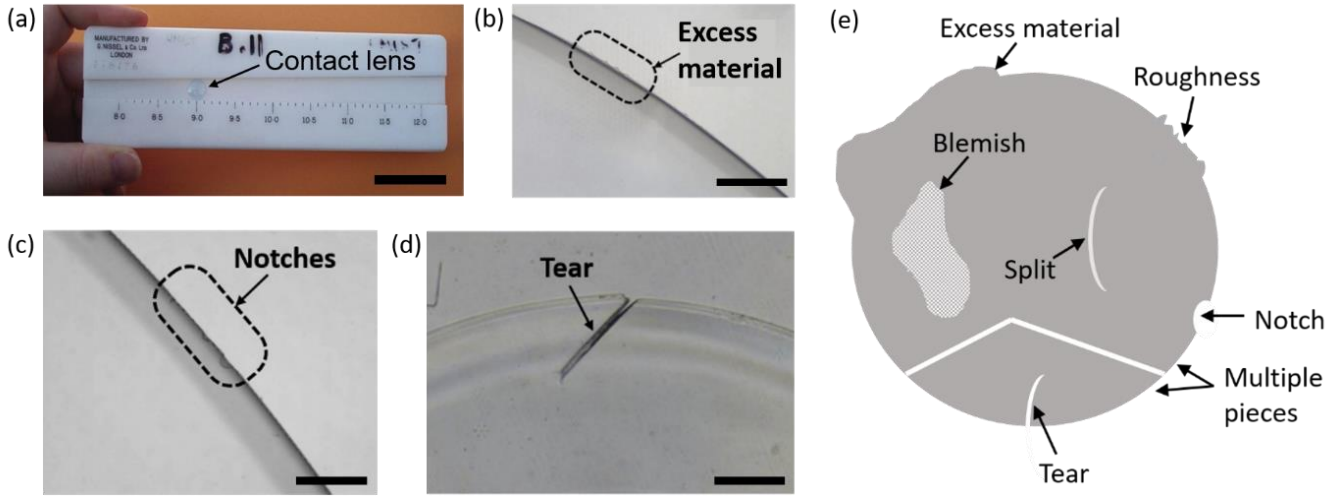

Figure 6. Contact lens design, inspection, and measurement. (a) Measuring the diameter of a contact lens using a v-gauge. Reproduced with permission.[111] Copyright 2018, Elsevier. Scale bar: 4 cm. (b-e) Contact lens fabrication defects. (b) Excess material. Scale bar: 5 mm. Reproduced with permission.[109] Copyright 2018, Elsevier. (c) Notches. Scale bar: 5 mm. Reproduced with permission.[109] Copyright 2018, Elsevier. (d) Tear. Scale bar: 3 mm. Reproduced with permission.[109] Copyright 2018, Elsevier. (e) Illustration of the most common defects found in contact lenses.

1.5. Applications

The intended use of contact lenses drives their design and materials. Contact lenses are classified in corneal, mini-scleral, and scleral, according to their diameter (**Figure 7**). Contact lenses are also classified in corneal, mini-scleral, and scleral based on the ocular structure they lay on. Hence, rigid lenses may be corneal, mini-scleral, and scleral. Note that mini-scleral rigid lenses are sometimes called scleral lenses. Soft and hybrid lenses only exist with a diameter of 13.0 to 14.5 mm, and they are referred to as corneal lenses because they are mechanically hold by the cornea. Primary applications of contact lenses are the correction of refractive errors, prosthetics, and therapeutics. Novel contact lenses are being used as sensing platforms and as vehicles for ocular drug delivery, exploring their potential to be adopted as theranostic devices. The versatility and the popularity of contact lenses make them suitable to be used as smart platforms in personalized medicine.[8, 15] The functionalization of contact lenses for ocular drug delivery allows to achieve slow releasing times.[126, 127] Integrating sensors within contact lenses has a

broad range of applications, including continuous health monitoring,[8, 12] wearable displays.[128] and minimally-invasive screening methods.[16, 19] Contact lenses produced with new technologies may also improve the performances of existing applications. Switchable liquid crystal contact lenses were developed as an alternative to bifocal contact lenses for presbyopia correction.[129] Photochromic contact lenses were developed to adapt the wearer's vision at different sunlight levels,[130] and to block ultra-violet (UV) radiation.[131] Contact lenses for color vision deficiency (CVD) were obtained by submerging the lenses in a color filtering dye.[132]

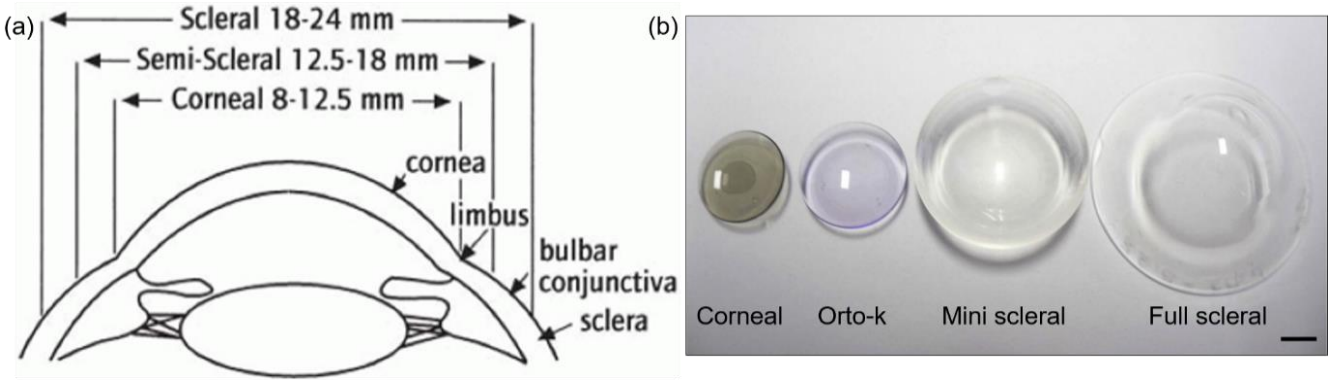

Figure 7. Classification of contact lenses based on the geometrical features. (a) Diagram displaying the difference between scleral, semi-scleral (also called mini-scleral), and corneal lenses. (b) Photograph of corneal, orto-k, mini-scleral, and full scleral lenses. Scale bar: 5.0 mm. Reproduced with permission.[133] Copyright 2017, Elsevier.

1.5.1. Refractive disorders

Eye disorders of refractive nature consist of the inability to focus light on a single focal point on the retina, leading to poor visual performances. All refractive errors result from a re-shape of the eyeball, which can occur because of genetic predisposition, environmental factors, and visually intensive occupations. Refractive errors are one of the most common causes of blindness, along with cataracts, macular degeneration, and vitamin A deficiency. An eye free from refractive errors is defined as emmetropic. An eye that needs accommodation to properly focus light on the retina is called ametropic. In optometry, an object is defined as distant when it is located beyond 6.0 meters from the eye. Considering the limitations

of the human visual system, 6 meters is considered as the threshold beyond which the light impinges on the eye in the form of parallel rays. On the contrary, an object is defined as near when it is located at a maximum distance of 6.0 meters from the eye. The most common forms of ametropias are myopia or near-sightedness, hyperopia or far-sightedness, and astigmatism.[2, 3, 6] The myopic eye features an elongated eyeball that focuses light anteriorly to the retina, leading to blurred vision of distance objects. Myopia is the most common among refractive disorders, whereas hyperopia primarily affects children and elder individuals. The eyeball of a hyperopic eye is shortened, and it focuses light beyond the retina, leading to a blurred vision of near objects. The cornea of the astigmatic eye features an irregular shape that focuses light on multiple focal points, resulting in a stretched vision. The astigmatic eye features a higher optical power across one meridian. The corneal shape is approximated to a cylinder having an axis defined by the angle between the high-performance meridian and the horizontal. This results in a vision quality dependent on the spatial orientation. Another leading refractive disorder is presbyopia, induced by a functional loss of ciliary muscles in the elder eye, which causes the inability to sufficiently shape the lens to adjust the focal power needed to properly focus the light entering the eye on the retina. This results in a hyperopia-like visual deficiency, with near distance objects appearing blurred. Presbyopia affects most people over the age of 35.[2, 3] Refractive errors are corrected with eyeglasses, contact lenses, or LASER surgery, and they are diagnosed by eye examination comprising an objective refraction test using a retinoscope, and a test by elimination, known as subjective refraction. The latest consists of applying glass or plastic lenses with different optical powers to the exterior of the eye, until the one that produces an optimal vision is identified.

Contact lenses can provide a wider field of vision than spectacles, and they are convenient in a series of circumstances where eyeglasses wear is not recommended. Examples include sport activities, humid environments, and situations where a wide field of vision is necessary (e.g. driving). However, spectacles are an external, non-invasive method to correct eye refractive errors, and they are preferred in some cases. LASER refractive surgery permanently changes the shape of the cornea to restore visual capabilities.

Figure 8 presents the most common eye refractive errors and their correction via convex or concave lenses. Nearsightedness and farsightedness correction are addressed using concave and convex lenses respectively, to diverge/converge light rays prior to reaching the cornea. Presbyopia can be corrected with bifocal or progressive lenses. Astigmatism is addressed with cylindrical lenses, to induce refraction of light in a preferential meridian.

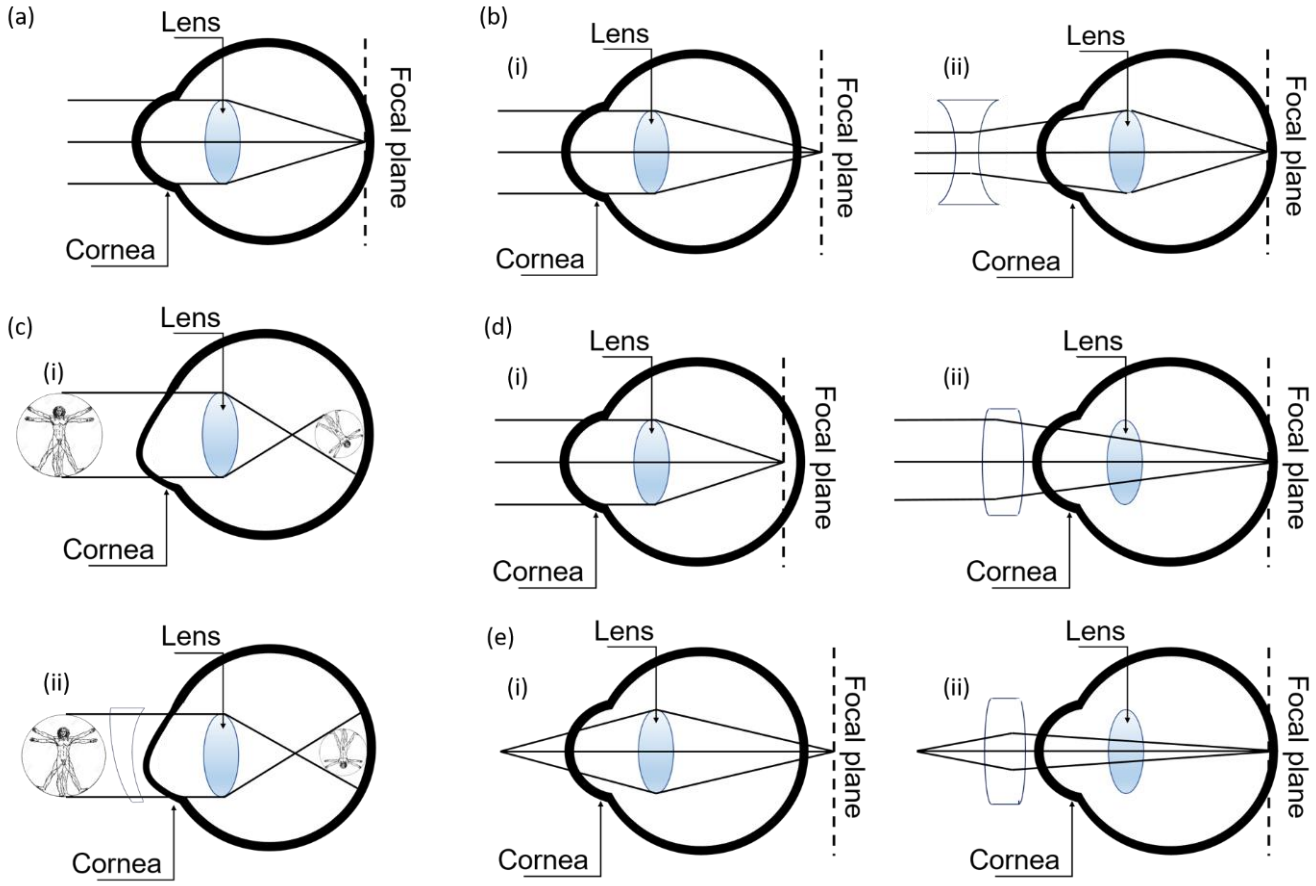

Figure 8. The most frequent refractive errors in the human visual system. (a) Normal vision or emmetropia: light focuses on the retina in a single focal point. (b) Presbyopia: the lens hardens with age losing the ability to modulate its shape. (c) Hyperopia or far-sightedness: light focuses on a focal point posterior to the retina. (d) Myopia or near-sightedness: light focuses on a focal point anterior to the retina. (e) Astigmatism: light focuses on multiple focal points, resulting in blurred vision.

1.5.2. Prosthetics

An important slice of contact lenses market is reserved to tinted contact lenses with prosthetic purposes. They are used to aid the management of aniridia, ocular albinism, leukoma, diplopia, and iris atrophies.[40, 41] Prosthetic lenses are produced in different designs, including pupil and iris occlusion, clear iris, and clear pupil. Diameters can be varied according to the prescription. Soft tinted lenses may be produced with pupil and iris occlusion, and iris pigment on the frontside. Patients who have permanent dilated pupils may use front-painted, iris-occluded lenses. Patients who have dark iris color may choose a black iris occlusion lens. Pupil-occluded lens feature a black central area to reproduce the shape and color of a regular pupil, and they do not provide any vision.[134, 135] They may be used to hide a white pupil, for vision occlusion, or for the correction of aesthetic defects in a blind eye. Prosthetic contact lenses may be soft or rigid. The most diffused types of prosthetic lenses are translucent tinted lenses, computer-generated printed lenses, and hand painted lenses. Translucent tinted lenses feature a homogeneously colored iris, and they offer a low degree of customization. Pigments are not dense enough to provide a good contrast in patients with light colored iris. Computer-generated lenses can be designed in specific colors and diameters. Pupil and iris occlusion can be achieved, as well as dark or light back iris occlusion. Limitations are the predefined colors and geometrical parameters. Hand painted lenses have the highest degree of customization, and they can be produced in any diameter. Prosthetic contact lenses may be grouped based on their applications, with regards to the eye-site, as presented in **Table 9**.

Table 9. Applications of prosthetic contact lenses based on defective eye site.[136]

Cornea	Iris	Lens	Globe	Other
Leukoma	Heterochromia	Leukoria	Phthisis bulbi	Photophobia
Band keratopathy	Aniridia		Buphthalmos	Rod cone dystrophy
Advanced Arcus	Polycoria			Color deficiency
Scarring	Coloboma			Strabismus
Keratopathy	Albinism			Migraines
Microcornea				

1.5.3. Therapeutics

Therapeutic contact lenses are primarily used to provide relief of discomfort, for vision aid in eyes with irregular corneas, and to heal injured ocular tissues. Therapeutic contact lenses as drug delivery vehicles will be individually addressed in the next subsections. Soft contact lenses are used to aid the management of post-refractive surgery eyes that under epithelial removal, and in corneal degenerations. The high oxygen permeability of silicone hydrogels allows to minimize the induced hypoxic stress. Silicone hydrogel lenses are largely used in post- photorefractive keratectomy (PRK) and laser-assisted subepithelial keratomileusis (LASEK), and they reported better results when compared to hydrogels. Rigid lenses are used as therapeutic devices to correct corneal abnormalities and eye disorders related to deficiencies of the tear film. The most common corneal abnormalities are keratoconus, keratoglobus, and cornea plana. **Figure 9a** presents the different shapes of a normal cornea, a keratoconic cornea, a keratoglobic cornea, and a planar cornea. In the last decade, successful results in correcting corneal ecstasia with soft contact lenses has been achieved, but scleral lenses remain the gold standard.[137] Contact lens wear is reported to be the best existing solution to corneal aberrations, as an alternative to both surgical treatments and implantation of intrastromal corneal rings. Aqueous leakage post-surgery or

trauma can be sealed with a hydrogel or silicone hydrogel contact lens (**Figure 9b**).[137] Scleral lenses are also used for the correction of advanced Sjogren's syndrome (**Figure 9c**), associated to a dysfunction of the Meibomian glands in tear film secretion, or to a high evaporation rate of the tear film. The lens ensures the formation of a fluid reservoir over the eye, by covering the surface and limiting tear evaporation. Rigid lenses can be used to protect the cornea undergoing re-epithelialization following a chemical burn (**Figure 9d**) and to address Steven Johnson syndrome (**Figure 9e**). Rigid corneal lenses are used to protect the cornea from abnormal lashes and keratinized lid margins. Rigid scleral lenses can fit any eye shape, they provide complete protection of cornea and bulbar conjunctiva, and overnight wear can be targeted using RGP materials.[137]

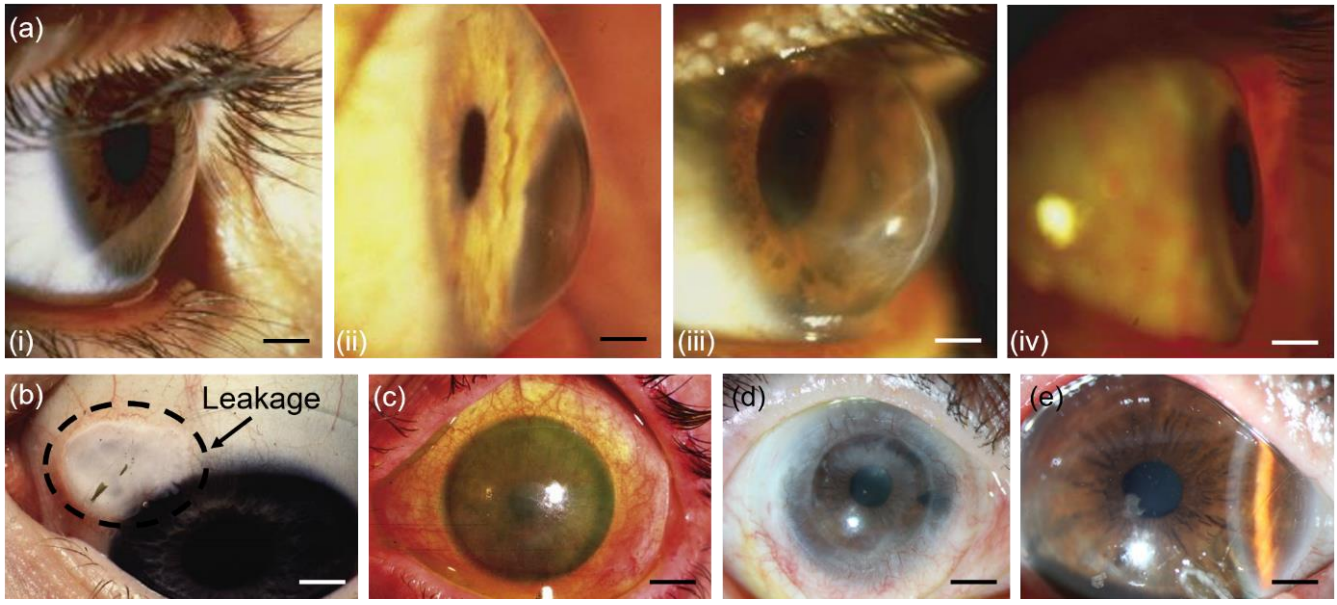

Figure 9. Eye disorders and therapeutic contact lenses. (a) Corneal shapes. (i) Normal cornea, (ii) keratoconus, (iii) keratoglobus, (iv) cornea plana. Scale bars: 3.0 mm. Reproduced with permission.[138] Copyright 2018, Elsevier. (b) Post-surgery aqueous leakage sealed with a soft contact lens. Scale bar: 1 cm. Reproduced with permission.[136] Copyright 2018, Elsevier. (c) A rigid contact lens fitted on an eye affected by Sjogren's syndrome. Scale bar: 2.0 cm. Reproduced with permission.[138] Copyright 2018, Elsevier. (d) Mini sclerals fitted on an eye with chemical burn. Reproduced with permission.[139] Copyright 2012, Elsevier. (e) Mini sclerals fitted on an eye with Steven Johnson syndrome. Reproduced with permission.[139] Copyright 2012, Elsevier.

1.5.4. Contact lens sensors

Contact lens sensors have been primarily targeted as sensing platforms for point-of-care settings in glaucoma,[8] and continuous monitoring of glucose in tears.[140, 141] The Triggerfish silicone lens was developed by Sensimed to monitor the intraocular pressure in glaucoma patients.[142] Triggerfish underwent animal test and clinical trials, and received the FDA and CE approval to be worn for 24 consecutive hours. It integrates two strain gauge sensors, a microprocessor, and a three-loop antenna. The sensor measures minute changes in the ocular dimensions through the strain gauge, recording for 30 seconds at 5 minutes intervals over 24 hours. The information is transmitted wirelessly from the sensor to the antenna, and then transferred via a wire to the recorder. The recorder is worn by the patient. The information can be retrieved from the recorder via a USB Bluetooth adapter. A single-pixel GaN LED display was integrated within a contact lens and tested in rabbit eyes, powered by a remote radiofrequency transmitter.[143] Fluorescein tests showed no corneal epithelial damages. **Figure 10a** presents a prototype of a wearable contact lens sensors for continuous glucose monitoring.[16] Microstructures with a periodicity of 1.6 were patterned on a glucose-selective hydrogel film functionalized with phenylboronic acid. Glucose binding induced a local volumetric increase, leading to a change in the Bragg diffraction. Graphene films were also used in contact lenses for various applications.[144, 145]

An example of device for full-corneal electroretinogram (ERG) recording is shown in **Figure 10b.**[144] The device consisted on a contact lens-shaped parylene covered with a graphene layer on the concave side. Graphene was CVD-grown on a lens-shaped quartz mold to avoid the formation of wrinkles. ERGs were recorded on cynomolgus monkeys with a Ganzfeld flash stimulation, resulting in negligible corneal irritation. A contact lens glucose sensor featuring a LED display was recently reported **(Figure 10c)**.[128] The lens featured a reinforced region to host LED, rectifier, and glucose sensor. A transparent AgNF-based antenna and interconnects were located on an elastic region. In vivo test on a rabbit eye showed the turn-on and off states of the LED based on glucose concentration in an injected tear fluid. Several contact lens-compatible technologies have also been investigated. A potential power source for contact lenses[146]

consisted on a lactate/O_2 enzymatic biofuel cell (EBFC), based on flexible nano-porous gold (NPG) electrodes. The EBFCs was tested in artificial tears, exhibiting a decrease in performance in tears with respect to the buffer solution due to ascorbate interference, suggesting that a coating film on the biocathode might improve the performances in future developments. The response of the EBFC was limited by current density of the biocathode, which further improvements may enable the development of a self-powered lactate biosensor where the power density is correlated to lactate concentration.

Stretchable photodetectors based on a crumpled graphene–gold nanoparticle (AuNP) hybrid structure were successfully integrated within contact lenses,[147] exhibiting a plasmonically enhanced photoresponsivity of 1200% compared to a conventional flat graphene photodetector, and mechanical stretchability up to a 200% tensile strain. A new biomaterial for bio-friendly and green optoelectronics applications was recently demonstrated with applications in soft contact lenses.[148] The lens is made of silk fibroid protein in hydrogel form for applications in light emitting diodes (LEDs). The optical properties of the resulting lens are influenced by the concentration of the protein as well as the cross-linking agent. The lens showed a light extraction efficiency over 0.95 on a white LED. Recently, a stretchable electronic platform for contact lens smart applications was developed.[18] The electronics was based on thermoplastic polyurethane (TPU) with an outer diameter of 10mm and curvature radius of 9.0 mm featuring a silicon chip, an RF antenna and thin film interconnections placed in polymeric semirigid islands. The antenna is thought to be implemented at 13.56 MHz with near-field communication protocols for smart lenses applications. In the last decades, many efforts were put in the development of materials with high transparency, oxygen permeability, and outstanding mechanical stretchability, to be utilized in contact lens sensing systems.[149-152]

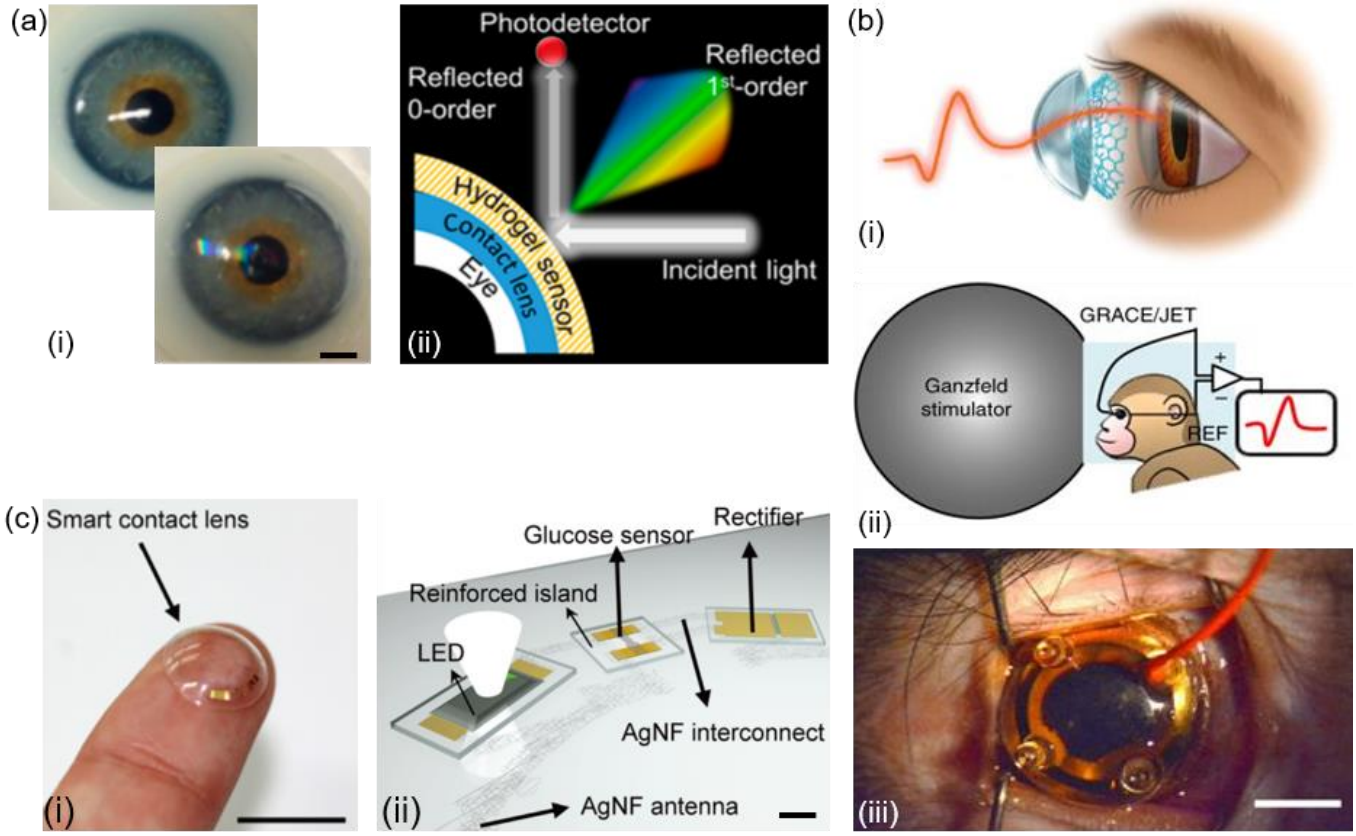

Figure 10. Selected contact lens sensors. (a) A contact lens for glucose continuous monitoring. Reproduced under the terms of the CC BY 4.0 license.[16] Copyright 2018, American Chemical Society. (b) Graphene contact lens electrode for ERG measurements. (i) Schematic drawing with ERG recording. (ii) Representation of a ffERG recording on cynomolgus monkeys with ganzfeld stimulation. (iii) Photograph of a Jet electrode applied to an eye of a cynomolgus monkey. Scale bar, 5 mm. Reproduced under the terms of the CC BY 4.0 license.[144] Copyright 2018, NPG. (c) A smart contact lens integrating wireless circuits with stretchable interconnects, a glucose sensor, and a display. Reproduced under the terms of the CC BY NC license.[128] Copyright 2018, American Association for the Advancement of Science.

1.5.5. Contact lenses as drug delivery systems

Despite being an easily accessible organ, the physiology of the eye poses hard challenges in drug delivery.[153-155] The ocular environment acts as a barrier to external organisms. Hence, ocular drug delivery must be designed to target specific tissues. Current drug delivery methods are primarily based on eye drops, emulsions, and gels. Innovative methods include implants, iontophoresis, and microneedles. Contact lenses provide a fascinating mean to achieve extended drug exposure time. Drugs can be loaded on contact lenses in different ways: soak-and-release, molecular imprinting (MI),[137] modification of lens

matrix composition, and using colloidal and nano-carriers.[127] The soak-and-release method consists on soaking the lens in an aqueous drug solution resulting in the drug being trapped in the hydrophilic matrix of the lens. This method is commonly used for delivery of anti-glaucoma drugs, antihistamines, and antibiotics.[126] The drug encounters a boost first release, followed by a gradual release. Soak-and-release method is being currently investigated for delivery of hyaluronic acid to treat dry eye disease.[153] To retard the release of hydrophilic drugs from contact lenses, Vitamin E (VE) has been incorporated into the lens matrix to act as a hydrophobic barrier.[126] Molecular imprinting consists on etching nano-cavities to incorporate functional monomers within the lens. This enhances the active area and maximize drug absorption within the lens. Using NSAIDs as a monomer, ibuprofen and antibiotics were delivered to ophthalmic tissues via contact lenses.[126] Self-responsive, molecular-imprinted contact lenses were used for the controlled release of timolol.[123] A visible color change is observable in the lens based on the amount of released drug (**Figure 11a**).

Modifying the lens matrix composition consists of obtaining specific binding sites on the surface of hydrogel lenses. Examples include hydrogel lenses with cationic functional groups to store anionic drugs and release them in physiological conditions. MAA was added to p(HEMA) lenses for extended release of naphazoline.[126] Drugs can also be incorporated into nanocarriers. Liposomes were used to carry hydrophilic and lipophilic drugs (idoxuridine, penicillin G, lidocaine, levofloxacin). Polymeric micelles were also used as nanocarriers to deliver dexamethasone acetate.[156] Cyclodextrins were functionalized to carry hydrophobic drugs.[157] Drug nanosuspensions were loaded in a contact lens for delivery of triamcinolone acetonide, showing significantly increased drug load capacity and releasing times.[158] Silicone hydrogel contact lenses functionalized with epalrestat were successful in addressing diabetic eye complications and cataract, by inhibiting aldose reductase (AR) and preventing protein glycation (**Figure 11b**).[159] Nanogels were used as timolol maleate carriers and loaded into enzyme-responsive contact lenses, for tear lysozyme-activated release of timolol maleate for the treatment of glaucoma (**Figure 11c**).[160] Nanoparticles were reported to allow extended delivery of lidocaine, timolol, meloxicam-

nanoaggregates, antibacterial silver nano-particles, antifungal agent voriconazole and indomethacin.[126] An example is presented in **Figure 11d**, where an hybrid hydrogel-based contact lens comprising quaternized chitosan (HTCC), silver nanoparticles and graphene oxide (GO) was used for the treatment of fungal keratitis in mice.[125]

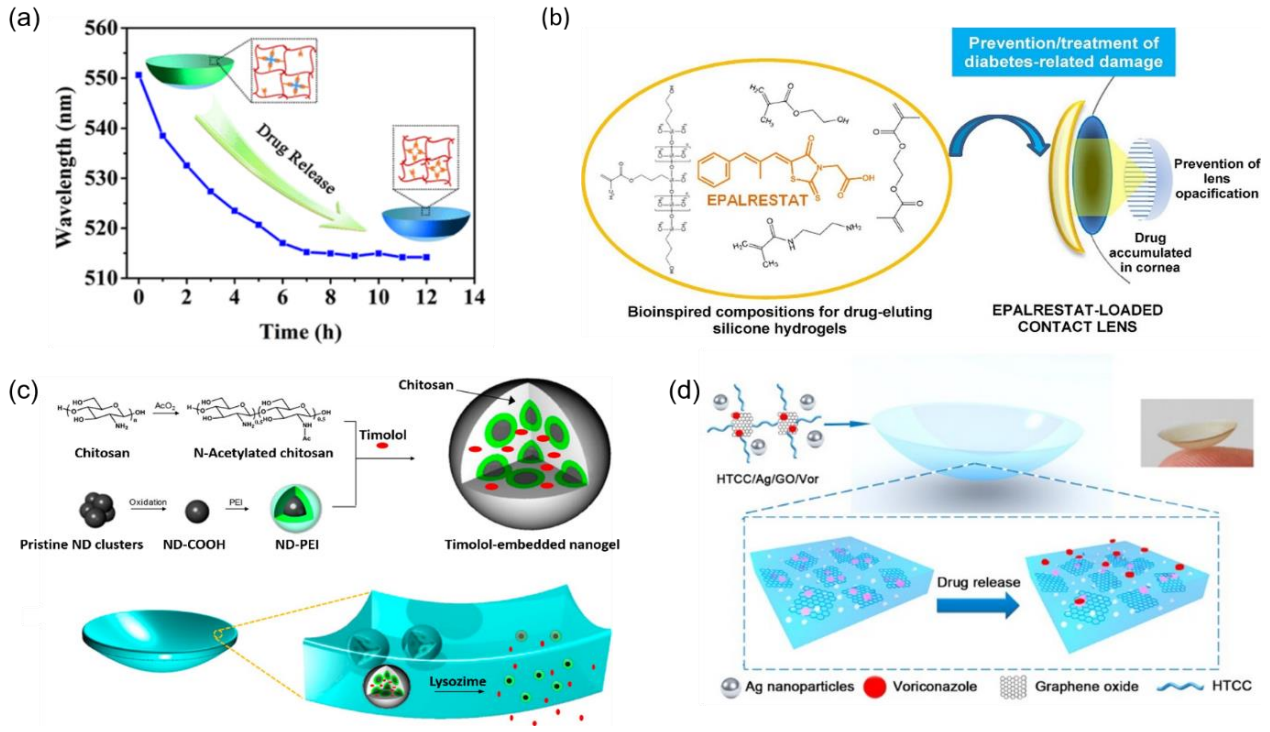

Figure 11. Selected contact lenses as drug delivery systems. (a) Self-responsive soft contact lens for timolol ophthalmic delivery, exhibiting a visible color change to monitor releasing times and quantities. Reproduced with permission.[123] Copyright 2018, American Chemical Society. (b) Bioinspired composition of drug-eluting silicone hydrogel loaded into soft contact lenses for treating diabetic eye complications. Bovine tests showed drug accumulation within the cornea. Reproduced with permission.[159] Copyright, Elsevier. (c) Lysozyme-activated drug eluting contact lens. Drugs are loaded in ND nanogels by cross-linking PEI-acoated NDs and partially N-acetylated chitosan in presence of timolol maleate. Nanogels are further embedded within enzyme-responsive contact lenses. Tear lysozyme degrades the nanogel, resulting in timolol maleate release whilst leaving the lens intact. Reproduced with permission.[160] Copyright 2014, American Chemical Society. (d) Hybrid hydrogel-based contact lens comprising HTCC, silver nanoparticles and GO to treat fungal keratitis with targeted ophthalmic drug delivery. Reproduced with permission.[125] Copyright 2016, American Chemical Society.

1.6. Contamination in contact lenses

Bacteria are highly present in nature in the form of aggregates named biofilms, i.e. dense polymeric matrices where bacterial communities are entrapped. Biofilms act as a cohesion media for microbes, and as a vehicle to exchange nutrients, enriching and strengthening the biofilm itself.[161] Cells in biofilms have been found to be 100 to 1000 times more resistant to antibiotics with respect to planktonic cells.[162] The formation of a biofilm articulates in two steps: a first temporary adhesion mediated by Van der Waal forces, followed by an irreversible adhesion with the formation of a matrix.[161] Biofilm formation by pathogenic bacterial strain is a major cause of infections in medicine,[163] dentistry,[164, 165] food processing,[166] and water treatment.[167] Surface modification is an emerging strategy either to prevent biofilm formation, or to induce bacterial detachment.[168] Microbial contamination of contact lenses is the cause of several eye diseases.[23, 95, 169] Both bacterial and contact lens material characteristics play an important role in the adhesion process. The most commonly isolated organisms from contact lenses are *Pseudomonas species, Serratia marcescens, coagulase-negative Staphylococci and Staphylococcus Aureus.*[91] Treatment of *Pseudomonas Aeruginosa* eye infections often becomes a challenge due to the ability of this bacterium to be naturally resistant to some antibiotics, and its capacity to acquire mobile genetic elements (MGEs) that induce a rapid spread of drug resistance.[161] Despite *P. Aeruginosa*'s pili and flagella have shown to be involved in the adhesion process, both piliated and non-piliated *P. Aeruginosa* adhere to contact lenses, suggesting that other factors are involved.[170, 171] The main factors influencing bacteria adhesion are cell surface hydrophobicity, strain and suspension media, with *P. Aeruginosa* being the quickest to adhere and the one isolated in the highest percentage. Bacteria with a high surface hydrophobicity adhere more than hydrophilic organisms, indeed *P. Aeruginosa* adheres more than *Staphylococcus* (132° VS 20-35° contact angles) and other strains.[170] *P. aeruginosa* isolated from cornea during keratitis adhere more than when isolated from other body parts. *P. Aeruginosa* adhesion under different media has been studied, including using PBS, nutritionally rich media and artificial tears to better simulate the ocular environment. Several bacterial strains can form a biofilm on the same surface and influence each other.[171] It has been shown that the presence of *S. epidermis* on hydrogel lenses affects

the growth of *P. Aeruginosa*, but not vice-versa. The same *P. Aeruginosa* exposed to a contact lens for a second time have shown to adhere less than at the first exposure, suggesting that a selection of cells promote adhesion.[171] Characteristics of the targeted surface are also relevant to bacterial adhesion, the main being ionicity, water content, hydrophobicity, topography, and tear protein absorption. It has been demonstrated that both *P. Aeruginosa* and *S. Aureus* adhere more to ionic hydrogel lenses.[170] An inversely proportional dependence has been observed between bacterial adhesion and water content of the surface.[170, 172] Surfactant-laden contact lenses have a higher equilibrium water content (EWC) and a lower hydrophobicity which results in less bacterial attachment.[172] A higher surface roughness has shown to favor adhesion, and contact lens wear has shown to induce surface roughness due to attachment of tear compounds. In particular, mucin, IgA, BSA, lysozyme and lactoferrin absorption enhance *P. Aeruginosa* adhesion.[172] Studies reported the ability of multiple bacteria genera to form biofilms on silicone hydrogel contact lenses in presence of dying neutrophils,[173] which can be blocked using specific contact lens solutions.[174] A portable lens-free microscope for computational sensing of *S. Aureus* on contact lenses was recently developed, with a resolution of 16 CFU μL^{-1}.[175]

Several studies demonstrated changes in the ocular microbiota of contact lens wearers.[91, 95, 98, 176] Bacterial communities of the conjunctiva and skin under the eye of 20 subjects, 9 contact lens wearers and 11 controls, were compared.[176] It resulted that dry conjunctival swabs from lens wearers featured more skin-like bacterial types, the most highly represented of which were *Methylobacterium, Lactobacillus, Acinetobacter and Pseudomonas*.[176] *Haemophilus, Streptocossus, Staphylococcus and Corynebacterium* have also been found, but they appear in lower concentrations than in non-lens wearers.[176] The conjunctival microbiota of both lens and non-lens wearers had higher concentrations of hand-like bacteria than of face-like bacteria. Overall, the eye microbiota of contact lens wearers resembles the one of the skin, suggesting that there might be a transfer of bacteria from the skin to the ocular surface via contact lenses.[91, 176] Bacteria isolated from the eyes of non-contact lens wearers and bacteria isolated from contact lenses of asymptomatic patients are summarized in **Table 10**.

Table 10. The microbiota in conjunctiva, lids, and tears of a healthy eye, and in contact lenses of asymptomatic patients.[91-99, 176]

Microbe	Healthy eye		Contact lenses
	Conjunctiva	Lids and tears	
Gram-positive bacteria			
Coagulase-negative staphylococci	**Yes**	**Yes**	**Yes**
Propionibacterium sp.	**Yes**	**Yes**	**Yes**
Corynebacterium sp.	**Yes**	**Yes**	**Yes**
Clostridium sp.	No	**Yes**	No
Bacillus sp.	**Yes**	**Yes**	**Yes**
Micrococcus sp.	**Yes**	**Yes**	**Yes**
S. Aureus	**Yes**	**Yes**	**Yes**
Stromatococcus sp.	No	No	**Yes**
Streptococcus sp.	No	**Yes**	No
Micrococcus sp.	No	No	No
Enterococcus sp.	**Yes**	No	No
Lactobacillus sp.	**Yes**	No	No
Peptococcus niger	**Yes**	No	No
Peptostreptococcus sp.	**Yes**	No	No
Gram-negative bacteria			No
Pseudomonas sp.	**Yes**	**Yes**	**Yes**
Enterobacter sp.	**Yes**	No	No
E. coli	**Yes**	No	No
Neisseria sp.	No	**Yes**	No

Proteus sp.	**Yes**	**Yes**	No
Acinetobacter sp.	**Yes**	No	No
Citrobacter sp.	**Yes**	No	No
Moraxella sp.	No	**Yes**	**Yes**
Fungi			
Fungus	**Yes**	**Yes**	**Yes**

1.6.1. Contamination of contact lens cases

Contamination of contact lens cases is reported to be a major cause of infection for contact lens wearers.[23, 177, 178] It has been found that over 90% of the subjects with contaminated case also had contaminated lens or solutions, suggesting that bacteria might be transferred from the case to the lens. Differently from contamination of contact lenses, which is primarily prompt by bacteria, contamination of contact lens cases includes bacteria, fungi, protozoa, viruses in over 70% of the cases.[177, 178] Lens cases can develop moderate or heavy contamination after two weeks of use. Biofilms in contact lens cases are thicker than the ones formed on contact lenses.[178] Bacterial diversity in contact lens cases has shown to be related to the severity of the disease. So far, a threshold defining an acceptable contamination level has not been identified. Novel case designs to reduce microbial contamination are being studied.[179] Contact lenses handled inappropriately can adversely affect most anterior ocular structures.[20, 179, 180] The most frequent complications are summarized in **Table 11.** In **Figure 12,** clinical cases of corneal staining, conjunctival redness, and papillary conjunctivitis, at different grading scales, are presented.

Table 11. Contact lens complications based on eye site.[169, 181].

Complication	Eye site
Microcysts	Corneal epithelium
Epithelial staining	
Oedema	Corneal stroma
Neovascularization	
Keratitis [25, 26]	
Bedewing	Corneal endothelium
Blebs	
Polymegethism	
Meibomian gland dysfunctions	Eyelid
Lid wiper epitheliopathy	
Blinking rate variations	
Mucin balls	Tear film
Dry eye	
Conjunctival staining	Conjunctiva
Conjunctival redness	
Papillary conjunctivitis	
Limbal redness	Limbus
Vascularized limbal keratitis	
Limbal stem cells deficiency	

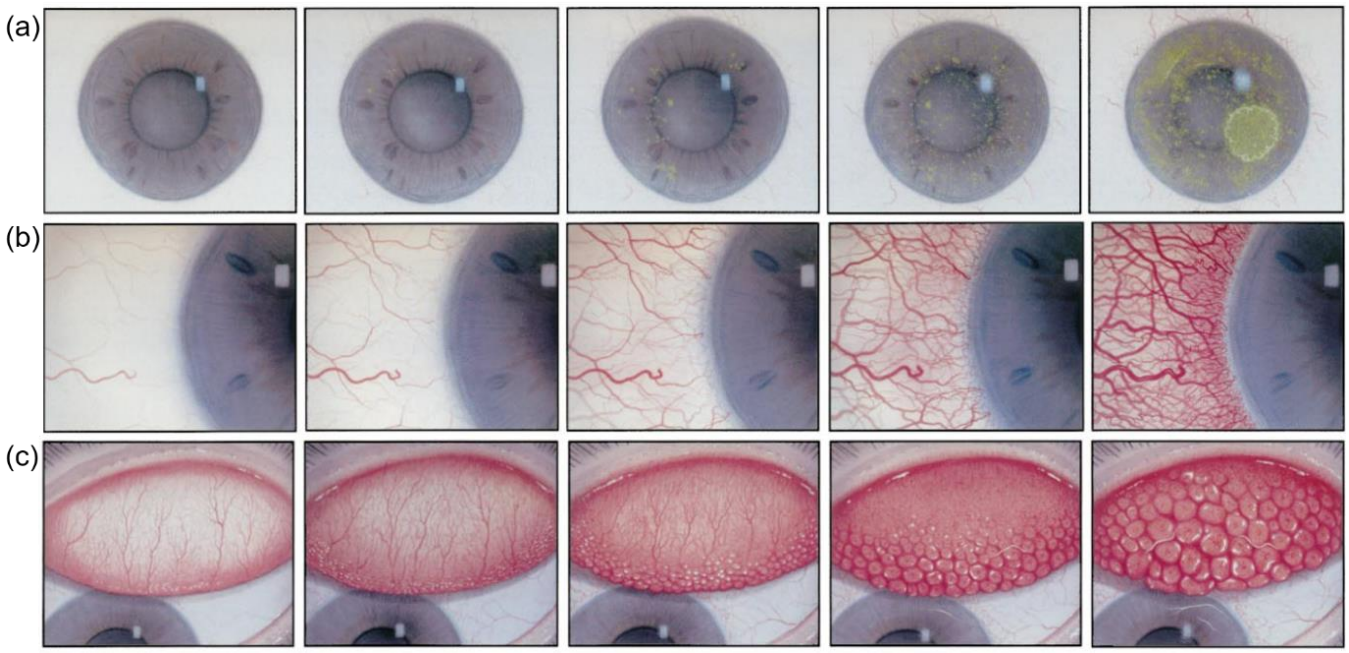

Figure 12. Contact lens complications. (a) Corneal staining; (b) Conjunctival redness; (c) Papillary conjunctivitis. Grading scale, from left to right: normal, trace, mild, moderate, severe. Reproduced with permission.[182] Copyright 2002, John Wiley and Sons.

1.6.2. Contact lens care

Antimicrobial methods can be generally classified into two main groups: active chemical strategies and passive chemical strategies, the first aimed in killing bacterial already attached to a surface by using microbicidal chemicals, the second based on preventing biofilm formation. Contact lenses and lens cases are mostly disinfected with Hydrogen Peroxide and multipurpose solutions (Polyhexamethylene biguanide (PHMB) and Polyquad).[183, 184] The literature concerning the effectivity of hydrogen peroxide as a disinfection system is controversial. It has been demonstrated that *P. Aeruginosa* biofilms grown in vitro are better attacked by Hydrogen Peroxide,[184, 185] but other studies report that *Staphylococci* is able to unbound Hydrogen Peroxide molecules, neutralizing its effect.[184, 186] *Serratia marcenses* can only be treated with Hydrogen Peroxide.[184] Polyquad has been found to reduce the transfer of bacteria from the case to the lens.[187, 188] It has also shown higher disinfection results with several bacterial species when compared to PBHS. A reduction in bacterial flora (>99%) on the surface of the periocular skin without altering the bacterial species has also been recently demonstrated by using a hypochlorous acid hygiene

solution.[189] The disinfection efficacy of CLEAR CARE, RevitaLens OcuTec, OPTI-FREE PureMoist and Biotrue solutions was compared. It resulted that CLEAR CARE cleaned lens cases exhibited much higher bacterial concentration than the ones cleaned with RevitaLens OcuTec.[190] The same result was observed comparing PureMoist with Biotrue. A recent study successfully demonstrated the use of a povidone-iodine as a disinfection system for contact lenses.[191] The case design might be also relevant to bacterial adhesion. Silver impregnated lens cases and selenium lens cases have been designed with anti-microbial purposes.[178] Other methods have been investigated for prevention and disinfection purposes, including the use of free-radical producing agents, quorum-sensing blockers, antimicrobial peptides, and non-steroidal anti-inflammatory drugs.[179] To minimize microbial contamination, hygiene measures have to be taken. These include disinfecting lens and cases frequently, case replacement every two weeks, facing down the case during air drying, avoiding using tap water, do not top-off contact lens solution, wash hands before insertion and removal.[192]

1.7. Regulations of contact lenses

Contact lenses are prosthetic devices categorized as direct contact devices, i.e. “devices or device components that come into physical contact with body tissue” (ISO 10993-1).[193] To introduce a contact lens device to the market, standards and regulations must be fulfilled to assess its safety, functionality, and reliability. The International Organization for Standardization (non-acronymic abbreviation: ISO) is the world's largest developer of voluntary international standards to facilitate world trade by providing common standards between nations.[194] However, it has no role in enforcing its standards and it is not compulsory for marketed products to legally meet the ISO requirements.[195] Nevertheless, governmental bodies exist to supervise and control medical devices, and they substantially adopt the ISO standard.[196, 197] Therefore, a device that fulfils ISO requirements is eligible to hit the market. In the US, regulations are established by the Food and Drug Administration (FDA), which from 2019 plans to officially use ISO 13485 as the basis for its legislation on medical devices.[196] Biocompatibility standards for medical devices are well stated in ISO 10993 – “Biological Evaluation of Medical Devices”. ISO 10993-1 is the

Guidance on Selection of Tests.[193] ISO 10993-2 covers animal welfare requirements.[198] ISO 10993-10 assesses possible contact hazards from device-released chemicals that may produce skin and mucosal irritation, eye irritation and delayed contact sensitization.[199] ISO 10993-(3-19) are guidelines for specific test procedures.[199-208] The most important tests in the biocompatibility assessment of a contact lens device are the *in vitro* test and the *in vivo* test. ISO 10993-5 describes the *in vitro* toxicological testing procedure,[200] and ISO-9394 describes the biocompatibility test in rabbit eyes.[209]

1.7.1. In vitro toxicological test

Cytotoxicity test can be performed either on an extract or on the entire sample, in direct contact mode with mammalian cells. The cell sample is prepared in accordance with ISO 10993-12[207] and handled aseptically throughout the procedure. Sterile, mycoplasma-free cell lines are obtained from living tissues and stored at −80 °C or below in the culture medium with cryoprotectant in the pH range 7.2-7.4. In qualitative evaluations, the text sample is exposed to a known amount of cell suspension through a vessel. Vessels can be cleaned and replenished with new culture medium. The culture is incubated at 37 ± 1 °C in air. Changes in morphology, vacuolization, detachment, cell lysis, and membrane integrity are evaluated by inspection under a microscope, using cytochemical staining. The interpretation of the results is done accordingly to the classification of the device, as given in ISO 10993-1.[193] *In vitro* evaluation is primarily run to evaluate a potential *in vivo* toxicity. A reduction of cell viability higher than the 30% is considered cytotoxic. Direct contact cytotoxicity test is also performed on contact lens/contact lens solution combination in extended wear contact lenses.

1.7.2. In vivo animal test

Animal testing of contact lens devices is carried out in compliance with ISO-9394: “Ophthalmic optics — Contact lenses and contact lens care products: Determination of biocompatibility by ocular study with rabbit eyes.”.[209] The irritant properties of materials which come in contact with ocular tissue are evaluated on ocular tissue of rabbit eyes, complying to the regulations defining animal welfare (ISO

10933-2)[198] and good laboratory practice (ISO/IEC 17025).[210] Animal test is performed after a positive outcome of the irritation and sensitization tests (ISO 10993-10)[199] and *in vitro* biocompatibility assessment (ISO-10993-2).[198] New Zealand white strain rabbits (male, female, or mixed sexes) or equivalent albino rabbits are used to test contact lenses. Animal models are young adults, from a single strain, weighing more than 2.5 kg, and free from clinically significant ocular irritation or corneal retention of fluorescein stain. A minimum number of six animals need to be tested, and a 100% positive result need to be met. Each animal is uniquely identified by either a numbered ear tag, a tattoo, or a microchip. The animals are acclimatized to the laboratory conditions for at least five days prior to testing. Contact lenses must produce an optimal fit. If the intended use of contact lenses includes contact lens care products, those must be tested. The lens is inserted in one eye of the rabbit and the other is used as a control. The lens is left on the eye's animal for 7 hours, then removed. This procedure is repeated for 21 days. Eyes are examined visually and evaluated according to both the Draize and the McDonald-Shadduck scoring systems. The eyes are excised and preserved in a fixation solution (e.g. 10 % neutral buffered formalin, Zenker's acetic fixative or Davidson's solution). Eyes are further sectioned to divide cornea, conjunctivae, iris and lens and each part is stained for microscope evaluation.

1.8. Contact lens market

Contact lens technology gained increasing popularity and a broader range of applications since it was commercialized. The contact lens global market exceeded the value of $8.5 billion in 2018 with an over 6% growth, and a continue transition to silicone hydrogel materials. In 2018, the 69% of contact lens sales were silicone hydrogel contact lenses, followed by hydrogel lenses (19%), RGP (9%) and hybrid lenses (2%). Monthly and daily contact lenses were reported to be the most popular (41% and 35% respectively), over contact lenses with weekly (21%) or 3+ months (3%) replacement schedule (**Figure 13a**). From data in 15 countries worldwide in 2018 resulted that a portion of contact lens patients are part-time wearers, with the highest percentages reported in Finland (34%), Czech Republic (30%), and Australia (29%) (**Figure 13b)**. Over the last decade, a decrease in the use of hydrogen peroxide solutions was reported,

but chemical care systems continued to dominate the market (**Figure 13c**).[211] Contact lens wearers in 2018 were over the 35% globally, with a higher net practice revenue when compared to the previous years in relation with the gross revenue. Weekly fits and refits were reported to increase comparing to the previous years. In 2018, the US marked was led by Clear Eyes, Bausch & Lomb with BioTrue, and Alcon with Opti-Free Pure Moist (**Figure 13d**). The global contact lens market is estimated to grow from 12.4 billion USD in 2018 to 15.53 billion USD in 2021 and 19.45 billion USD in 2024 (**Figure 13e**). **Figure 13f** presents the contact lens market value in 2018 in 20 countries. The US market was valued over 4.5 billion USD, with a net gap compared to the other countries.[10] An analysis of the new-born market of smart contact lenses revealed a value of 59.9 million USD in 2018, estimated to reach over one billion USD in 2022.[212]

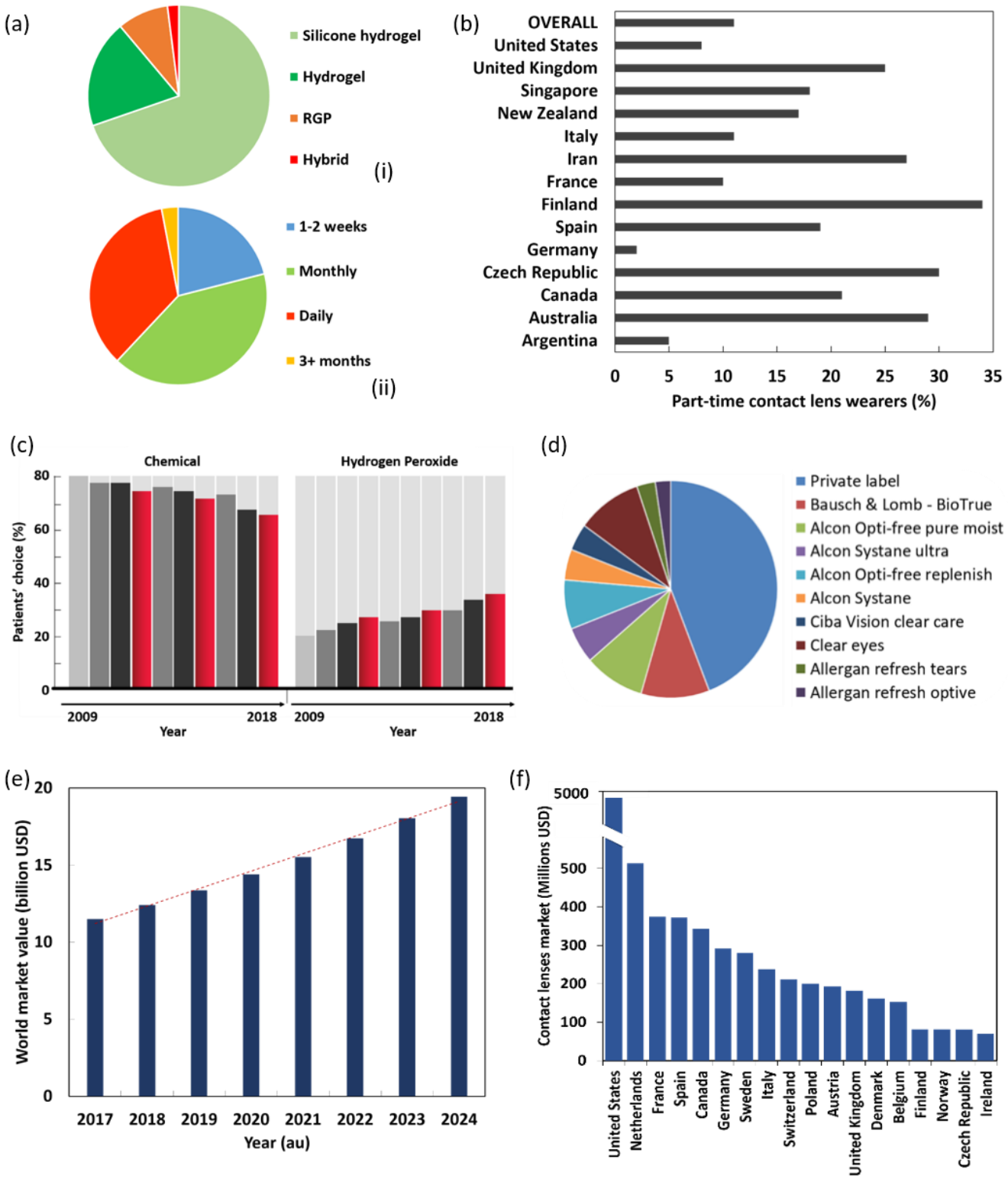

Figure 13. Latest trends on contact lens usage, as of January 2019. (a) Contact lens fits and refits in 2018 based on (i) material classes and (ii) replacement schedule. Data from reference [181]. (b) Part-time contact lens wearers in 2018, with data for 14 countries worldwide. Data from reference [181]. (c) 2009 to 2019 contact lens care trends.[213] (d) Unit sales of the leading contact lens companies in the US in 2018. The private label portion corresponds to 55 million USD.[211] Latest analysis of the

contact lens market, as of January 2019. (e) Values and estimations of the global contact lens market from 2017 to 2024.[10] (f) Contact lenses market analysis in 20 countries worldwide in 2018.[213]

1.9. Conclusions

Contact lenses are a well-established, yet a constantly expanding technology. Polymers in contact lenses have evolved to address the limitations with regards to ocular complications induced by contact lens wear. The choice of the polymer type utilized in contact lens manufacture is driven by the application, with RGP and soft contact lenses leading the market of ocular therapeutics and vision correction, respectively. The global contact lens market in 2018 amounted to over 8 billion USD. In the last decade, contact lenses have been targeted as diagnostic wearable platforms with a variety of applications. The main disadvantages of current technologies include the use of lab-made contact lenses over commercial materials (e.g. PDMS or poly-HEMA), the high variability introduced by process complexity (e.g. multi-step fabrication of individual devices). In the following chapters, these limitations are addressed by employing rapid and precise technologies (e.g. single-step laser writing) to directly functionalize commercial contact lenses as sensing platforms.

1.10. References

1. J.N. Tinsley, M.I. Molodtsov, R. Prevedel, D. Wartmann, J. Espigule-Pons, M. Lauwers, A. Vaziri. *Nat Commun*, **2016**, *7*, 12172.
2. R.R.A. Bourne, S.R. Flaxman, T. Braithwaite, M.V. Cicinelli, A. Das, J.B. Jonas, J. Keeffe, J.H. Kempen, J. Leasher, H. Limburg, K. Naidoo, K. Pesudovs, S. Resnikoff, A. Silvester, G.A. Stevens, N. Tahhan, T.Y. Wong, H.R. Taylor, G. Vision Loss Expert. *Lancet Glob Health*, **2017**, *5*, e888-e897.
3. T.R. Fricke, N. Tahhan, S. Resnikoff, E. Papas, A. Burnett, S.M. Ho, T. Naduvilath, K.S. Naidoo. *Ophthalmology*, **2018**, *125*, 1492-1499.
4. J.B. Randleman, B. Russell, M.A. Ward, K.P. Thompson, R.D. Stulting. *Ophthalmology*, **2003**, *110*, 267-75.
5. K.D. Solomon, L.E. Fernandez de Castro, H.P. Sandoval, J.M. Biber, B. Groat, K.D. Neff, M.S. Ying, J.W. French, E.D. Donnenfeld, R.L. Lindstrom, L.S.T.F. Joint. *Ophthalmology*, **2009**, *116*, 691-701.
6. M.O. Price, D.A. Price, F.A. Bucci, Jr., D.S. Durrie, W.I. Bond, F.W. Price, Jr. *Ophthalmology*, **2016**, *123*, 1659-1666.
7. J.B. Randleman, R.D. Shah. *J Refract Surg*, **2012**, *28*, 575-86.
8. F.N. M., Y.A. K., M.M. J., L.C. R., Y.S. Hyun. *Advanced Healthcare Materials*, **2015**, *4*, 792-810.
9. M.W. Swanson. *Optom Vis Sci*, **2012**, *89*, 839-48.
10. Statista, *Value of the global contact lens market from 2017 to 2024*. 2019: Statista. p. https://www.statista.com/statistics/485820/global-value-of-the-contact-lens-market/.
11. K.Y. Chan, P. Cho, M. Boost. *Cont Lens Anterior Eye*, **2014**, *37*, 267-72.
12. J. Kim, M. Kim, M.S. Lee, K. Kim, S. Ji, Y.T. Kim, J. Park, K. Na, K.H. Bae, H. Kyun Kim, F. Bien, C. Young Lee, J.U. Park. *Nat Commun*, **2017**, *8*, 14997.
13. A.G.s. Chambers. *Ministry of Health Singapore. Ch 213A*, **2008**,
14. *Ophthalmic Devices Panel of the Medical Devices Advisory Committee (May 13, 2014). Accessed 3 March 2019*,
15. A.K. Yetisen, J.L. Martinez-Hurtado, B. Unal, A. Khademhosseini, H. Butt. *Adv Mater*, **2018**, e1706910.
16. M. Elsherif, M.U. Hassan, A.K. Yetisen, H. Butt. *ACS Nano*, **2018**, *12*, 5452-5462.
17. W.C. Mak, K.Y. Cheung, J. Orban, C.J. Lee, A.P. Turner, M. Griffith. *ACS Appl Mater Interfaces*, **2015**, *7*, 25487-94.
18. A.V. Quintero, R. Verplancke, H. De Smet, J. Vanfleteren. *Advanced Materials Technologies*, **2017**, *2*,
19. R. Moreddu, M. Elsherif, H. Butt, D. Vigolo, A.K. Yetisen. *RSC Advances*, **2019**, *9*, 11433-11442.
20. S.J. Lea, M.A. Neugebauer, R.G. Smith, S.A. Vernon. *Eye (Lond)*, **1990**, *4 (Pt 5)*, 706-11.
21. K.D. D Fonn. *Eye & Contact Lens*, **2003**,
22. D. Fonn. *Optom Vis Sci*, **2007**,
23. C.H. Lim, N.A. Carnt, M. Farook, J. Lam, D.T. Tan, J.S. Mehta, F. Stapleton. *Eye (Lond)*, **2016**, *30*, 447-55.
24. F. Stapleton, N. Carnt. *Eye (Lond)*, **2012**, *26*, 185-93.
25. P.C. Donshik, W.H. Ehlers. *Int Ophthalmol Clin*, **1991**, *31*, 133-45.
26. V.Y. Hayes, C.M. Schnider, J. Veys. *Cont Lens Anterior Eye*, **2003**, *26*, 85-93.
27. H. Hamano, K. Watanabe, T. Hamano, S. Mitsunaga, S. Kotani, A. Okada. *CLAO J*, **1994**, *20*, 103-8.
28. N. Efron, *Hystory*, in *Contact lens practice*. 2017.
29. T. Young. *Phil. Trans. R. Soc. Lon. [Biol. Sci.]*, **1801**, *91*, 23-88.
30. J.F.W. Herschel. *Encyclopedia Metropolitana*, **1845**, *4*, 341–586.
31. N. Efron, & Pearson, R. M. . *Arch. Ophthalmol.,* , **1988**, *106*

1370–1377.
32. O. Wichterle, Lim, D. *Nature*, **1960**, *185*, 117-118.
33. H. Kobayashi, S. Kohshima. *Nature*, **1997**, *387*, 767-8.
34. R.A. Gordon, P.B. Donzis. *Archives of Ophthalmology*, **1985**, *103*, 785-789.
35. A.R. Parker. *Philos Trans A Math Phys Eng Sci*, **2009**, *367*, 1759-82.
36. A.R. Parker. *J R Soc Interface*, **2005**, *2*, 1-17.
37. J. Sun, B. Bhushan, J. Tong. *RSC Advances*, **2013**, *3*,
38. P. Ahlberg. *Lethaia*, **1988**, *21*, 115-120.
39. K.M. Towe, A. Urbanek. *Nature*, **1972**, *237*, 443-&.
40. S.F.E.N. Leonard A. Levin, James Ver Hoeve, Samuel Wu, Paul L. Kaufman, Albert Alm, *Physiology of the Eye*. 2011: Elsevier.
41. Z. Lei, R.W. Beuerman, A.P. Chew, S.K. Koh, T.A. Cafaro, E.A. Urrets-Zavalia, J.A. Urrets-Zavalia, S.F. Li, H.M. Serra. *J Proteome Res*, **2009**, *8*, 1992-2003.
42. M. Park, H. Jung, Y. Jeong, K.H. Jeong. *ACS Nano*, **2017**, *11*, 438-443.
43. L. Zhou, R.W. Beuerman, C.M. Chan, S.Z. Zhao, X.R. Li, H. Yang, L. Tong, S. Liu, M.E. Stern, D. Tan. *J Proteome Res*, **2009**, *8*, 4889-905.
44. H.J. An, M. Ninonuevo, J. Aguilan, H. Liu, C.B. Lebrilla, L.S. Alvarenga, M.J. Mannis. *J Proteome Res*, **2005**, *4*, 1981-7.
45. N. Tomosugi, K. Kitagawa, N. Takahashi, S. Sugai, I. Ishikawa. *J Proteome Res*, **2005**, *4*, 820-5.
46. A.M. Masmali, C. Purslow, P.J. Murphy. *Clin Exp Optom*, **2014**, *97*, 399-406.
47. M.D. Yoshiki Ohashi, Kazuo Tsubota. *Clinica Chimica Acta*, *369*, 17-28.
48. S. Hagan, E. Martin, A. Enriquez-de-Salamanca. *EPMA J*, **2016**, *7*, 15.
49. N. Li, N. Wang, J. Zheng, X.M. Liu, O.W. Lever, P.M. Erickson, L. Li. *J Proteome Res*, **2005**, *4*, 2052-61.
50. L. Chen, L. Zhou, E.C. Chan, J. Neo, R.W. Beuerman. *J Proteome Res*, **2011**, *10*, 4876-82.
51. K. Karns, A.E. Herr. *Anal Chem*, **2011**, *83*, 8115-22.
52. A.H. Rantamaki, T. Seppanen-Laakso, M. Oresic, M. Jauhiainen, J.M. Holopainen. *PLoS One*, **2011**, *6*, e19553.
53. B.J. Glasgow, A.R. Abduragimov, O.K. Gassymov, T.N. Yusifov, E.C. Ruth, K.F. Faull. *Adv Exp Med Biol*, **2002**, *506*, 567-72.
54. M.S. Ubels JL. *Curr Eye Res.* , **1984**, *3,* 815-22.
55. M. Khaksari, L.R. Mazzoleni, C. Ruan, R.T. Kennedy, A.R. Minerick. *Exp Eye Res*, **2017**, *155*, 54-63.
56. A.W.M.K. Galloway N.R., Galloway P.H., Browning A.C., *Common Diseases of the Eyelids.*, in *Common Eye Diseases and their Management.* 2016, Springer, Cham.
57. C. Chao, K. Richdale, I. Jalbert, K. Doung, M. Gokhale. *Cont Lens Anterior Eye*, **2017**, *40*, 273-282.
58. J.G. Lawrenson, *Anterior eye*, in *Contact lens practice*. 2017.
59. R.O. Paananen, A.H. Rantamaki, J.M. Holopainen. *Langmuir*, **2014**, *30*, 5897-902.
60. P. Versura, A. Bavelloni, M. Grillini, M. Fresina, E.C. Campos. *Mol Vis*, **2013**, *19*, 1247-57.
61. J. Soria, J.A. Duran, J. Etxebarria, J. Merayo, N. Gonzalez, R. Reigada, I. Garcia, A. Acera, T. Suarez. *J Proteomics*, **2013**, *78*, 94-112.
62. B.M. Argüeso P, Spurr-Michaud S, Keutmann HT, Dana MR, Gipson IK. *Invest Ophthalmol Vis Sci.* , **2002**, *43*,
63. N. Von Thun Und Hohenstein-Blaul, S. Funke, F.H. Grus. *Exp Eye Res*, **2013**, *117*, 126-37.
64. R. Sharif, S. Bak-Nielsen, H. Sejersen, K. Ding, J. Hjortdal, D. Karamichos. *Exp Eye Res*, **2018**, *179*, 55-63.
65. F.E.C. Andrade, J.L. Covre, L. Ramos, R.M. Hazarbassanov, M.S.D. Santos, M. Campos, J.A.P. Gomes, C.D. Gil. *Br J Ophthalmol*, **2018**, *102*, 700-707.
66. K. Nishtala, N. Pahuja, R. Shetty, R.M. Nuijts, A. Ghosh. *Eye Vis (Lond)*, **2016**, *3*, 19.

67. K.S. Park, S.S. Kim, J.C. Kim, H.C. Kim, Y.S. Im, C.W. Ahn, H.K. Lee. *Am J Ophthalmol*, **2008**, *145*, 432-7.
68. B.P. Csősz E, Csutak A, Berta A, Tóth F, Póliska S, Török Z, Tőzsér J. *J Proteome*, **2012**, *75*, 2196-204.
69. K.P. Kim HJ, Yoo HS, Kim CW. . *Clin Biochem.* , **2012**, *45*, 60-7.
70. C. Costagliola, V. Romano, M. De Tollis, F. Aceto, R. dell'Omo, M.R. Romano, C. Pedicino, F. Semeraro. *Mediators Inflamm*, **2013**, *2013*, 629529.
71. T. Nguyen-Khuong, A.V. Everest-Dass, L. Kautto, Z. Zhao, M.D. Willcox, N.H. Packer. *Glycobiology*, **2015**, *25*, 269-83.
72. E. Csosz, E. Deak, G. Kallo, A. Csutak, J. Tozser. *J Proteomics*, **2017**, *150*, 351-358.
73. Z. Torok, T. Peto, E. Csosz, E. Tukacs, A.M. Molnar, A. Berta, J. Tozser, A. Hajdu, V. Nagy, B. Domokos, A. Csutak. *J Diabetes Res*, **2015**, *2015*, 623619.
74. M. Dor, S. Eperon, P.H. Lalive, Y. Guex-Crosier, M. Hamedani, C. Salvisberg, N. Turck. *Exp Eye Res*, **2018**, *179*, 64-74.
75. A. Rentka, J. Harsfalvi, A. Berta, K. Koroskenyi, Z. Szekanecz, G. Szucs, P. Szodoray, A. Kemeny-Beke. *Mediators Inflamm*, **2015**, *2015*, 573681.
76. A. Rentka, J. Harsfalvi, G. Szucs, Z. Szekanecz, P. Szodoray, K. Koroskenyi, A. Kemeny-Beke. *Immunol Res*, **2016**, *64*, 619-26.
77. A. Rentka, K. Koroskenyi, J. Harsfalvi, Z. Szekanecz, G. Szucs, P. Szodoray, A. Kemeny-Beke, *Ophthalmological Manifestations and Tear Investigations in Systemic Sclerosis*, in *Systemic Sclerosis*. 2017.
78. M. Mrugacz, B. Zelazowska, A. Bakunowicz-Lazarczyk, M. Kaczmarski, J. Wysocka. *J Interferon Cytokine Res*, **2007**, *27*, 491-5.
79. M. M. *J Interferon Cytokine Res.*, **2010**, *30*, 509-12.
80. K.K. Böhm D, Pieter J, Boehm N, Wolters D, Siggelkow W, Lebrecht A, Schmidt M, Kölbl H, Pfeiffer N, Grus FH. *Oncol Rep.*, **2012**, *28*, 429-38.
81. V. Evans, C. Vockler, M. Friedlander, B. Walsh, M.D. Willcox. *Clin Exp Ophthalmol*, **2001**, *29*, 161-3.
82. A. Lebrecht, D. Boehm, M. Schmidt, H. Koelbl, F.H. Grus. *Cancer Genomics Proteomics*, **2009**, *6*, 75-83.
83. D. Karley, D. Gupta, A. Tiwari. *World J Oncol*, **2011**, *2*, 151-157.
84. P.K. Coyle, P. Sibony, C. Johnson. *Neurology*, **1987**, *37*, 853-6.
85. G. Calais, G. Forzy, C. Crinquette, A. Mackowiak, J. de Seze, F. Blanc, C. Lebrun, O. Heinzlef, P. Clavelou, T. Moreau, B. Hennache, H. Zephir, A. Verier, V. Neuville, C. Confavreux, P. Vermersch, P. Hautecoeur. *Mult Scler*, **2010**, *16*, 87-92.
86. C.M. Abreu, R. Soares-Dos-Reis, P.N. Melo, J.B. Relvas, J. Guimaraes, M.J. Sa, A.P. Cruz, I. Mendes Pinto. *Front Mol Neurosci*, **2018**, *11*, 164.
87. T.Y. Wei, Y. Fu, K.H. Chang, K.J. Lin, Y.J. Lu, C.M. Cheng. *Trends Biotechnol*, **2018**, *36*, 290-303.
88. S.S. Comoglu, H. Guven, M. Acar, G. Ozturk, B. Kocer. *Neurosci Lett*, **2013**, *553*, 63-7.
89. C. Tamer, I.M. Melek, T. Duman, H. Oksuz. *Ophthalmology*, **2005**, *112*, 1795.
90. M. Börger, S. Funke, M. Bähr, F. Grus, P. Lingor. *Basal Ganglia*, **2015**, *5*, 63-69.
91. M.D. Willcox. *Exp Eye Res*, **2013**, *117*, 99-105.
92. J.E. Graham, J.E. Moore, X. Jiru, J.E. Moore, E.A. Goodall, J.S. Dooley, V.E. Hayes, D.A. Dartt, C.S. Downes, T.C. Moore. *Invest Ophthalmol Vis Sci*, **2007**, *48*, 5616-23.
93. G. Hovding. *Acta Ophthalmologica*, **2009**, *59*, 387-401.
94. D.F. Larkin, J.P. Leeming. *Eye (Lond)*, **1991**, *5 (Pt 1)*, 70-4.
95. E.C. Leitch, N.Y. Harmis, K.M. Corrigan, M.D. Willcox. *Optom Vis Sci*, **1998**, *75*, 258-65.
96. H. Mino de Kaspar, T.C. Kreutzer, I. Aguirre-Romo, C.N. Ta, J. Dudichum, M. Bayrhof, V. Klauss, A. Kampik. *Am J Ophthalmol*, **2008**, *145*, 136-142.

97. L. Ramachandran, S. Sharma, P.R. Sankaridurg, C.M. Vajdic, J.A. Chuck, B.A. Holden, D.F. Sweeney, G.N. Rao. *CLAO J*, **1995**, *21*, 195-9.
98. J. Ozkan, H. Zhu, M. Gabriel, B.A. Holden, M.D. Willcox. *Optom Vis Sci*, **2012**, *89*, 326-35.
99. Q.F. Dong, J.M. Brulc, A. Iovieno, B. Bates, A. Garoutte, D. Miller, K.V. Revanna, X. Gao, D.A. Antonopoulos, V.Z. Slepak, V.I. Shestopalov. *Investigative Ophthalmology & Visual Science*, **2011**, *52*, 5408-5413.
100. D. Monsalvez-Romin, A. Dominguez-Vicent, S. Garcia-Lazaro, J.J. Esteve-Taboada, A. Cervino. *Clin Exp Optom*, **2018**, *101*, 57-63.
101. M. Griffiths, K. Zahner, M. Collins, L. Carney. *CLAO J*, **1998**, *24*, 76-81.
102. E. van der Worp, D. Bornman, D.L. Ferreira, M. Faria-Ribeiro, N. Garcia-Porta, J.M. Gonzalez-Meijome. *Cont Lens Anterior Eye*, **2014**, *37*, 240-50.
103. N. Efron, *Rigid lens materials*, in *Contact lens practice*. 2017.
104. A. Dominguez-Vicent, J.J. Esteve-Taboada, T. Ferrer-Blasco, S. Garcia-Lazaro, R. Montes-Mico. *Clin Exp Optom*, **2016**, *99*, 39-46.
105. C. Maldonado-Codina, *Soft lens materials*, in *Contact lens practice*. 2017.
106. N. Efron, *Soft lens manufacture*, in *Contact lens practice*. 2017, Elsevier. p. 62-64.
107. N. Efron, *Soft lens design and fitting*, in *Contact lens practice*. 2017.
108. P.C. Nicolson, J. Vogt. *Biomaterials*, **2001**, *22*, 3273-3283.
109. K. Ehrmann, *Soft lens measurement*, in *Contact lens practice*. 2017, Elsevier. p. 85.
110. N. Efron, *Soft-toric lens design and fitting*, in *Contact lens practice*. 2017.
111. K. Ehrmann, *Rigid Lens Measurement*, in *Contact Lens Practice*, Elsevier, Editor. 2017. p. 136.
112. B. Pilskalns, B.A. Fink, R.M. Hill. *Optom Vis Sci*, **2007**, *84*, 334-42.
113. D. Obendorf, M. Wilhelm. *Analytical Chemistry*, **2003**, *75*, 1374-1381.
114. N. Tahhan, R. Du Toit, E. Papas, H. Chung, D. La Hood, A.B. Holden. *Optom Vis Sci*, **2003**, *80*, 796-804.
115. N. Efron, *Rigid-toric lens design and fitting*, in *Contact lens practice*. 2017.
116. A.S.B. Milton M. Hom, *Manual of Contact Lens Prescribing and Fitting*. 2006: Elsevier Health Sciences.
117. N. Efron, *Rigid lens design and fitting*, in *Contact lens practice*. 2017.
118. C. Manicam, N. Perumal, J. Wasielica-Poslednik, Y.C. Ngongkole, A. Tschabunin, M. Sievers, W. Lisch, N. Pfeiffer, F.H. Grus, A. Gericke. *Sci Rep*, **2018**, *8*, 11526.
119. H.A. Ketelson, D.L. Meadows, R.P. Stone. *Colloids Surf B Biointerfaces*, **2005**, *40*, 1-9.
120. M.E. Seitz, M.E. Wiseman, I. Hilker, J. Loos, M. Tian, J. Li, M. Goswami, V.M. Litvinov, S. Curtin, M. Bulters. *Polymer*, **2017**, *118*, 150-162.
121. N. Efron, *Rigid lens manufacture*, in *Contact Lens Practice*. 2017.
122. A. Childs, H. Li, D.M. Lewittes, B. Dong, W. Liu, X. Shu, C. Sun, H.F. Zhang. *Sci Rep*, **2016**, *6*, 34905.
123. J. Deng, S. Chen, J. Chen, H. Ding, D. Deng, Z. Xie. *ACS Appl Mater Interfaces*, **2018**, *10*, 34611-34617.
124. D. Lee, S. Cho, H.S. Park, I. Kwon. *Sci Rep*, **2016**, *6*, 34194.
125. J.F. Huang, J. Zhong, G.P. Chen, Z.T. Lin, Y. Deng, Y.L. Liu, P.Y. Cao, B. Wang, Y. Wei, T. Wu, J. Yuan, G.B. Jiang. *ACS Nano*, **2016**, *10*, 6464-73.
126. F.A. Maulvi, T.G. Soni, D.O. Shah. *Drug Deliv*, **2016**, *23*, 3017-3026.
127. A. Guzman-Aranguez, B. Fonseca, G. Carracedo, A. Martin-Gil, A. Martinez-Aguila, J. Pintor. *Eye Contact Lens*, **2016**, *42*, 280-8.
128. J. Park, J. Kim, S.Y. Kim, W.H. Cheong, J. Jang, Y.G. Park, K. Na, Y.T. Kim, J.H. Heo, C.Y. Lee, J.H. Lee, F. Bien, J.U. Park. *Sci Adv*, **2018**, *4*, eaap9841.
129. J. Bailey, P. Morgan, H. Gleeson, J. Jones. *Crystals*, **2018**, *8*,
130. Y.L. Donnie J. Duis, Leilani K. Sonoda, Holly L. Grammer *Pupil-only photochromic contact lenses displaying desirable optics and comfort*. 2018, Johnson & Johnson.
131. Y.S. Pek, H. Wu, E.P. Chow, J.Y. Ying. *Nanomedicine (Lond)*, **2016**, *11*, 1599-610.

132. A.R. Badawy, M.U. Hassan, M. Elsherif, Z. Ahmed, A.K. Yetisen, H. Butt. *Adv Healthc Mater*, **2018**, *7*, e1800152.
133. N. Carnt, Y. Wu, F. Stapleton, *Contact Lenses☆*, in *Reference Module in Neuroscience and Biobehavioral Psychology*. 2017, Elsevier.
134. D. Lam, *Soft Contact Lenses for Prosthetic Fitting*, in *Contact Lens Spectrum*. 2015.
135. S.M. Sanders, *Prosthetic Lens Patient Management*, in *Contact Lens Spectrum*. December 2008.
136. in *Contact Lens Spectrum*. May 2018.
137. F. Tashakori-Sabzevar, S.A. Mohajeri. *Drug Dev Ind Pharm*, **2015**, *41*, 703-13.
138. S.E.E. Nathan Efron, *Therapeutic applications*, in *Contact Lens Practice*. 2015.
139. F. Alipour, A. Kheirkhah, M. Jabarvand Behrouz. *Cont Lens Anterior Eye*, **2012**, *35*, 272-6.
140. R. Badugu, J.R. Lakowicz, C.D. Geddes. *Anal Chem*, **2004**, *76*, 610-8.
141. M. Falk, V. Andoralov, M. Silow, M.D. Toscano, S. Shleev. *Anal Chem*, **2013**, *85*, 6342-8.
142. *The SENSIMED Triggerfish contact lens sensor for continuous 24-hour recording of ocular dimensional changes in people with or at risk of developing glaucoma*. National Institute for Health and Care Excellence (NICE) Accessed January 2019; Available from: https://www.nice.org.uk/advice/mib14/chapter/technology-overview.
143. A.R. Lingley, M. Ali, Y. Liao, R. Mirjalili, M. Klonner, M. Sopanen, S. Suihkonen, T. Shen, B.P. Otis, H. Lipsanen, B.A. Parviz. *Journal of Micromechanics and Microengineering*, **2011**, *21*,
144. R. Yin, Z. Xu, M. Mei, Z. Chen, K. Wang, Y. Liu, T. Tang, M.K. Priydarshi, X. Meng, S. Zhao, B. Deng, H. Peng, Z. Liu, X. Duan. *Nat Commun*, **2018**, *9*, 2334.
145. K. Choi, H.G. Park. *ACS Nano*, **2017**, *11*, 5223-5226.
146. X. Xiao, T. Siepenkoetter, P.O. Conghaile, D. Leech, E. Magner. *ACS Appl Mater Interfaces*, **2018**, *10*, 7107-7116.
147. H. Kim, J. Kim, J. Kang, Y.W. Song. *ACS Appl Mater Interfaces*, **2018**, *10*, 28086-28092.
148. R. Melikov, D.A. Press, B.G. Kumar, I.B. Dogru, S. Sadeghi, M. Chirea, I. Yilgor, S. Nizamoglu. *Sci Rep*, **2017**, *7*, 7258.
149. B.W. An, J.H. Shin, S.Y. Kim, J. Kim, S. Ji, J. Park, Y. Lee, J. Jang, Y.G. Park, E. Cho, S. Jo, J.U. Park. *Polymers (Basel)*, **2017**, *9*,
150. C. Pan, K. Kumar, J. Li, E.J. Markvicka, P.R. Herman, C. Majidi. *Adv Mater*, **2018**, *30*, e1706937.
151. J. Jang, B.G. Hyun, S. Ji, E. Cho, B.W. An, W.H. Cheong, J.-U. Park. *NPG Asia Materials*, **2017**, *9*,
152. H.G. Im, B.W. An, J. Jin, J. Jang, Y.G. Park, J.U. Park, B.S. Bae. *Nanoscale*, **2016**, *8*, 3916-22.
153. F.A. Maulvi, T.G. Soni, D.O. Shah. *J Biomater Sci Polym Ed*, **2015**, *26*, 1035-50.
154. I.M. Carvalho, C.S. Marques, R.S. Oliveira, P.B. Coelho, P.C. Costa, D.C. Ferreira. *J Control Release*, **2015**, *202*, 76-82.
155. C.C. Peng, M.T. Burke, A. Chauhan. *Langmuir*, **2012**, *28*, 1478-87.
156. A. Mandal, R. Bisht, I.D. Rupenthal, A.K. Mitra. *J Control Release*, **2017**, *248*, 96-116.
157. B. Gidwani, A. Vyas. *Biomed Res Int*, **2015**, *2015*, 198268.
158. E. Garcia-Millan, M. Quintans-Carballo, F.J. Otero-Espinar. *Int J Pharm*, **2017**, *525*, 226-236.
159. F. Alvarez-Rivera, A. Concheiro, C. Alvarez-Lorenzo. *Eur J Pharm Biopharm*, **2018**, *122*, 126-136.
160. H.J. Kim, K. Zhang, L. Moore, D. Ho. *ACS Nano*, **2014**, *8*, 2998-3005.
161. P.S. Stewart. *Microbiol Spectr*, **2015**, *3*,
162. M.D. Macia, E. Rojo-Molinero, A. Oliver. *Clinical Microbiology and Infection*, **2014**, *20*, 981-990.
163. H. Wu, C. Moser, H.Z. Wang, N. Hoiby, Z.J. Song. *International Journal of Oral Science*, **2015**, *7*, 1-7.
164. T. Larsen, N.E. Fiehn. *APMIS*, **2017**, *125*, 376-384.
165. M. Wroblewska, I. Struzycka, E. Mierzwinska-Nastalska. *Przegl Epidemiol*, **2015**, *69*, 739-44, 879-83.

166. S. Galie, C. Garcia-Gutierrez, E.M. Miguelez, C.J. Villar, F. Lombo. *Front Microbiol*, **2018**, *9*, 898.
167. S. Sehar, I. Naz, *Role of the Biofilms in Wastewater Treatment*, in *Microbial Biofilms - Importance and Applications*. 2016.
168. R. Moreddu, N. Boechler, A.M. Krachler, P.M. Mendes. *Embec & Nbc 2017*, **2018**, *65*, 960-963.
169. N. Efron, *Contact Lens Complications*, in *Contact Lens Practice*. 2017.
170. M. Henriques, C. Sousa, M. Lira, M. Elisabete, R. Oliveira, R. Oliveira, J. Azeredo. *Optom Vis Sci*, **2005**, *82*, 446-50.
171. D. Dutta, N. Cole, M. Willcox. *Mol Vis*, **2012**, *18*, 14-21.
172. R. Mosuela, S. Mustafa, S. Gould, H. Hassanin, R.G. Alany, A. ElShaer. *Colloids Surf B Biointerfaces*, **2018**, *163*, 91-99.
173. N.B. Patel, J.A. Hinojosa, M.F. Zhu, D.M. Robertson. *Molecular Vision*, **2018**, *24*, 94-104.
174. J.A. Hinojosa, N.B. Patel, M. Zhu, D.M. Robertson. *Transl Vis Sci Technol*, **2017**, *6*, 11.
175. M. Veli, A. Ozcan. *ACS Nano*, **2018**, *12*, 2554-2559.
176. H. Shin, K. Price, L. Albert, J. Dodick, L. Park, M.G. Dominguez-Bello. *MBio*, **2016**, *7*, e00198.
177. M.S. Yung, M. Boost, P. Cho, M. Yap. *Ophthalmic Physiol Opt*, **2007**, *27*, 11-21.
178. J. Dantam, D.J. McCanna, L.N. Subbaraman, D. Papinski, C. Lakkis, A. Mirza, D.A. Berntsen, P. Morgan, J.J. Nichols, L.W. Jones, P.C.L. Solutions. *Optometry and Vision Science*, **2016**, *93*, 925-932.
179. A. Xiao, C. Dhand, C.M. Leung, R.W. Beuerman, S. Ramakrishna, R. Lakshminarayanan. *Journal of Materials Chemistry B*, **2018**, *6*, 2171-2186.
180. F. Alipour, S. Khaheshi, M. Soleimanzadeh, S. Heidarzadeh, S. Heydarzadeh. *J Ophthalmic Vis Res*, **2017**, *12*, 193-204.
181. in *Contact Lens Spectrum*. December 2018.
182. N. Efron, P.B. Morgan, S.S. Katsara. *Ophthalmic and Physiological Optics*, **2001**, *21*, 17-29.
183. L.B. Szczotka-Flynn, E. Pearlman, M. Ghannoum. *Eye Contact Lens*, **2010**, *36*, 116-29.
184. L.B. Szczotka-Flynn, Y. Imamura, J. Chandra, C. Yu, P.K. Mukherjee, E. Pearlman, M.A. Ghannoum. *Cornea*, **2009**, *28*, 918-26.
185. R.A. Ferris, P.M. McCue, G.I. Borlee, K.D. Loncar, M.L. Hennet, B.R. Borlee. *J Clin Microbiol*, **2016**, *54*, 631-9.
186. N. Nair, R. Biswas, F. Gotz, L. Biswas. *Infect Immun*, **2014**, *82*, 2162-9.
187. C. Hildebrandt, D. Wagner, T. Kohlmann, A. Kramer. *BMC Infect Dis*, **2012**, *12*, 241.
188. D. Callahan, C. Kovacs, S. Lynch, M. Rah. *Clin Exp Optom*, **2017**, *100*, 357-364.
189. D.W. Stroman, K. Mintun, A.B. Epstein, C.M. Brimer, C.R. Patel, J.D. Branch, K. Najafi-Tagol. *Clin Ophthalmol*, **2017**, *11*, 707-714.
190. N. Garcia-Porta, L. Rico-del-Viejo, H. Ferreira-Neves, S.C. Peixoto-de-Matos, A. Queiros, J.M. Gonzalez-Meijome. *Biomed Res Int*, **2015**, *2015*, 216932.
191. K. Yamasaki, F. Saito, R. Ota, S. Kilvington. *Cont Lens Anterior Eye*, **2018**, *41*, 277-281.
192. N. Efron, *Aftercare*, in *Contact lens practice*. 2017.
193. *ISO 10933*, **2018**,
194. *All about ISO*. https://www.iso.org/about-us.html. Accessed: 12 March 2019.
195. *University of Pittsburg*. http://www.sis.pitt.edu/mbsclass/standards/martincic/isohistr.htm **Accessed 12 March 2019.**,
196. *International Organization for Standardization (ISO)*, https://www.iso.org/news/ref2318.html, Accessed 12 March 2019.
197. M.T. Marie B. Teixeira, Richard Bradley, *Design Controls for the Medical Device Industry*, C. press, Editor. 2012.
198. *ISO 10933*, **2006**,
199. *ISO 10933*, **2010**,
200. *ISO 10933*, **2009**,
201. *ISO 10933*, **2014**,

202. *ISO 10933*, **2017**,
203. *ISO 10933*, **2016**,
204. *ISO 10933*, **2008**,
205. *ISO 10933*, **2009**,
206. *ISO 10933*, **2017**,
207. *ISO 10933*, **2012**,
208. *ISO 10933*, **2010**,
209. *ISO 9394*, **2012**,
210. *ISO 17025*, **2017**,
211. Statista, *Unit sales of the leading eye/lens care solution brands in the United States in 2018*. 2019. p. https://www.statista.com/statistics/463052/us-unit-sales-of-the-leading-eye-lens-care-solution-brands/.
212. Statista, *Market value of smart contact lenses worldwide in 2016 and 2022*. 2019. p. https://www.statista.com/statistics/822951/global-value-of-the-smart-contact-lens-market/.
213. *2018 Annual Report*, in *Contact Lens Spectrum*. January 2019. p. 18-23.

Chapter 2

Design of the sensing platforms

The building blocks for developing contact lens sensors may be defined as follows:

- Functionalization of contact lenses
- Finite element modelling (FEM)
- Synthesis of chemical sensors
- Development of readout methods

In this framework, contact lenses were functionalized by either laser inscription, to produce microfluidic networks, or nano-patterning. The first process was implemented on rigid contact lenses, made of hard polymers such as fluorosilicone acrylates, making them easier to be locally modified with laser light. The second process was implemented on lab-made soft contact lenses, made of hydrogels such as p(HEMA), or PDMS, where nanostructures were replicated from a silicon master. Chemical sensors consisted of colorimetric dyes exhibiting a consistent behavior when exposed to pH variations, glucose, proteins, nitrite ions, L-ascorbic acid, and uric acid. Readout methods were based on MATLAB and smartphone apps. Each of these topics will be individually discussed when encountered in the context of its application.

2.1 Contact lens patterning

Contact lens patterning was carried out by direct laser inscription, and by polymeric nanopatterning.

2.1.1. Laser inscription of contact lenses

Contact lens sensing platforms have drawn interests in the last decade for the possibility of providing a sterile, fully integrated ocular screening technology. However, designing scalable and convenient processing methods while keeping a high resolution is still an unsolved challenge. In this chapter, femtosecond laser writing was employed as a rapid and precise process to engrave microfluidic networks into commercial contact lenses. Functional microfluidic components such as flow valves, resistors, multi-inlet geometries, and splitters were produced using a bespoke 7-axis femtosecond laser system, yielding a resolution of 80 μm. The ablation process and the tear flow within microfluidic structures was evaluated both experimentally and computationally using finite element modeling. Flow velocity drops of the 8.3%, 20.8%, and 29% were observed in valves with enlargements of the 100%, 200% and 300%, respectively. Resistors yielded flow rate drops of 20.8% 33% and 50% in the small, medium, and large configurations, respectively. Two applications were introduced, namely a tear volume sensor and a tear uric acid sensor (sensitivity 16 mgL^{-1}), which are both painless alternatives to current methods and provide reduced contamination risks of tear samples.

Introduction

The World Health Organization reports that in 2020 approximately 2.2 billion people worldwide suffered of ocular impairment caused by a number of preventable factors, including age-related macular degeneration, cataracts, infectious diseases of the cornea, trachoma, and systemic diseases like diabetes.[1] Despite ophthalmology being one of the busiest departments in public and private hospitals worldwide, the lack of technological innovation in the field results in the inability to address these problems timely and effectively.

Currently, ocular health screening is carried out one-off only by physicians in clinics, using expensive machinery which set a global screening standard based on reaction over prevention. Extensive investigations on the tear fluid composition revealed the potential of this body fluid in the prevention and

monitoring of both ocular and systemic diseases, accompanied by the possibility to be collected painlessly and non-invasively.[2, 3]

At present, the gold standards for tear fluid collection are the Schirmer's test and the capillary tube methods.[3] The Schirmer's test consists on inserting a paper strip in the lower eyelid of the patient's eye for five minutes. A large number of studies agree on the low reliability of such test as a tear sampling method, due to the compositional variations in the tear fluid induced by local irritation of the eye, as well as by contaminants introduced by further extraction of the fluid from the paper strip.[4-6] In addition, tear fluid extraction and laboratory analysis are expensive and time-consuming procedures . The Schirmer's test is also largely used to aid the diagnosis of dry eye disease, by evaluating the amount of tear fluid collected.[3, 4, 6] This methodology has also been considered obsolete and often unreliable, given that the presence of an external body in the lower eyelid induces tear overflow, leading to false positive results.[4, 6] The capillary tube method involves a similar process where the tear fluid is collected in a glass or plastic tube, and further stored in a sterile container. This partially overcomes the problems of contamination, but keeps the disadvantages associated to external tear analysis.

The need for innovation in ophthalmology drives the development of alternative solutions to sample and analyse the tear fluid painlessly and precisely. Contact lenses can be a suitable platform to embed such functionalities, being already used by 150 million people worldwide for vision correction and cosmetics.[3] Microfluidic contact lenses have thus attracted particular interest in the last few years, due to their potential of allowing on-eye, real-time tear fluid processing.[7-10] The crucial advantages lie on the reduced contamination risks compared to current methods, fast analysis times at point-of-care settings, and the possibility of achieving continuous monitoring.[9, 11, 12]

Recent studies report on the development of enhanced contact lens devices.[7-10, 12-17] However, most of them rely on processes that are not scalable. Lab-made microfluidic contact lenses in the literature are primarily based on replica moulding of hydrogels into curved surfaces.[10] It is intuitive that such processes present several limitations: they use materials which are different from the complex polymers patented by contact lens companies and utilised in contemporary contact lens manufacturing, they require days of

work to produce a single device, and for this reason they also lack repeatability. Laser ablation has been previously used to produce structures in contact lenses by direct writing. For example, a CO_2 laser was used to inscribe microfluidic structures into soft contact lenses.[18] However, soft contact lenses are obtained by hydrophilic materials made of poly-HEMA as the core polymer, which makes them unsuitable to be used as microfluidic platforms (e. g. the liquid spreads all over the contact lens instead of following a predictable flow pattern within the microfluidic network). In this context, rigid contact lenses represent a more suitable option.[3, 7] They are made of hydrophobic silicone acrylates, making them easier to handle and process.[3] We previously demonstrated the possibility of incorporating sensors within microcavities or milli-fluidic channels in contact lenses for ocular temperature and tear analytes monitoring.[7, 8, 12] These processes involved the use of paper-assisted fluid flow, and inscription was performed by CO_2 laser ablation, yielding larger and irregular structures, that do not allow to integrate complex networks in a single device.

Femtosecond laser ablation allows to directly write extremely tiny features (down to 30 µm of width) in a single step (**Figure 14A**). The inscription takes place by cold ablation rather than melt ejection and does not require internal water cooling. The laser emits ultra-short pulses (< 400 fs) that leave no thermal fingerprint on the contact lens, avoiding thermal tension in the material and preserving its characteristics.[19] Fine features can be cut into thin substrates (10-100 µm), while still maintaining mechanical and material integrity (**Figure 14B**). They do not produce microcracks, recast layers or debris, as observed with CO_2 lasers (**Figure 14C**). Femtosecond lasers are currently used for the fine machining of stents,[20] catheters, heart valves, polymer fibres and tubes.[21, 22] Recent studies also report on the use of femtosecond laser ablation to produce periodic structures[23-26] and to aid the synthesis of nanoparticles for medical application.[22, 27, 28]

Here, femtosecond laser inscription technology was applied to commercial contact lens devices. Multiple microfluidic elements (valves, resistors, mixers, splitters, reservoirs, sensing cavities and more complex geometries) were produced into contact lenses. Two applications of this technology are demonstrated, in

the form of a tear volume sensor for dry eye disease, and a uric acid sensor to monitor gout disease progression from tears. This approach has achieved the highest resolution (80 µm) observed thus far to produce tiny channels into contact lenses in a single step. This work paves the way towards the incorporation of complex fluidic networks, and hence complex functionalities, within a single contact lens and in establishing femtosecond laser inscribed contact lenses as the pillar platform for monitoring both ocular and systemic health.

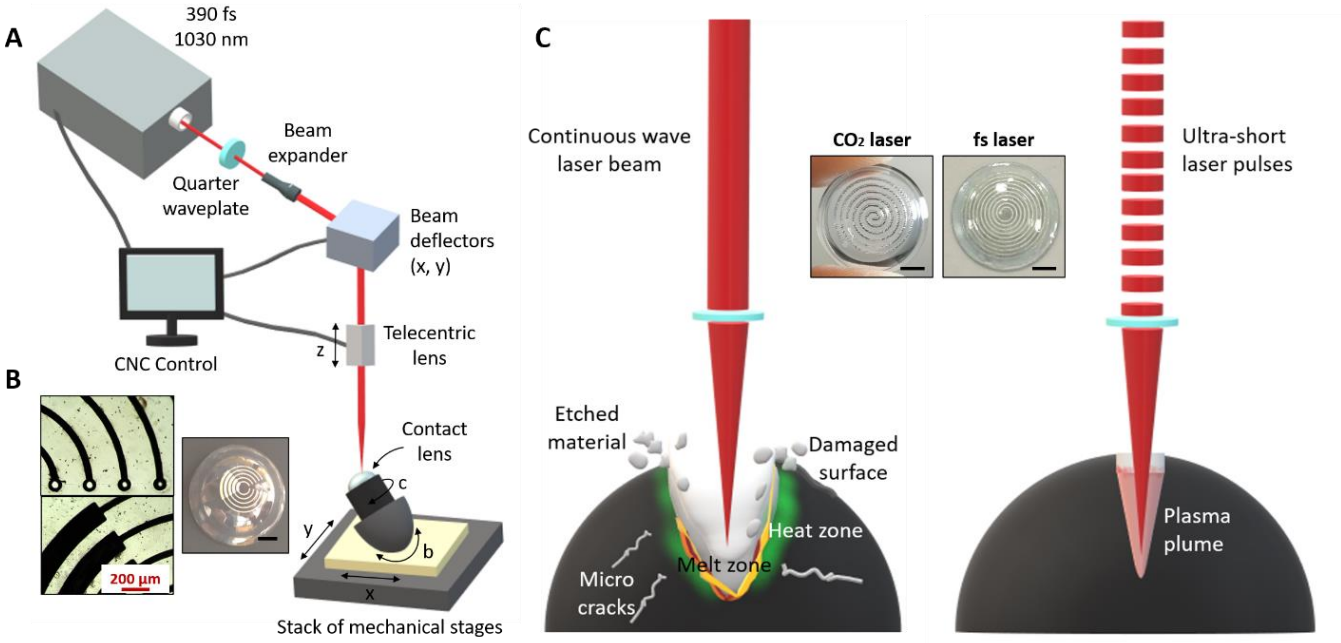

Figure 14. Femtosecond laser ablation. A) Schematic of the laser multi-axis processing setup. B) Examples of microstructures inscribed in contact lenses: micrographs of a micro-valve system (scale bar: 200 µm), photograph of an engraved contact lens (scale bar: 3 mm). C) Schematic comparing laser ablation performed with a long pulse laser beam (e.g. nanosecond and CW CO_2 lasers) and ultra-short laser pulses (femtosecond lasers). The insets show a contact lens engraved with each process, where the higher resolution obtained by ultra-short laser pulses is clearly visible. Scale bars: 3 mm.

Results

Microfluidic elements and networks were engraved into commercial fluorosilicone acrylate commercial contact lenses, with a thickness of 120 µm, using a 7-axis femtosecond laser workstation. Details on the components are presented in **Appendix I**. This allowed to uniformly engrave each area of the sample,

regardless of the curvature. The settings were optimized to yield features with a depth of 80-100 µm, and microchannels with a base width of 100 µm. Optimized parameters are primarily scanning speed, pulse energy, frequency, and 7-axis machining protocol.

Ultrafast laser ablation of polymethyl methacrylate (PMMA) has been explained by photochemical, photothermal, and photophysical models.[29] The photochemical model is based on PMMA direct bond breaking, which results in products such as CO, CO_2, CH_4, CH_3OH, and $HCOOCH_3$. The photothermal model considers thermal bond breaking induced by ultra-short laser pulses which induce the formation of PMMA monomers. The photophysical model includes bond breaking processes happening simultaneously. The three main processes of photophysical laser-induced breakdown are the excitation of conduction band electrons through ionization, heating of conduction band electrons through irradiation of the dielectric, and plasma energy transfer to the lattice.[30, 31]

This is observable when looking at the roughness profiles of microchannels etched in contact lenses using a CO_2 or a femtosecond laser. **Figure A2** (**Appendix I**) displays the surface topography, where a difference in both geometrical consistency and damaging of the surrounding material can be noticed (**Figure S2A,B**). In particular, the microchannel obtained using a femtosecond laser displayed higher uniformity in depth, higher geometrical confinement, and sharper edges. The roughness profile yielded empirical values of $S_a(CO_2)$ = 10.7 µm and S_a(fs) = 3.4 µm (**Figure S2C-F**). Roughness 3-dimensional (3D) plots also allowed to visualize a consistent depth of ~ 100 µm along the microchannels, 10 µm larger than the depth previously calculated with FEM. This was attributed to additional physics phenomena involved in ablation by ultra-short laser pulses, described in the introduction of this chapter. In fact, the finite-element computational model was purely based on thermal effect. It should also be noted that microfluidic geometries were designed such to be placed outside of the pupil area, to avoid visual impairment during wearing. However, multi-inlet geometries were patterned towards the center to allow a better visualization in the context of this thesis.

Figure 15 shows a computational evaluation on the impact of scanning speed and pulse energy on ablation depth and ablated mass (intended to be the amount of material (pg) etched away during laser writing), performed by the finite element method (FEM) and considering a pure photothermal process. **Figure 15A** displays the effect of gradually increasing the pulse energy while keeping a constant beam scanning speed of 10 mm/s and pulse frequency of 50 kHz. We can observe a linear behavior for pulse energy values from 20 μJ to 60 μJ (**Figure 15B**). A speed of 10 mm/s and pulse energy of of 50 μJ yields an average ablation depth of 90 μm. Similarly, as observed in **Figure 15C**, at a constant pulse energy of 50 μJ beam powers of 2.5 W, an increase in velocity results in a lower ablation depth, going from 180 μm at a speed of 6 mm/s to 40 μm at a speed of 16 mm/s (**Figure 15D**). In the experiments, for all devices a speed of 10 mm/s and a pulse energy of 50 μJ were used. In the simulations, the pulse frequency was set to 50 kHz, the pulse duration to 390 fs, and beam spot diameter of 35 μm at a wavelength of 1030 nm. Laser ablation computational results were obtained with a MATLAB model tailored to PMMA, a well-known material that most resembles the mechanical and physical properties of fluorosilicone acrylates.[3]

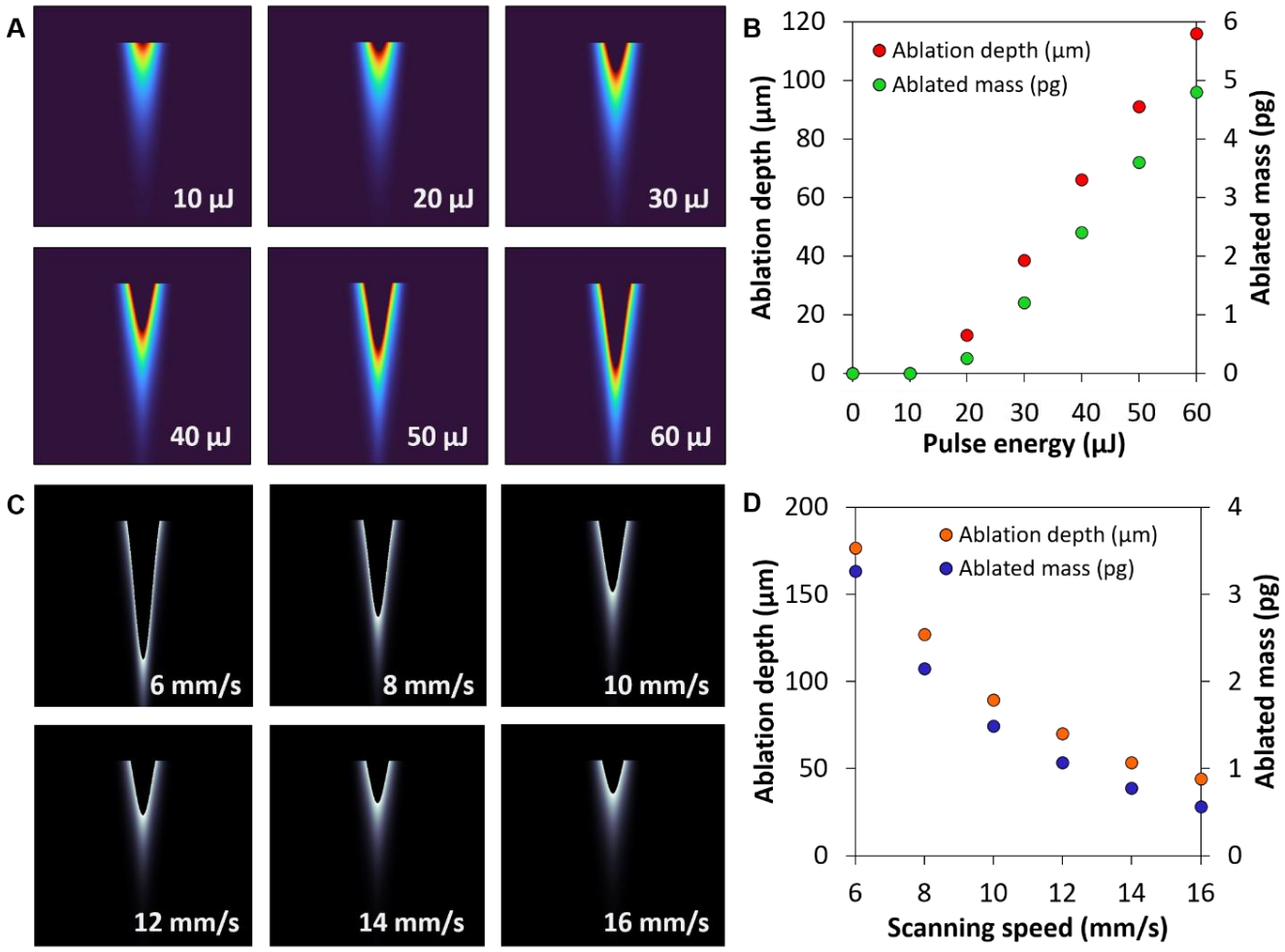

Figure 15. Computational evaluation of the laser ablation process by time-resolved FEM modelling. A-B) Influence of pulse energy (0-60 µJ) on ablation depth and ablated mass of PMMA for a speed of 10 mm/s. C-D) Influence of beam scanning speed (6-16 mm/s) on ablation depth and mass for a laser power of 2.5 W.

Figure 16 shows a set of valves engraved onto contact lenses. Microfluidic valves are used to adjust the flow velocity in certain areas of the channel. Photographs of the devices are showed in **Figure 16A**, namely a regular microchannel with a uniform width of 100 µm, and the same channel with the addition of three different valve geometries, having width enlargements of the 100%, 200% and 300% (200 µm, 300 µm and 400 µm, respectively), compared to the base channel. Micrographs of the valves are shown in **Figure 16B**. Geometrical details are presented in **Appendix II**. Prior to experimental flow evaluations, contact lenses were hydrophilized via oxygen plasma treatment (**Appendix II**). A blue dye and a smartphone camera were used to evaluate the filling time of each geometry, resulting in an average

decrease of 0.25 s per 100% of channel enlargement (**Figure 16C**). The flow velocity profile within the same geometries was computed with FEM (**Figure 16D**). At time t = 0 ms, all profiles appear dark blue (null velocity). At t = 0.5 ms, the velocity profile reaches a value of 6.5 mm/s in the base channel, 4.0 mm/s in V1 (100%), 3.0 mm/s V2 (200%), and 2 mm/s in V3 (300%). Similarly, at t = 1 ms, the base channel draws a velocity profile with an average of 7 mm/s, compared to 5 mm/s in V1, 3.5 mm/s in V2, and 3 mm/s in V3. The plots next to each set of figures display the cross-sectional velocity profile comparison between channel and valve in the four geometries at the three times of consideration (0 ms, 0.5 ms, 1 ms).

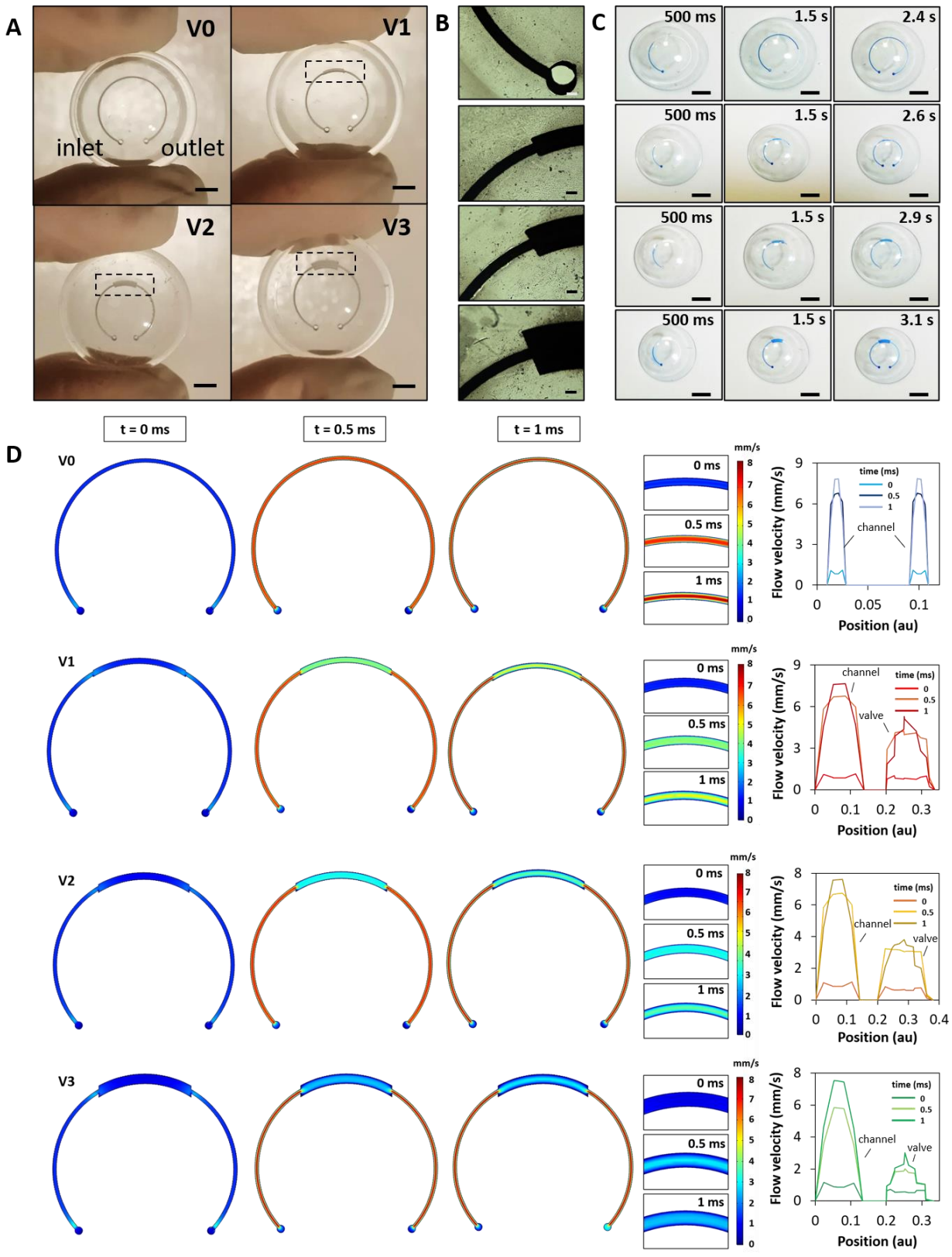

Figure 16. Flow valves engraved in contact lenses. A) Photographs of base channel V0 (constant thickness of 120 μm), V1 (100% enlargement), V2 (200% enlargement), and V3 (300% enlargement). Scale bars: 3 mm. B) Micrographs of flow valves:

inlet, 100%, 200%, 300%. Scale bars: 100 μm. C) Fluid flow within microfluidic contact lens valves. Scale bars: 5 mm. D) Computational fluid flow within valves.

Figure 17 shows a set of resistors engraved in contact lenses. Microfluidic resistors are used to either reduce the fluid flow velocity in certain sections, or to decrease the overall velocity by increasing the total volume of the network, while keeping it confined to the same area. In this case, three types of resistors were compared. Photographs of the devices are shown in **Figure 17A**, named R1 to R3. R0 is the base channel, also shown for comparison. Micrographs of the resistors are shown in **Figure 17B**. Blue or green dyes were injected in the contact lenses via the inlet (concave side) using a PCV tube (diameter 0.5 mm) and a syringe, and a smartphone camera was used to capture the filling time (**Figure 17C**). It is observed that the fluid filled geometry R1 in 2.9 s, R2 in 3.2 s, R3 in 3.6 s, compared to the base channel which was filled in 2.4 s. This is explained by the gravity contribution. Overall, all geometries exhibited visible increased filling time compared to the base channel. This was also observed in computational studies (**Figure 17D**), where at t = 1 ms all geometries reach velocities above 6.5 mm/s in correspondence of the resistors. However, at 0.5 ms the velocity profile is higher in R1, the resistor with the largest width. R2 and R3 register comparable profiles, with slightly lower velocities in R3. The plots next to each set of figures display the cross-sectional velocity profiles taken by drawing a horizontal line along the resistors, hence 4 peaks. Geometrical details are presented in **Appendix II**.

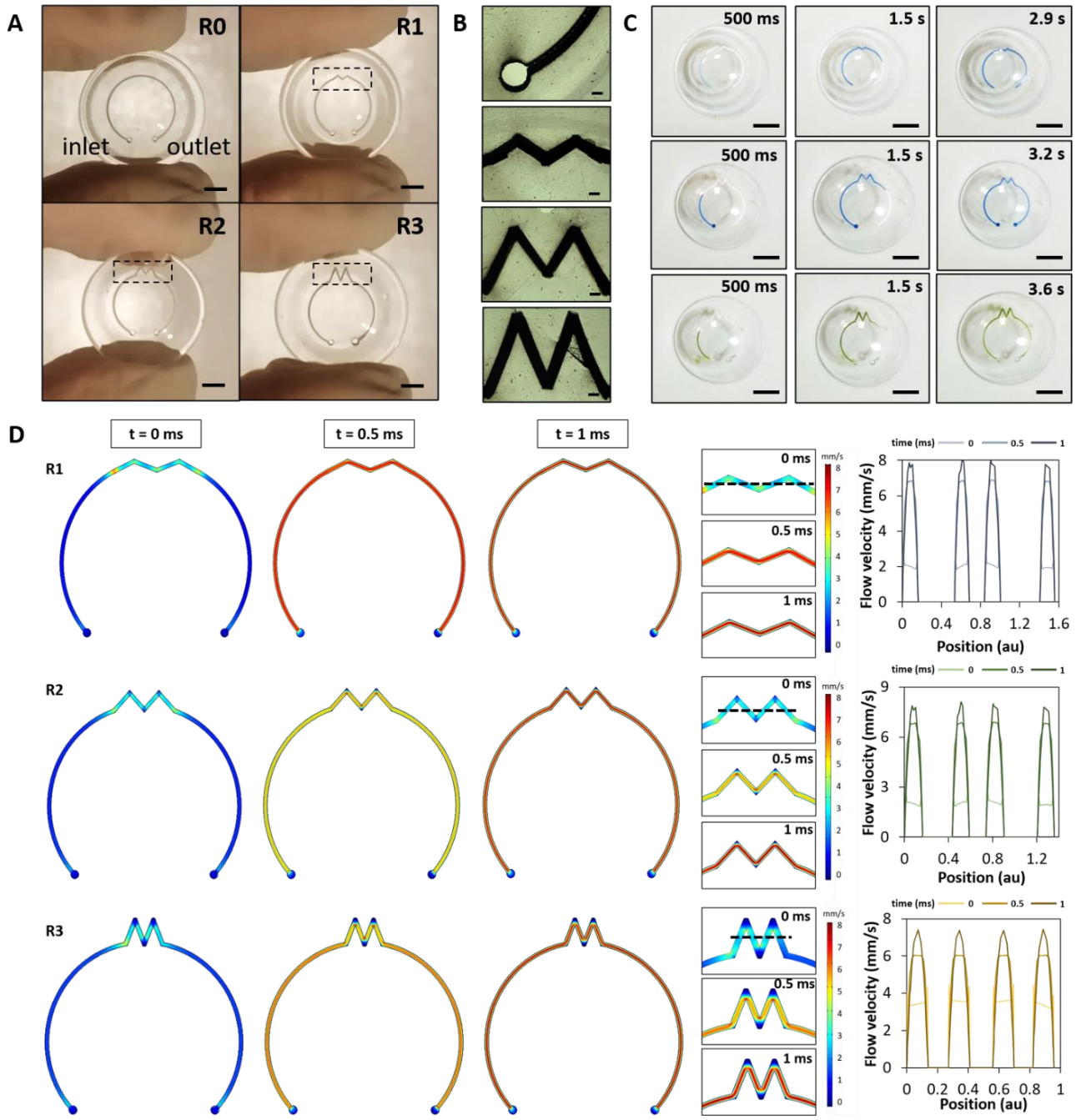

Figure 17. Flow resistors engraved in contact lenses. A) Photographs of base channel R0, R1 (wide resistor), R2 (standard resistor), and R3 (narrow resistor). Scale bars: 3 mm. B) Micrographs of flow resistors: inlet, wide, standard, narrow. Scale bars: 100 µm. C) Fluid flow within microfluidic contact lens resistors. Scale bars: 5 mm. D) Computational fluid flow within resistors.

Mixers are highly used in microfluidics, and they are a useful tool in sensing applications, where two solutions may need to be mixed before encountering tear fluid, or before interacting with a chemical sensor. In this framework, two mixing geometries were fabricated on contact lenses (**Figure 18**). **Figure 18A** displays photographs of the mixers, namely the two-branched M1 and four-branched M2. Their micrographs are shown in **Figure 18B**. Blue and green dyes were injected in the contact lenses at the same time via the inlets, and a smartphone camera was used to capture the filling time (**Figure 18C**). It resulted that M1 had a total filling time of 1.7 s, lower than the one registered for the base channel (2.4 s), attributed to the gravity contribution and the presence of two inlet sources. M2 was filled in 2.3 s from four inlets. Computational studies were performed to evaluate the velocity profiles in such geometries (**Figure 18D**), yielding a higher velocity in the branches of M1 (12 mm/s at t = 1 ms) than M2 (10 mm/s at t = 1 ms). The plots next to each set of figures represent the velocity profile in the cross-section, traced by drawing a horizontal line along the inlet branches. Geometrical details are presented in **Appendix II**.

Similarly, splitters are used in microfluidics to guide the flow towards different areas of the network. In contact lenses this is particularly interesting when multiplexing chemical sensors to detect multiple tear analytes in the same device. In fact, in the case of optical sensor (e.g. colorimetric, fluorescent) the fluid coming from the sensing area may be contaminated with sensing material. This can be prevented by devoting different microfluidic areas to different sensors. Here, two splitter geometries were fabricated on contact lenses. **Figure 18E** displays photographs of the splitters, namely the two-branched S1 and four-branched S2. Their micrographs are shown in **Figure 18F**. Blue and green dyes were injected in the contact lenses, and a smartphone camera was used to capture the filling time (**Figure 18G**). S1 had a total filling time of 2.1 s, again lower than the one registered for the base channel (2.4 s), attributed to the gravity contribution. In S2, the four outlets were reached in 2.8 s. Computational studies were performed to evaluate the velocity profiles in splitter geometries (**Figure 18H**), yielding an average velocity profile of 3.8 mm/s at t = 1 ms in the branches of S1. In S2, we observed higher velocity profiles in the inner branches (1.3 mm/s at t = 1 ms), compared to the outer branches (1.1 mm/s at t = 1 ms). In both cases, the

highest velocity profiles were found to be near the inlet, right before splitting (7.5 mm/s at t = 0.5 ms). The plots next to each set of figures represent the velocity profile in the cross-section, traced by drawing a horizontal line along the outlet branches. Geometrical details are presented in **Appendix II**.

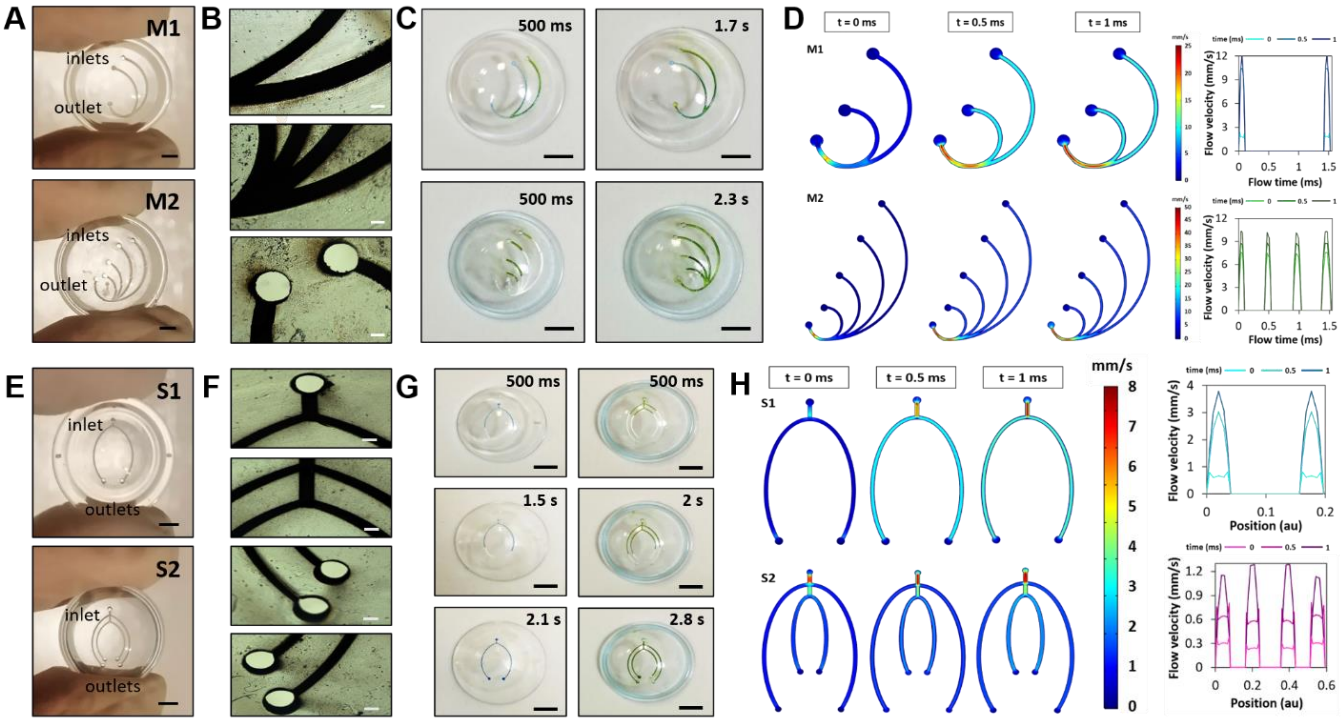

Figure 18. Flow mixers and splitters engraved in contact lenses. A) Photographs of microfluidic mixers M1 (two inlets, one outlet), and M2 (four inlets, one outlet). Scale bars: 3 mm. B) Micrographs of fluid mixers: two-branched, four-branched, inlet-outlet. Scale bars: 50 µm. C) Fluid flow within microfluidic mixers. Scale bars: 5 mm. D) Computational fluid flow within mixers. E) Photographs of microfluidic splitters S1 (one inlet, two outlets), and S2 (one inlet, four outlets). Scale bars: 3 mm. F) Micrographs of fluid splitters: two-branched, four-branched, outlets (right side), outlets (left side). Scale bars: 150 µm. C) Fluid flow within microfluidic mixers. Scale bars: 4 mm. D) Computational fluid flow within mixers.

Precisely inscribing microfluidic elements in contact lenses opens the way to a broad range of applications. These can be achieved by combining multiple elements to create a microfluidic network that performs a specific function. Microchannels on their own can already provide a smart alternative to current methods. On the other end, they may constitute the pillar platform to capitalize on for theranostic applications, by integrating sensors, drug delivery mechanisms, or both.

Here, two possible applications in the context of tear fluid monitoring are discussed. Both are addressed in the closed configuration, where the inlet is patterned as a hole in the concave side of the bottom lens, in direct contact with the ocular surface, and the outlet is a hole etched from the convex side in the top lens. Closed configurations were only presented for the applications, where a full device is a must. On the contrary, microfluidic elements were assessed earlier in this article in an open configuration (both inlets and outlets engraved as holes in a single lens). In fact, in those cases the scope was to evaluate the "absolute" impact of valves and resistors on the flow velocity, and neither of them has an application on their own.

A tear fluid volume wearable sensor based purely on microfluidics may be an alternative to the Schirmer's test (**Figure 19**). A spiral microfluidic channel was engraved on a contact lens (**Figure 19A**). Micrographs of the channel are shown in **Figure 19B**. The spiral features an inlet in the center, around the pupil area. The outlet is placed on the outer turn of the spiral. In this case, the outlet acts as a pressure regulator more than just strictly as an outlet. In fact, the spiral can host a tear volume of 30 μL, whilst the total average tear volume on the anterior eye amounts to 5 to 7 μL. Computational evaluations suggest that the velocity profile is uniform along the spiral (**Figure 19C**). To close the microfluidic channel, a lab-made PDMS contact lens was fabricated by replica molding from a curved contact lens mold (**Figure 19D**), and chemically bonded to the engraved lens, based on oxygen plasma treatment, silanization with APTES and GPTES, and direct contact, as shown in **Figure 19E**.[32] In an industrial setting, this process could be automated by using a thinner rigid contact lens as a top layer. The method currently used to assess the tear volume in dry eye patients is the Schirmer's test.[3] This consists on inserting a paper strip in the lower eyelid of the patient for 5 minutes, followed by visual readout of the wetted area to semi-quantitatively assess the tear fluid production (**Figure 19F**). This process is painful, adds up contamination risks, and induces local irritation which results in tear overflow and false negative results. The spiral lens may be a promising alternative. **Figure 19G** displays the proposed use of such device. Upon inserting the lens, the tear flows from the channel inlet, placed on the concave side of the lens, though the spiral. The contact

lens was exposed to 3 µL and 8 µL of artificial tears, respectively. The volume of the tear film may be assessed by visual method, based on the wetted spiral area after 10 s.

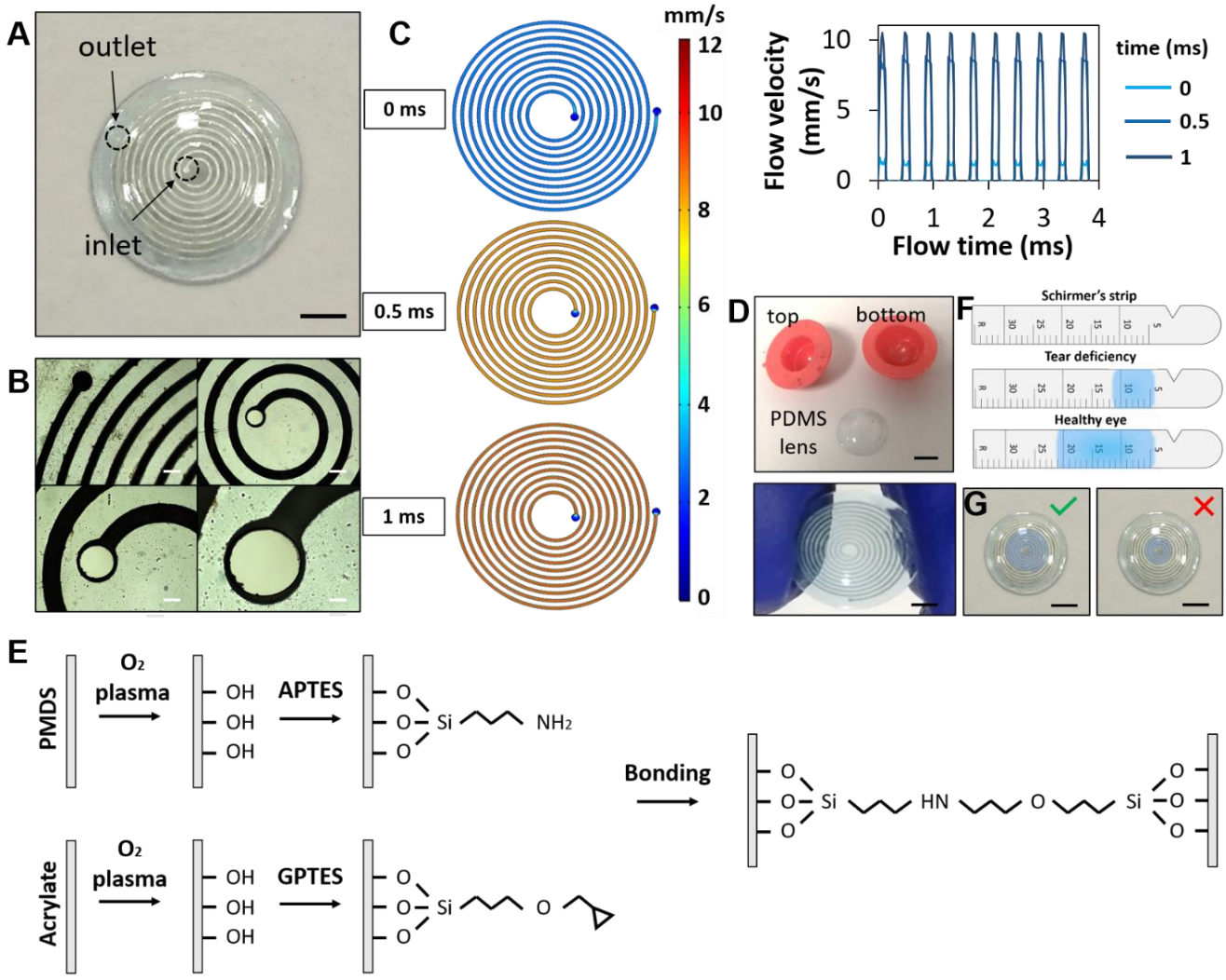

Figure 19. Microfluidic tear volume sensor. A) Photographs of the volume sensor (spiral channel engraved on a contact lens). Scale bar: 5 mm. B) Micrographs of the spiral channel. Scale bars: 150 µm. C) Computational velocity profile within the spiral lens. D) Contact lens sensor: PDMS lens fabricated in a plastic mold, and bonded to the spiral acrylic lens. Scale bars: 1 cm (top), 3 mm (bottom). E) PDMS-to-acrylic chemical bonding process. F) Working principle of the Schirmer's test to assess tear fluid volume. G) Visual readout of fluid volume from a microfluidic contact lens, based on the wetted spiral area. Scale bar: 5 mm.

The tear volume sensor may be re-used. After sampling the tear fluid from a patient, the liquid may be collected using a capillary tube and stored in a sterile container or thrown away if the lens was to be used

to evaluate the tear fluid production. Following that, the lens may be disinfected, dried and re-used. A cleaning protocol would need to be tailored for this specific need. The tear uric acid sensor is disposable and meant for one-off measurements.

Another application is presented in **Figure 20**. Here, a microfluidic channel featuring an inlet, sensing area, fluidic valve and a reservoir is demonstrated for the detection of uric acid on-eye (**Figure 20A, B**). Uric acid is an extensively known biomarker for gout disease progression, as well as to monitor the antioxidant status in the eye.[30-32] The tear flows from the inlet to the sensing area, where the colorimetric uric acid sensor is embedded. From the sensing area, the fluid encounters a valve with an enlargement of the 300% compared to the base channel, which decreases the flow velocity of the 60%, until reaching a reservoir, where the fluid velocity stops (**Figure 20C**). Computational evaluations show that there is no backflow from the reservoir to the valve, nor from the valve to the sensing area (**Figure 20D**).

The uric acid sensor was based on uricase and horseradish peroxidase (HRP). In the presence of oxygen, water and uricase, uric acid is converted into 5-hydroxyisourate and hydrogen peroxide. 5-hydroxyisourate further reacts with water to produce allantoin and CO_2. Hydrogen peroxide, in the presence of HRP, reacts with 4-aminoantipyrine and with N-Ethyl-N-(2-hydroxy-3-sulfopropyl)-3,5-dimethoxyaniline (MAOS) to produce a blue dye. The amount of blue dye produced is proportional to the amount of hydrogen peroxide obtained by reaction of uric acid, yielding a color scale proportional to uric acid concentration (**Figure 20E**). The reflection spectra of the uric acid sensor at concentrations of 0, 50, 100, 150, 200 and 250 mg/L are shown in **Figure 20F**. The calibration curve is displayed in **Figure 20G**, from which a sensitivity of 16 mg/L was calculated. The sensor is embedded in the sensing cavity etched in the contact lens, and the color of the sensor could be readout using a smartphone app (Color Grab) to assess the red, green, and blue (RGB) composition, and correlated to a discrete concentration value in the range 0-250 mg/L of uric acid (**Figure 20H, I**). Geometrical details of the contact lens sensors are presented in **Appendix II**.

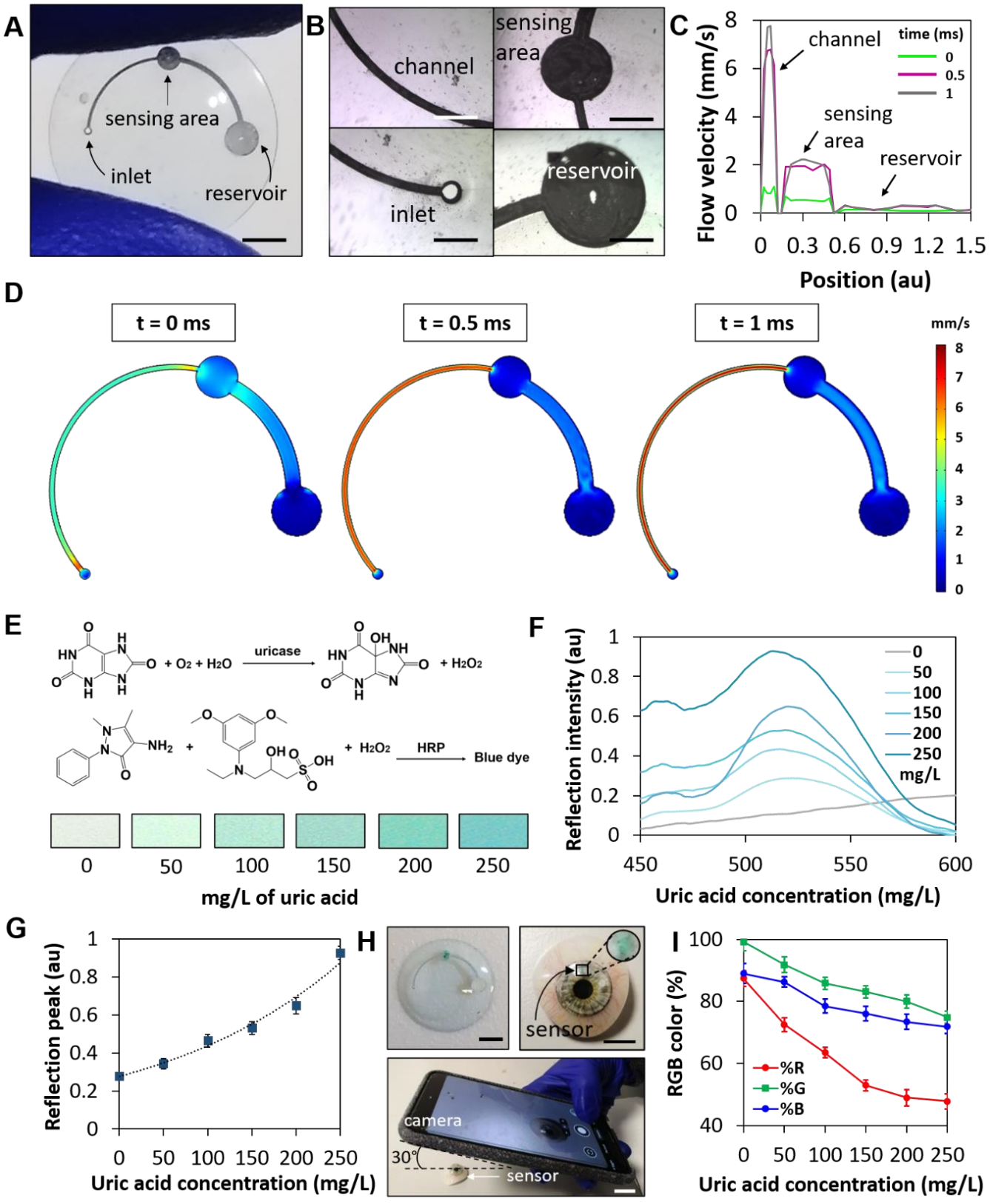

Figure 20. Microfluidic contact lens as a tear uric acid sensor. A) Photograph of the engraved contact lens, featuring inlet, channel, sensing area, flow valve, and reservoir. Scale bar: 3 mm. B) Micrographs of the microfluidic areas. Scale bars: 400 µm. C) Velocity profile along the contact lens: the flow velocity is at its maximum within the channel section, decreases at the sensing area and stops in correspondence of the reservoir. D) Computational velocity profile within the geometry. E) Sensing

reaction. Uric acid is converted into hydrogen peroxide, which further reacts with 4-AMP to produce a blue dye. Insets show the color change of the sensor in the concentration range 0-250 mg/L. F) Reflection spectra of the uric acid sensor in the concentration range 0-250 mg/L. G) Calibration curve of the sensor. H) Uric acid sensor embedded in a contact lens and placed on an eye model where artificial tear flows. The color is captured with a smartphone camera. Scale bars (left, right, bottom): 3 mm, 7 mm, 1.5 cm. I) RGB color characterization of the uric acid sensor.

Materials and Methods

Materials. Rigid contact lenses (Boston XO) were obtained from Bausch & Lomb, Canada. Sylgard 184 silicone elastomer kit (1:10) was purchased from Dow Corning, USA. (3-Aminopropyl)triethoxysilane (APTES), (3-Glycidyloxypropyl)triethoxysilane (GPTES), uric acid, D-(+)-glucose (99.5%), protein standard (200 mg/mL), boric acid, ethylenediaminetetraacetic acid (EDTA), 10% triton X-100, sodium borate, isopropanol (IPA) and phosphate buffered saline (PBS) were purchased from Sigma-Aldrich, UK and used without further purification. Uric acid colorimetric assays were purchased online from Health Mate, UK. Green and blue food coloring dyes (Waitrose Essentials) were purchased from Waitrose & Partners, UK. Systane artificial tears were purchased from Boots Ltd., UK and modified as needed.

Equipment. The laser system consisted of a LS4 LASEA workstation integrating a femtosecond laser source (YUJA from Amplitude Systemes) with 10W average power, 100 µJ maximum pulse energy, 390 fs pulse duration, 2 MHz maximum repetition rate, 1030 nm center wavelength and beam quality M2 > 1.2. The beam delivery system is equipped with a X-Y beam deflector, synchronized with a stack of mechanical stages (3 linear stages X-Y-Z and 2 rotary stages B, C). Other equipment included oxygen plasma system Atto Model 4 with a 40 kHz 200 W generator (Diener electronic GmbH + Co. KG, Germany), Smartphone camera (photo 12 MP, f/2.2, 1/2.8", 1.25µm, PDAF; video 1080p@30fps), FLAME-S-VIS-NIR-ES Spectrometer Assembly 350-1000nm (Ocean Insight, USA), pH meter FiveEasy F20 (Mettler Toledo, USA), Pioneer PX 323/E Precision Balance (Ohaus, USA), Vortex Mixer (Fisherbrand, UK), Visible Light Source HL-2000-HP-FHSA 20W (Ocean Optics, USA), Leica DM2700 P Upright Microscope (Leica Microsystems GmbH, Germany), Contact angle measurements: VHX-1000

digital microscope (Keyence Corporation, Japan) with a custom 3D printed fixture for dispensing deionized water droplets with a 10 µl pipette (Eppendorf, Germany).

Software. MATLAB R2020B (MathWorks, USA), COMSOL Multiphysics v5.3a (Comol Inc., Sweden), Color Grab application (Loomatix Ltd) installed on a Huawei P10 Lite (Huawei Technologies Co., Ltd, China) running Android 10.0 mobile operating system (Google LLC, USA), contact angle measurements using the contact angle measurement plug-in in ImageJ.

Laser ablation simulations. Femtosecond laser ablation of PMMA was simulated using time-domain FEM modeling, assuming a purely photothermal process, described by the heat equation:

$$\mathrm{Q} = \frac{\partial U}{\partial t} - \mathrm{D}\nabla^2 U \text{ (Eq. 1)}$$

where *Q* is the heat transferred from the laser and to PMMA and *D* the thermal diffusivity of PMMA. Beam spot diameter, step over, frequency, wavelength, and pulse duration were set to 35 µm, 20 µm, 50 kHz, 1030 nm and 390 fs, respectively. Beam scanning speed and pulse energy were set in the range 6-16 mm/s and 0-60 µJ, respectively, to estimate their impact on ablation depth and ablated mass of PMMA. The properties of PMMA were obtained from the literature:[36] thermal capacity (1418 J kg^{-1} K^{-1}), density (1180 kg m^{-3}), and thermal diffusivity (0.115e-6 m^2 s^{-1}).

Femtosecond laser micro-processing of contact lenses. A fractional factorial design was conducted for the optimization of laser parameters, yielding optimized values of 50 kHz (pulse frequency), 50 µJ (pulse energy), 10 mm/s (scanning speed) and 20 µm (step over). To achieve a uniform geometry of the micro-features regardless of the contact lens curvature, the laser beam focused was continuously monitored and kept normal to the surface. For a freeform surface like a contact lens this was achieved by implementing two rotary stages and X-Y-Z linear stages, synchronized with a X-Y beam deflector.

Microfluidic simulations. Microfluidic 2D geometries were designed on COMSOL and tear flow was evaluated under laminar regime. The solid material was defined as PMMA and assigned to the

microchannel area. The liquid material was customized to reproduce the aqueous tear film by defining an incompressible Newtonian fluid with viscosity $\mu = 1.3\times 10^{-3}$ Pa s, surface tension $\sigma = 0.045$ N m^{-1}, thermal conductivity $k = 0.68$ W m^{-1} K^{-1}, density $\rho = 103$ kg m^{-3}, and characteristic speed $U_0 = 5 \times 10^{-3}$ m s^{-1}.[37] An incompressible, single-phase fluid assumes that temperature variations in the flow are small, which means that the density is constant, described by the continuity and the momentum equations:

$$\rho\nabla \cdot \mathbf{u} = 0 \text{ (Eq. 2)}$$

$$\rho\frac{\partial \boldsymbol{u}}{\partial t} + \rho(\mathbf{u} \cdot \nabla)\mathbf{u} = \nabla \cdot [-p\mathbf{I} + \mu(\nabla\mathbf{u} + (\nabla\mathbf{u})^T)] + \mathbf{F} \text{ (Eq. 3)}$$

Initial values for pressure and velocity were set to zero. At the microchannel walls, the equation was solved with an initial $\mathbf{u} = 0$, with "no slip" as the boundary condition. At the inlet, the equation was solved for $\mathbf{u} = -U_0\mathbf{n}$ as the boundary condition, with $U_0 = 0.1$ µm s^{-1}. The time-dependent flows were computed for the interval (0:0.1:1) ms. The same constraints at the inlet and outlet were applied in all geometries.

Flow characterization. Flow experiments were conducted by injecting 10 µL of dye via the inlet of the microchannels using a PVC tube with a diameter of 0.5 mm and connected to a liquid dispenser. The flow was recorded with a smartphone camera.

Hydrophilization of contact lenses. Contact lenses were O_2 plasma treated for 1 min at full power (200 W). During the pumping down period the pressure was set to 0.07 mbar. The O_2 gas supply was set to 5 min at a gas flow of 100% and a process pressure of 0.2 mbar.

Preparation of PDMS contact lenses. PDMS was obtained by mixing the elastomer pre-polymer and curing agent in a 10:1 weight ratio, followed by 2 h degassing at ambient temperature and manual removal of bubbles by exerting air flow using a pipette. 100 µL of the uncured mixture was then poured into the contact lens mold and cured on a hot plate at 80° C for 15 minutes. The lenses were then removed from the mold, rinsed in isopropanol, and blow dried.

Preparation of uric acid buffer solutions. Uric acid has a low solubility in water, but it can be dissolved in borate buffer, NaOH and DI water. First, the borate buffer solution was prepared by dissolving boric acid (6.2 g), sodium borate (9.5 g) and EDTA (1.2 g) in 10% Triton X-100 (400 µL) and deionized water (200 mL), adjusting to a pH of 8.5 with NaOH. The uric acid diluent solution was further obtained by mixing deionized water (150 mL) with borate buffer storage solution (8 mL), adjusting to a pH of 8.5 with NaOH. Uric acid was then diluted in the diluent solution to yield concentrations of 0, 50, 100, 150, 200, 250 mg/L. Uric acid buffer solutions were then mixed with Systane artificial tears, and the pH was adjusted to 7.0 using tris buffers.

Characterization of uric acid sensors. Uric acid paper sensors were exposed to artificial tears containing uric acid in the concentration range 0-250 mg/L, at steps of 50 mg/L. Their colorimetric response was imaged with a smartphone camera placed at normal incidence at an ambient lighting of 250 lux (lx), monitored with Photometer PRO app, and the color was readout using Color Grab app. The reflection spectra and related calibration curve were acquired using a reflection setup consisting of a bifurcated optical fiber connected to a spectrometer and a light source, taking as a background reference the spectra obtained by irradiating a black-colored paper sensor made of the same material.

Conclusions

Femtosecond laser ablation is a simple and effective method to produce fine microfluidic structures onto rigid contact lenses. It overcomes the limitations encountered with longer pulse lasers, i.e. nanosecond and CW CO_2 lasers. When designing microfluidic contact lenses, a crucial parameter to consider is the analysis time, hence the wearing time, to avoid tear overflow and, where present, leakage of the sensing materials. In this context, multiple microfluidic elements were demonstrated to provide a tool of playing with filling time (e.g. fluidic valves and resistors) and waste tears collection systems (e.g. reservoirs). The integration of colorimetric sensor was demonstrated in the mm range to allow an easier visualization with a smartphone camera. However, the sensing area may be scaled down to the µm range when designing

sensors based on a different optical mechanism (e.g. fluorescence), coupled to a smartphone-compatible readout device. Microfluidic contact lenses are a promising alternative to current sampling and screening methods in ophthalmology, offering the possibility to sample the tear fluid with a sterile method, as well as integrating complex fluidic networks to continuously monitor the tear fluid directly on eye. Such devices may find application in ophthalmic theranostics, by incorporating sensing technologies, drug delivery mechanisms, or both.

2.1.2. Replica molding

The replica molding process consisted of etching a pattern on a silicon master, further used as a mold to reproduce the reciprocal pattern on a soft polymer. The silicon masters were fabricated by electron beam lithography. This process will be discussed in the framework of ocular pressure sensing, **Chapter 4.** The design of nanostructures is summarized in **Appendix III.**

2.2. Multiphysics simulations

Multiphysics simulations were run using COMSOL 5.3 and MATLAB, to estimate and visualize:

- Laser ablation simulations (**Chapter 2.1**)
- Tear flow within microfluidic contact lenses (**Chapter 2.1**)
- Stress/strain of PDMS nanobuttons (**Chapter 4**)

Each method is described in the framework of its application.

2.3. Chemical sensing

The materials and sensing mechanisms will be individually addressed in each dedicated section throughout this thesis. In particular:

- Cholesteric liquid crystals were employed as the active element in contact lenses for ocular surface temperature (OST) continuous monitoring (**Chapter 3**).

- Uric acid paper sensors were utilized to demonstrate the possibility of integrating a tear sensor within a microfluidic system obtained by femtosecond laser ablation (**Chapter 2.1.**).
- Colorimetric dyes to monitor glucose, proteins, nitrite ions, pH, and L-ascorbic acid are described in **Chapter 5**.

2.4. Readout methods

Readout methods used in this work mainly involved the use of MATLAB e the development of a smartphone app prototype. Both were based on the nearest neighbor mode, an efficient algorithm for detecting discrete concentration values. The algorithm is described in the next sections.

The color gamut is a scalar field that defines all the displayable and visible colors to the human eye of a certain output device.[35] According to the CIE colorimetric standards from 1931, it is composed of x and y values, depending on the particular tuple location it constitutes the associated color.[36] As a first step, a calibration curve was generated. For this, pictures of the colorimetric results of the calibration points need to be taken and located inside of the color gamut. To gain the 2D (x, y) CIE 1931 chromaticity space, RGB values of every pixel from the pictures needs to be read out and saved. It is important to note that the usual color space for images whose pixels are stored in 8-bit integers per color channel is the sRGB, standard RGB, color space and are not in RGB values.[37] The choice of this color space is the human perception of color. Its sensitivity to light and therefore the discrimination between lighter and darker shades is finer at low than at high intensities.[35] If a linear RGB scale is saved, more lighter colors appear but since they are barely specifiable for the human eye the storage is chosen unfavorably. Therefore, to make most out of the storage, a non-linear RGB curve with a shallower bottom is generated monitoring more darker shades and hence a seemingly wider variety of color. This procedure is known under the name of gamma correction and is mathematically defined as:[38]

$$Output(Ix) = Input(V)^{\gamma}$$

Firstly, the average of the non-linear RGB values of every pixel is calculated and saved. After the determination of the sRGB values, the values are linearized using following equations:[35]

$$R_l = \left(\frac{0.055 \times R_c}{1.055}\right)^{2.4}; G_l = \left(\frac{0.055 \times G_c}{1.055}\right)^{2.4}; B_l = \left(\frac{0.055 \times B_c}{1.055}\right)^{2.4}$$

with (R_c, G_c, B_c) being non-linear and (R_l, G_l, B_l) being the linearized values and a gamma correction of 2.4. As a next step the new tristimulus values X, Y, Z must be calculated. Since negative values are present in color-matching functions while working with RGB values, the CIE recommended to execute a base transformation, so that the possibility of error and misgivings is diminished.[35] The new tristimulus values X, Y, Z are obtained by following equation:[37]

$$\begin{bmatrix} X \\ Y \\ Z \end{bmatrix} = \begin{bmatrix} 0{,}4124564 & 0{,}3575761 & 0{,}1804375 \\ 0{,}2126729 & 0{,}7151522 & 0{,}0721750 \\ 0{,}019339 & 0{,}1191920 & 0{,}9503401 \end{bmatrix} \begin{bmatrix} R \\ G \\ B \end{bmatrix}$$

With this base transformation, another advantage occurs: with the Y value the brightness of the color can be adjusted, on the other hand X and Z set the hue. As a last step, the X, Y, Z values are converted into the 2D (x, y) CIE 1931 chromaticity using following equation:[36]

$$x_j = \frac{X}{X+Y+Z}; y_j = \frac{Y}{X+Y+Z}$$

Where the subscript j defines the amount of calibration points. Three calibration images for each discrete concentration value are loaded in the algorithm. Upon taking a new photo, the algorithm plots the color in the chromaticity diagram, it compares it to the calibration points, and outputs the nearest calibration value.[39] The shortest distance from the unknown concentration to calibration points is computed by:

$$d_k = \sqrt{(x_k - x_m)^2 + (y_k - y_m)^2}$$

Where k is the number of the (1, 2, 3, …j) calibration points. The closest value is given as an output.

The code is included in **Appendix IV**.

2.5. References

1. The World Health Organization, Eye care, vision care, vision impairment and blindness. https://www.who.int/health-topics/blindness-and-vision-loss#tab=tab_1. Accessed in March 2021.
2. S. Hagan, E. Martin, A. Enríquez de Salamanca, Tear fluid biomarkers in ocular and systemic disease: potential use for predictive, preventive and personalised medicine. *EMPA Journal* **2016,** *7* (1), 15.
3. R. Moreddu, D. Vigolo, A. K. Yetisen, Contact Lens Technology: From Fundamentals to Applications. *Advanced Healthcare Materials* **2019,** *8* (15), 1900368.
4. M. Senchyna, M. B. Wax, Quantitative assessment of tear production: A review of methods and utility in dry eye drug discovery. *Journal of Ocular Biology, Diseases, and Informatics* **2008,** *1*, 1–6.
5. P. Versura, M. Frigato, M. Cellini, R. Mulè, N. Malavolta, E. C. Campos Diagnostic performance of tear function tests in Sjogren's syndrome patients. *Eye* **2007,** *21*, 229–237.
6. N. Li, X. G. Deng, M. F. He, Comparison of the Schirmer I test with and without topical anesthesia for diagnosing dry eye. *International Journal of Ophthalmology* **2012,** *5* (4), 478–481.
7. R. Moreddu, J. S. Wolffsohn, D. Vigolo, A. K. Yetisen, Laser-inscribed contact lens sensors for the detection of analytes in the tear fluid. *Sensors and Actuators B: Chemical* **2020,** *317*, 128183.
8. R. Moreddu, M. Elsherif, H. Adams, D. Moschou, M. F. Cordeiro, J. S. Wolffsohn, D. Vigolo, H. Butt, J. M. Cooper, A. K. Yetisen, Integration of paper microfluidic sensors into contact lenses for tear fluid analysis. *Lab on a Chip* **2020,** *20*, 3970-3979.
9. R. S. Riaz, M. Elsherif, R. Moreddu, I. Rashid, M. U. Hassan, A. K. Yetisen, H. Butt, Anthocyanin-functionalized contact lens sensors for ocular pH monitoring. *ACS Omega* **2019,** *4* (26), 21792–21798.
10. Y. Chen, S. Zhang, Q. Cui, J. Ni, X. Wang, X. Cheng, H. Alem, P. Tebon, C. Xu, C. Guo, R. Nasiri, R. Moreddu, A. K. Yetisen, S. Ahadian, N. Ashammakhi, S. Emaminejad, V. Jucaud, M. R. Dokmeci, A. Khademhosseini, Microengineered poly(HEMA) hydrogels for wearable contact lens biosensing. *Lab on a Chip* **2020,** *20*, 4205-4214.
11. N. M. Farandos, A. K. Yetisen, M. J. Monteiro, C. R. Lowe, S. H. Yun, Contact lens sensors in ocular diagnostics. *Advanced Healthcare Materials* **2015,** *4* (6), 792-810.
12. R. Moreddu, M. Elsherif, H. Butt, D. Vigolo, A. K. Yetisen, Contact lenses for continuous ocular temperature monitoring. *RSC Advances* **2019,** *9*, 11433-11442.
13. D. H. Keum, S. K. Kim, J. Koo, G. H. Lee, C. Jeon, J. W. Mok, B. H. Mun, K. J. Lee, E. Kamrani, C. K. Joo, S. Shin, J. Y. Sim, D. Myung, S. H. Yun, Z. Bao, S. K. Hahn, Wireless smart contact lens for diabetic diagnosis and therapy. *Science Advances* **2020,** *6* (17), 3252.
14. J. Kim, E. Cha, J. U. Park, Recent Advances in Smart Contact Lenses. *Advanced Materials Technologies* **2019,** *5* (1), 1900728.
15. M. Ku, J. Kim, J. E. Won, W. Kang, Y. G. Park, J. Park, J. H. Lee, J. Cheon, H. H. Lee, J. U. Park, Smart, soft contact lens for wireless immunosensing of cortisol. *Science Advances* **2020,** *6* (28), 2891.
16. S. Kim, H. J. Jeon, S. Park, D. Y. Lee, E. Chung Tear Glucose Measurement by Reflectance Spectrum of a Nanoparticle Embedded Contact Lens. *Scientific Reports* **2020,** *10*, 8254.
17. Y. Wang, Q. Zhao, X. Du Structurally coloured contact lens sensor for point-of-care ophthalmic health monitoring. *Journal of Materials Chemistry B* **2020,** *8*, 3519-3526.
18. N. Jiang, Y. Montelongo, H. Butt, A. K. Yetisen, Microfluidic contact lenses. *Small* **2018,** *14*, 1704363.
19. B. Guo, J. Sun, Y. Hua, N. Zhan, J. Jia, K. Chu, Femtosecond Laser Micro/Nano-manufacturing: Theories, Measurements, Methods, and Applications. *Nanomanufacturing and Metrology* **2020,** *3*, 26–67.
20. C. H. Hung, F. Y. Chang, Curve micromachining on the edges of nitinol biliary stent by ultrashort pulses laser. *Optics & Laser Technology* **2017,** *90*, 1-6.

21. A. Tavangara, B. Tan, K. Venkatakrishnana, Synthesis of bio-functionalized three-dimensional titania nanofibrous structures using femtosecond laser ablation. *Acta Biomaterialia* **2011,** *7* (6), 2726-2732.
22. D. F. Farson, H. W. Choi, B. Zimmerman, J. K. Steach, J. J. Chalmers, S. V. Olesik, L. J. Lee, Femtosecond laser micromachining of dielectric materials for biomedical applications. *Journal of Micromechanics and Microengineering 18* (3), 35020.
23. H. Liu, W. Lin, Z. Lin, L. Ji, M. Hong, Self-Organized Periodic Microholes Array Formation on Aluminum Surface via Femtosecond Laser Ablation Induced Incubation Effect. *Advanced Functional Materials* **2019,** *29* (42), 1903576.
24. Y. Xu, L. Yan, X. Li, H. Xu Fabrication of transition metal dichalcogenides quantum dots based on femtosecond laser ablation. *Scientific Reports* **2019,** *9*, 2931.
25. M. Keshavarz, P. Kassanos, B. Tan, K. Venkatakrishnan, Metal-oxide surface-enhanced Raman biosensor template towards point-of-care EGFR detection and cancer diagnostics. *Nanoscale Horizons* **2020,** *5*, 294-307.
26. M. Keshavarz, A. K. M. Rezaul Haque Chowdhury, P. Kassanos, B. Tan, K. Venkatakrishnan, Self-assembled N-doped Q-dot carbon nanostructures as a SERS-active biosensor with selective therapeutic functionality. *Sensors and Actuators B: Chemical* **2020,** *323*, 128703.
27. M. Dhanunjaya, C. Byram, V. S. Vendamani, S. V. Rao, A. P. Pathak, S. N. Rao, Hafnium oxide nanoparticles fabricated by femtosecond laser ablation in water. *Applied Physics A* **2019,** *125*, 74.
28. M. G. John, K. M. Tibbetts, One-step femtosecond laser ablation synthesis of sub-3 nm gold nanoparticles stabilized by silica. *Applied Surface Science* **2019,** *475*, 1048-1057.
29. S. R. Cain, A photothermal model for polymer ablation: chemical modification Journal of Physical Chemistry. *Journal of Physical Chemistry* **1993,** *97*, 051902.
30. R.R. Gattass, E. Mazur, Femtosecond laser micromachining in transparent materials. *Nature Photonics* **2008,** *2*, 219-225.
31. M. Li, S. Menon, J.P. Nibarger, G.N. Gibson, Ultrafast electron dynamics in femtosecond optical breakdown of dielectrics. *Physical Review Letters* **1999,** *82* (11), 2394–2397.
32. L. Tanga, N. Y. Lee, A facile route for irreversible bonding of plastic-PDMS hybrid microdevices at room temperature. *Lab on a Chip* **2010,** (10), 1274-1280.
33. M. Park, H. Jung, Y. Jeong, K. H. Jeong, Plasmonic Schirmer Strip for Human Tear-Based Gouty Arthritis Diagnosis Using Surface-Enhanced Raman Scattering. *ACS Nano* **2017,** *11* (1), 438-443.
34. E. F. Gabriel, P. T. Garcia, T. M. Cardoso, F. M. Lopes, F. T. Martinsa, W. K. Coltro Highly sensitive colorimetric detection of glucose and uric acid in biological fluids using chitosan-modified paper microfluidic devices. *Analyst* **2016,** *141*, 4749-4756.
35. J. Horwath-Winter, S. Kirchengast, A. Meinitzer, C. Wachswender, C. Faschinger, O. Schmut, Determination of uric acid concentrations in human tear fluid, aqueous humour and serum. *Acta Ophthalmologica* **2009,** *87* (2), 188-192.
36. AZOM Materials, Polymethylmethacrylate. https://www.azom.com/article.aspx?ArticleID=788. Accessed in March 2021.
37. L. Li, R. J. Braun, K. L. Maki, W. D. Henshaw, P. E. King-Smith, Tear film dynamics with evaporation, wetting, and time-dependent flux boundary condition on an eye-shaped domain. *Physics of Fluids* **1994,** *26* (5), 052101.

Chapter 3

Ocular Temperature Monitoring

Temperature variation is a ubiquitous medical sign to monitor ocular conditions including dry eye disease (DED), glaucoma, carotid artery stenosis, diabetic retinopathy, and vascular neuritis. The ability to measure OST in real time is desirable in point-of-care diagnostics. Here, we developed minimally invasive contact lens temperature sensors for continuous monitoring of the corneal temperature. The contact lens sensor consisted of a laser patterned commercial contact lens embedding temperature-sensitive Cholesteric Liquid Crystals (CLCs), which exhibited a fully reversible temperature-dependent color change in the visible spectrum. The contact lens allowed the corneal temperature to be mapped in four key areas, at distances of 0.0, 1.0, 3.0, and 5.0 mm from the pupil's edge. Liquid crystals exhibited a wavelength shift from 738 ± 4 nm to 474 ± 4 nm upon increasing the temperature from 29.0 °C to 40.0 °C, with a time responsivity of 490 ms and a negligible hysteresis. Readouts were performed using a smartphone, which output RGB triplets associated to temperature values. Contact lens sensors based on CLCs were fitted and tested on an *ex vivo* porcine eye and readouts were compared with infrared thermal measurements, resulting in an average difference of 0.3 °C.

3.1. Introduction

The interest in monitoring the Ocular Surface Temperature dates back to 1875, with the first successful measurement using a glass mercury thermometer placed on the conjunctival sac to evaluate OST variations in healthy and acute iritis conditions.[1] Currently, infrared thermography is the gold standard to measure OST with a sensitivity of 0.1 °C. [1, 2] An infrared camera is used to record a thermal pattern in a non-invasive procedure performed by a specialist in clinics. Thermal ocular patterns were recently studied by image analysis techniques.[3, 4] Among the most immediate responses to an inflammatory state lies an increase in body temperature, and positive correlations between body temperature and ocular

temperature were reported.[1] Many efforts have been put in mapping the ocular temperature across the anterior eye, giving particular attention to the visible ocular surface. The latest exhibits local temperature variations.[5-7] The literature indicates healthy temperature values in the range 32.9°C to 36.6°C referring to an average across the cornea.[1, 8] Several factors showed to have an impact on OST, including ambient temperature[9, 10] and humidity,[11] age of the subject (average decrease of 0.015°C per year),[12] use of eye-drops,[13] contact lens wear,[14] tear film instability.[8] OST was found not to vary between right and left eye, and among genders.[15] OST variation was targeted as a potential stimulus to blink.[1] Ocular temperature was also studied in animal models to develop novel drug delivery systems.[16] The Intra-Ocular Pressure (IOP),[17] corneal elasticity and related refractive properties of the eye[18] were also demonstrated to be related to the temperature of the ocular anterior chamber. Several ocular conditions were reported to be linked to OST variations, resulting from a change in blood flow to the sclera and conjunctiva.[19] OST was found to variate in cases of inflammation, among which Dry Eye Disease (DED),[20-28] glaucoma,[29] diabetic retinopathy,[30, 31] and vascular neuritis.[1] Strong positive correlations were reported between ocular temperature difference values (TDVs) and dry eye parameters, including tear meniscus height (TMH) and Schirmer's test results.[22] Evaporative Dry Eye (EDE) patients were found to have a higher initial OST than those with Aqueous Deficient Dry Eye (ADDE), suggesting that OST monitoring might be an effective tool to differentiate between different DED aetiologies.[23] An average increase of 0.8 °C was observed in the OST of Meibomian Gland Dysfunction (MGD) patients when compared to matched controls.[32] Attempts were made in DED screening by OST measurement.[24, 25] Vannetti *et al.* suggested that OST might be a promising test to evaluate ocular vasoregulation, reporting an increase in OST as a response to peripheral vasoconstriction.[33] An increase of 1.18 °C in OST was found in post-corneal transplant patients undergoing an inflammation that would have leaded to a rejection of the implant.[34] Differences in ocular temperature were found among phakic and pseudophakic patients when compared to matched controls.[35] OST variations were also reported in dogs with keratoconjunctivitis sicca.[36] Eye surface temperature showed to be correlated to stress responses in budgerigars[37] and mice.[38]

Corneal temperature variations may be also associated to psychiatric disorders, including schizophrenia (SCZ) and Major Depressive Disorder (MDD), due to induced alterations in thermoregulatory processes related to human homeostasis,[15, 39] that result in variations in core body temperature,[40] as well as in superficial tissues such as the cornea.[41] Corneal temperature was reported to be correlated with clinical severity of MDD and SCZ.[39] Ocular infections with the parasitic apicomplexan *T. gondii, associated to substantial increases in OST,* might explain some of the perceptual distortions experienced in schizophrenia.[42] Drug-free SCZ patients showed 1.55 °C higher corneal temperatures when compared to matched controls.[43] Another study reported that the corneal temperature of neuroleptic-treated patients was significantly lower than that of the drug-free patients.[44] OST has a high potential to be targeted as a parameter for real-time monitoring the ocular physiology.[30, 31, 45] Contact lenses have recently attracted particular interest to be used as wearable sensing systems for point-of-care medicine.[46, 47] In particular, scleral contact lenses are ocular prosthetic devices obtained from rigid polymers with high oxygen permeability for preserving corneal metabolism.[48] They rest on the sclera creating a tear fluid reservoir over the cornea.[49] They are already used to treat a number of eye diseases and injuries,[48, 50] including Dry Eye syndrome,[51] keratoconus,[48, 52] Steven-Johnson syndrome,[48] post Laser Assisted In Situ Keratomileusis (LASIK) complications,[50, 53] as well as post corneal transplant complications.[48] Hence, the measurement of ocular surface temperature on a continuous basis is highly desirable in a wide range of physiological conditions to monitor disease progression in personalized diagnostics. Here, we developed scleral contact lenses for continuous OST monitoring. Temperature-sensitive cholesteric liquid crystals based on cholesteryl oleyl carbonate (COC), cholesteryl nonanoate (CN), and cholesteryl benzoate (CB) were embedded within fluorosilicone acrylate scleral lenses (Boston XO) inside micropatterns etched in the contact lens by laser ablation. Colorimetric readouts were performed using Color Comparator and Color Name smartphone applications,[54] based on the Red, Green and Blue (RGB) color model.[55]

3.2. Materials and Methods

Materials. Boston XO commercial scleral lenses (diameter = 17mm) were supplied by Horus INC. (Verona, Italy). Cholesteryl oleyl carbonate (COC), cholesteryl nonanoate (CN) and cholesteryl benzoate (CB) were purchased from Sigma Aldrich. Norland Adhesive NOA68 UV curable glue was purchased from Thorlabs.

Fabrication of contact lens sensors. Contact lens sensors were fabricated by etching microstructures within the lens and embedding CLCs mixtures. The layout of the micropatterns were previously designed on CorelDraw software. Microstructures were obtained by laser ablation, using a CO_2 Rayjet laser engraver at a wavelength of 11.6 μm. Settings were optimized resulting in best results when using laser powers of 40-60%, engraving speed 50%, and standard material with a thickness of 200 μm. The devices were then assembled. Cholesteric liquid crystals mixtures were produced by melting COC, CN and CB in weight ratios of 0.40:0.58:0.10 and 0.36:0.58:0.10. The micropatterns were filled with liquid crystal. To avoid any leakage, liquid crystals were embedded by epoxy bonding a 50 μm thin glass circular sheet to the contact lens, using a UV-curable glue. A tiny amount of glue was spread around the microstructures using a cotton bud. The glass top layer was then laid over the structures and cured in a UV oven for 30 minutes to achieve bonding. The contact lens was rinsed in DI water and dried at ambient temperature.

Equipment. A CO_2 Rayjet laser engraver was used to fabricate the structures. A customized setup was used for reflection efficiency measurements, comprising a hot plate, a bifurcated optical fiber purchased from Thorlabs, USB2000+ miniature spectrometer for VIS-NIR measurements and a tungsten halogen light source, both purchased from Ocean Optics, an infrared thermometer, and a computer with a dedicated software for spectral acquisition. Imaging was performed using a Zeiss optical microscope. The optical fiber was kept firm by a probe holder, to provide irradiation and detection at normal incidence (90°). One probe was connected to a tungsten halogen light source to irradiate the lens, whilst the reflectance probe was connected to a miniaturized optical detector. The detector was connected to a computer with a dedicated software for spectral acquisition.

Optical characterization of contact lens sensors. Contact lens sensors were characterized on a hot plate using an infrared thermometer to precisely control temperature variations in a point. The thermometer was operated at normal incidence to the sensors, at 15 cm of distance. The sensors were exposed to temperatures in the range 29.0-40.0 °C with steps of 0.5°C. Spectra were acquired in reflection mode and the reflection peak shift over temperature was calculated. Hysteresis was evaluated by swinging the temperature from 33.0 °C to 38.0 °C and from 32.0 °C to 33.0 °C. The latest measurement was meant to reproduce a dry eye symptom.[1, 4, 6, 49] A stabilization time of 10 minutes was given to the hot plate before spectral acquisition. The time response of contact lens sensors was evaluated by placing the sensor on a pre-heated hot plate at 40.0 °C while continuously screen recording Color Comparator live app with a smartphone working at 60 fps. Time intervals were estimated by evaluating the time needed by the sensor to switch to specific RGB triplets, associated to temperature values in the range 29-40.0 °C.

Smartphone readouts. Colors were recorded using Color Comparator[54] and Color Name[59] applications, installed on an iPhone 6s. The phone camera was placed normal to the sample at 5 cm of distance, under ambient light conditions of 200 lux. Light levels were measured using Lightmeter app[58] installed on an iPhone 6s. Color recognition applications identify each color with its RGB triplet. When controlling the applied temperature, each RGB triplets (or group of triplets) can be associated to a specific value. Smartphone readouts were tested on an *ex-vivo* porcine eye. Eyes were heated on a hot plate at 40.0 °C. After visual color stabilization, the readout of the sensors was performed by taking a photo and performing colorimetric analysis using Color Name app. Thermal images were acquired with a smartphone compatible FLIR Pro camera for iOS, and image analysis was performed using MATLAB.

3.3. Results

Thermochromic liquid crystals (TLC) were obtained by melting cholesteryl oleyl carbonate, cholesteryl nonanoate and cholesteryl benzoate (COC/CN/CB wt%, 0.40:0.58:0.10). The three esters share the same molecular skeleton, bonded to a different radical (**Figure 21a**). They can be melted together to obtain a

liquid crystal mixture, in which each compound retains its own chemical properties, whilst forming weak inter- and intra- molecular interactions. The physical properties of the mixture, such as the temperature sensitivity range, can be modulated by varying the concentration of each compound within the mixture. Thermochromic liquid crystalline (TLC) materials have been widely reported.[55, 56] Their reversibility, fast response times, multiple color transitions, and high temperature accuracy (0.1 °C) makes them a promising alternative to electronic sensors for precision thermal mapping in wearable medicine. Chiral, rigid, and rod-shaped molecules can form the cholesteric phase across a defined temperature range, exhibiting a layered structure with a gradual twisting in the molecular orientation[55, 56] (**Figure 21b, c**). This helical arrangement results in a Bragg reflection-like mechanism where incident light normal to the molecular orientation and circularly polarized with the same sense as the helix is reflected according to the formula $\lambda = nP$,[56, 57] where λ is the reflected wavelength, n is the refractive index of the material, and P is the pitch, defined as the distance between two equally-oriented layers, which variates over temperature following a non-linear dependence. This results in a more rapid shift in color at the red end of the visible spectrum compared to the blue.[56, 57] Upon a temperature increase during the cholesteric phase, a shortening of the helical stack is observable. The pitch decreases from P_1 to P_2, resulting in a reflection peak shift from λ_1 to λ_2, that in turns induces a color change visible at the macro scale. **Figure 21d** presents a schematic of the fabrication of contact lens temperature sensors. Micropatterns are etched on scleral lenses by CO2 laser ablation. Liquid crystal mixtures with different temperature sensitivities are prepared and embedded in the micro-structures by UV epoxy bonding 150 μm thin, circular glass piece to the lens, to cover the pattern. Contact lens sensors can be rinsed in commercial saline solutions or in DI water.

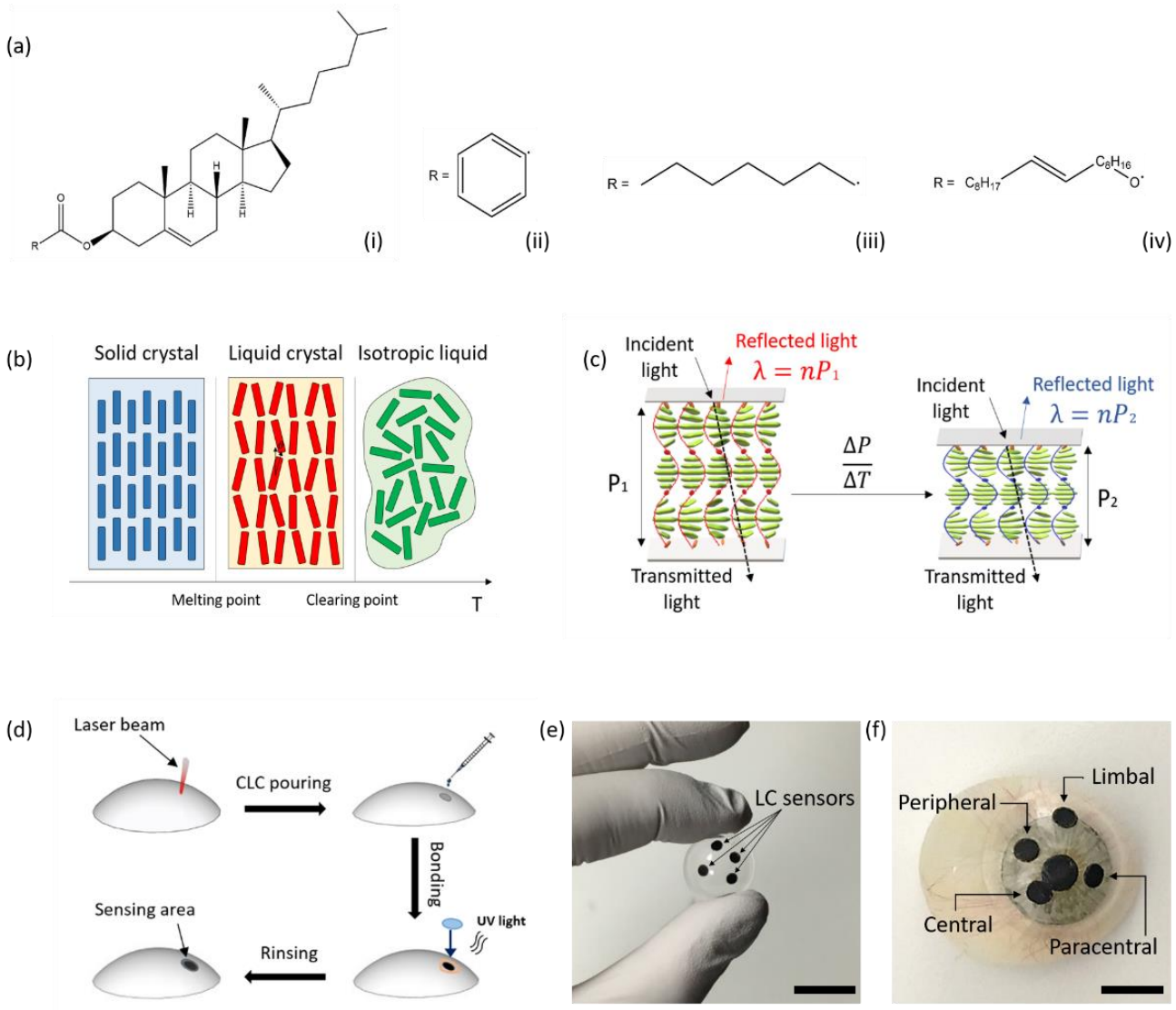

Figure 21. Contact lens temperature sensor. (a) Chemical composition of thermochromic liquid crystals. (i) Common cholesteryl esteric skeleton, (ii) cholesteryl oleyl carbonate, (iii) cholesteryl benzoate, (iv) cholesteryl nonanoate. (b, c) Sensing mechanism of thermochromic liquid crystals: (b) temperature-triggered state change, (c) reflection peak shift over temperature in the cholesteric phase, resulting from the preferentially reflected wavelength corresponding to the distance over which a 360° rotation of the field director occurs, namely the pitch, P_1 and P_2. (d) Fabrication of the contact lens sensor. (e, f) Photos of a contact lens sensor with four active areas for continuous corneal temperature mapping. Scale bars: 5 cm and 1.5 cm.

Characterization of the liquid crystal. Optical characterization of liquid crystals was performed using the reflection spectroscopy setup depicted in **Figure 22a**. A bifurcated optical fiber for both illumination and detection at an angle of 90° was used. Standard errors were calculated from three measurements per point. **Figure 22b** shows the wavelength shift of liquid crystal (COC/CN/CB wt%, 0.40:0.58:0.10) within

the visible spectrum from 738±4 nm to 474±4 nm upon increasing the temperature from 29.0 °C to 40.0 °C with steps of 0.5 °C. The reflection peak shift over temperature can be nicely approximated by a second order polynomial fitting (R^2=0.98) that individuates a hyperbolic behavior, typical of liquid crystals (**Figure 22c**). The reflection efficiency trend was measured within the same temperature range (**Figure 22d**). It was found to gradually increase from 14±4% at 29.0 °C until reaching its highest value at 31.5 °C, which amounted to 46±2%, followed by a decrease from 31.5 °C to 40.0 °C. The lowest efficiency was measured at 40.0 °C (4±3%), where the liquid crystal exhibited a color that resembled a dark blue under naked eye. A color can be uniquely identified by a point on the CIE 1931 chromaticity diagram, and it can be defined by a couple or a triplet of coordinates, according to different models. In this framework, the (x, y) system was adopted. The chromaticity diagram of liquid crystal (COC/CN/CB wt%, 0.40:0.58:0.10) in the temperature range 29.0-40.0 °C with steps of 0.5 °C is presented in **Figure 22e**. The first value (1) corresponds to 29.0 °C, and the last value (23) corresponds to 40.0 °C. Figure 2d shows the gradual variation from the red spectrum to the blue, passing by green, resulting from an increase in temperature range (please insert the range here). The (x, y) coordinates in the CIE 1931 space follow a reciprocal trend (**Figure 22f**). An increase in the x coordinate was observed from 29.0 to 29.5 °C, followed by an interval with small variations in the range 30.0-31.5 °C. A substantial decrease was measured over temperature variations in the range 32.0-34.5 °C, and a minimal decrease from 35.0 °C to 38.5°C. Small variations were observed from 39.0 °C to 40.0 °C, with a peak at 39.5 °C. The y coordinate followed a mirrored trend to x, with a decrease from 29.0 °C to 31.0 °C, an increase from 31.0 °C to 34.5 °C, minimal variations from 34.5 °C to 36.5 °C, and a gradual decrease when increasing the temperature from 36.5 °C to 40.0 °C, with exception for 39.5 °C, in correspondence of which a slightly larger value was measured.

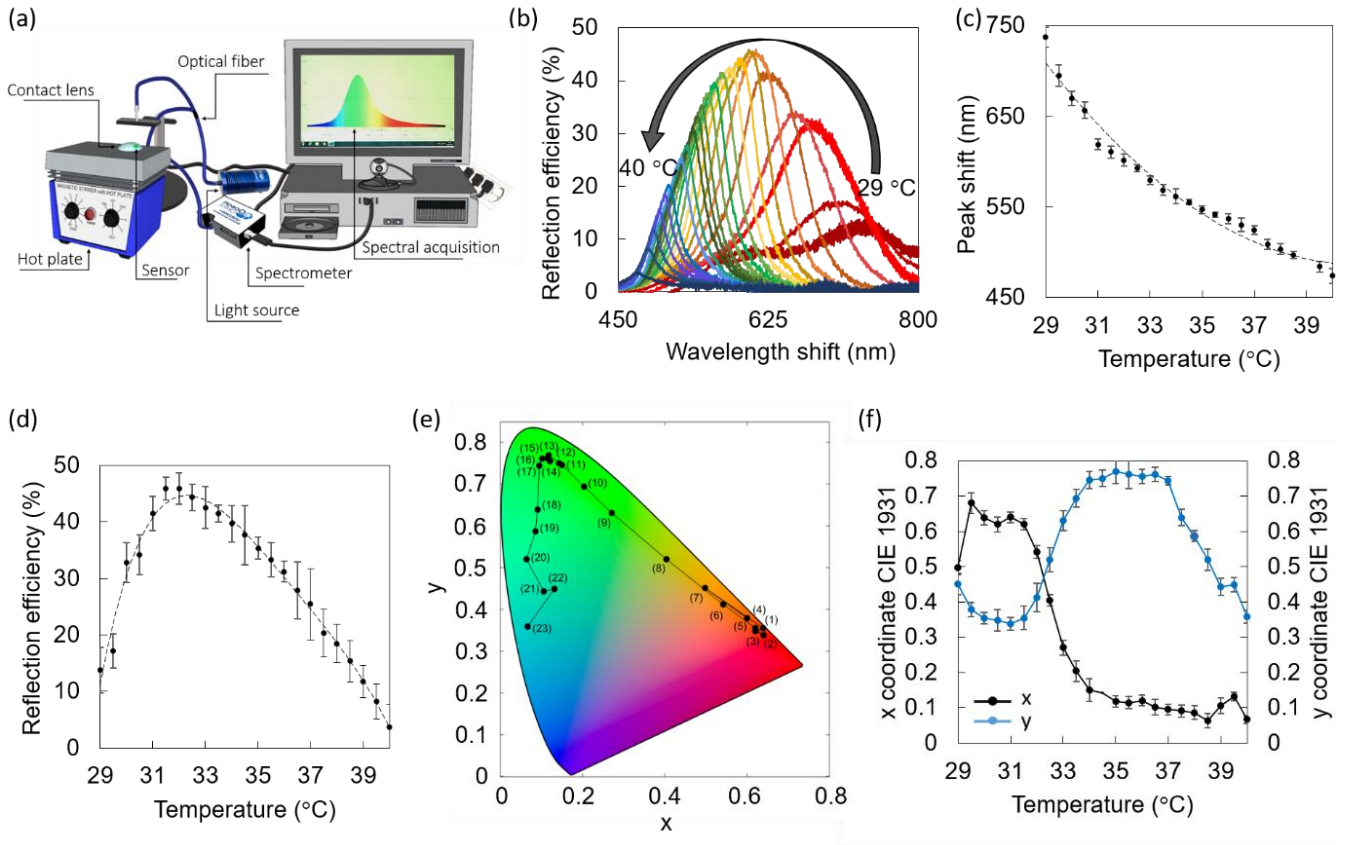

Figure 22. Characterization of liquid crystal (COC/CN/CB wt%, 0.40:0.58:0.10) in the temperature range 29.0-40.0 °C. (a) Reflection spectroscopy setup. (b) Wavelength shift over temperature. (c) Reflection peak shift over temperature trend. (d) Reflection efficiency over temperature trend. (e CIE 1931 chromaticity diagram over temperature. Values from (1) to (23) correspond to reflection spectra of the liquid crystal from 29.0 °C to 40.0 °C. (f) CIE 1931 (x,y) coordinates over temperature trend.

Smartphone readouts. Colorimetric smartphone readouts were performed to individuate the RGB triplets identifying the colors of the liquid crystals as a response to temperature variations in the range 29.0-40.0 °C. Color Comparator and Color Name smartphone applications installed on an iPhone 6s were used. It is well known that RGB output triplets are dependent on the brightness and luminosity of the environment, and consequently of the material. For this reason, readouts were performed at ambient light levels of 20, 200, and 300 lux, to provide a broader spectrum of the color to be expected in different conditions. The phone camera was kept at normal incidence to the sensor, at 5 cm of distance. An illustrative example of the readout configuration is reported in **Figure 23a**, where the contact lens sensors is fitted on an orbital

prosthesis at ambient temperature, and the sensor displays a black color, which is detected by the smartphone app (**Figure 23b**). Color Comparator used the smartphone camera to record live images of the sensor heated up at 29.0 °C to 40.0 °C with steps of 0.5 °C and identified the RGB triplets associated to each temperature. Color Comparator expressed RGB triplets in bit, as a value comprised between 0 and 255 for R, G and B, respectively. These values were converted in percentage. **Figure 23c** shows the RGB percentage in the range 29.0-40.0 °C, under ambient light levels of 200 lux. Note that the plot reflects a gradual shift from red to blue, where the red contribution lies between the 50% and the 80% for lower temperatures, with a further decrease. Blue contribution follows the opposite behavior, with a 25% at 29.0 °C and approaching the 60% around 39.0 °C. Green is more present for medium temperature values, lying between the 55% and the 70% for temperatures in the range 32.0-36.0 °C. **Figure 23d-f** show the scatter of individual red, green and blue contributions at ambient light levels of 20, 200, and 300 lux, graphically indicated with an increasing color intensity of the dots. The three scatters for each color (R, G, B) reported similar trends in the range 29.0-40.0 °C, and slightly different intensities. Considering the color contributions as percentages, it is intuitive that, regardless of the intensity, a red color will exhibit a higher percentage of red, and the same applies to all colors. The ambient light intensity variation is easier to appreciate when considering RGB triplets expressed in bits, where absolute red is (255, 0, 0), absolute green is described by (0, 255, 0) and absolute blue by (0, 0, 255). What we can observe here is that color contributions are consistent at different light levels, and they can be detected in environmental light conditions as low as 20 lux. Red peaks were reported to be at 29.0 °C and 31.0°C, where they reached the 60% and the 80% in 20-200 and 300 lux, respectively. Green peaks were observed at 33.5 °C and 35.5°C, with contributions of the 55%, 50%, and 70% at 20, 200, and 300 lux, respectively. Blue peaks were found at 39.0 °C, 39.5 °C and 40.0 °C, with contributions around the 70-80%. **Figure 23g** shows the color of the sensor associated to different temperatures, as seen with naked eye, captured using an iPhone 6s camera under ambient light of 200 lux.

Hysteresis. The hysteresis of the contact lens sensor was experimentally evaluated by increasing the temperature from 33.0 °C to 38.0 °C with steps of 0.5 °C, and further bringing it back to 33.0 °C, with a

stabilization time of 10 minutes at each step (**Figure 23h**). This range is particularly interesting to simulate temperature variations in clinical cases.[4, 6] Reflection peak shifts increased in all cases during the receiving mode, i.e. from 38.0 °C to 33.0 °C. At 33.0 °C, the reflection peak shift varied from 655±5 nm to 660±3 nm. At 34.0 °C, the reflection peak shifted from 610±8 to 616±7. Shifts of 573±8 nm to 579±11 nm, 553±9 nm to 560±5 nm, and from 537±11 nm to 546±7 nm was measured at 35.0 °C, 36.0 °C, and 37.0 °C, respectively. At 38.0 °C, the reflection peak was observed at 526±6 nm. Hysteresis was also evaluated by swinging the temperature from 32.0 °C to 33.0 °C to simulate a possible symptom of dry eye infection[1, 4, 49] (**Figure 23i**). In this case, the reflection peak shifts were found to slightly decrease in the third and fourth round when compared to the first and the second. Reflection peak shifts of 699±6 nm and 694±7 nm were observed at 32.0 °C; shifts of 580±5 nm and 573±4 nm were measured at 33.0 °C.

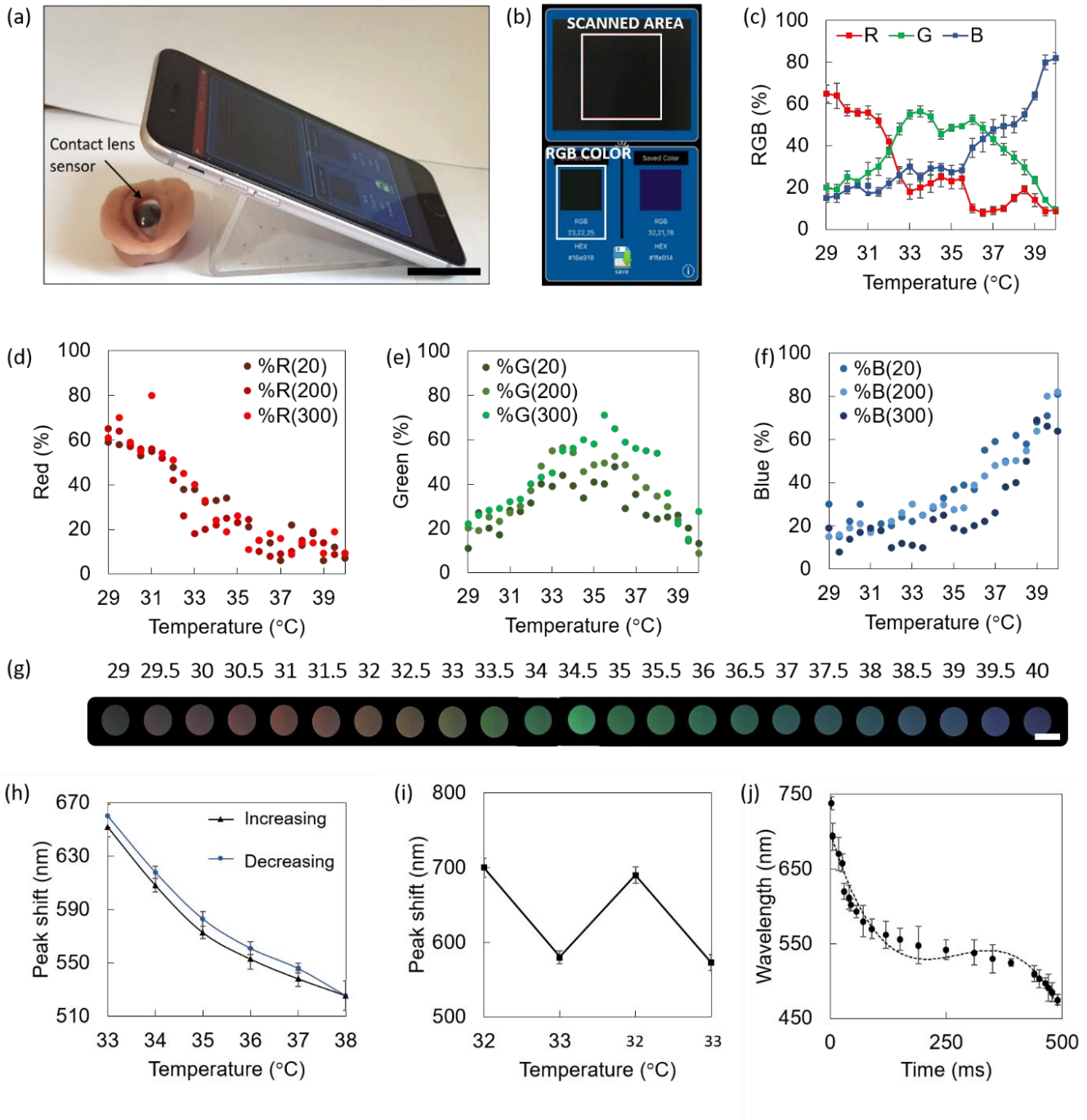

Figure 23. Readouts, hysteresis, and time response of contact lens temperature sensors. (a-b) Smartphone readout method. (a) The smartphone is placed with the camera pointing at normal incidence to the sensor, at 5 cm of distance. A contact lens sensor is fitted on an orbital prosthesis at ambient temperature. Scale bar: 2.5 cm. (b) Screenshot of colorimetric readout. The black color is detected and its RGB triplet is given as an output. Scale bar: 2.5 cm. (c) RGB percentages in the range 29.0-40.0 °C at ambient light 200 lux. (d-f) Individual red (d), green (e) and blue (f) contributions at ambient light levels of 20, 200 and 300 lux. (g) Color palette associated to the sensor under 200 lux in the range 29.0-40.0 °C, captured with a smartphone camera. Scale bar: 2 mm. (h) Hysteresis evaluation by swinging the temperature from 33.0 °C to 38.0 °C at steps of 1.0, and back. (i)

Hysteresis evaluation by swinging the temperature between 32.0 °C and 33.0 °C. (j) Time response over temperature in the range 29.0-40.0 °C.

Time response. The time response of liquid crystals was back-evaluated based on the smartphone detection of the RGB color code associated to temperature values in the range 29.0-40.0 °C under light levels of 200 lux. The liquid crystal switched from %RGB (65, 20, 15), associated to a temperature of 29.0 °C to (10, 8, 82), associated to a temperature of 40 °C, in 490 ms, with quicker response for wavelengths below 550 nm. The time response trend approximated with a three-degree polynomial curve (R^2=0.96) is shown in **Figure 23j**. A stabilization time of 1-2 seconds would be enough for ocular temperature readouts in a real-case scenario.

Readout on an ex-vivo porcine eye. Contact lens sensors were fitted on a porcine eye and heated up at 40.0 °C. Colorimetric readouts were performed on contact lenses using smartphones, and on the whole eye using an infrared (IR) camera. The results were compared. **Figure 24a** shows a photo of the lens fitted on the eye with heating off, at ambient temperature. Temperature sensors appear black. The photo in **Figure 24b** displays a contact lens sensor fitted on the heated porcine eye. The sensor is imaged using a smartphone camera at normal incidence, and at 5 cm of distance (**Figure 24c**). The photo is uploaded in Color Name app for iPhone 6s, where colorimetric readouts are individually performed in the areas of interest (**Figure 24d**). The applications output a set of RGB codes associated to the color identified in each area, and the resulting normalized color is displayed. Colorimetric results are summarized in the RGB plot of **Figure 24e**. By interpolation with the RGB characteristic of contact lens sensors, previously displayed in Figure 3c, four temperature readouts could be individuated, namely 34.5±0.4 °C at the central sensor, 36.0±0.5 °C at the paracentral sensor, 37.0±0.3 °C at the peripheral sensor, and 39.0±0.3 °C at the limbal sensor (**Figure 24f**).

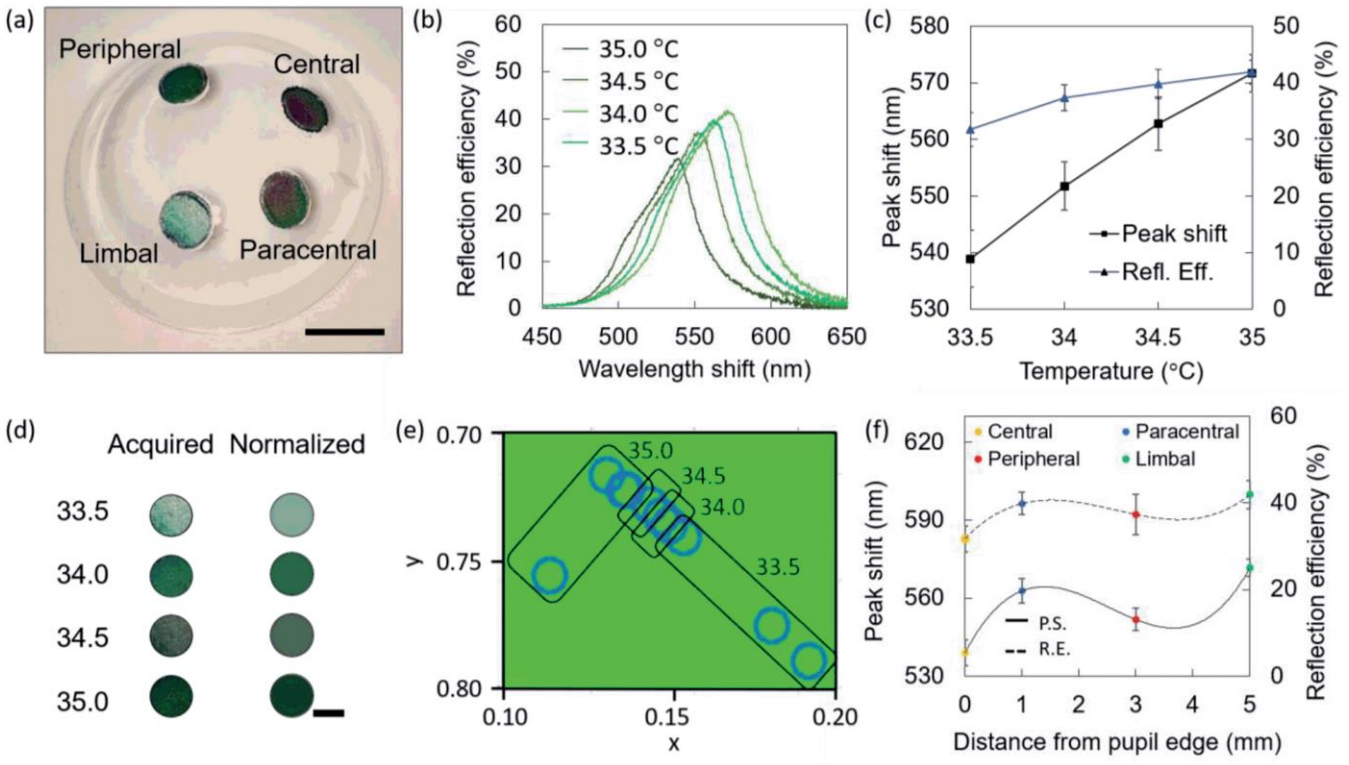

Figure 24. Optical characterization of a contact lens temperature sensor with four active areas. (a) Photograph of a contact lens for corneal temperature mapping, differentially heated at 33.5 °C, 34.0 °C, 34.5 °C, and 35.0 °C. Scale bar: 1.0 cm. (b) Reflection spectra of the four sensors. (c) Reflection peak shift and reflection efficiency trends over temperature within the contact lens. (d) Color of the four sensors, as seen when acquired and after average on the smartphone app. Scale bar: 2.0 mm. (e) Wavelengths of the colors observed within the contact lens plotted on the CIE 1931 chromaticity diagram. (f) Reflection peak shift and reflection efficiency trends plotted over distance from pupil's edge to individuate the four sensors.

At the same times, the eye was imaged using a smartphone-compatible IR thermal camera. **Figure 25a** shows a comparison between the frequency of occurrence of different temperature values before and after applying heat to the sample. The corresponding thermal images are displayed in **Figure 25b** and **Figure 25c**, at room temperature and under heating, respectively. These two images are the thermal images corresponding to Figure 5a and 5b. At heating off, an average of the corneal temperature was extracted, with a measured value of 25.6 °C. At heating on, the four sensing points were spotted in the image, and their temperature was measured. Reported values were 34.8±0.2 °C 36.4±0.2 °C 36.8±0.3 °C 38.6±0.2 °C. Note that thermal images are specular to phone camera images in the y axis. The infrared camera is

plugged in the charging port and the phone is turned 180° during thermal acquisition. Hence, the point of maximum temperature (limbal sensor) is located at the top right in **Figure 25d**, and at the bottom left in **Figure 25e**. **Figure 25f** shows the comparison between temperature values measured with the infrared camera and with contact lens sensors. An average difference of ±0.3 °C was observed. This method demonstrated a proof of principle. The porcine eye was chosen to simulate a more realistic scenario. This method may be improved by developing a customized smartphone application that outputs temperature values.

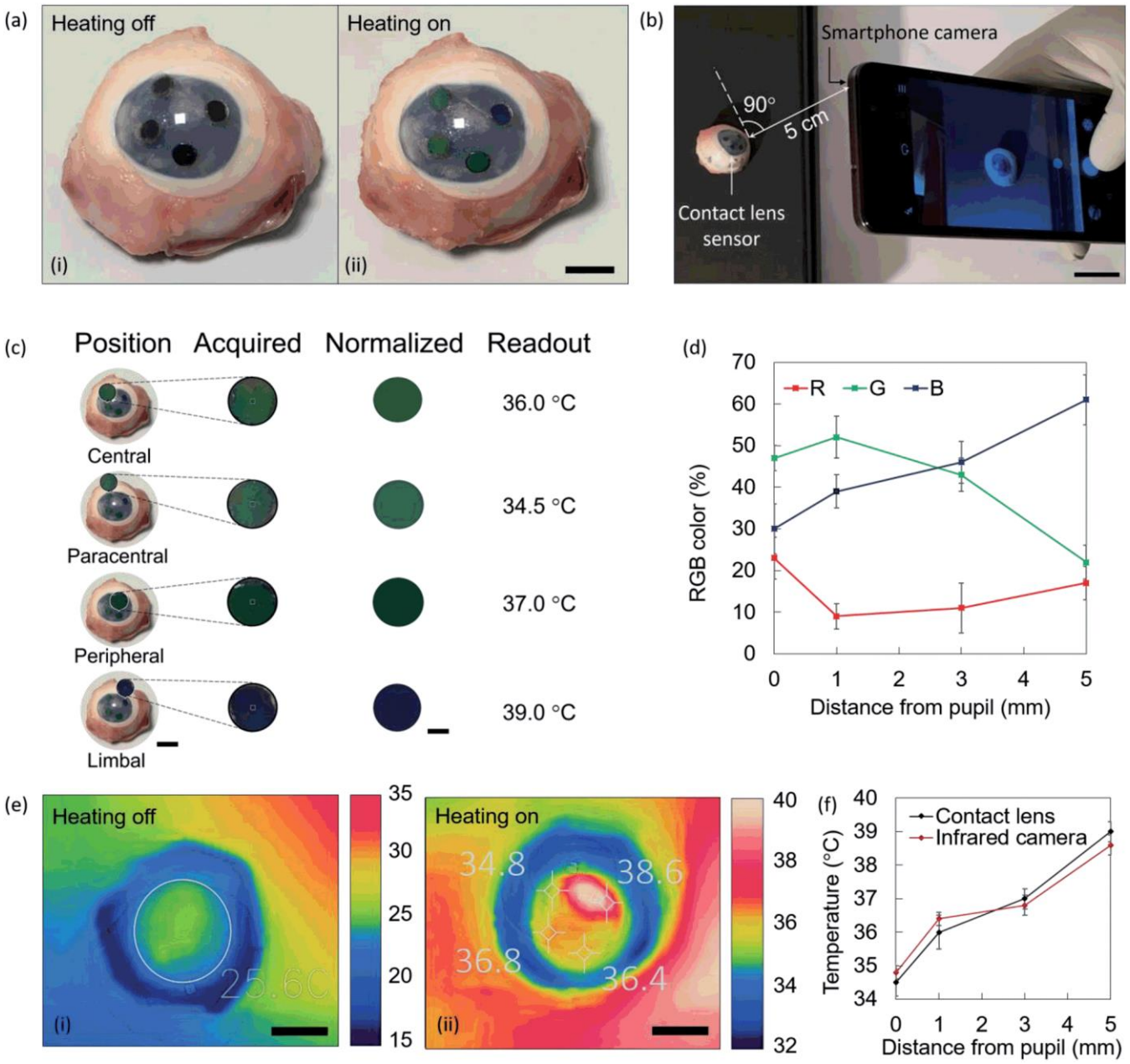

Figure 25. Readout process tested on an *ex-vivo* porcine eye. (a) Photograph of a contact lens sensor fitted on a porcine eye at ambient temperature. Scale bar: 1.5 cm. (b) Photograph of a contact lens sensor fitted on a porcine eye under heating. Scale bar: 1.5 cm. (c) The sensor under heating is imaged using a smartphone at normal incidence and at 5 cm of distance. Scale bar: 3 cm. (c) Readouts performed with Color Name app. Eyes with inset colors are shown. Eye insets scale bar: 1 mm. Eyes' scale bar: 2 cm. Scale bar of colored circles: 2 mm. (e) RGB readout of contact lens sensors fitted on a porcine eye under heating. (f) Estimated temperature values from contact lens sensors. Scale bar: 1 cm. (g) Temperature distribution within thermal images acquired with an IR camera at ambient temperature and under eating. (h) IR photo of a contact lens fitted on a porcine eye at ambient temperature. Scale bar: 1.5 cm. (i) IR photo of a contact lens fitted on a porcine eye under heating. Scale bar: 1.5 cm. (j) Comparison of the temperature measurements using contact lens sensors and infrared cameras.

3.4. Discussion

Liquid crystals were obtained by mixing three cholesteric esters (CLC, CN, and CB), obtaining a temperature sensitivity range of 29.0-40.0 °C with steps of 0.5 °C. The same materials may be capable to discriminate among temperature intervals as small as 0.1 °C[57] when controlling the temperature at shorter steps with instruments operating with higher precision. Liquid crystals showed a decrease in the reflected wavelength for increasing temperature values. This is due to an increase in the displacement angle between the long axes of adjacent molecules in the helical stack defined in the cholesteric phase of these molecules, with a decrease in the pitch. The pitch dictates the preferentially reflected and transmitted wavebands within the material. No overlaps were observed between reflection peaks in the liquid crystals at consecutive temperature values. Overlaps were observed in the time response, suggesting that a stabilization time of 2 s would be enough for ocular temperature measurements. The reflection efficiency showed a peak at 32.0 °C. The colorimetric characterization of liquid crystals was performed using smartphone apps at different light levels, and they exhibited a consistent trend. Corneal temperature values of 34 °C and above were reported multiple times in literature, as a target threshold for diagnostic purposes. [17, 27, 34] Other studies[6, 49] reported that temperatures in the range 32.0-33.5 °C were found across the corneal area. The hysteresis of the sensor was evaluated by temperature swing in the range 33.0 °C to 38.0 °C, and from 32.0 °C to 33.0 °C, with a stabilization time of 10 minutes at each 1.0 °C step, showing average variations of ≈ 8 nm between advancing and receding measurements. The sensors took less than 500 ms to undergo a black-to-black shift in the full temperature range. Liquid crystals embedded in contact lenses were optically characterized, showing a consistent behavior. The readout principle was shown on an *ex-vivo* porcine eye, where readouts were compared with infrared thermal measurements, resulting in an average difference of 0.3 °C. Contact lens temperature sensors may be used to monitor dry eye disease (0.5 °C decrease),[26] post-corneal transplant infections (1 °C increase),[34] IOP modifications (0.5 °C variations),[17] as well as to monitor ocular temperature variations in individuals for research purposes, to contribute to trace the confines of healthy/unhealthy ocular temperature values, and external factors

influencing the same. Scleral lenses are an attractive device for point-of-care medicine applications, being them used daily by patients suffering from a variety of diseases where corneal temperature monitoring may be desirable.

3.5. Conclusions

A contact lens sensor to monitor the ocular surface temperature was developed, using thermochromic liquid crystal esters. Cholesteryl oleyl carbonate, cholesteryl nonanoate and cholesteryl butonate were mixed with proportions wt%, 0.40:0.58:0.10, to obtain a temperature sensitivity range of 29.0-40.0 °C with steps of 0.5 °C. A reflection peak shift from 738±4 nm at 29.0 °C to 474±4 nm at 40.0 °C was observed. Temperature-sensitive contact lenses using liquid crystals as active elements have the potential to discriminate between temperature values as small as 0.1 °C. Contact lens temperature sensors can be a low cost, minimally invasive and portable method to perform continuous corneal temperature monitoring in a range of ocular conditions. Readouts were performed using smartphones with color recognition applications, where RGB triplets identified each color, which was associated to a temperature value. Further work will be focused on improving the resolution of the contact lens sensor by analyzing the color shades while precisely controlling the applied temperature at smaller steps. A more detailed measurement of the OST at a point-of-care level can be then performed by developing a customized smartphone app that displays the temperature value to the user. Simplifying OST measurement techniques to a point of care setting could help targeting early-stage diagnosis and ocular infections monitoring.

3.6. References

1. Purslow, C. and J.S. Wolffsohn, *Ocular Surface Temperature: A Review.* Eye & Contact Lens, 2005. **31**(3): p. 117-123.
2. Tan, J.H., et al., *Infrared thermography on ocular surface temperature: A review.* Infrared Physics & Technology, 2009. **52**(4): p. 97-108.
3. Banerjee, S.J., et al., *Using complex networks towards information retrieval and diagnostics in multidimensional imaging.* Sci Rep, 2015. **5**: p. 17271.
4. Tan, J.-H., et al., *Study of normal ocular thermogram using textural parameters.* Infrared Physics & Technology, 2010. **53**(2): p. 120-126.
5. Craig, J.P., et al., *The role of tear physiology in ocular surface temperature.* Eye, 2000. **14**: p. 635.
6. Efron, N., G. Young, and N.A. Brennan, *Ocular surface temperature.* Current eye research, 1989. **8**(9): p. 901-906.
7. Tan, J.H., E.Y.K. Ng, and U.R. Acharya, *Evaluation of topographical variation in ocular surface temperature by functional infrared thermography.* Infrared Physics & Technology, 2011. **54**(6): p. 469-477.
8. Yang, W. and L. Zhang, *Association of Tear Film Stability and Corneal Surface Temperature in Pudong Patients.* Current Eye Research, 2017. **42**(5): p. 655-660.
9. Abusharha, A.A., E.I. Pearce, and R. Fagehi, *Effect of Ambient Temperature on the Human Tear Film.* Eye Contact Lens, 2016. **42**(5): p. 308-12.
10. Slettedal, J.K. and A. Ringvold, *Correlation between corneal and ambient temperature with particular focus on polar conditions.* Acta Ophthalmol, 2015. **93**(5): p. 422-6.
11. Freeman, R.D. and I. Fatt, *Environmental Influences on Ocular Temperature.* Investigative Ophthalmology & Visual Science, 1973. **12**(8): p. 596-602.
12. Morgan, P.B., M.P. Soh, and N. Efron, *Corneal surface temperature decreases with age.* Contact Lens and Anterior Eye, 1999. **22**(1): p. 11-13.
13. Shawaf, S.S., N. Elkum, and K.F. Tabbara, *Effect of cold BSS vs naphazoline 0.025% on ocular surface temperature.* Eye (Lond), 2006. **20**(8): p. 964-5.
14. Purslow, C., J.S. Wolffsohn, and J. Santodomingo-Rubido, *The effect of contact lens wear on dynamic ocular surface temperature.* Cont Lens Anterior Eye, 2005. **28**(1): p. 29-36.
15. Tan, L., Z.Q. Cai, and N.S. Lai, *Accuracy and sensitivity of the dynamic ocular thermography and inter-subjects ocular surface temperature (OST) in Chinese young adults.* Cont Lens Anterior Eye, 2009. **32**(2): p. 78-83.
16. Lorget, F., et al., *Characterization of the pH and Temperature in the Rabbit, Pig, and Monkey Eye: Key Parameters for the Development of Long-Acting Delivery Ocular Strategies.* Mol Pharm, 2016. **13**(9): p. 2891-6.
17. Fabiani, C., et al., *Relationship between Corneal Temperature and Intraocular Pressure in Healthy Individuals: A Clinical Thermographic Analysis.* J Ophthalmol, 2016. **2016**: p. 3076031.
18. Lucia, U., et al., *Constructal approach to bio-engineering: the ocular anterior chamber temperature.* Sci Rep, 2016. **6**: p. 31099.
19. Parver, L.M., *Temperature modulating action of choroidal blood flow.* Eye (Lond), 1991. **5 (Pt 2)**: p. 181-5.
20. Morgan, P.B., A.B. Tullo, and N. Efron, *Infrared thermography of the tear film in dry eye.* Eye (Lond), 1995. **9 (Pt 5)**: p. 615-8.
21. Mathers, W., *Evaporation from the ocular surface.* Exp Eye Res, 2004. **78**(3): p. 389-94.
22. Su, T.Y., et al., *Correlations among ocular surface temperature difference value, the tear meniscus height, Schirmer's test and fluorescein tear film break up time.* British Journal of Ophthalmology, 2015. **99**(4): p. 482-487.
23. Matteoli, S., et al., *Ocular surface temperature in patients with evaporative and aqueous-deficient dry eyes: a thermographic approach.* Physiological Measurement, 2017. **38**(8): p. 1503.

24. Tan, L.L., S. Sanjay, and P.B. Morgan, *Screening for dry eye disease using infrared ocular thermography.* Contact Lens and Anterior Eye, 2016. **39**(6): p. 442-449.
25. Kamao, T., et al., *Screening for dry eye with newly developed ocular surface thermographer.* Am J Ophthalmol, 2011. **151**(5): p. 782-791 e1.
26. Versura, P., et al., *Subjective Discomfort Symptoms Are Related to Low Corneal Temperature in Patients With Evaporative Dry Eye.* Cornea, 2015. **34**(9): p. 1079-85.
27. Tan, L.L., S. Sanjay, and P.B. Morgan, *Static and Dynamic Measurement of Ocular Surface Temperature in Dry Eyes.* J Ophthalmol, 2016. **2016**: p. 7285132.
28. Kovacs, I., et al., *Abnormal activity of corneal cold thermoreceptors underlies the unpleasant sensations in dry eye disease.* Pain, 2016. **157**(2): p. 399-417.
29. Galassi, F., et al., *Evaluation of ocular surface temperature and retrobulbar haemodynamics by infrared thermography and colour Doppler imaging in patients with glaucoma.* British Journal of Ophthalmology, 2007. **91**(7): p. 878-881.
30. Sodi, A., et al., *Ocular surface temperature in diabetic retinopathy: a pilot study by infrared thermography.* European Journal of Ophthalmology, 2009. **19**(6): p. 1004-1008.
31. Sodi, A., et al., *Ocular surface temperature in central retinal vein occlusion: preliminary data.* Eur J Ophthalmol, 2007. **17**(5): p. 755-9.
32. Terada, O., et al., *Ocular surface temperature of meibomia gland dysfunction patients and the melting point of meibomian gland secretions.* Nippon Ganka Gakkai Zasshi, 2004. **108**(11): p. 690-3.
33. Vannetti, F., et al., *Relationship between ocular surface temperature and peripheral vasoconstriction in healthy subjects: a thermographic study.* Proc Inst Mech Eng H, 2014. **228**(3): p. 297-302.
34. Sniegowski, M.C., M. Erlanger, and J. Olson, *Thermal imaging of corneal transplant rejection.* Int Ophthalmol, 2018. **38**(6): p. 2335-2339.
35. Sniegowski, M., et al., *Difference in ocular surface temperature by infrared thermography in phakic and pseudophakic patients.* Clin Ophthalmol, 2015. **9**: p. 461-6.
36. Biondi, F., et al., *Infrared ocular thermography in dogs with and without keratoconjunctivitis sicca.* Vet Ophthalmol, 2015. **18**(1): p. 28-34.
37. Ikkatai, Y. and S. Watanabe, *Eye surface temperature detects stress response in budgerigars (Melopsittacus undulatus).* Neuroreport, 2015. **26**(11): p. 642-6.
38. Gjendal, K., et al., *Eye, body or tail? Thermography as a measure of stress in mice.* Physiol Behav, 2018. **196**: p. 135-143.
39. Monge-Roffarello, B., et al., *The medial preoptic nucleus as a site of the thermogenic and metabolic actions of melanotan II in male rats.* Am J Physiol Regul Integr Comp Physiol, 2014. **307**(2): p. R158-66.
40. Simon Elsenga, R.H.V.d.H., *Body core temperature and depression during total sleep deprivation in depressives.* Biomedical Psychiatry, 1988. **24**(5): p. 531–540.
41. Maller, J.J., et al., *Using thermographic cameras to investigate eye temperature and clinical severity in depression.* J Biomed Opt, 2016. **21**(2): p. 26001.
42. Torrey, E.F. and R.H. Yolken, *Schizophrenia and Infections: The Eyes Have It.* Schizophr Bull, 2017. **43**(2): p. 247-252.
43. Shiloh, R., et al., *Increased corneal temperature in drug-free male schizophrenia patients.* Eur Neuropsychopharmacol, 2003. **13**(1): p. 49-52.
44. Shiloh, R., et al., *Lower corneal temperature in neuroleptic-treated vs. drug-free schizophrenia patients.* Neuropsychobiology, 2003. **48**(1): p. 1-4.
45. Galassi, F., et al., *Evaluation of ocular surface temperature and retrobulbar haemodynamics by infrared thermography and colour Doppler imaging in patients with glaucoma.* Br J Ophthalmol, 2007. **91**(7): p. 878-81.
46. M., F.N., et al., *Contact Lens Sensors in Ocular Diagnostics.* Advanced Healthcare Materials, 2015. **4**(6): p. 792-810.

47. Yetisen, A.K., et al., *Wearables in Medicine.* Adv Mater, 2018. **0**(0): p. e1706910.
48. Schornack, M.M., *Scleral lenses: a literature review.* Eye Contact Lens, 2015. **41**(1): p. 3-11.
49. Efron, N., *Contact lens practice*. Third ed. 2018: Elsevier.
50. Parminder, A. and D.S. Jacobs, *Advances in scleral lenses for refractive surgery complications.* Curr Opin Ophthalmol, 2015. **26**(4): p. 243-8.
51. Bavinger, J.C., K. DeLoss, and S.I. Mian, *Scleral lens use in dry eye syndrome.* Curr Opin Ophthalmol, 2015. **26**(4): p. 319-24.
52. Mauro Frisani, M.G., Marina Serio, *Changes of ocular wave aberration in keratoconus eyes wearing mini-scleral contact lens.* **41**(1).
53. Kramer, E.G. and E.L. Boshnick, *Scleral lenses in the treatment of post-LASIK ectasia and superficial neovascularization of intrastromal corneal ring segments.* Cont Lens Anterior Eye, 2015. **38**(4): p. 298-303.
54. Buttua, N., *https://itunes.apple.com/gb/app/color-comparator-lite/id1244696055?mt=8*. Color Comparator - Lite, Accessed December 2018.
55. Gevers, T. and A.W.M. Smeulders, *Color-based object recognition.* Pattern Recognition, 1999. **32**(3): p. 453-464.
56. Abdullah, N., et al., *The basics and issues of Thermochromic Liquid Crystal Calibrations.* Experimental Thermal and Fluid Science, 2010. **34**(8): p. 1089-1121.
57. Sage, I., *Thermochromic liquid crystals.* Liquid Crystals, 2011. **38**(11-12): p. 1551-1561.
58. Mobil, V., *https://itunes.apple.com/gb/app/luxmeter/id1031742488?mt=8*. Luxmeter, Accessed December 2018.

Chapter 4

Ocular Pressure Monitoring

The Intraocular pressure (IOP) is a physiological parameter that plays a crucial role in preventing, diagnosing, and treating ocular diseases. For example, lowering the IOP is the primary focus of glaucoma management. However, IOP is a widely varying parameter, and one-off measurements are prompt to errors. Developing portable solutions for continuous monitoring of the IOP is a critical goal in ophthalmology. Here, stretchable nanostructures were developed as strain-tunable diffraction gratings and integrated into a contact lens. They exhibited a limit of detection (LOD) <2 mmHg and a linear response in the range of interest (15-35 mmHg). Nanopatterns were characterized under monochromatic laser sources and further integrated into a soft contact lens. A smartphone readout method based on preferentially reflected colors was proposed to pave the way towards smartphone-based ocular health monitoring.

4.1. Introduction

The intraocular pressure (IOP) inside the human eye maintains a value of 10–21 mmHg in healthy conditions.[1] The IOP was not routinely assessed until the late 19th century, with the advent of the Maklakoff applanation tonometer. Following that, Schiötz developed an indentation tonometer that was widely used throughout the world during the first two thirds of the 20th century. In 1950, Goldmann's applanation tonometer began the era of accurate IOP measurement, the most widely used until today. Lately, transpalpebral tonometers became attractive as they do not require topical anesthesia. However, they lack accuracy. The role of IOP in the management of glaucoma remains critical, and continuous monitoring methods are desirable.[2]

Glaucoma is a group of progressive optic neuropathies characterized by a degeneration of retinal ganglion cells and retinal nerve fiber layers, that result in changes in the optical nerve head.[3, 4] A gradual

deterioration of the optic nerve is attributed to several triggering factors, primarily ocular hypertension, which causes damage to the optic nerve and a consequent build-up of aqueous humor (**Figure 26A**).[5] The World Health organization defines glaucoma as the second cause of avoidable blindness globally (12%), following cataract (47%) and before age-related macular degeneration (AMD, 9%). Glaucoma affects 7.7 million people worldwide, and this number is expected to rise to 112 million by 2040.[6] While half of glaucoma patients in high income countries is unaware of their disease, this figure surpasses the 90% in low and middle income countries.[7] Glaucoma is classified as open- or closed-angle, primary or secondary. Secondary glaucoma may be associated with underlying systemic inflammatory, vascular or malignant causes as well as specific ocular conditions.[8]

Lowering IOP remains the primary focus of glaucoma management.[9, 10] This is mainly achieved using IOP-lowering eye drops, containing active ingredients such as prostaglandin analogues, β-blockers, α-2 agonists, carbonic anhydrase inhibitors, and muscarinic receptors agonists.[11] Laser therapy is also available, both as a first treatment option and to patients who have failed medical management. At severe stages of the disease, surgical intervention is performed.[7] Early-stage glaucoma patients were found to benefit from yoga ocular exercise to lower IOP.[12] Increasing evidence suggests that oxidative stress may contribute to the induction and progression of glaucoma. Antioxidant use may help through reducing IOP, preserving vascular health, and preventing ganglion cell loss.[11]

The IOP was found to have seasonal fluctuations in glaucoma patients, with lower values reported in summer and highest in winter, particularly in cases of comorbidity with dry eye disease (DED).[13] Ocular changes also occur during pregnancy,[14] mainly as benign physiologic responses to hormonal modifications, as well as during weight lifting.[15] Moreover, IOP fluctuates between diurnal and nocturnal hours. Nocturnal supine IOP was reported to be higher than diurnal sitting IOP. However, glaucoma patients register a smaller diurnal-to-nocturnal increase in IOP when compared to healthy groups.[16] Caffeine consumption effect on IOP was also investigated, resulting in significant IOP increase in glaucoma patients, compared to a negligible effect in healthy subjects.[17] IOP was also found to be influenced by hemodialysis (HD),[18] exposing patients with a history of HD to a higher risk of developing

glaucoma. A lower IOP was observed in patients following cataract extraction, making it an effective treatment for ocular hypertension.[19, 20]

Monitoring glaucoma progression is of crucial importance but remains challenging despite new diagnostic technologies. Standard automated perimetry (SAP) for visual field (VF) testing is used in diagnosis and follow-up. Imaging devices such as the Heidelberg Retina Tomograph (HRT) can quantify glaucomatous progression of the optic nerve head by comparing baseline with follow-up images of the same patient. However, it is difficult to define the impact of IOP on glaucoma progression due to its fluctuation and lack of standardization.[21] Furthermore, one-off measurements of the IOP are an error-prone snapshot into a widely varying physiological parameter.[22]

Contact lenses have attracted particular interest as potential ophthalmic monitoring platforms, due to their popularity as ocular wearables for vision correction, cosmetics and therapeutics.[23] Several contact lens sensing platforms were developed in the last decade, including lenses for real-time monitoring the ocular temperature,[24] and for screening tear fluid biomarkers, such as pH,[25, 26] glucose,[27] and proteins.[28] Recent studies also report on the development of contact lenses for IOP continuous monitoring. However, they are primarily based on electrical readouts, they integrate antennas and radio-frequency (RF) transmitters, components that the Food and Drug Administration (FDA) has often been reluctant to approve for usage in real-case scenarios.[29-32] A recent work reports on the development of a contact lens tonometer employing graphene woven fabrics as a high-resolution sensing element. However, the process would be difficult to scale up.[33]

The technology paradigm with regards to IOP monitoring via contact lenses is shifting to the use of microfluidic methods, employing a mechanism where a liquid material, such as an oil or a dye, flows within a microfluidic system in amounts proportional to the ocular pressure fluctuations, and the device can be readout by visual methods. However, these cases involve the introduction of additional materials in the eyeball, and require multi-step processing of individual lenses.[34, 35]

Recent applications of PDMS nanostructures have dramatically increased in the biomedical field due to their optical, mechanical and electrical properties.[36, 37] PDMS nanobuttons have been designed to

develop antimicrobial surfaces,[38] fluorescence imaging technologies,[39] live cell analysis platforms,[40] and enhanced glucose sensors.[41] In this chapter, we report on the use of PDMS nanostructures as stretchable, optical pressure sensors for integration into contact lenses (**Figure 26B**). Stretchable nanobuttons were obtained by e-beam lithography on silicon, followed by replica molding with PDMS to produce flexible gratings. Upon stretching the sample, the grating spacing increases, resulting in a proportional change in the diffraction pattern, according to the formula

$$d \sin \vartheta = n\lambda$$

where d is the grating spacing (considered as the distance between the center of a pillar and its consecutive pillar in the grating), ϑ is the angle between the diffracted ray and the grating's normal vector, n is the order of diffraction, and λ is the wavelength of the incident monochromatic light. Hence, a larger d results in a smaller ϑ (**Figure 26C**).

Three nanopatterns with a pillar diameter of 700 nm, height of 800 nm, and spacing of 500 nm, 1 μm and 2 μm between pillars were fabricated and compared by optical characterization using lasers with wavelengths of 450 nm, 532 nm and 670 nm. The geometrical features allowed to achieve sensitivities in the range of interest (15-35 mmHg). The finite element method was used to visualize the stress/strain in three model structures. Stretchable pressure sensors were integrated into a soft contact lens and colorimetric readouts were performed using a smartphone to achieve a portable, reflection-based method to capture the sensor response directly on-eye. The proposed pressure-sensitive contact lens represents a low-cost paradigm shift and a critical innovation for the monitoring of glaucoma and, more broadly, ocular hypertension, particularly due to the use of a smartphone camera and simple image analysis software for sensor readout, that are widely available and that can streamline the adoption of the proposed technology.

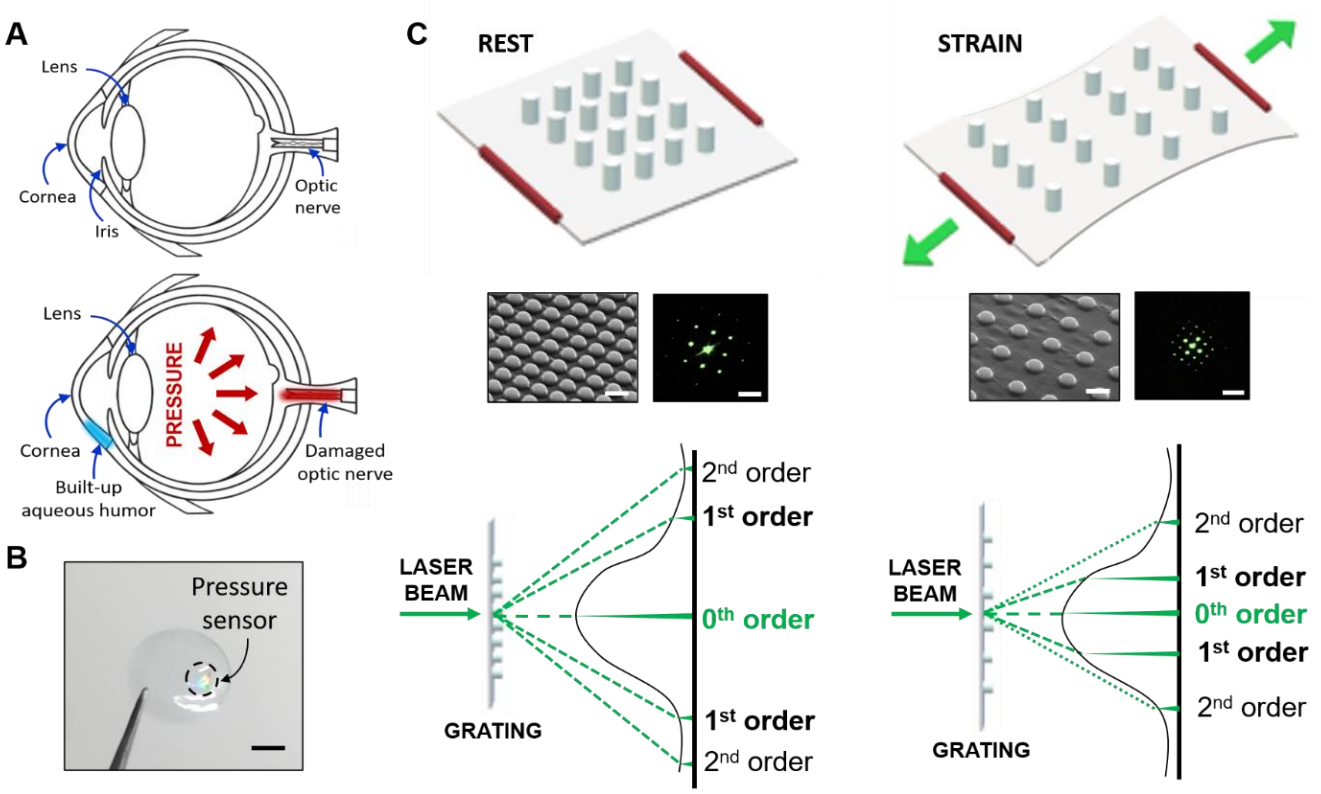

Figure 26. Tunable diffraction gratings as ocular pressure sensors. A) Schematic of the eye in healthy subjects and glaucoma patients. B) Photograph of a contact lens integrating an optical strain sensor based on PDMS nanobuttons. Scale bar: 5 mm. C) Working principle of the strain sensor. Left: sensor at rest; right: sensor under strain. The application of a strain causes the sensor to stretch, inducing a change in the grating spacing. This, in turn, results in a change in the diffraction pattern. SEM micrographs (scale bars: 2 µm) and diffraction patterns (scale bars: 1 cm) are displayed to show the concept. Further down, the schematics illustrate the angular diffraction shift, resulting in a change in position of non-0^{th} orders according to the equation $d \sin \vartheta = n\lambda$.

4.2. Materials and Methods

Materials. Sylgard 184 silicone elastomer kit was purchased from Dow Corning.

Equipment. Collimated laser diode modules (450nm, 4.5 mW (CPS450); 532nm, 4.5mW (CPS532); 670nm, 4.5mW (CPS670F), Thorlabs), Visible Near-Infrared Light Source, HL-2000-HP-FHSA (20W) (Ocean Optics), FLAME-S-VIS-NIR-ES Spectrometer Assembly (350-1000nm) (Ocean Insight), Ø1" Motorized Precision Rotation Stage (Metric) Bundled with DC Servo Motor Driver and Power Supply (KPRM1E/M, Thorlabs), 400 um Premium Bifurcated Fiber, VIS/NIR, 2 m (QBIF400-VIS-NIR, Ocean

Insight), Leica DM2700 P Upright Microscope (Leica), SEM XL-30 FEG at 10 kV (Philips), Surface coater Emscope SC500 (Emscope Laboratories).

Software. CleWin 5**,** ImageJ, SolidWorks, COMSOL Multiphysics 5.4, Color Grab and Photometer PRO smartphone applications running on a Huawei P10 Lite smartphone with an Android (Google, USA) operating system.

Fabrication of silicon nano-holes. Nanopatterns were designed on CleWin 5 and reproduced on single side polished **(**SSP) 4 inches silicon wafers obtained through from the Southampton Nanofabrication Centre, UK. The process involved free nitrous acid (FNA) cleaning of the silicon wafer followed by spin coating of PMMA photoresist, e-beam writing, and development. The pattern was finally coated with a Teflon layer to facilitate PDMS peel off.

Fabrication of PDMS nanobuttons. Nanostructured PDMS surfaces were obtained by replica molding from the silicon master. PDMS was obtained by mixing elastomer and curing agent with 10:1 ratio, followed by 2 h degassing at ambient temperature. 1 mL of PDMS was then poured onto the silicon wafer and cured at 60°C in an oven for 6 hours. The cured PDMS was then removed from the mold, yielding 0.2 mm thick PDMS nanostructured layers.

Imaging of PDMS nanobuttons. The 3D topography of the surface was observed by Scanning Electron Microscopy (SEM) at 10 kV and 10 mA. Samples were placed on a double-sided adhesive carbon tape and sputter coated with 100 nm of gold. At 25 mA for 3 minutes prior to the imaging.

Calculation of the limit of detection (LOD). Individual LODs for each diffraction order (n) and wavelength of incident light (λ) were calculated using the σ method:[42]

$$LOD_{n,\lambda} = 3 \times \frac{stdev}{m},$$

where $stdev$ is the standard deviation and m is the slope of the calibration curve (linear trendline, $y = mx + q$) of the sensor for the diffraction order n and wavelength λ (obtained from the individual curves showed in **Appendix VII**). To estimate the LOD of the sensor, the average of the two (1st orders LODs for pattern 1) or four (2nd and 3rd orders LODs for pattern 2 and 3) was taken.

Preparation of pressure-sensitive contact lenses. PDMS was obtained by mixing elastomer and curing agent (10:1), followed by 2 h degassing at ambient temperature and manual removal of bubbles by exerting air flow using a pipette. 100 µL of uncured PDMS was then poured into the contact lens mold and cured at 80°C on a hot plate for 15 minutes. The lenses were then removed from the mold, rinsed in isopropanol, and blow dried. PDMS nanopatterns with an area of 500 μm^2 were then bonded by activating both surfaces with an oxygen plasma pen and bringing them into contact for 15 minutes.

Strain-dependent optical characterization of PDMS nanobuttons. The stress/strain optical setup consisted of a laser source held by a mechanical support which included a motor to adjust the rotation angle. Monochromatic light was placed by default at normal incidence to the grating, held by two 3D printed clamps that were customized to apply strains with a resolution of 0.1 Nm^{-2}. The applied strain could be visualized on a monitor connected to the strain stage. This was achieved by using a 500 N force sensor (FH500, Sauter, DE) fitted on a fixed mechanical breadboard using a 3D-printed fixture. One of the 3D printed clamps was fitted on the force sensor. The second clamp was fitted on a manual linear translation stage with an end-mounted micrometer (PT1/M, ThorLabs, USA) allowing controlled elongations along the device axis. The 3D printed parts were fabricated using a Fortus 400mc 3D Printing System (Stratasys, USA). Upon applying strains in the range 15-35 mmHg, the diffraction pattern changes projected on the wall was imaged with a camera. Laser sources emitting at 450 nm, 532 nm and 670 nm were placed at 1 cm from the grating. The spacing between the grating and the screen was 1 m. Diffraction peaks were recorded with a spectrometer connected to an optical fiber placed at normal incidence to the screen on one side (1 m distance) and connected to a laptop on the other side.

Strain simulations of PDMS nanobuttons. Stress/strain simulations were performed using COMSOL Multiphysics 5.3A. Three geometries were designed, with constant parameters (nanopillar height: 800 nm; nanopillar diameter: 700 nm; thickness of the base substrate: 3 µm; width and height of the base substrate: 10 µm), whilst varying the grating spacing. Patterns 1, 2 and 3 were designed with a spacing of 500 nm, 1 µm, and 2 µm, respectively. The computational model was implemented using the solid mechanics module. PDMS was assigned as a library material to the whole geometry and defined as a

linear elastic material ($\Delta \cdot s + \boldsymbol{F}_V = 0$). Initial values for the displacement and structural velocity fields were both set to zero ($\boldsymbol{u} = 0$; $\frac{\partial \boldsymbol{u}}{\partial t} = 0$). The bottom face of the base substrate was set as the fixed constraint ($\boldsymbol{u} = 0$), and the rest of the geometry was free to move. Strains were added to the mechanics as boundary loads to the face of the geometry placed in the direction of interest ($S \cdot \boldsymbol{n} = \boldsymbol{F}_A$). Strains of 15, 20, 25, 30 and 35 mmHg were applied in the x, y and xy axes to induce expansion and/or compression. Results were obtained from stationary studies for each strain.

Colorimetric optical characterization of PDMS nanobuttons. The measurement setup consisted of a bifurcated optical fiber connected to a spectrometer on a side, and to a white light source on the other side. The single end of the fiber was placed at 45° to the grating. Upon direct irradiation at 45°, the nanopatterns exhibited a preferentially reflected color, visible with the naked eye, which was recorded in reflection mode by the spectrometer.

Colorimetric smartphone characterization of PDMS nanobuttons. The same concept was replicated using a smartphone, exploiting its light sensor, torch, and camera. Ambient light levels were monitored using the Photometer PRO application and kept in the range 249-251 lux (lx). The smartphone torch acted as the light source, which was tilted such that the incidence of light to the grating was 45°. The smartphone camera, placed right below, was used to identify the color with its RGB coordinates. This concept may be expanded into a smartphone app that outputs the corresponding pressure value.

4.3. Results

Nanoholes were obtained on silicon by e-beam lithography and reactive ion etching (RIE), using polymethyl methacrylate (PMMA) as the resist. The silicon chip was then used as a mold to produce PDMS replicas with a thickness of 200 µm (**Figure 27A**). Nanoholes had constant diameter (700 nm) and heights (800 nm) and varying spacing of 500 nm (pattern 1), 1 µm (pattern 2), and 2 µm (pattern 3). SEM micrographs of the three PDMS nanopatterns are shown in **Figure 27B**. Surface profiles are displayed in **Figure 27C**.

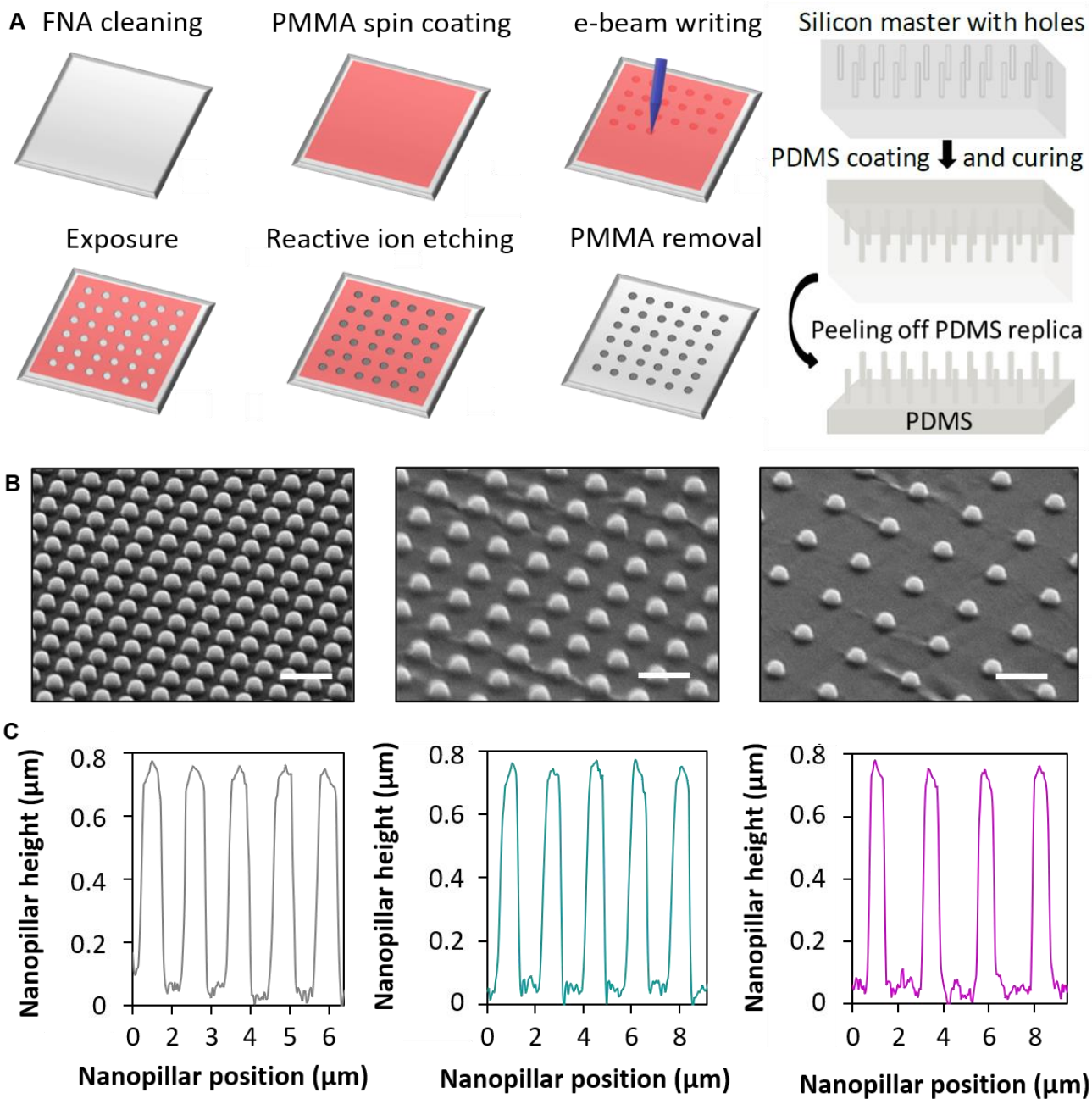

Figure 27. Fabrication of PDMS nanobuttons. A) Electron beam lithography on silicon and replica molding on PDMS. B) SEM micrographs of the three gratings made of pillars with diameter d = 700 nm and increasing spacings of 500 nm, 1 µm and 2 µm. Scale bars: 1.5 µm. C) Surface profile of the gratings.

Strain-dependent optical characterization of PDMS nanobuttons was performed using a customized setup (**Figure 28A**), consisting of a red, blue, or green laser at normal incidence to the grating. The laser motor allowed to tune the angular rotation of the laser beam. The grating was held by two clamps, one connected to a fixed position force sensor (applied force displayed on the instrument's screen) and the second

connected to a manual linear stage that controlled through a micrometer to define the distance between the two clamps and thus the applied strain. Upon irradiating the nanostructures, their diffraction pattern was visualized on a screen (placed at 1 m of distance from the grating) and imaged with a camera. **Figure 28B** shows the normalized emission of the monochromatic laser sources used in this work (450 nm, 532 nm and 670 nm). **Figure 28C-H** displays the optical characterization of the first pattern, featuring a spacing of 500 nm. **Figure 28C** shows the diffraction pattern at different wavelengths (including white light, 400-1100 nm, where three diffraction orders are visible). The grating at rest exhibited the diffraction peaks presented in **Figure 28D**, with the 0^{th} diffraction order set at 0° as a reference for all wavelengths. The 1^{st} diffraction order at rest was observed at angular rotations of -53° and 52° at 450 nm, -60° and 61° at 532 nm, -65° and 65° at 670 nm, suggesting that higher wavelengths correspond to larger diffraction angles of non-0^{th} order ($\lambda\ \alpha\ \vartheta$). The strain-dependent optical response was recorded in the physiological range of interest (15-35 mmHg). **Figure 28E** displays the 1^{st} order diffraction shift at 450 nm, 532 nm and 670 nm at applied pressures of 15, 20, 25, 30 and 35 mmHg, taking the angular position of the first order diffraction peak at rest as a reference (e.g. if the first order peak with null strain has a rotation of 30° and the first order peak at strain 20 mmHg has a rotation of 50° with respect to the baseline (0^{th} order, 0°), the result is displayed as 50° - 30° = 20°). The slope of the curves and the standard deviation were used to calculate a limit of detection (LOD) of 1.36 mmHg and a sensitivity of 0.43°/mmHg in the linear range (15-35 mmHg, **Appendix VII**). Individual angular rotation peaks at 450 nm are presented in **Figure 28F**. The angular rotation is inversely proportional to the applied pressure. Here, the x-axis displays the total rotation compared with the baseline. The negative first diffraction peaks were observed by rotating the laser to -49° (15 mmHg), -46° (20 mmHg), -43° (25 mmHg), -41° (30 mmHg) and -38° (35 mmHg). Similarly, the positive first diffraction peaks were recorded at angular rotations of 49° (15 mmHg), 46° (20 mmHg), 44° (25 mmHg), 42° (30 mmHg) and 40° (35 mmHg). The top-left image shows the gradual decrease in the diffraction pattern spacing, corresponding to an increase in the grating spacing. **Figure 28G** shows the angular rotation of diffraction peaks observed when irradiating with a green laser source emitting at 532 nm. The top-left image displays the gradual decrease of the diffraction spacing. First order

diffraction peaks were observed at ±60° (15 mmHg), ±59° (20 mmHg), ±58° (25 mmHg), ±57° (30 mmHg), -55° and 56° (35 mmHg). The angular diffraction peaks at 670 nm are presented in **Figure 28H**, together with the gradual decrease of the red diffraction spacing. First order diffraction peaks were observed at -62° and 58° (15 mmHg), -60° and 56° (20 mmHg), -56° and 50° (25 mmHg), -53° and 48° (30 mmHg) and at±42° (35 mmHg).

The optical characterization of pattern 2 is presented in **Figure 29**. Pattern 2 has a grating spacing of 1 µm, resulting in smaller diffraction angles with a higher number of diffraction orders visible in the same area when compared to pattern 1. **Figure 29A** displays the diffraction pattern when irradiating with white light (400-1100 nm), blue (450 nm), green (532 nm), and red (670 nm). As expected, we can see larger diffraction angles for larger wavelength of the incident light. The diffraction profile at rest is displayed in **Figure 29B**, where the 1st and 2nd order diffraction peaks are visible. The pressure-dependent behavior is summarized in the graph in **Figure 29C**. Diffraction shifts around 25° (compared to the 1st and 2nd order angular rotation at rest) were observed at 670 nm. At 532 nm and 450 nm, the shift amounted to 10° and 5° on average, respectively. A LOD of 1.42 mmHg and a sensitivity of ±0.48°/mmHg were calculated in the linear range 15-35 mmHg (**Appendix VII**). **Figure 29D** presents the angular rotation of the 1st order diffraction peaks when tuning the applied pressure in the physiological range. It yielded rotations of -48° and 47° (15 mmHg), -47° and 45° (20 mmHg), -45° and 43° (25 mmHg), -43° and 42° (30 mmHg), -40° and 41° (35 mmHg) compared to the baseline (0th order, 0°).

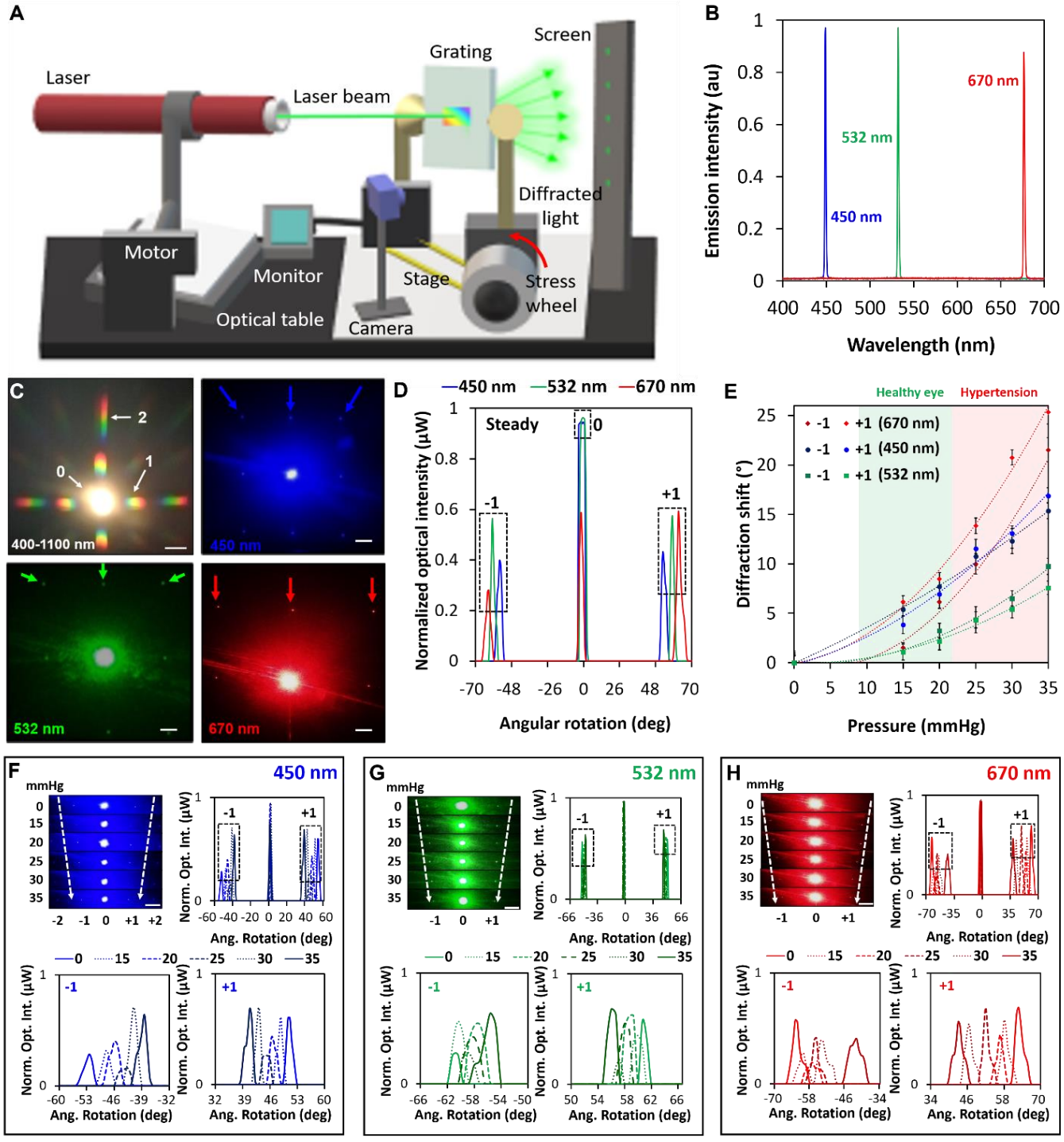

Figure 28. Optical characterization setup and characterization of pattern 1 (spacing 500 nm). A) Strain-dependent diffraction setup. A laser beam is kept at a normal incidence to the fabricated molded PDMS gratings, held by two clamps with tunable distance. The diffraction is observed on a screen and recorded with a camera. B) Emission spectra of the monochromatic laser sources used for characterization. C) Diffraction patterns obtained from the white light (400-1100 nm), 450 nm, 532 nm and 670 nm light sources. Scale bars: 2 cm. D) Diffraction peaks at rest. E) Pressure-dependent diffraction shift in the range 15-35 mmHg. F) Diffraction peaks at 450nm, G) 532 nm and H) 670 nm, in the pressure range of 15-35 mmHg. Scale bars for F), G) and H) are 1.5 cm.

The inset shows the grating spacing variations. **Figure 29E** displays the pressure-dependent diffraction shift observed when irradiating at 532 nm, yielding rotations of -40° and 36° (15 mmHg) -39° and 38° (20 mmHg) -38° and 39° (25 mmHg) -37° and 43° (30 mmHg) and -32° and 49° (35 mmHg). The inset displays the gradual decrease in grating spacing when increasing the applied pressure. Similarly, Figure 4F shows the diffraction shift at 670 nm, with angular rotations of -50° and 59° at 15 mmHg, -45° and 51° at 20 mmHg, -40° and 47° at 25 mmHg, -34° and 35° at 30 mmHg, ±30° at mmHg. The inset displays the spacing variations.

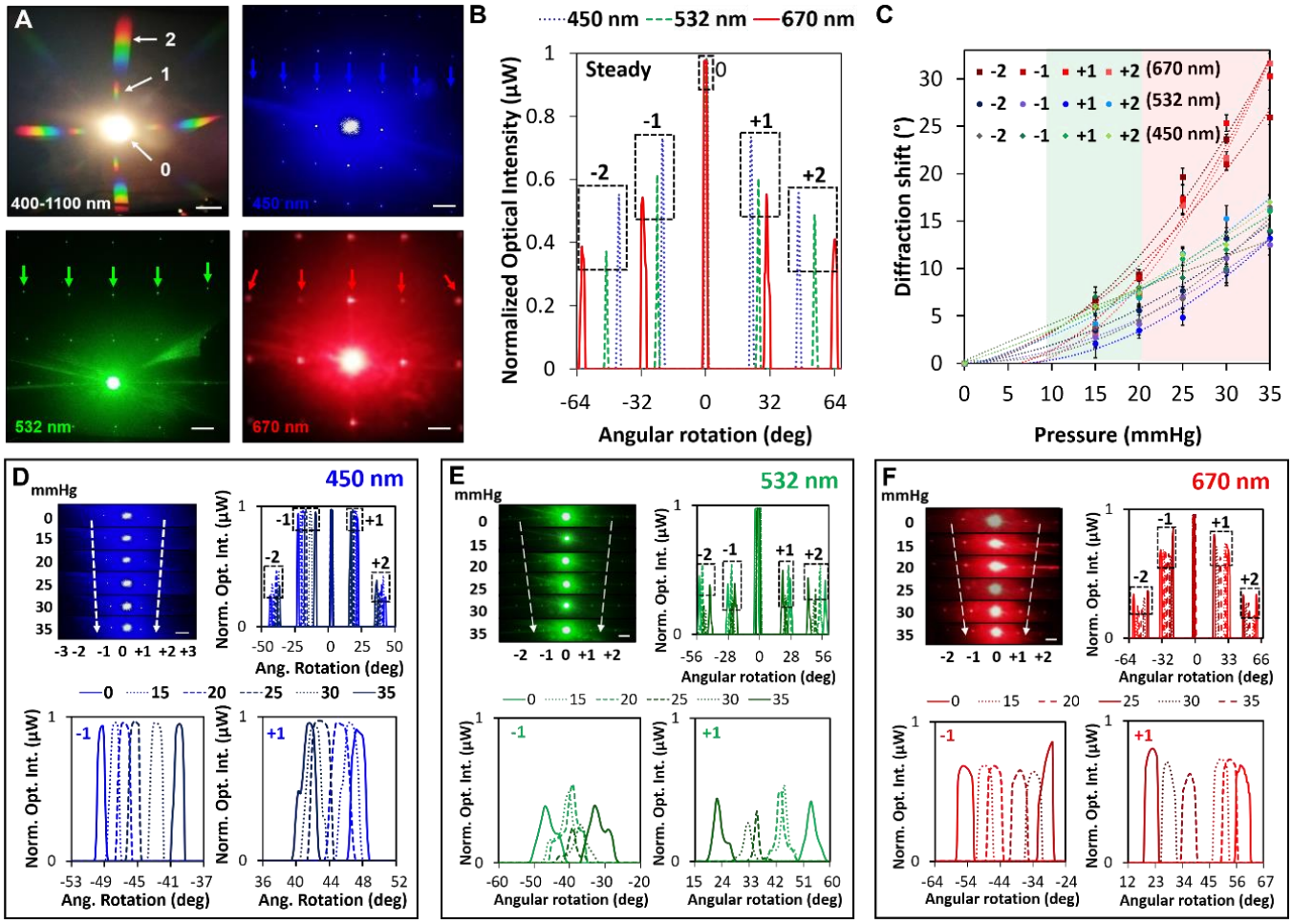

Figure 29. Optical characterization of pattern 2 (spacing 1 µm). A) Diffraction pattern at 400-1100 nm, 450 nm, 532 nm and 670 nm. Scale bars: 2 cm. B) Diffraction peaks at rest. C) Pressure-dependent diffraction shift in the range 15-35 mmHg. D) Diffraction peaks at 450 nm, E) 532 nm and F) 670 nm, in the pressure range of 15-35 mmHg. Scale bar in D), E) and F): 1.5 cm.

The optical characterization of pattern 3 is presented in **Figure 30**. Pattern 3 features a grating spacing of 2 µm, resulting in a denser diffraction pattern, with shorter spacings compared to pattern 1 and 2 (**Figure 30A**).

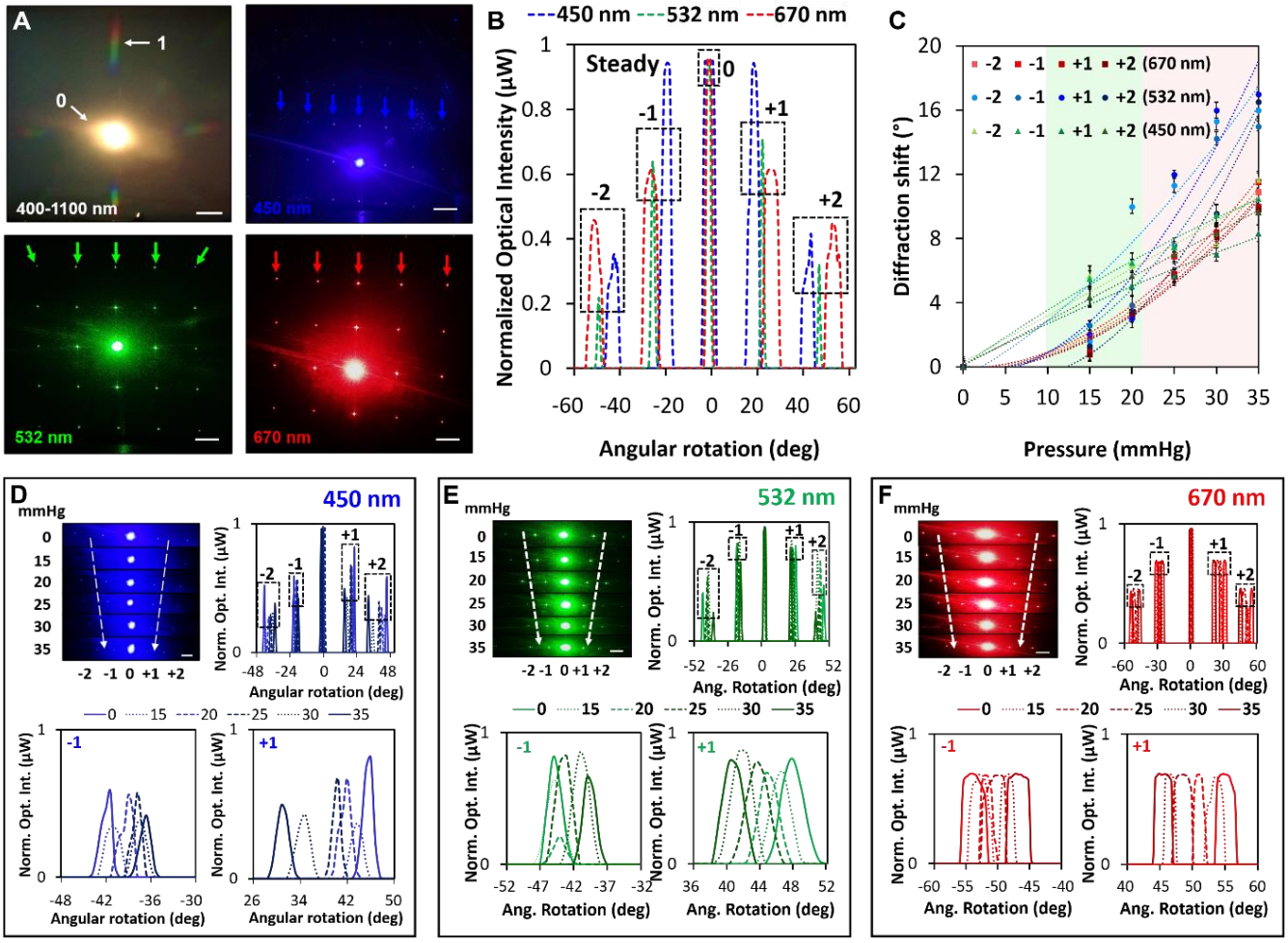

Figure 30. Optical characterization of pattern 3 (spacing 2 µm). A) Diffraction pattern at 400-1100 nm, 450 nm, 532 nm and 670 nm. Scale bars: 2 cm. B) Diffraction peaks at rest. C) Pressure-dependent diffraction shift in the range 15-35 mmHg. D) Diffraction peaks at 450 nm, E) 532 nm and F) 670 nm, in the pressure range of 15-35 mmHg. Scale bars for D), E) and F): 1.5 cm.

The diffraction profile at rest when irradiating the grating at 450 nm, 532 nm and 670 nm is presented in **Figure 30B**. **Figure 30C** shows the cumulative angular rotation of 1st and 2nd order diffraction based on the applied pressure in the range 15-35 mmHg, taking as a reference the angular rotation of the 1st and 2nd order diffraction peaks at rest. Average rotations of 15°, 9° and 7° were observed under blue, red, and green monochromatic light sources. A LOD of 1.86 mmHg and a sensitivity of ±0.56°/mmHg was

calculated in the linear range (15-35 mmHg, **Appendix VII**) **Figure 30D-F** display the pressure-dependent diffraction shifts. At 450 nm, the grating yielded angular rotations of -41° and 44° at 15 mmHg, -39° and 42° at 20 mmHg, -38° and 41° at 25 mmHg, -37° and 39° at 30 mmHg, -36° and 34° at 35 mmHg. At 532 nm, rotations of ±45° at 15 mmHg, ±44° at 20 mmHg, ±43° at 25 mmHg, ±41° at 30 mmHg, ±40° at 35 mmHg were observed (**Figure 30E**). At 670 nm, the diffraction peaks shifted of -54° and 53° at 15 mmHg, -53° and 52° at 20 mmHg, -52° and 48° at 25 mmHg, -50° and 47° at 30 mmHg, -48° and 45° at 35 mmHg (**Figure 30F**).

To visualize the stress distribution along PDMS nano-patterned surfaces under strain, the geometries were computed using the finite element method. Nanobuttons were designed to have diameters of 700 nm, heights of 800 nm, and spacings of 500 nm, 1 μm and 2 μm, over a 2 μm thin PDMS layer (**Figure 31A**). Despite the actual sample having a thickness of 200 μm, in the computational model the focus was put on the surface to allow visualization of the nanostructures.

The curve in **Figure 31B** displays the maximum spacing variation computed in the range 15-35 mmHg, yielding a symmetric behavior in expansion/compression and a maximum variation of the 9-5%. This means that pattern 1 upon expansion at 35 mmHg would see a grating spacing increase of 66.5 nm, pattern 2 of 95 nm, and pattern 3 of 142.5 nm. The graph below displays the maximum von Mises stress computed for the three patterns in the pressure range 15-35 mmHg in absolute value, as results were x symmetrical. All of them reported similar values and errors and could be fitted with a linear trendline (R^2=0.99).

The von Mises stress distribution along the geometries at under lateral, vertical, and cumulative strain of 20 mmHg is displayed in **Figure 31C** (pattern 1), **Figure 31D** (pattern 2) and **Figure 31E** (pattern 3). In all cases, it is possible to observe the increase (decrease) in the grating spacing upon a positive (negative) applied strain in x, y, or both. Insets show the front and side views of the main picture.

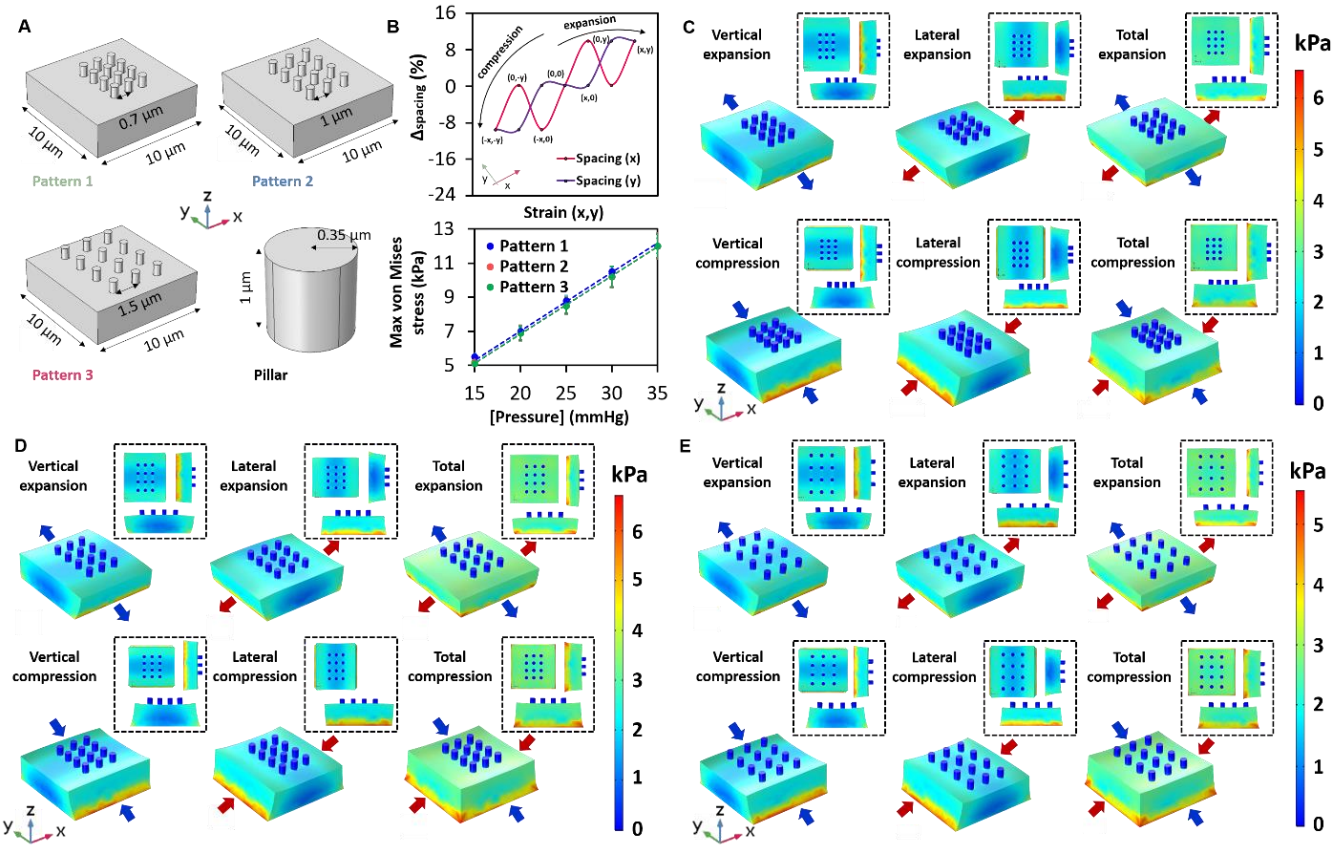

Figure 31. Computation of PDMS nanostructures. A) Geometrical details of the three patterns and the nanopillar. B) Simulated behavior of the nanopatterns: strain-dependent grating spacing (top) stress-strain curve (bottom). Linear fitting with R^2=0.99. C-E) x, y, and xy strain simulations at 20 mmHg for pattern 1 (C), pattern 2 (D), and pattern 3 (E). Insets show the side and front views.

To propose a way of reading out the sensor from the convex side, the grating's reflection properties under direct illumination with a white light source were investigated. Diffraction gratings split white light into its components of the visible spectrum, resulting in a rainbow coloring. However, when tilting the incident light's angle, preferentially diffracted and reflected wavelengths may be observed. In this context, preferentially reflected colors were recorded with incident light at 45° for the three patterns. **Figure 32A** displays the optical characterization setup. A bifurcated optical fiber was connected to a tungsten light source and a spectrometer, and the single end of the fiber was placed at 45° to the grating, at 2 cm of distance. **Figure 32B** shows the normalized pressure-dependent spectra measured in reflection mode, taking white light source irradiating a bare PDMS sample as a background reference. For pattern 1 (left),

blue and red wavelengths were preferentially diffracted, resulting in a blue/violet coloring. Pattern 2 (center) exhibited a coloring in the green area of the spectrum (510-540 nm), and pattern 3 (right) diffracted mainly in the red (> 600 nm) and slightly in the blue, yielding a purple/pink palette. As shown in **Figure 32C**, the sensor can be integrated into a contact lens to monitor the ocular pressure, either by replica molding of curved surfaces, or by direct bonding the grating to the contact lens. In this case, the grating was obtained on a flat PDMS surface and bonded to a PDMS lab-made contact lens (thickness ~ 160 µm, **Appendix VII**) by surface activation with an oxygen plasma pen. Color characterization was performed using a smartphone (**Figure 32D**), with the smartphone camera and light source placed at an incidence of 45° to the sample, at 2 cm of distance. **Figure 32E** shows the recorded coordinates in the RGB color space using Color Grab smartphone application. Insets display the corresponding color. For pattern 1, a constant blue component was observed, with varying green and red components in the pressure range 15-35 mmHg, yielding a blue/violet color palette. Pattern 2 exhibited high green and blue components, with a linear increase of the red component for higher applied pressures. Pattern 3 displayed a high blue component at low pressures, that shifted to red at pressures ≥ 20 mmHg, resulting in a violet to pink transition.

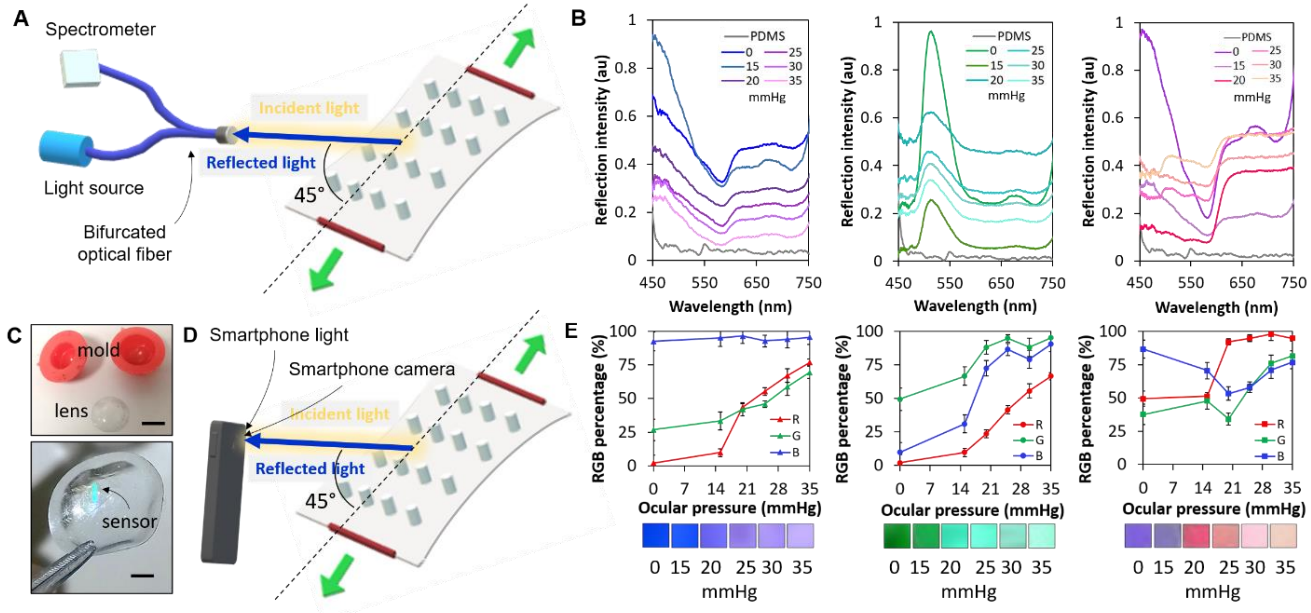

Figure 32. Color characterization of the diffraction gratings in reflection mode. A) Optical setup used for spectrophotometric reflection measurements. A bifurcated optical fiber is connected to a white light source and a spectrometer, and the single end is placed at 45° to the sample, at 2 cm of distance. B) Strain-dependent reflection spectra of pattern 1 (left), pattern 2 (center), and pattern 3 (right). C) Integration of stretchable diffraction gratings into a contact lens for ocular pressure monitoring. Top: fabrication of a PDMS lab-made contact lens, using a curved mold. Bottom: Photograph of a pressure-sensitive contact lens, obtained by oxygen plasma bonding of the grating to the PDMS lens. D) Setup for color characterization using a smartphone. Smartphone light and camera are used, both placed at 45° and 2 cm of distance from the sample. E) Smartphone pressure dependent RGB characterization: pattern 1 (left), pattern 2 (center), pattern 3 (right).

4.3. Discussion

All nanopatterns showed an acceptable sensitivity in the physiological range of interest. The grating with the smallest spacing was found to be the most sensitive, and a gradually decreasing sensitivity trend was observed for larger spacings (**Appendix VII**). Larger spacings yielded denser diffraction patterns that may be more challenging to observe accurately. Based on the colorimetric readout, pattern 1 and 2 (with spacings of 500 nm and 1 μm, respectively) report a more readable color change, with clearer blue or green palettes.

Sensors were integrated into contact lenses by oxygen plasma bonding to demonstrate the possibility of developing a wearable ocular sensor based on tunable diffraction gratings. This work may be further improved by fabricating the structures directly on the contact lens, by replica molding of nanobuttons on curved surfaces. This would allow to predict more accurately the behavior of the sensors by computational modelling, by removing the mechanical stress at the interface between the two plasma-bonded structures. Such process may be easier to scale up for commercial applications and could be performed on any curable polymer, including p(HEMA), the core polymer used in soft contact lens manufacturing. However, it could be more challenging due to the hydrophilic nature of p(HEMA), as hydrogels tend to swell in wet environments and crack in dry conditions.

With regards to smartphone readout, color imaging can be influenced by external factors, such as light level and color of the cornea. To standardize the measurements as much as possible, readout was

performed under constant ambient light levels of 249-251 lux, monitored with Photometer PRO smartphone app (**Appendix VII**) and colors were imaged at 45° using Color Grab smartphone app (**Appendix VII**). To ensure meeting the right tilt during imaging, a bespoke readout device may be designed, as previously done elsewhere.[28] It should also be noted that the color of the patient's cornea may influence the readout. In this case, a smartphone app with preliminary calibration step may be employed.

4.4. Conclusions

Stretchable diffraction gratings with sensitivities in the physiological range of interest (15-35 mmHg) were developed on PDMS, by replica molding of silicon nano-holes, and characterized with a white light source and red, green, and blue laser sources. Integration of the proposed structures on contact lenses was demonstrated and the potential of direct patterning of the structures into soft poly-HEMA contact lenses was discussed. A smartphone readout method was demonstrated, based on the observable color of the sensor under different strains. Tunable gratings were compared and discussed as a step forward to achieve point-of-care, continuous monitoring of the ocular pressure in glaucomatous patients with ocular hypertension. The experimental results demonstrated that an increasing micropillar spacing improved LOD and sensitivity.

4.6. References

1. J. J. Pang, Roles of the ocular pressure, pressure-sensitive ion channel, and elasticity in pressure-induced retinal diseases. *Neural Regeneration Research* **2021,** *16* (1), 68-72.
2. R. L. Stamper, History of Intraocular Pressure and Its Measurement. *Optometry and Vision Science* **2011,** *88* (1), E16-E28.
3. P. Harasymowycz, C. Birt, P. Gooi, L. Heckler, C. Hutnik, D. Jinapriya, L. Shuba, D. Yan, R. Day, Medical Management of Glaucoma in the 21st Century from a Canadian Perspective. . *Journal of Ophthalmology* **2016**, 6509809.
4. The World Health Organization, https://www.who.int/bulletin/volumes/82/11/feature1104/en/#:~:text=Glaucoma%20is%20the%20general%20term,causes%20gradual%20loss%20of%20vision. Accessed in March 2021.
5. R. N. Weinreb, C. K. Leung, J. G. Crowston, F. A. Medeiros, D. S. Friedman, J. L. Wiggs, K. R. Martin, Primary open-angle glaucoma. *Nature Reviews Disease Primers* **2016,** *2*, 16067.
6. The World Health Organization, Eye care, vision care, vision impairment and blindness. https://www.who.int/health-topics/blindness-and-vision-loss#tab=tab_1. Accessed in March 2021.
7. J. Lusthaus, I. Goldberg, Current management of glaucoma. *The Medical Journal of Australia* **2019,** *210* (4), 180-187.
8. A. V. Mantravadi, N. Vadhar, Glaucoma. *Primary care: clinics in office practice* **2015,** *42*, 437–449.
9. M. O. Gordon, M. A. Kass, The Ocular Hypertension Treatment Study: design and baseline description of the participants. *Archives of Ophthalmology* **1999,** *117*, 573– 583.
10. J. H. Liu, R. N. Weinreb, Monitoring intraocular pressure for 24 h. *British Journal of Ophthalmology* **2011,** *95*, 599-600.
11. S. Jabbehdari, J. L. Chen, T. S. Vajaranant, Effect of dietary modification and antioxidant supplementation on intraocular pressure and open-angle glaucoma. *European Journal of Ophthalmology* **2020**.
12. G. Dimitrova, A. Trenceva, The short-term effect of yoga ocular exercise on intra-ocular pressure. *Acta Ophthalmologica* **2017,** *95* (1), e81-e82.
13. M. Kuze, M. Ayaki, K. Yuki, M. Kawashima, M. Uchino, K. Tsubota, K. Negishi, Seasonal variation of intra-ocular pressure in glaucoma with and without dry eye. *Scientific Reports* **2020,** *10*, 13949.
14. M. Naderan, Ocular changes during pregnancy. *Journal of Current Ophthalmology* **2018,** *30* (3), 202-210.
15. G. M. Vieira, H. B. Oliveira, D. T. de Andrade, M. Bottaro, R. Ritch, Intraocular Pressure Variation During Weight Lifting. *Archives of Ophthalmology* **2006,** *124* (9), 1251-1254.
16. J. H. Liu, X. Zhang, D. F. Kripke, R. N. Weinreb, Twenty-four-Hour Intraocular Pressure Pattern Associated with Early Glaucomatous Changes. *Investigative Ophthalmology & Visual Science* **2003,** *44*, 1586-1590.
17. M. Li, M. Wang, W. Guo, J. Wang, X. Sun, The effect of caffeine on intraocular pressure: a systematic review and meta-analysis. *Graefe's Archive for Clinical and Experimental Ophthalmology* **2011,** *249*, 435–442.
18. J. Hu, K. M. Bui, K. H. Patel, H. Kim, J. A. Arruda, J. T. Wilensky, T. S. Vajaranant, Effect of Hemodialysis on Intraocular Pressure and Ocular Perfusion Pressure. *JAMA Ophthalmology* **2013,** *131* (12), 1525-1531.
19. A. Shrivastava, K. Singh, The effect of cataract extraction on intraocular pressure. *Current Opinion in Ophthalmology* **2010,** *21* (2), 118-122.
20. C. E. Young, L. K. Seibold, M. Y. Kahook, Cataract surgery and intraocular pressure in glaucoma. *Current Opinion in Ophthalmology* **2020,** *31* (1), 15-22.

21. J. Matlach, S. Bender, J. König, H. Binder, N. Pfeiffer, E. M. Hoffmann, Investigation of intraocular pressure fluctuation as a risk factor of glaucoma progression. *Clinical Ophthalmology* **2019,** *13*, 9-16.
22. K. C. Okafor, J. D. Brandt, Measuring intraocular pressure. *Current Opinion in Ophthalmology* **2015,** *26* (2), 103-109.
23. R. Moreddu, D. Vigolo, A. K. Yetisen, Contact Lens Technology: From Fundamentals to Applications. *Advanced Healthcare Materials* **2019,** *8* (15), 1900368.
24. R. Moreddu, M. Elsherif, H. Butt, D. Vigolo, A. K. Yetisen, Contact lenses for continuous ocular temperature monitoring. *RSC Advances* **2019,** *9*, 11433-11442.
25. R. S. Riaz, M. Elsherif, R. Moreddu, I. Rashid, M. U. Hassan, A. K. Yetisen, H. Butt, Anthocyanin-functionalized contact lens sensors for ocular pH monitoring. *ACS Omega* **2019,** *4* (26), 21792–21798.
26. Y. Chen, S. Zhang, Q. Cui, J. Ni, X. Wang, X. Cheng, H. Alem, P. Tebon, C. Xu, C. Guo, R. Nasiri, R. Moreddu, A. K. Yetisen, S. Ahadian, N. Ashammakhi, S. Emaminejad, V. Jucaud, M. R. Dokmeci, A. Khademhosseini, Microengineered poly(HEMA) hydrogels for wearable contact lens biosensing. *Lab on a Chip* **2020,** *20*, 4205-4214.
27. R. Moreddu, J. S. Wolffsohn, D. Vigolo, A. K. Yetisen, Laser-inscribed contact lens sensors for the detection of analytes in the tear fluid. *Sensors and Actuators B: Chemical* **2020,** *317*, 128183.
28. R. Moreddu, M. Elsherif, H. Adams, D. Moschou, M. F. Cordeiro, J. S. Wolffsohn, D. Vigolo, H. Butt, J. M. Cooper, A. K. Yetisen, Integration of paper microfluidic sensors into contact lenses for tear fluid analysis. *Lab on a Chip* **2020,** *20*, 3970-3979.
29. J. Kim, M. Kim, M. S. Lee, K. Kim, S. Ji, Y. T. Kim, J. Park, K. Na, K. H. Bae, H. K. Kim, F. Bien, C. Y. Lee, J. U. Park, Wearable smart sensor systems integrated on soft contact lenses for wireless ocular diagnostics. *Nature Communications* **2017,** *8*, 14997.
30. M. Leonardi, E. M. Pitchon, A. Bertsch, P. Renaud, A. Mermoud, Wireless contact lens sensor for intraocular pressure monitoring: assessment on enucleated pig eyes. *Acta Ophthalmologica* **2009,** *87* (4), 433-437.
31. T. Eggers, J. Draeger, K. Hille, C. Marschner, P. Stegmaier, J. Binder, R. Laur, Wireless intra-ocular pressure monitoring system integrated into an artificial lens, *1st Annual International IEEE-EMBS Special Topic Conference on Microtechnologies in Medicine and Biology*, Lyon, France, Lyon, France, 2000; pp 466-469.
32. V. Laukhin, I. Sanchez, A. Moya, E. Laukhina, R. Martin, F. Ussa, C. Rovira, A. Guimera, R. Villa, J. Aguiló, J. C. Pastor, J. Veciana, Non-invasive intraocular pressure monitoring with a contact lens engineered with a nanostructured polymeric sensing film. *Sensors and Actuators A: Physical 170* (1-2), 36-43.
33. Y. Zhang, Y. Chen, T. Man, D. Huang, X. Li, H. Zhu, Z. Li, High resolution non-invasive intraocular pressure monitoring by use of graphene woven fabrics on contact lens. *Microsystems & Nanoengineering* **2019,** *5* (39).
34. H. An, L. Chen, X. Liu, B. Zhao, H. Zhang, Z. Wu, Microfluidic contact lenses for unpowered, continuous and non-invasive intraocular pressure monitoring. *Sensors and Actuators A: Physical* **2019,** *295*, 177-187.
35. S. Agaoglu, P. Diep, M. Martini, K. T. Samudhyatha, M. Baday, I. E. Araci, Ultra-sensitive microfluidic wearable strain sensor for intraocular pressure monitoring. *Lab on a Chip* **2018,** *18*, 3471-3483.
36. D. Jang, X. Li, H. Gao, J. R. Greer, Deformation mechanisms in nanotwinned metal nanopillars. *Nature Nanotechnology* **2012,** *7*, 594-601.
37. L. Jang, J. Lee, M. E. Razu, E. C. Jensen and J. Kim, Fabrication of PDMS Nanocomposite Materials and Nanostructures. *Biomedical Nanosystems in IEEE Transactions on NanoBioscience*, **2015**, 841-849.
38. R. Moreddu, N. Boechler, A. M. Krachler, P. M. Mendes (**2018**) A piezoelectric organic surface to control bacterial adhesion and growth. In: Eskola H., Väisänen O., Viik J., Hyttinen J. (eds) EMBEC

& NBC 2017. EMBEC 2017, NBC 2017. IFMBE Proceedings, vol 65. Springer, Singapore, A piezoelectric organic surface to control bacterial adhesion and growth.
39. C. Xie, L. Hanson, Y. Cui, B. Cui, Vertical nanopillars for highly localized fluorescence imaging. *Proceedings of the National Academy of Sciences* **2011,** *108* (10), 3894-3899.
40. V. Solis-Tinoco, S. Marquez, T. Quesada-Lopez, F. Villarroy, A. Homs-Corbera, L. M. Lechuga, Building of a flexible microfluidic plasmo-nanomechanical biosensor for live cell analysis. *Sensors and Actuators B: Chemical* **2019,** *291*, 48-57.
41. R. Gangadharan, V. Anandan, A. Zhang, J. C. Drwiega, G. Zhang, Enhancing the performance of a fluidic glucose biosensor with 3D electrodes. *Sensors and Actuators B: Chemical* **2011,** *160* (1), 991-998.
42. A. Shrivastava, V. B. Gupta, Methods for the determination of limit of detection and limit of quantitation of the analytical methods. *Chronicles of Young Scientists* **2011,** *2*, 21-25.

Chapter 5

Sensing Tears Analytes

Contact lens sensors have been used as wearable devices for *in situ* monitoring of tear composition, although the functionality of the devices has thus far been limited. Here, using the integration of paper microfluidics within laser-inscribed commercial contact lenses, the multiplexed detection of a series of clinically relevant analytes is demonstrated, including proteins, glucose, nitrites, and L-ascorbic acid, all sampled directly from model tears. Two flow methods were investigated, namely capillary flow in hydrophilized polymeric channels, and paper-assisted flow within contact lenses. *In vitro* measurements involved the optimization of colorimetric assays, with readouts collected, stored, and analyzed using a bespoke Tears Diagnostics smartphone application. The potential of the device to perform discrete measurements either for medical diagnosis or disease screening in the clinic or at the point-of-care is demonstrated, with future applications including monitoring of ocular infections, uveitis, diabetes, keratopathies and assessing oxidative stress.

5.1. Introduction

Diagnostic devices that can monitor metabolites in body fluids have the potential to revolutionize healthcare.[1] It has already been shown that the detection of such analytes can enable opportunities both for disease screening and early-stage diagnostics using affordable technologies that can be operated by non-specialists in clinical or point-of-need settings.[2-4] Despite being an easily accessible organ, the physiology of the eye poses diagnostic challenges. Recent advances have been made towards the investigation of the composition of tears as a potential medium to monitor ocular health.[5] Tears are bio-fluids that may reflect both ocular and systemic physiological states by expressing a variety of biomarkers, as proxies either for chronic or acute disease (including infections) as well as local trauma or injury. The

tear fluid nourishes the ocular proximal tissues, and it contributes towards regulating corneal homeostasis. The "proximal fluid" is the final output of the lacrimal function unit, and it faces the external environment.[6] The tear fluid is complex and comprises a mixture of lipids, electrolytes, proteins, peptides, glucose, and amino acids. In general, the composition dynamically reflects the physiological state, including levels of hydration, infection, and general well-being. For example, whilst the normal protein concentration in tears lies in the range 3-7 mg mL^{-1},[7] recent reports in tear proteomics has enabled the diagnosis of diabetic retinopathy, aniridia,[8] keratopathies, and dry eye[9] (for example, a two-fold decrease in protein levels is reported in keratopathic tears (3.86 mg mL^{-1}) when compared to healthy controls (7.00 mg mL^{-1})). Vitamins C, A, E, and of the B family are also found in tears. In particular, ocular tissues and fluids contain high levels of L-ascorbic acid (vitamin C)[10] which play a role in antioxidant protection,[11] wound healing and inflammatory processes in the cornea.[12] In patients undergoing early-stage corneal damage, it has been argued that leakages of ascorbic acid from the corneal epithelial cells may be found in the tear films, making it a potential biomarker for corneal disorders, alkali burns,[13] and inflammation after excimer laser corneal surgery.[14] Thus in general the tear ascorbate levels can be related to the corneal health status.

Current techniques for pH measurement have included micro-combinations glass probes,[15] and microelectrodes[16] inserted in the eye, showing that the healthy tear pH ranges from 6.0 to 7.6.[15] Tear pH is crucial with regards to the ocular penetration of drugs[16] and in the early diagnosis of ocular rosacea (where the tear pH of non-treated ocular rosacea patients was found to be 8.0±0.32, compared to 7.0±0.18 in healthy controls).[17] Tear pH was also found to increase in pre- and post-operative senile cataract patients, resulting in pH values ranging from 7.26±0.23 on the day before the operation to 7.50±0.23 on the first post-operative day.[18] Nitric oxide is an important mediator of homeostatic processes in the eye, such as regulation of aqueous humour dynamics, retinal neurotransmission, and phototransduction.[19] Changes in its generation or action may be associated with diverse inflammatory states, including uveitis, retinitis, Behcet's syndrome, and degenerative diseases such as glaucoma. These variations can be

monitored by measuring tear nitrites as nitric oxide by-products. Healthy tears were reported to have nitrite levels of the order of 110-120 μmol L^{-1},[19] compared to the values of near 80 μmol L^{-1} in uveitis patients.[19] In uveitis patients, both with and without ocular complications, tear nitric oxide was found to quickly oxidize in peroxynitrite, a highly oxidizing cytotoxic substance.[19] Nitrites and nitrates levels as nitric oxide cytotoxic end products were found to significantly decrease, with average concentrations of 82.3 μmol L^{-1} in active Behçet's patients.

Tear fluid has previously been extensively investigated as an alternative body fluid for the monitoring of body sugar levels in diabetic patients.[20, 21] The correlation between tear glucose and capillary blood glucose can allow for the assessment of the diabetic status of a subject exclusively using tear glucose values.[20, 22, 23] Many of these efforts have been dedicated to the development of methods for tear glucose detection and monitoring, including glucose-sensitive photonic crystals,[24] holographic sensors[5] and molecularly-imprinted fluorescent sensors.[25] Glucose sensitive-contact lenses have also been proposed, [26, 27] although it is noted that these methods are often based upon electrical readouts, do not operate within normal physiological ranges, and that their readout mechanisms are impracticable or unfeasible.[28-30]

Currently, tears screening is performed in two steps: tear sampling and tear analysis. The gold standard method for tear extraction is Schirmer's test, which involves draining a few microliters of tear sample using capillary flow in a paper strip inserted in the lower eyelid for 5 minutes, which is subsequently screened using mass spectroscopy techniques. The Schirmer's test has several drawbacks, including a high contamination risk and tear overflow due to irritation. Moreover, with the corneal area being the most relevant source of information with regards to the ocular health, the composition fluid may vary at different regions on the ocular surface.[7]

Contact lenses are ocular prosthetic devices used by over 150 million people worldwide, which have recently been targeted as wearable sensing platforms.[3, 7, 31] Examples of smart contact lenses include the integration of electronic components, such as circuitry and displays,[32] continuous monitoring of glucose

in tears via diffractive microstructures,[26] and graphene-functionalized contact lenses with a variety of applications.[33, 34] However, the integration and management of electronic components interfaced directly with soft body tissues remains a challenge, and contact lenses which detect tear fluid analytes with optical methods generally either lack a reliable readout system, or their tear collection mechanisms are impractical. Tear collection and processing with simpler methods open other, different challenges, due to the small volumes of tear samples in unstimulated eyes, and the altered composition of the tear composition in stimulated eyes.[35]

5.2. Materials and methods

Materials. Deionized water, D-(+)-glucose (99.5%), L-ascorbic acid, $NaNO_3$, KCl, NaCl, urea, citric acid, protein standard (200 mg mL^{-1}), HEMA, 2-hydroxy-2-methylpropiophenone, ethylene glycol dimethacrylate, bromothymol blue, methyl red, and phenolphthalein, glucose oxidase, peroxidase, and 3,3',5,5'-tetramethylbenzidine, phosphomolybdic acid, 3',3",5',5"- tetrachlorophenol- 3,4,5,6-tetrabromosulfophthalein, sulfanilamide, N-(1-naphthyl)- ethylenediamine dihydochloride, 3-aminopropyltriethoxysilane, 3-glycidoxypropyltriethoxysilane, Tris HCl, Tris base, sodium fluorescein, and phosphate buffered saline (PBS) tablets were purchased from Sigma-Aldrich and used with no additional purification. Filter paper was purchased from Fisher Scientific. Commercial contact lenses based on Boston XO (fluorosilicone acrylate) material were supplied by No7 Contact Lenses, UK.

Laser inscription of acrylate contact lenses and laser cutting of paper microfluidic systems. Microfluidic patterns were designed on CorelDraw and further inscribed in commercial acrylate contact lenses using a CO_2 Rayjet laser system, operating at a wavelength of 11.6 μm, with a speed of 60% and a power of 50%. The material thickness was set to 100 μm. The same software and equipment were used to design paper microfluidic chips via CO_2 laser cutting at power a laser power of 80%, scanning speed of 90%, and thickness of 200 μm.

Preparation of chemical sensors. The pH biosensor was synthesized using bromothymol blue (50.0 μg), methyl red (5.0 μg) and phenolphthalein (25.0 μg). The glucose biosensor was prepared diluting 3,3',5,5'-tetramethylbenzidine (250.0 μg), GOD (25 U) and POD (120 U) in DI water. The protein sensor contained 3',3",5',5"-tetrachlorophenol-3,4,5,6-tetrabromosulfophthalein (20.0 μg). The nitrite sensor contained 3-hydroxy-1,2,3,4-tetrahydro-7,8-benzoquinoline (50.0 μg) and sulfanilamide (40 μg). The ascorbic acid sensor contained phosphomolybdic acid (100.0 μg). The liquid-state sensors were deposited on paper circles with a diameter of 2.0 mm, and air-dried.

Fabrication of poly-HEMA contact lenses. HEMA (95 vol/vol %), the photoinitiator 2-hydroxy-2-methylpropiophenone (1 vol/vol %), and the cross-linker ethylene glycol dimethacrylate (4 vol/vol %) were mixed, pipetted into a contact lens mold, and cured under UV light (λ = 365 nm) for 5 min.

Poly-HEMA to acrylate chemical bonding. As a first step, -OH groups are obtained on both surfaces (poly-HEMA and fluorosilicone acrylate) by activating them via O_2 plasma for 1 minute at 60W, using a Henniker Plasma System. Following this, the poly-HEMA lens is soaked in a 1:100 (v/v) 3-aminopropyltriethoxysilane (APTES) aqueous solution and the acrylate lens is soaked in a 1:100 (v/v) 3-glycidoxypropyltriethoxysilane (GPTES) aqueous solution for 20 minutes. The lenses are then rinsed in deionized water, and air-dried. The surfaces are now ready to be brought into contact applying a slight pressure, after depositing the microfluidic paper in the acrylate contact lens.

Preparation of artificial tear fluid. Artificial tear fluid contained NaCl (125.0 mmol L^{-1}), KCl (20.0 mmol L^{-1}), urea (5.0 mmol L^{-1}), citric acid (31.0 μmol L^{-1}), L-ascorbic acid (0-1.0 g L^{-1}), $NaNO_2$ (0-160.0 μmol L^{-1}), glucose (0-10.0 mmol L^{-1}), albumin (0-8.0 g L^{-1}), and the pH value was adjusted to 5.0 -8.0 using Tris HCl and Tris base.

Readout smartphone application. A customized smartphone application was developed using the module Mobile app.net with Xamarin forms on Visual Studio 2019. Colorimetric changes were captured by a complementary metal-oxide-semiconductor (CMOS) sensor equipped in a smartphone camera. The

captured images served as inputs to the smartphone applications, based on the nearest neighbor problem. The color gamut is a scalar field that standardizes colors, which are univocally identified by their (x, y) coordinates on the CIE color plot. In this work, a calibration curve was created for each sensor, by locating colors associated with discrete concentration values in the CIE diagram. Upon readout, the smartphone application located the new color in the color gamut and compared it to the calibration points. The output was given by the nearest neighbor value in the color plot.

5.3. Results and Discussion

5.3.1. Capillary flow along microfluidic channels

Here, semi-quantitative microfluidic contact lens sensors were developed for the detection of pH, glucose, protein, and nitrite levels in tears. Microchannels were etched in commercial rigid gas permeable (RGP) contact lenses by laser ablation, and colorimetric biochemical sensors were deposited over four sensing areas within the microfluidic system (**Figure 33a**). Upon binding tear metabolites, biochemical sensors exhibited a reflection peak shift in the visible spectrum, resulting in a color change visible with the naked eye. To achieve precision readout, biosensors were imaged using a smartphone camera (**Figure 33b**), and further processed using a MATLAB algorithm based on the nearest neighbor method, which outputted the concentration of analytes corresponding to the detected color (**Figure 33c**).

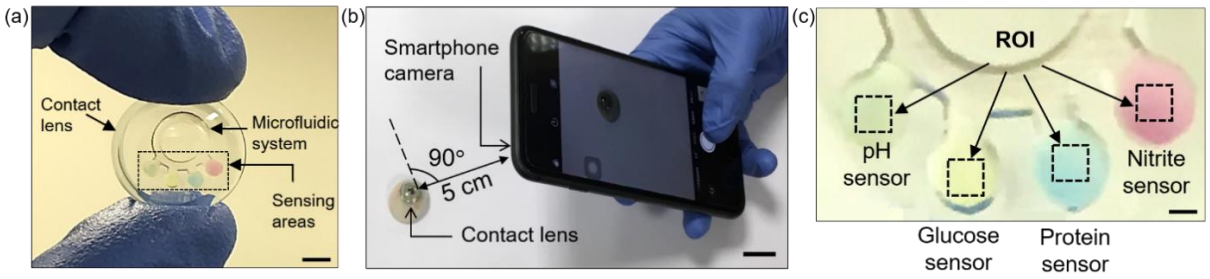

Figure 33. Microfluidic contact lenses for the colorimetric sensing of tear metabolites. (a) Photo of a contact lens sensing platform. Scale bar: 5.0 mm. (b) The color change of the sensors is imaged using a smartphone camera. Scale bar: 1.0 cm. (c) Photographs of the sensors serve as inputs to the customized MATLAB algorithm, where the region of interest (ROI) can be

selected. Discrete concentration values are identified based on the comparison between the (x, y) coordinates defining the color in the CIE 1931 chromaticity space, and the position of the calibration points. Scale bar: 1.0 mm.

Tear fluid biosensors based on chromogenic compounds sensitive to pH, glucose, proteins, and nitrites, were synthetized. The sensors exhibited a variation of the reflected light within the visible spectrum upon variations in the concentration of tear metabolites. The tear pH sensor was based on methyl red, bromothymol blue, and phenolphthalein (**Figure 34a**), and it reflected wavelengths in the green in neutral solution. Methyl red is an organic compound comprising a carboxylic acid group and an amine functional group, that confer it the ability to serve either as acid or base, and to detect pH variations from 4.3 to 6.2. Bromothymol blue is a weak acid that forms triphenylmethane in alkaline media, reporting a shift in the reflected light from yellow to blue. Phenolphthalein switches from a colorless lactonic ring structure in acidic media to a quinoid-carboxylated structure in alkaline media. It exhibited a color shift from pink to fuchsia upon pH variations from 8.2 to 12.0. The tear pH sensor was tested in aqueous solution in the physiological range of interest, at values of 6.0, 6.5, 7.0, 7.3, 7.6, 8.0. **Figure 34b** shows the absorbance spectra of tear pH sensors. The inset shows the calibration curve, from which a sensitivity of 12.23 nm/pH and a LOD of 0.25 pH units were calculated. The optical density (absorbance) trend at 610 nm (linear fitting, R^2=0.99) is shown in **Figure 34c**. The inset figure shows the pH-dependent color variation of the sensor, ranging from dark yellow at 6.0 to blue at 8.0. These colors were used as calibration inputs to the MATLAB algorithm. The percentage of RGB colors over the pH value is shown in **Figure 34d**. The corresponding calibration points are plotted in the chromaticity diagram in **Figure 34e**. The algorithm processed the imaged biosensors embedded in contact lenses and calculated the related concentrations by locating the detected color in the chromaticity space and comparing it to the position of the calibration points. The algorithm returned concentration values corresponding to the nearest calibration value in the diagram, compared to the color under examination. The nearest neighbor was calculated considering the point with the (x, y) shorter distance in the 2D CIE1931 chromaticity space. **Figure 34f** presents the variation of (x, y) CIE 1931 coordinates over variations in pH values. The two coordinates are ideally expected to follow a reciprocal behavior.

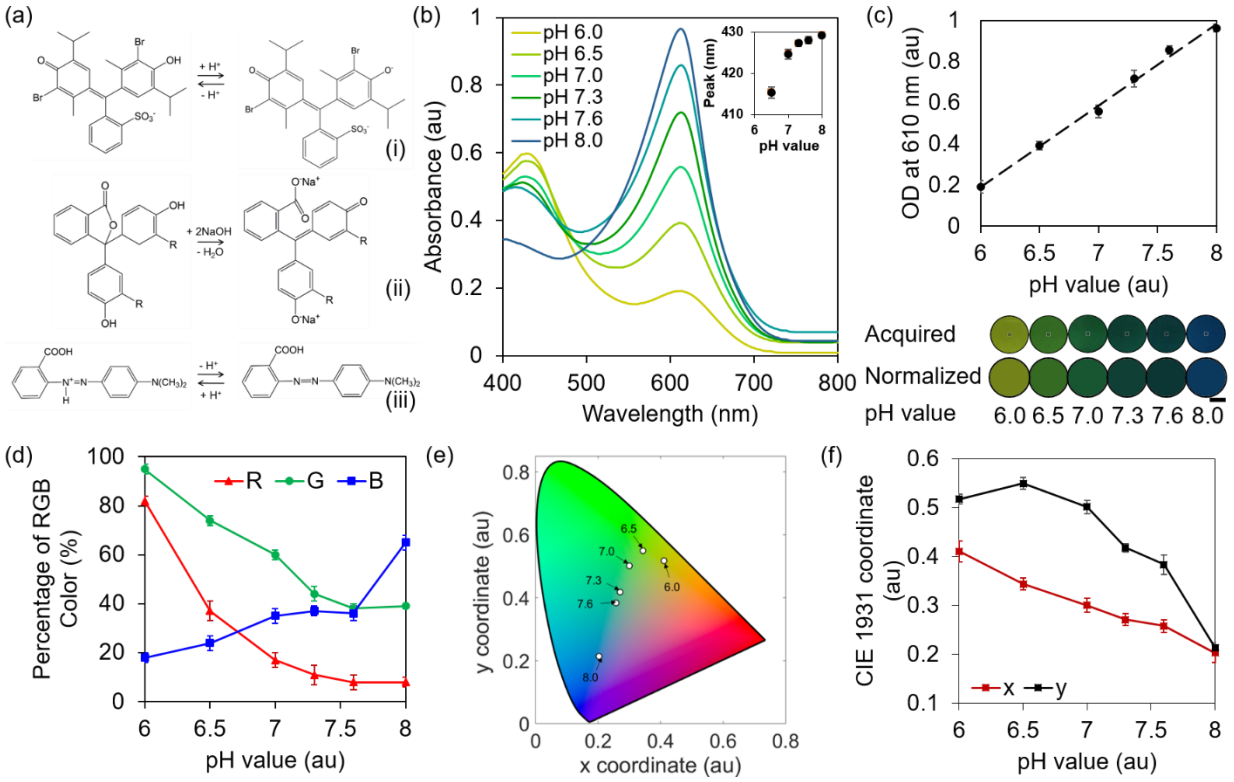

Figure 34. Characterization of the tear pH sensor. (a) Chemical structures of methyl red (i), bromothymol blue (ii), and phenolphthalein (iii). (b) Absorption spectra of 6.0, 6.5, 7.0, 7.3, 7.6, and 8.0 pH buffers. The inset shows the calibration curve. (c) Optical density trend at 610 nm. The inset figure shows the acquired (first row) and normalized (second row) colors imaged in solutions containing different concentrations of hydrogen ions. Scale bar: 500 µm. (d) Colorimetric characterization of pH sensors according to the RGB color model. (e) Chromaticity diagram displaying the calibration points. (f) Trend of the (x, y) coordinates at different pH levels, plotted in the CIE 1931 chromaticity space.

The tear glucose sensor was based on a two-step enzymatic method, using glucose oxidase/peroxidase (GOD/POD) (**Figure 35a**). The oxidation of D-glucose to D-gluconolactone in air forms hydrogen peroxide, which in turn oxidizes 3,3',5,5'-tetramethylbenzidin (TMB) under peroxidase catalysis. Tear glucose sensors yielded a color shift from yellow to different shades of green, upon varying glucose concentration from 0, 2, 5, 10, 15, 20 mmol L^{-1}. The absorbance spectra of the sensors tested in glucose PBS solutions at different concentrations are shown in **Figure 35b**. The calibration curve is shown in the inset and yielded a sensitivity of 1.4 nm/mmolL^{-1} of glucose, and a LOD of 1.84 mmolL^{-1}. The optical density trend at 670 nm is shown in **Figure 35c**, with a second order polynomial fitting (R^2=0.99). The

inset figure shows the colors of the different solutions as acquired with the smartphone applications, and the corresponding normalized pixels. These images were used as inputs to the MATLAB algorithm to identify the reference points. RGB triplets associated to each color are plotted in **Figure 35d**. The associated colors are plotted in the chromaticity diagram of **Figure 35e**. **Figure 35f** shows the behavior of the (x, y) CIE 1931 coordinates related to the calibration values.

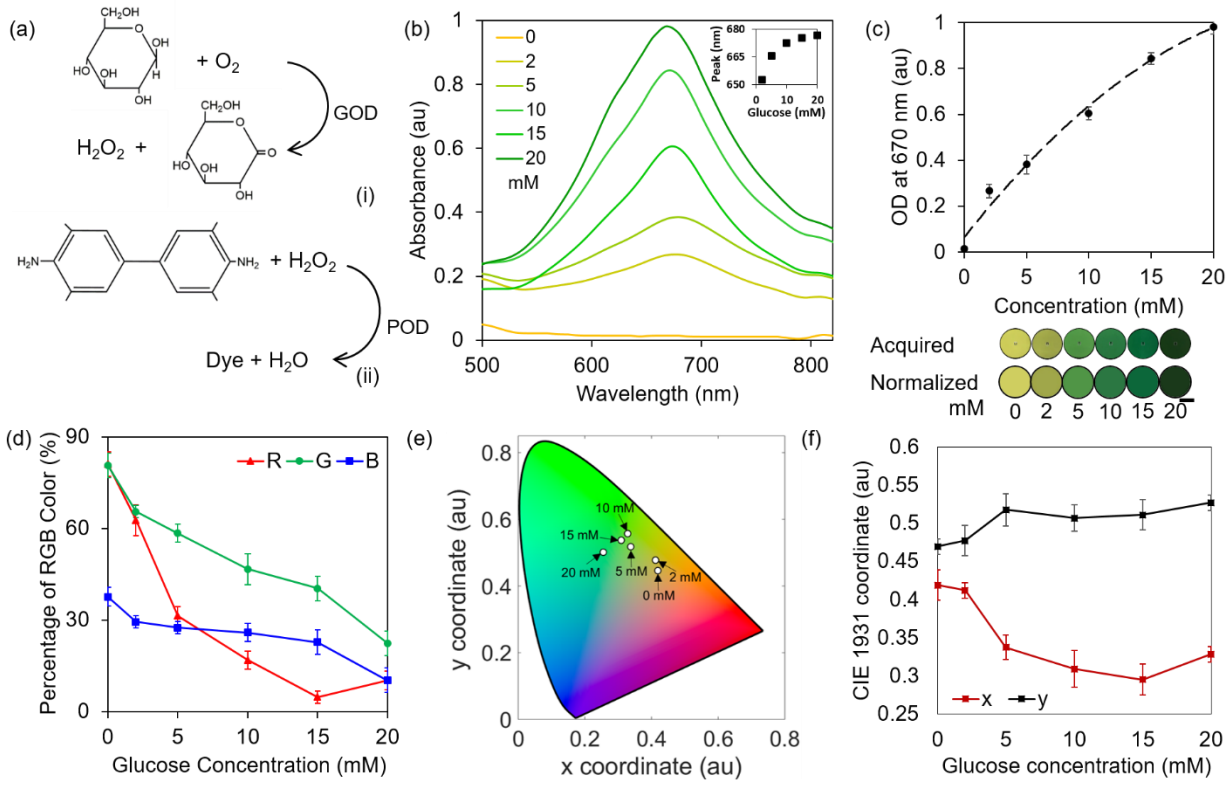

Figure 35. Characterization of the tear glucose sensor. (a) Working principle of the glucose biosensor. β-D glucose reacts with oxygen producing hydrogen peroxide (i), which oxidizes 3,3',5,5'-tetramethylbenzidin (ii). (b) Absorption spectra of solutions at glucose concentration of 0.0, 2.0, 5.0, 10.0, 15.0, 20.0 mmol L^{-1}. The inset shows the calibration curve. (c) Optical density trend of tear glucose sensors at 670 nm. The inset figure shows the acquired (first row) and normalized (second row) colors imaged in solutions having different glucose concentration. Scale bar: 500 μm. (d) RGB characterization of glucose sensors. (e) Chromaticity diagram displaying the calibration points. (f) Trend of the (x, y) coordinates at different glucose levels, plotted in the CIE 1931 chromaticity space.

Tear protein sensors were based on the reaction of 3',3",5',5"-tetrachlorphenol-3,4,5,6-tetrabromsulfophthalein with free amino groups (**Figure 36a**), that induced a color change from beige to light blue for protein concentration values of 0.5, 1.0, 2.0, 3.0, 4.0 and 5.0 g L^{-1}. **Figure 36b** shows the absorption spectra of tear protein sensors in PBS solutions at different concentration levels, and the corresponding calibration curve is plotted as an inset. The protein sensors yielded a sensitivity of 0.49 nm/gL^{-1} of proteins, and a LOD of 0.63 gL^{-1}.

The optical density trend of the sensor with the second order polynomial fitting (R^2=0.97) is presented in **Figure 36c**. The inset figure shows the colors of the different solutions as acquired with the smartphone applications (first row), and the corresponding normalization (second row). These images were used as calibration colors for the MATLAB algorithm, from which concentrations in artificial tear fluid were estimated. RGB triplets associated to each color are plotted in **Figure 36d**. The associated colors are indicated in the chromaticity diagram of **Figure 36e**. **Figure 36f** shows the behavior of the (x, y) CIE 1931 coordinates.

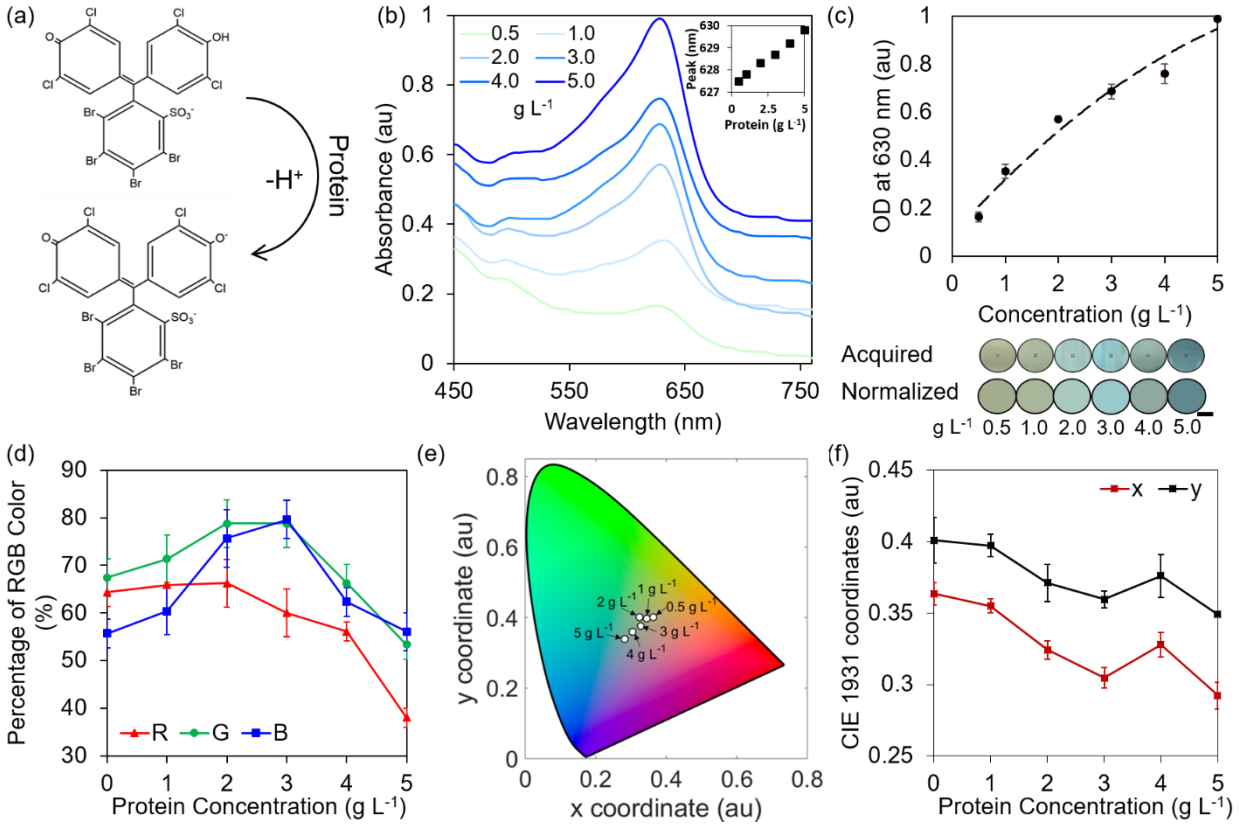

Figure 36. Characterization of the tear protein sensor. (a) Working principle of the protein biosensor. A 3',3",5',5"-tetrachlorphenol-3,4,5,6-tetrabromsulfophthalein molecule binds an amino-acidic hydrogen ion, yielding an anode of the same compound which reflects a different color. (b) Absorption spectra of solutions at protein concentrations of 0.5, 1.0, 2.0, 3.0, 4.0, and 5.0 g L^{-1}. The inset shows the calibration curve. (c) Optical density trend of tear protein sensors at 630 nm. The inset figure shows the acquired and normalized colors imaged in solutions having different protein concentration. Scale bar: 500 μm. (d) RGB characterization of protein sensors. (e) Chromaticity diagram displaying the calibration points. (f) Trend of the (x, y) coordinates at different protein levels, plotted in CIE 1931 chromaticity space.

Tear nitrite sensors were based on the reaction of nitrite ions with sulfanilamide to form a diazonium salt, which further binds N-(1-naphthyl)- ethylenediamine dihydochloride (**Figure 37a**), to produce a pink azo dye yielding increasing intensities at higher concentrations of nitrite ions. The absorbance peak of the dye is measured at 528 nm. The tear nitrite sensors were tested in aqueous solutions at nitrite concentrations of 0, 10, 20, 80, 120, 150, 180, and 200 μmol L^{-1}. **Figure 37b** shows the absorption spectra of tear nitrite sensors, and the calibration curve as an inset. The nitrite sensor yielded a sensitivity of 0.03nm/μmolL^{-1} of nitrites, and a LOD of 24.4 μmolL^{-1}. **Figure 37c** depicts the corresponding optical density trend at 510 nm, with the second order polynomial fitting (R^2=0.99). The inset figure shows the acquired (first row) and normalized (second row) colors of the different solutions, which were given as inputs to the MATLAB algorithm to calibrate the outputs. The corresponding RGB triplets are plotted in **Figure 37d**. Chromogenic changes of the calibration points are indicated in the chromaticity diagram of **Figure 37e**. **Figure 37f** shows the behavior of the (x, y) CIE 1931 coordinates. At a concentration of 200 μmol L^{-1}, the coordinates stop following a reciprocal trend, indicating that the color change saturates, and the variation is appreciated due to a color intensification only (as visible in the RGB characterization, with a substantial increase in the blue percentage at 200 μmol L^{-1}).

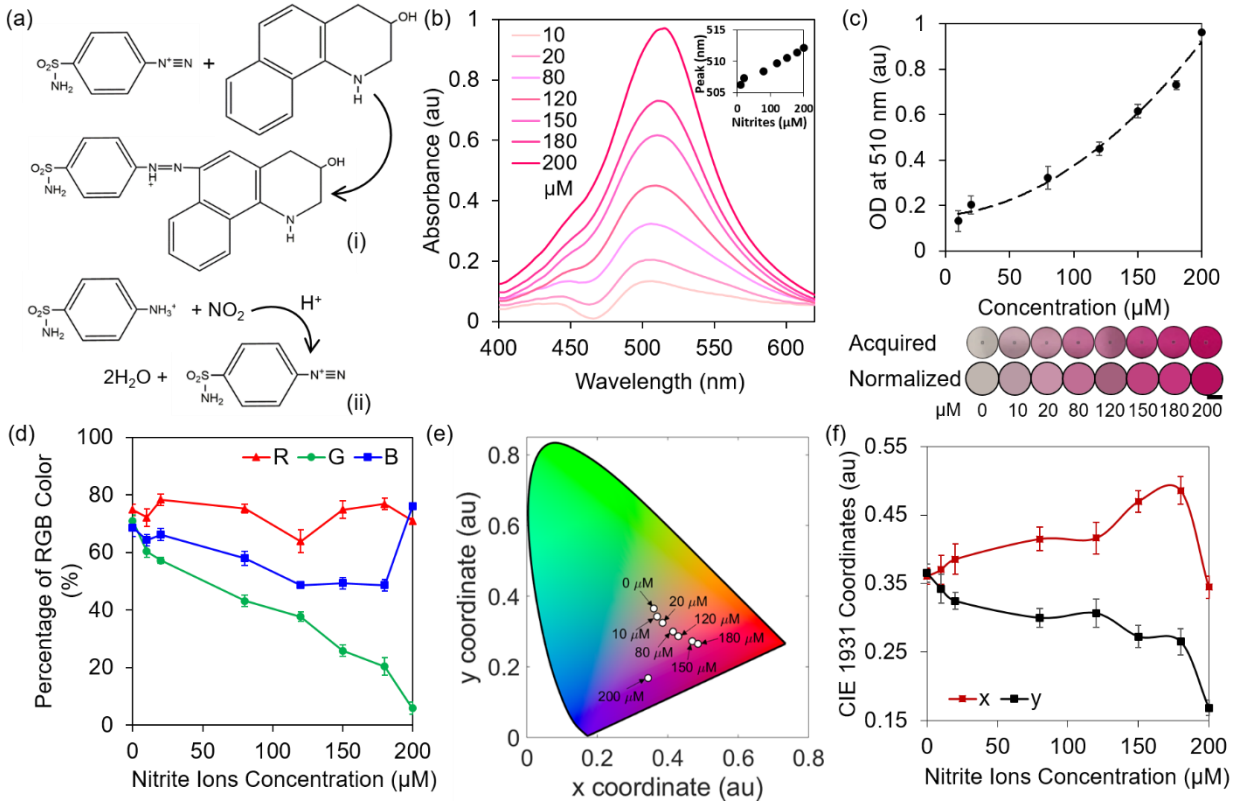

Figure 37. Characterization of the tear nitrite sensor. (a) Working principle of the nitrite biosensor. Nitrite ions react with sulfanilamide to form a diazonium salt (i), which in turn binds N-(1-naphthyl)-ethylenediamine dihydochloride, producing a pink azo dye (ii). (b) Absorption spectra of solutions at nitrite concentration of 10.0, 20.0, 80.0, 120.0, 150.0, 180.0, and 200.0 μmol L^{-1}. The inset shows the calibration curve. (c) Optical density trend of tear nitrite sensors at 510 nm. The inset figure shows the acquired and normalized colors imaged in solutions having different nitrite concentration. Scale bar: 500 μm. (d) RGB characterization of nitrite sensors. (e) Chromaticity diagram displaying the calibration points. (f) Trend of the (x, y) coordinates at different nitrite levels, plotted in CIE 1931 chromaticity space.

The tear metabolites sensors were embedded within laser patterned microfluidic RGP commercial contact lenses and characterized with artificial tear fluid. The microfluidic system was tested by injecting fluorescein aqueous solution (**Figure 38a**). Microchannels were filled with five continuous injections of 1.0 μL each, resulting in the channel being fully filled in 560 ms. Neutral tear biosensors were further embedded within microchannel cavities, and artificial tear fluid containing 5.0 g L^{-1} of protein standard, 5.0 mmol L^{-1} of glucose, 120 μmol L^{-1} of nitrite ions dissolved in a pH 8.0 buffer solution and in artificial eye drops, was injected with five continuous injections of 1 μL each. **Figure 38b** shows photographs of

the contact lens platform before and 15 seconds after artificial tear fluid injection, where color changes are visible. Insets show optical micrographs of a cavity and a section of the microchannel, under 5x magnification. The sensors were imaged with a smartphone camera kept normal to the contact lens sensing area, at 5.0 cm of distance and ambient light conditions of 200 lux, to emulate what would happen in a real case scenario, where microfluidic channels would be created by bonding a second contact lens on top and etching an inlet on the concave side of the contact lens sensor to directly access tear fluid from the patient's eye. **Figure 38c** shows photographs of the imaged sensors before and after artificial tear fluid injection, that were processed with the MATLAB algorithm. To evaluate the time response of each sensor, RGB color shift were examined over time (**Figure 38d**), resulting in a color saturation of the pH sensor after 5 s, and time responses of 15 s, 10 s, and 15 s, for glucose, protein, and nitrite sensors, respectively. Insets in figures show the color change at the considered discrete time intervals. **Figure 38e** displays the CIE 1931 chromaticity diagrams observable while operating the algorithm during image processing. The region of interest is selected within the imaged sensing area. The corresponding normalized color is plotted in the chromaticity space, where it is compared to the position of the calibration points. The value of the unknown concentration is given by considering the calibration point with the shortest distance from the point under analysis. This method guarantees a correct output for discrete concentration values, defined during the calibration step, when performing the measurement in the same light conditions.

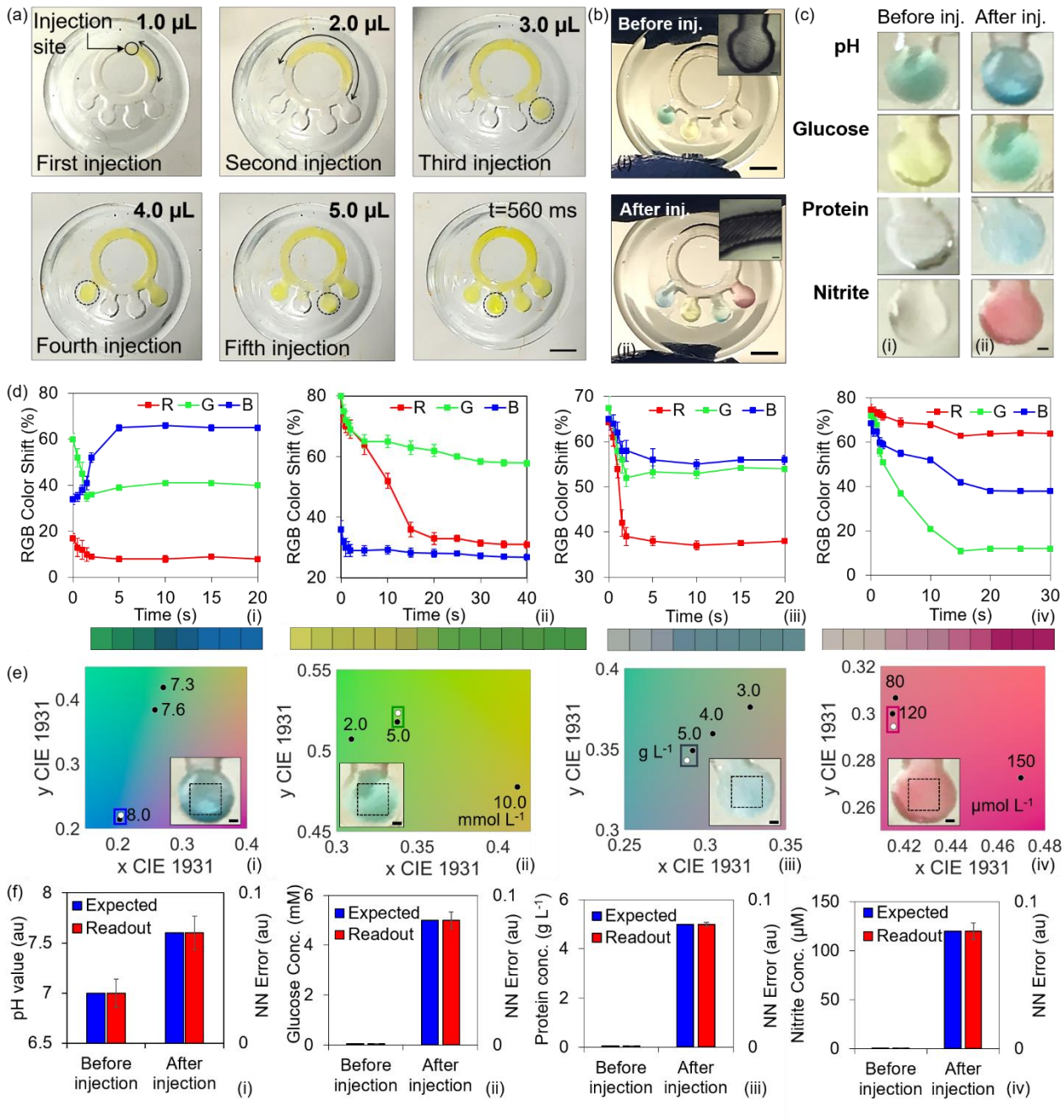

Figure 38. Characterization of microfluidic contact lenses. (a) Fluid flow characterization with fluorescein aqueous solution. Five consecutive injections amounting to 1 µL each were performed from the indicated injection site. Within 560 ms, the fluid reached all the sensing sites. Scale bar: 4.0 mm. (b) Characterization of contact lens sensors with artificial tear fluid. Photographs of a contact lens sensor before (i) and after (ii) artificial tear fluid injection. Scale bars: 4.0 mm. Insets show micrographs of a sensing cavity and of a channel section. Scale bars: 200 µm. (c) Representation of smartphone readouts on contact lens sensors before (i) and after (ii) artificial tear fluid injection. The pH sensor yielded a color shift from green to blue, corresponding to pH 8.0. The glucose sensor yielded a shift from yellow to green, detecting a concentration of 5.0 mmol L^{-1}. The protein sensor exhibited a light blue color upon interacting with the solution, corresponding to a concentration of 5 g L^{-1}.

The nitrite sensor reflected an intense pink color, corresponding to a concentration of 120 μmol L^{-1}. Scale bar: 300 μm. (d) Red, Green, and Blue color shift over time for pH (i), glucose (ii), protein (iii), and nitrite (iv) biochemical sensors, where t=0 is set as the time in which the artificial tear fluid reaches each respective sensing area. pH color saturation takes place after 5 s, glucose after 15 s, protein from 10 s, and nitrite at 15 s. Overall, readouts can be performed after 15 s. Color insets show the color evolution over time, corresponding to the discrete time values indicated in the x axis of the graphs. Scale bar: 200 μm. (e) CIE 1931 chromaticity diagrams obtained with the algorithm after inputting the imaged sensors. The algorithm allowed to select the region of interest, indicated with black dotted lines. The corresponding normalized color is plotted in the chromaticity space calibrated with the points of the sensor of interest (white dots) and compared to the calibration values (black dots). The nearest calibration point gives the concentration readout. Readouts refer to pH (i), glucose (ii), protein (iii), and nitrite (iv) sensors. Scale bars: 300 μm. (f) Smartphone-MATLAB algorithm readouts for pH (i), glucose (ii), protein (iii) and nitrites (iv), before and after artificial tear fluid injection. The y axis indicates the nearest neighbor error (NN Error), intended as the distance to the nearest calibration point in the CIE 1931 chromaticity space. Error bars are plotted in the secondary y axis.

This would be a realistic scenario when operating the device inside a medical clinic room. However, this algorithm may be improved to estimate intermediate concentration values. The box plots in **Figure 38f** display the expected concentration values versus the concentrations detected with smartphone-MATLAB readouts, before and after artificial tear fluid injection. Standard errors were calculated by measuring the (x, y) distance between the color under measurement and its nearest calibration point in the chromaticity diagram, and they were plotted in the y secondary axis. pH sensing in artificial tear fluid yielded mean standard errors of $2.0 * 10^{-2}$ and $2.3 * 10^{-2}$ before and after injection, respectively. Glucose, proteins, and nitrites had null concentrations before injection. After injection, they yielded mean standard errors of $1.2 * 10^{-2}$, $2.0 * 10^{-3}$, and $1.3 * 10^{-2}$. Tear pH sensors will exhibit a green color in healthy eyes. A yellow color may indicate a slightly acidic pH, attributed to an alteration of tear buffering capacity.[18] pH sensors will reflect a blue color in cases of alkaline pH, which may aid the early detection of rosacea disease.[17] Tear glucose sensors will exhibit a yellow-greenish color in healthy conditions. Down-regulated sugar levels will result in a null detection by this sensor, which will exhibit a clear yellow color. Upregulated glucose will display increasingly darker green colors when the glucose content increases. The range of interest for the tear glucose sensor is 0 to 5 mmol L^{-1}.[55] The protein sensor will always

display a light blue color, with the concentration given by the color intensity. An intense light blue will be displayed for healthy protein levels, of 5 g L^{-1} and above. Lower intensities are indicative of the presence of down-regulated proteins in the tear film, which may be related to the development of keratoconus, a disorder of the eye that results in the cornea progressively bulging into a conical shape.[29] Keratoconus patients have tear protein levels around 3 g L^{-1}, even in early stages of the disease.[29] In these cases, the protein sensor will display a light blue color with low intensity, which can be successfully detected with the algorithm. Tear nitrite sensors will always display a pink color, with varying intensity based on the concentration. An intense pink color will be associated to healthy tears (nitrite levels ≈ 120 μmol L^{-1}).[31] A light pink color may be associated to uveitis (nitrite levels ≈ 80 μmol L^{-1}).[31]

A contact lens sensor comprised a single microfluidic system consisting of one ring and four branches where the liquid was guided by capillarity toward four sensing areas. Selective hydrophilization of the microfluidic channel was achieved by oxygen plasma treatment at 100W for 80 seconds. A flexible shadow mask was laser-patterned such to protect the entire surface of the contact lens, except for the central ring of the microfluidic system. Hydrophobic cavities were preferred to embed liquid-state biochemical sensors and reduce leakage. An alternative method to reduce leakage could be to embed either paper or cotton pads soaked in biochemical sensors within the cavities in solid form. The device is designed for a single detection, rather than continuous monitoring. However, it may be emptied, disinfected, and reused.

The diameter of the contact lens and the position of the microfluidic system within the contact lens dictate the portion of the eye surface over which biochemical sensors will be located during wearing. Contact lenses of different diameters may be patterned with the proposed method. If overlying the iris, colorimetric smartphone readouts may need to be calibrated based on the iris color of the patient's eye. Alternatively, biochemical sensors may be embedded in paper/cotton pads and deposited in a solid form, or liquid-state biochemical sensors may be poured over a hydrophobic white plastic substrate. However, this may be simplified by using scleral contact lenses, where the microfluidic system can be inscribed such that

colorimetric sensors fall over the white scleral area. To address the influence of ambient light levels toward the resulting RGB triplet, the smartphone app may include a preliminary step of detecting ambient light hitting the sensors and filtering it out for readout. Colorimetric test strips may also be used for comparison.

5.3.2. Paper-assisted flow

Here we report upon the integration of biosensing functionalities within microfluidics contact lenses using a smartphone-based readout method to collect and store information, enabling *in situ* discrete direct collection and detection of analytes from the tear. A paper-based microfluidic approach was used within the contact lens itself, to minimize leakage and facilitate tear fluid flow by capillarity (**Figure 39**).

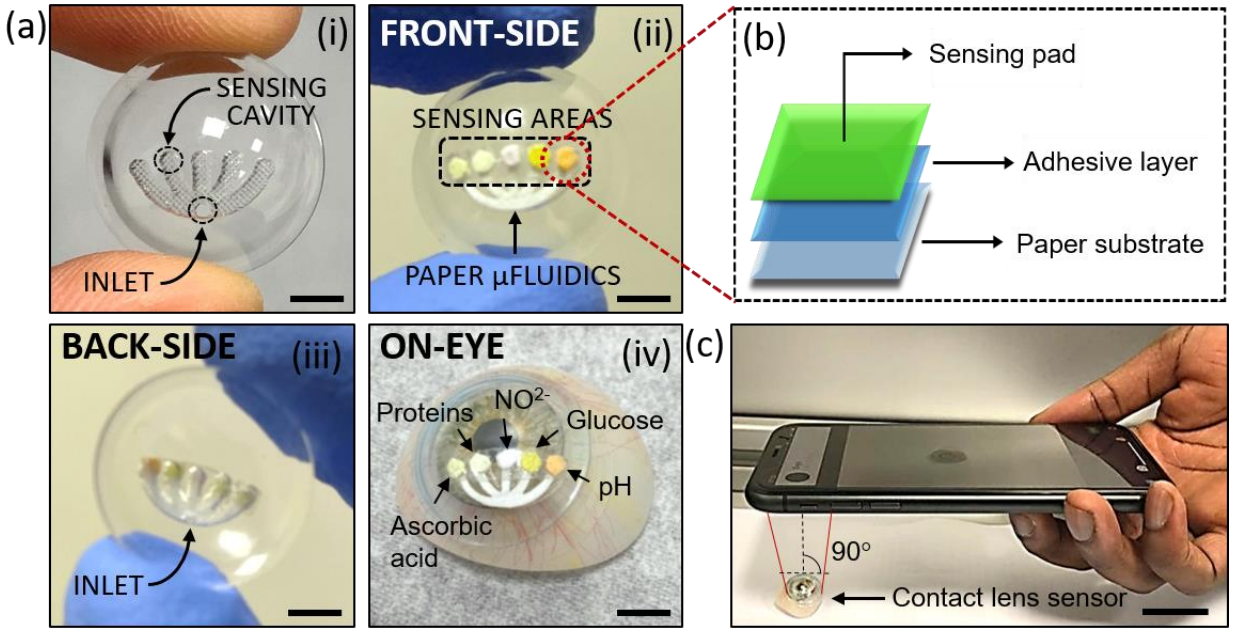

Figure 39. Microfluidic contact lens sensor based on paper-assisted flow. (a) Device fabrication: (i) Laser-inscribed microfluidic system on a contact lens; (ii) Embedding the paper microfluidic chip within the contact lens; (iii) Backside view of the contact lens sensor; (iv) Contact lens sensor on an artificial eye model. Scale bars: 1.5 cm. (b) Schematic of the structure of each sensing area; (c) Representative photograph of the readout method. Scale bar: 2.0 cm.

The device was manufactured using laser ablation of contact lenses (**Figure 39a**) and laser cutting of paper microchannels. Paper-embedded biochemical sensors (**Figure 39b**) were integrated within the microfluidic lenses. The system was finally closed using a poly-HEMA lab-made contact lens as a top layer, by chemical bonding. The inlet allows artificial tear fluid to flow form the concave side of the contact lens in the microchannel. Colorimetric readouts were collected stored and analysed on a smart phone app (**Figure 39c**), using a simple algorithm to remove background and noise, arising from changes in the eye colour or local lighting.

Chemical sensors, immobilized within paper matrices were embedded within microfluidic contact lens structures to detect tear pH, glucose, proteins, ascorbic acid, and nitrites in the physiological range. Upon changing the concentration of tear analytes, the chromogenic sensors yielded a variation in the primary reflected wavelength within the visible spectrum. pH sensors, based on methyl red and bromothymol blue, responded to the pH range between pH 5.0 to 8.0 (**Figure 40a**) providing a color shift from orange (pH 5.0) to yellow (pH 6.0) and green (7.0-8.0). Organic methyl red sensed acidic pH variations from 4.0 to 6.0 via its carboxylic and amine functional groups. Intermediate pH values (6.0-8.0) were detected by bromothymol blue, a weak acid that forms triphenylmethane in alkaline media. **Figure 40b** shows the reflection spectra of tear pH sensors, yielding a calibration curve with a linear fitting (R^2= 0.99) and a Limit of Detection (LOD) of 0.2 pH units within the physiological range 7.0 - 8.0 (**Figure 40c**). RGB triplets associated with each color were obtained by imaging the sensor with a smartphone camera, using the torch of the smartphone as the only light source, to standardize the color measurement. During imaging, the smartphone camera was kept at normal incidence to the sensor, at 5.0 cm of distance. The percentage of RGB colors over the pH value is shown in **Figure 40d**, where a decrease in the color intensity was observed upon increasing the pH, as well as a decrease in the red contribution when shifting from orange to green. The sensors were exposed to UV light at 355 nm to emulate the sun exposure of the eye, yielding a stable behavior up to 30 minutes of exposure (**Figure 40e, f**), with a stable reflection peak around 550 nm, corresponding to the imaged green color (**Figure 40g**). The pH sensor had a response time of 15 s, that remained stable for the following 15 s, as shown in **Figure 40h** to reach pH 7.0.

Appendix VIII shows the timed responses at pH 6.0 and 8.0. **Figure 40i** displays the CIE 1931 chromaticity plot of the pH sensors, where the calibration values that were used to design the smartphone application are plotted, and the color shift is observable.

Glucose sensors were produced based on glucose oxidase (GOD)/peroxidase (POD) method, comprising of GOD, POD, and 3,3′,5,5′-tetramethylbenzidine (TMB) (**Figure 41a**). Ambient oxygen oxidized β-D-glucose to D-gluconolactone, producing hydrogen peroxide which in turn oxidized TMB under peroxidase catalysis. **Figure 41b** displays the reflection spectra of the glucose sensors at different glucose concentrations (0 to 10.0 mmol L^{-1}). The reflection wavelength peak at 580 nm decreased upon increasing glucose concentration in artificial tears to 10.0 mmol L^{-1}. The calibration curve displayed in **Figure 41c** could be approximated with a linear fitting (R^2=0.93) and yielded a limit of detection of 1.1 mmolL^{-1}.

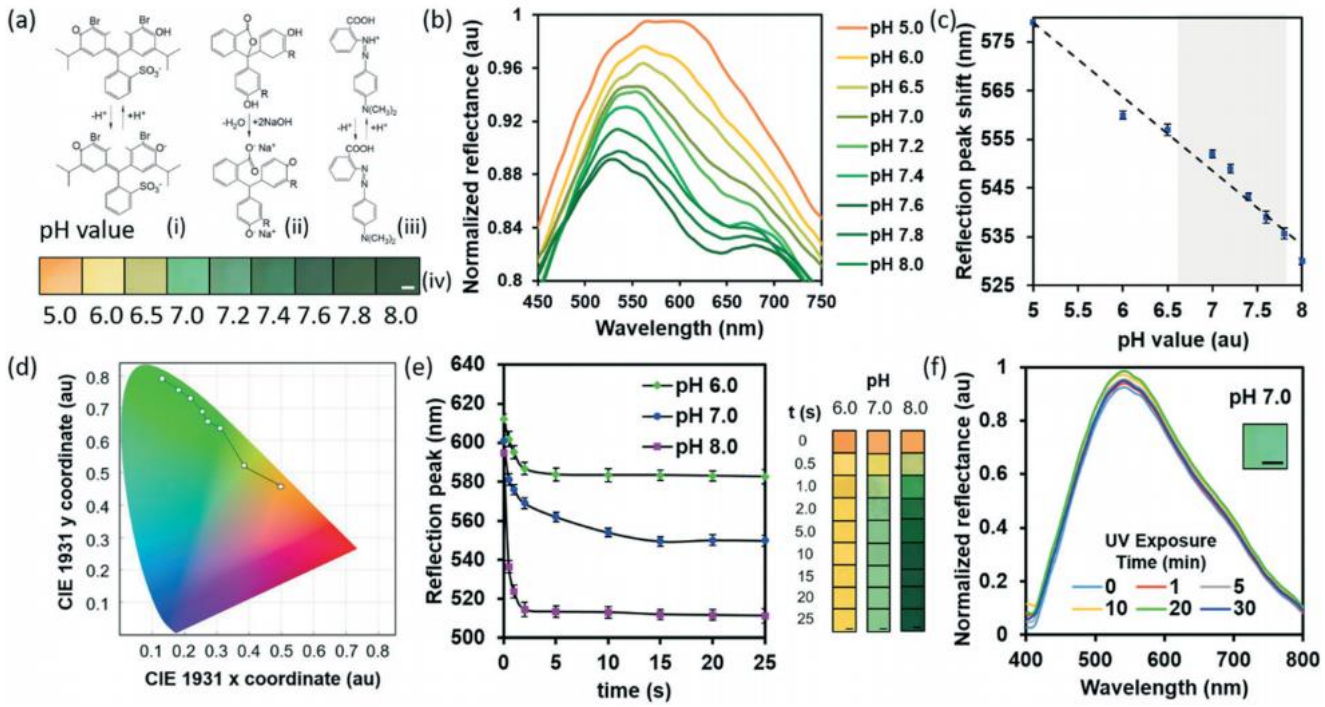

Figure 40. Characterization of the paper tear pH sensor over the range between 5.0 and 8.0. (a) shows the sensing mechanism of hydrogen ions; (i) Bromothymol Blue; (ii) Phenolphthalein; (iii) Methyl red; (iv) Photographs of the chromogenic sensors; scale bar: 1.5 mm. (b) Normalized reflection spectra between pH 5.0 to 8.0; (c) Calibration curve of the pH sensor (with the grey area highlighting the physiological range); (d) Red, green, blue (RGB) characterization of the pH sensor; (e) Influence of UV exposure from 0 to 30 minutes at pH 7.0; inset scale bar: 1.5 mm. (f) UV-dependent behavior of the pH sensor at pH 7.0; inset scale bar: 1.5 mm. (g) Time response of the pH sensor when exposed to a buffer solution at pH 7.0; inset scale bar: 1.5

mm. (h) Time-dependent reflection peak shift when exposed to a buffer solution at pH 7.0; (i) Chromaticity diagram of the pH sensor, displaying the color change from pH 5.0 to pH 8.0.

Figure 41d shows the RGB values of glucose sensors in the range 0 to 10.0 mmol L-1, imaged with a smartphone camera. The glucose sensor showed good stability when exposed to UV light up to 30 minutes, with a consistent reflection peak as well as color (**Figure 41e, f**). The response time of the glucose sensor was 15 s for a concentration of 2.0 mmol L^{-1} (**Figure 41g, h**), and a similar timing was measured for concentrations of 5.0 and 10.0 mM (**Appendix VIII**). **Figure 41i** shows the CIE 1931 chromaticity diagram of the calibration points corresponding to the color of the glucose sensor at different glucose concentrations.

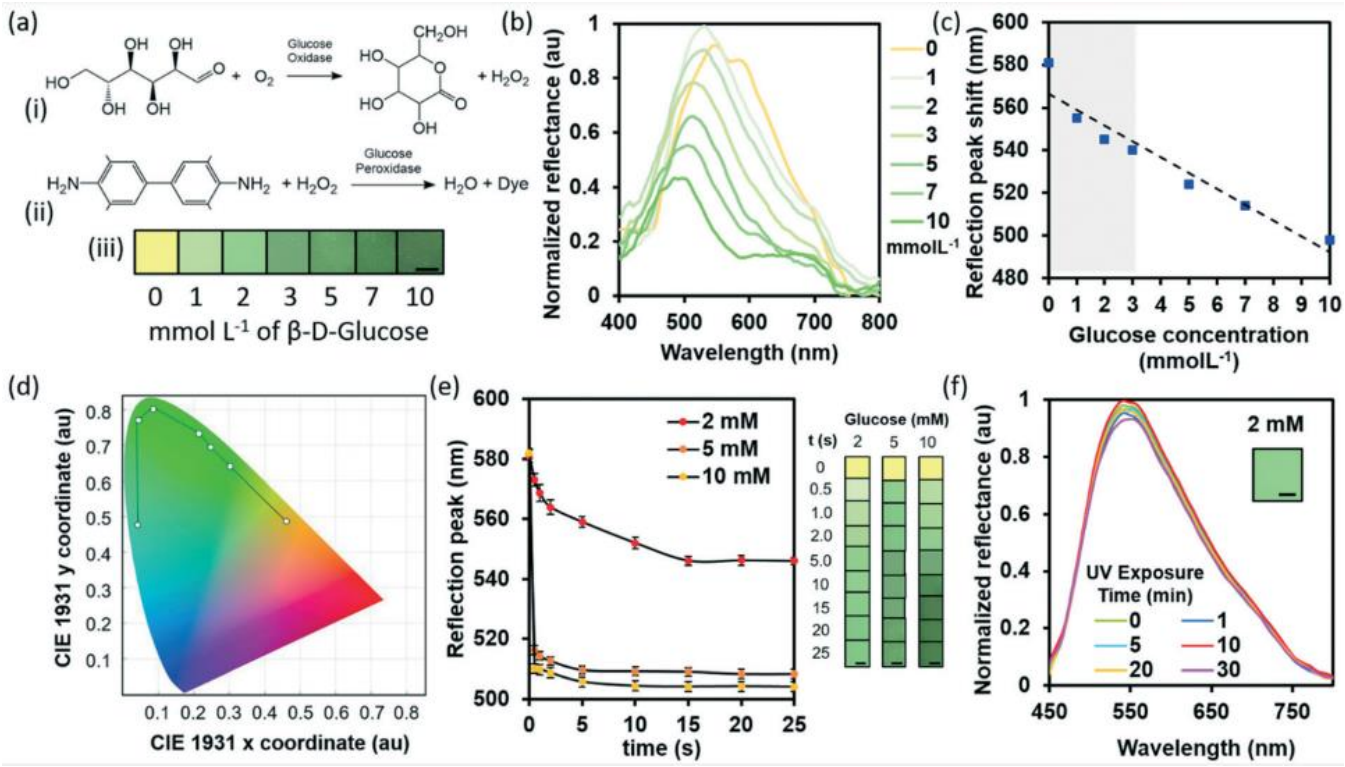

Figure 41. Characterization of the paper tear glucose sensor in the range between 0 and 10 mmolL^{-1}. (a) shows the sensing mechanism of β-D-glucose: (i) Formation of hydrogen peroxide from glucose and ambient oxygen, in the presence of glucose oxidase; (ii) 3,3',5,5'-Tetramethylbenzidin reacts with hydrogen peroxide in the presence of glucose peroxidase to form a dye. (iii) Photographs of the chromogenic sensor; scale bar: 1.5 mm. (b) Normalized reflection spectra of the glucose sensor at different concentrations; (c) Calibration curve of the glucose sensor (with the grey area highlighting the physiological range);

(d) RGB characterization of the glucose sensor. (e) Influence of UV exposure from 0 to 30 minutes at a glucose concentration of 2.0 mmolL^{-1}; inset scale bar: 1.5 mm. (f) UV-dependent behavior of the glucose sensor at a glucose concentration of 2.0 mmolL^{-1}; inset scale bar: 1.5 mm. (g) Time response of the glucose sensor when exposed to a 2.0 mM glucose solution; inset scale bar: 1.5 mm. (h) Time-dependent reflection peak shift when exposed to a 2.0 mM glucose solution. (i) Chromaticity diagram of the glucose sensor, displaying the color change with glucose concentration from 0 to 10.0 mmolL^{-1}.

Protein sensors detected bovine serum albumin (BSA) concentrations from 0 to 8.0 mg mL-1 (**Figure 42a**) and they were based on 3′,3″,5′,5″-tetrachlorophenol-3,4,5,6-tetrabromosulfophthalein, which interact with the proteins functional groups leading to protonation/deprotonation with consequent displacement of the π-electron system, exhibiting a color shift from yellow to green upon variations in protein concentration from 0 to 8.0 mg mL^{-1}. **Figure 42b** shows the absorbance spectra of protein sensors, displaying an increase in the reflection intensity upon variations in the protein concentration from 0.0 to 8.0 mg mL^{-1}, corresponding to increasingly brighter colors.

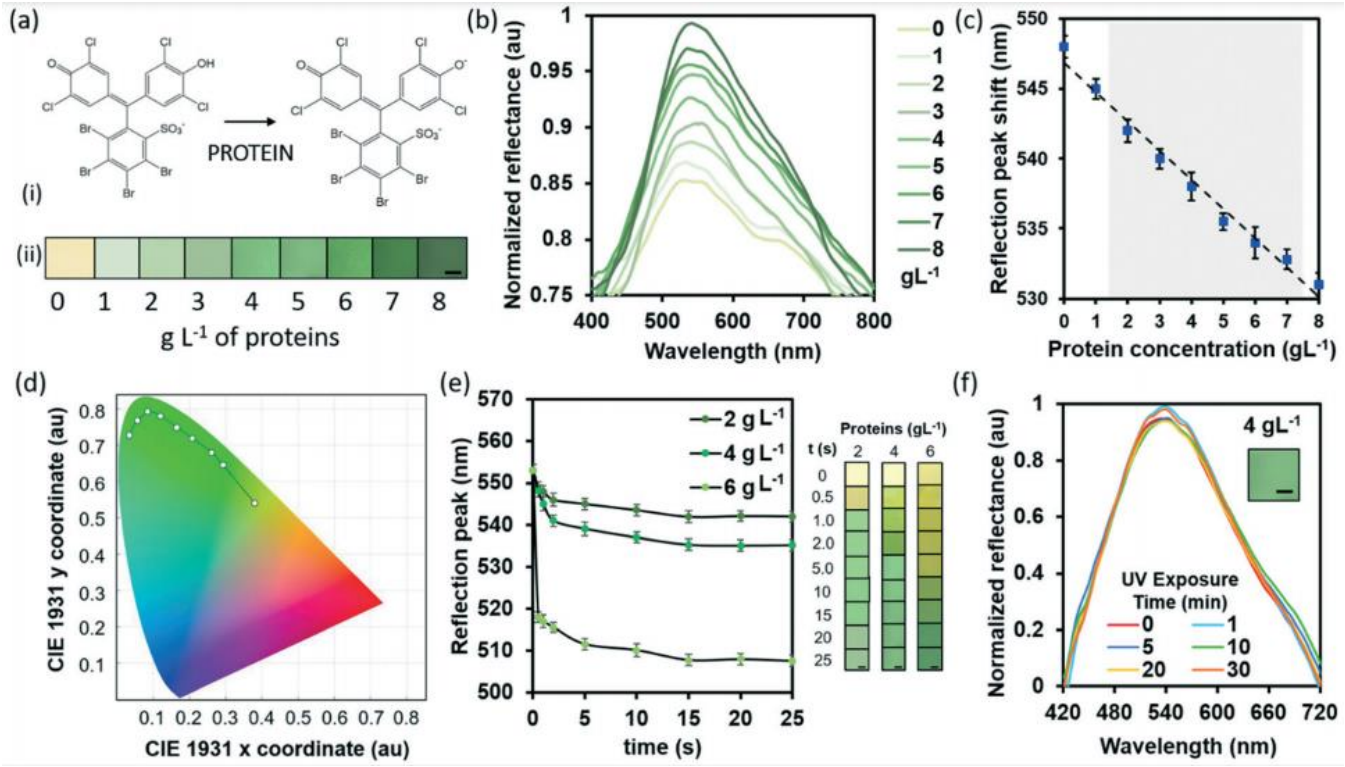

Figure 42. Characterization of the paper tear protein sensor in the range between 0 and 8.0 mg mL^{-1}. (a) Sensing mechanism of proteins; (i) 3',3",5',5"-tetrachlorphenol- 3,4,5,6- tetrabromsulfophthalein reacts with proteins to form an anion of the

compound; (ii) Photographs of the chromogenic sensor; scale bar: 1.5 mm. (b) Normalized reflection spectra of the protein sensor at different concentrations; (c) Calibration curve of the protein sensor (with the grey area highlighting the normal physiological range); (d) RGB characterization of the protein sensor; (e) Influence of UV exposure from 0 to 30 minutes at a protein concentration of 5.0 mg mL^{-1}; inset scale bar: 1.5 mm. (f) UV-dependent behavior of the glucose sensor at a protein concentration of 5.0 mg mL^{-1}; inset scale bar: 1.5 mm. (g) Time response of the glucose sensor when exposed to a 5.0 mg mL^{-1} protein solution. inset scale bar: 1.5 mm. (h) Time-dependent reflection peak shift when exposed to a 5.0 mg mL^{-1} protein solution; (i) Chromaticity diagram of the protein sensor, displaying the color change with protein concentration from 0 to 8.0 mg mL^{-1}.

The calibration curve is shown in **Figure 42c**. It was approximated by a linear fitting (R^2=0.98) and yielded a limit of detection of 1.1 mg mL^{-1}. The RGB characterization obtained with a smartphone camera is displayed in **Figure 42d**. The response time of the protein sensor at a concentration of 5.0 mg mL^{-1} was 15 s (**Figure 42e, f**), comparable with the response time at concentrations of 2.0 mg mL^{-1} and 7.0 mg mL^{-1} (**Appendix VIII**). Exposure to UV light at 355 nm showed good stability and reliability of the sensor up to 30 minutes (**Figure 42g, h**). **Figure 42i** displays the CIE 1931 chromaticity plot of the protein sensors, which displayed the discrete calibration points obtained by measuring the color change with variation in protein concentration.

L-ascorbic acid sensors (**Figure 43**) were based on the reduction of phosphomolybdic acid to phosphomolybdenum, to produce a color shift from yellow to green and blue, in the presence of 0-1.0 g L^{-1} of ascorbic acid (**Figure 43a**). **Figure 43b** shows the reflection spectra of the ascorbic acid sensor, with a calibration curve that could be approximated with a linear fitting (R^2=0.97) in the physiological range 50.0 -300.0 mg L^{-1} (**Figure 43c**), from which a limit of detection of 31.7 mg L^{-1} was calculated. The smartphone RGB characterization of the colorimetric response is presented in **Figure 43d**. No degradation of the sensors was observed after UV exposure for up to 30 minutes (**Figure 43e, f**). Ascorbic acid sensors had a time response of 30 s at a concentration of 200 mg L^{-1} (**Figure 43g, h**), and no variations in the time response can be observed at concentrations of 500 and 700 mg L^{-1} (**Appendix VIII**). The CIE

1931 chromaticity diagram in **Figure 43i** displays the calibration points, i.e. the color coordinates corresponding to the sensor at nitrites concentrations ranging from 0 to 160 µmol L^{-1}.

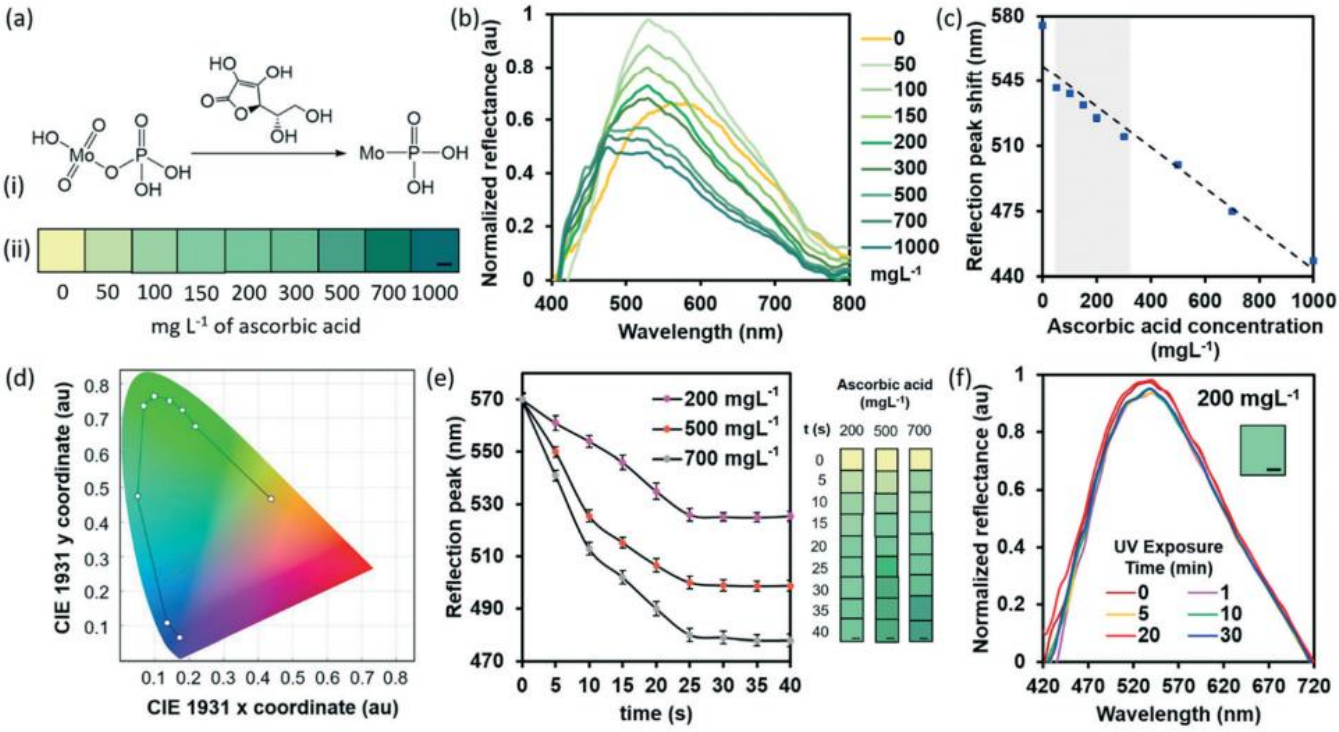

Figure 43. Characterization of the paper tear L-ascorbic acid sensor in the range between 0 and 1.0 g L^{-1}. (a) Sensing mechanism of L-ascorbic acid: (i) Reduction of phosphomolybdic acid to phosphomolybdenum in the presence of L-Ascorbic acid; (ii) Photographs of the chromogenic sensor; scale bar: 1.5 mm. (b) Normalized reflection spectra of the L-ascorbic acid sensor at different concentrations: (c) Calibration curve of the L-ascorbic acid sensor (with grey area highlighting the physiological range); (d) RGB characterization of the L-ascorbic acid sensor; (e) Influence of UV exposure from 0 to 30 minutes at an L-ascorbic acid concentration of 0.2 g L^{-1}; inset scale bar: 1.5 mm. (f) UV-dependent behavior of the L-ascorbic acid sensor at a protein concentration of 0.2 g L^{-1}; inset scale bar: 1.5 mm. (g) Time response of the L-ascorbic acid sensor when exposed to a 0.2 g L^{-1} L-ascorbic acid solution; inset scale bar: 1.5 mm. (h) Time-dependent reflection peak shift when exposed to a 0.2 g L^{-1} L-ascorbic acid solution; (i) Chromaticity diagram of the L-ascorbic acid sensor, displaying the color change with L-ascorbic acid concentration from 0 to 1 gL^{-1}.

Tear nitrite sensors were based on the reaction of nitrite ions with sulfanilamide to form a diazonium salt, which further binds N-(1-naphthyl)- ethylenediamine dihydochloride (**Figure 44a**), to produce a pink azo dye, yielding a color shift from light yellow to fuchsia upon changing the concentration of nitrites from 0

to 160.0 µmol L^{-1} (Figure 5a, iii). The absorbance peak of the dye is measured at 528 nm. **Figure 44b** shows the reflection spectra of tear nitrite sensors, and **Figure 44c** depicts the calibration curve with linear fitting (R^2=0.92) in the range 80.0 -140.0 µmol L^{-1}, from which a LOD of 19.5 µmol L^{-1} was calculated. The smartphone RGB characterization of the colorimetric response is presented in **Figure 44d**. The nitrite sensor showed a reliable behavior after up to 30 minutes of UV exposure (**Figure 44e,f**) and had a time response of 25 s at a nitrites concentration of 140.0 µmol L^{-1} (**Figure 44g,h**). Consistent time responses were observed at concentrations of 40.0 and 100.0 µmol L^{-1} (**Appendix VIII**). The CIE 1931 chromaticity diagram in **Figure 44i** displays the calibration points, i.e. the color coordinates corresponding to the sensor at nitrites concentrations ranging from 0 to 160.0 µmol L^{-1}.

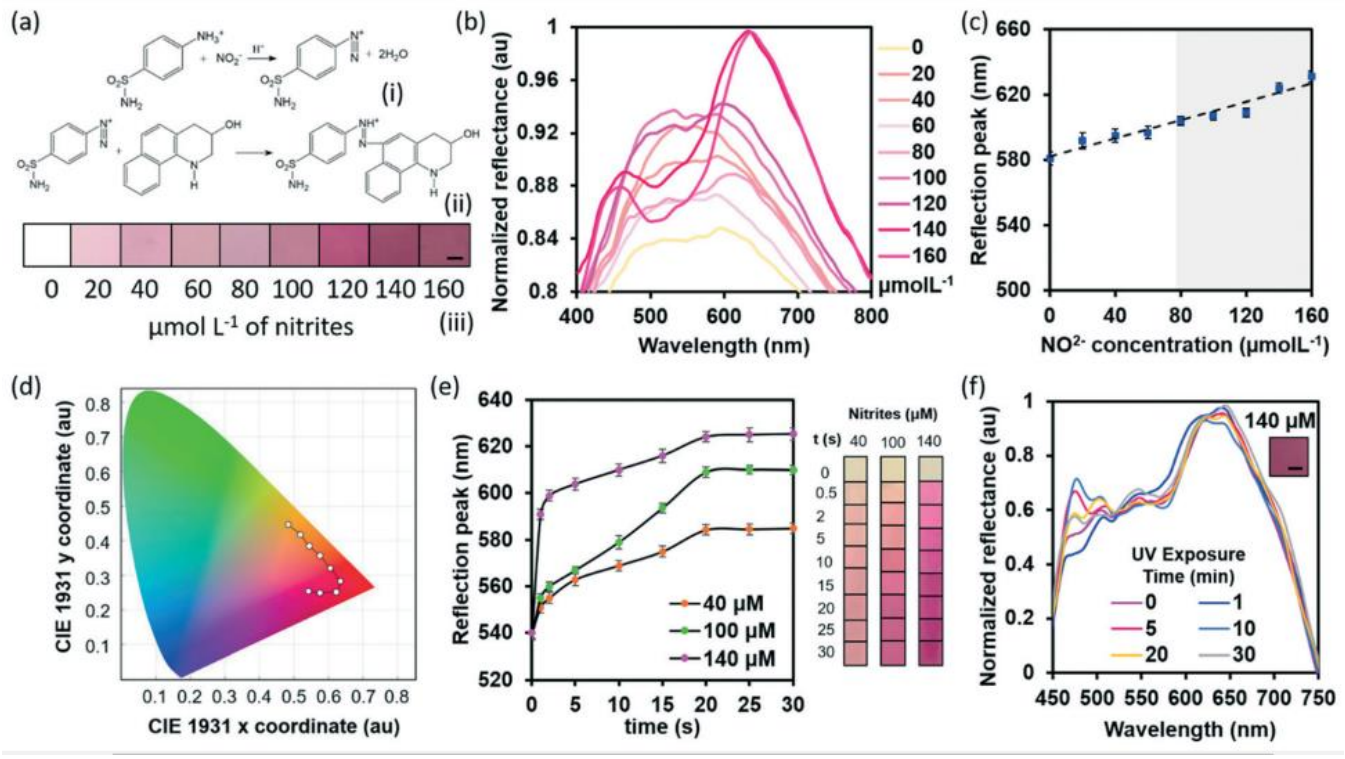

Figure 44. Characterization of the paper tear nitrite sensor in the range between 0 and 160 µmolL^{-1}. (a) Sensing mechanism of nitrites: (i) Nitrite ions react with sulfanilamide to form a diazonium salt; (ii) the diazonium salt binds N-(1-naphthyl)-ethylenediamine dihydochloride, producing a pink dye; (iii) Photographs of the chromogenic sensor; scale bar: 1.5 mm. (b) Normalized reflection spectra of the nitrite sensor at different concentrations; (c) Calibration curve of the nitrite sensor (with the grey area highlighting the physiological range); (d) RGB characterization of the nitrite sensor; (e) Influence of UV exposure from 0 to 30 minutes at a nitrite concentration of 140.0 µmolL^{-1}; inset scale bar: 1.5 mm. (f) UV-dependent behavior of the

glucose sensor at a nitrite concentration of 140.0 μmolL^{-1}; inset scale bar: 1.5 mm. (g) Time response of the nitrite sensor when exposed to a 140.0 μmolL^{-1} nitrite solution; inset scale bar: 1.5 mm. (h) Time-dependent reflection peak shift of the sensor when exposed to a 140.0 μmolL^{-1} nitrite solution; (i) Chromaticity diagram of the nitrite sensor, displaying the color change with nitrite concentration from 0 to 160.0 μmolL^{-1}.

Paper microfluidic paper "chips" with different geometries were obtained by laser cutting and an iterative process of testing resulted in an optimized design, able to host fluid amounts of 1-2 μL, with a wetting time of 1 to 2 s, as shown in **Figure 45a** (where an aliquot of 10.0 mM fluorescein solution was injected to quantify flow characteristics). These paper-based chemical sensors were embedded in the microfluidic system which were then sealed in place using a laboratory-made poly-HEMA contact lens, using acrylate chemical bonding (**Appendix VIII**). Chemical sensors integrated into contact lenses were characterized and compared to free-standing sensors (**Figure 45b**). Consistent results were observed, with standard variations in the reflection peak of 1.7 nm for the pH sensor (**Figure 45b, i**), 2.1 nm for the ascorbic acid sensor (**Figure 45b, ii**), 2.3 nm for the glucose sensor (**Figure 45b, iii**), 1.1 nm for the nitrite sensor (**Figure 45b, iv**), and 2.0 nm for the protein sensor (**Figure 45b, v**).

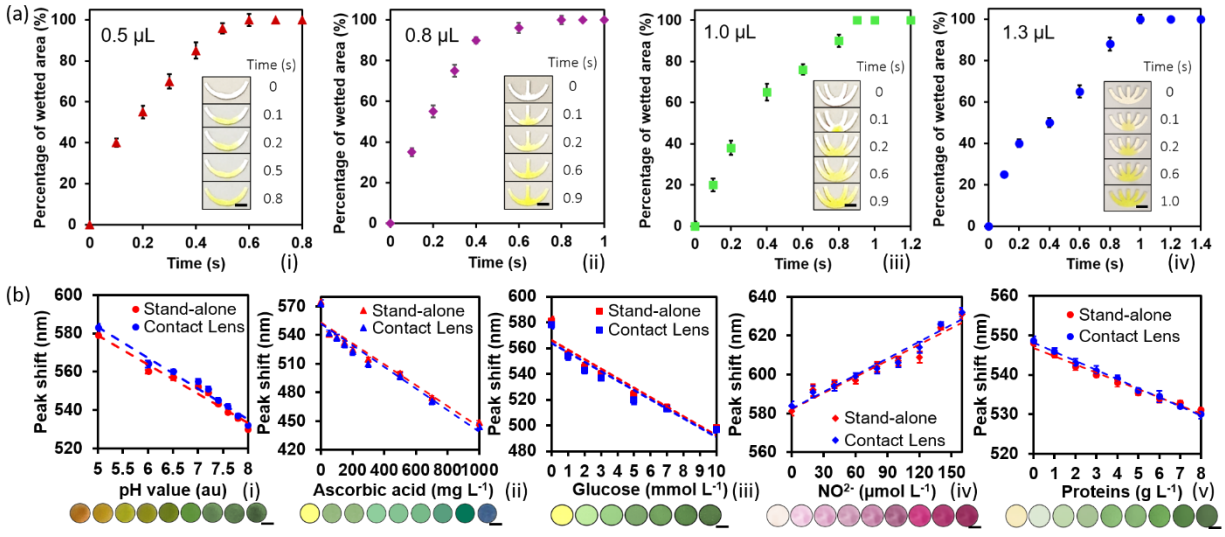

Figure 45. Capillary flow within the paper based microfluidic device and characterization of the tear fluid sensors embedded in the contact lenses. (a) Time characterization of capillary flow in paper based microchannels: (i) Two-branches channel, filled in 0.6 s with 0.5 μL of fluorescein solution: (ii) Three-branches channel, filled in 0.8 s with 0.8 μL of fluorescein solution;

(iii) Four-branches channel, filled in 0.9 s with 1.0 μL of fluorescein solution: (iv) Five-branches channel, filled in 1.0 s with 1.3 μL of fluorescein solution. The scale bar of the insets is 3.0 mm. (b) Comparison of the reflection peak shift between the stand-alone and the contact lens-embedded sensor for (i) the pH sensor in the range of 5.0 to 8.0; (ii) the ascorbic acid sensor, in the range 0 to 1.0 g L^{-1}; (iii) the glucose sensor, in the range 0 to 10.0 mmolL^{-1}; (iv) the nitrite sensor, in the range 0 to 160.0 μmolL^{-1}; and (v) the protein sensor in the range 0 to 8.0 mg mL^{-1}. The scale bar of the insets is 1.5 mm.

A bespoke 'Tears Diagnostics' smartphone application prototype was designed using Visual Studio tools Mobile App Net development in Xamarin forms. A customized readout device was designed which comprised a metallic black box with a front opening for the smartphone camera (**Figure 46a**). **Figure 46b** displays the ease of operation for the readout device. An image was either obtained before or whilst running the app. An example of an image to processes is displayed in **Figure 46c**. The use of a readout device allows for a higher readout precision, by minimizing the noise contribution given by ambient light fluctuations. The sensors were imaged under smartphone light only, at the same, normal angle of irradiation (90°). An example of readout is illustrated in **Figure 46d-k**, displaying the working principle of Tears Diagnostics app. Upon opening the app, the user is asked to insert their name (**Figure 46d**), which is accepted (**Figure 46e**) and the main menu of the app pops up, where the user can select to take a measurement, update personal information, consult the reference values, or check their medical records (**Figure 46f**). If "take measurement" was clicked, the user was asked to either take or upload a photo (**Figure 46g**). In this example, the photograph of the contact lens on an ex-vivo eye model is uploaded. The user was asked to select the region of interest, by simply drawing a circle around the sensor to be measured and indicating the analyte under measurement (**Figure 46h**). In this case, the pH sensor at the far left was selected. The app read the color and outputs a pH value of 7.2 (**Figure 46i**), based on the discrete calibration points defined in the nearest neighbor model. This method had a 100% success on the discrete concentration values defined by the developer, and it can be updated if new data points are inserted. **Figure 46j** and **Figure 46k** display the "medical record" and "reference values" windows. The medical record can be tracked in a calendar and sent to the healthcare professional. The reference values can be compared to a selected measurement. **Appendix V** presents another application of analytes-

sensitive dyes as smart tattoo ink. An alternative technology to functionalize a contact lens for pH sensing is presented in **Appendix VI**.

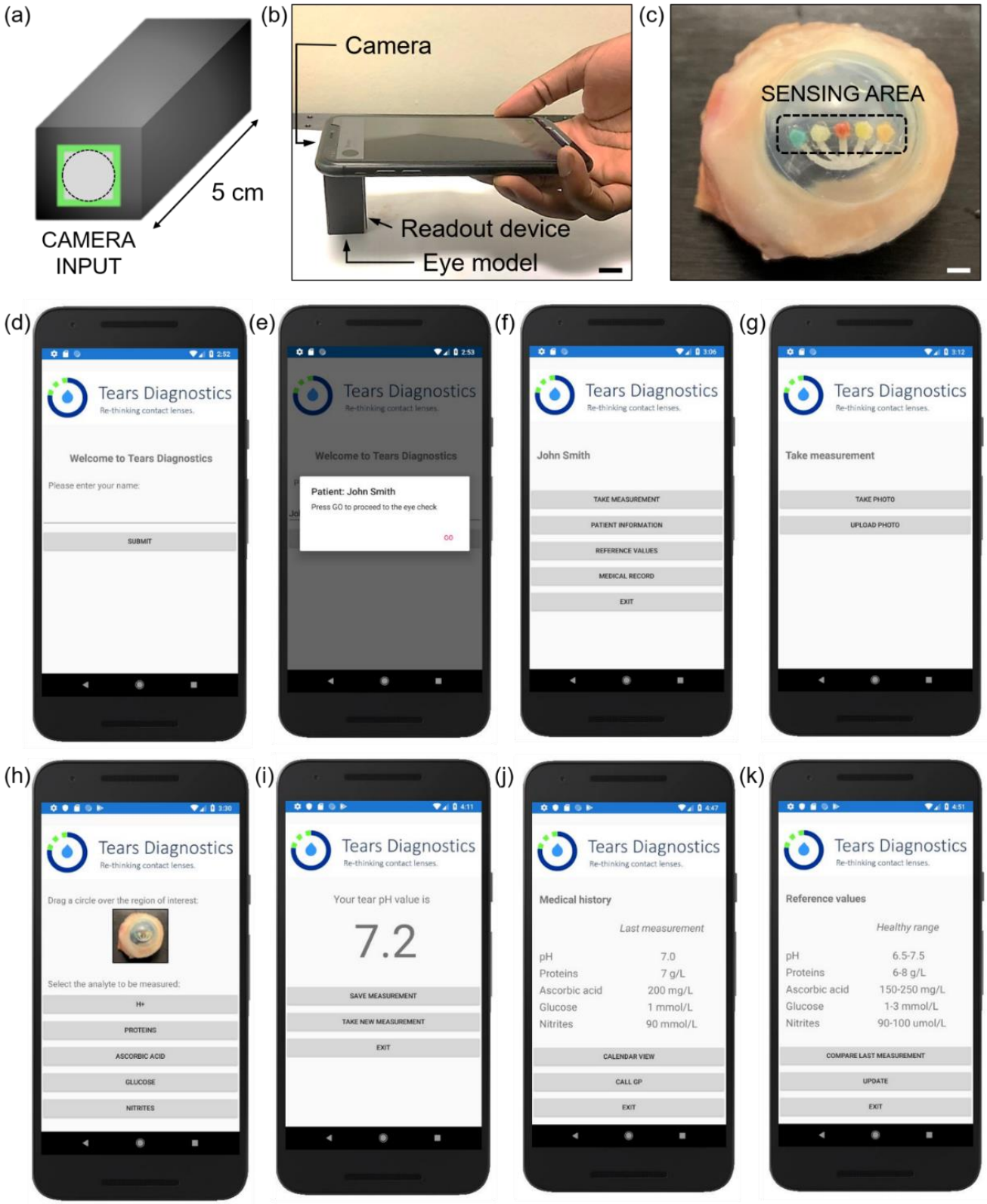

Figure 46. Smartphone readouts of contact lens sensors. (a) Schematic of the readout device; (b) Readout of a contact lens sensor exposed to artificial tear fluid on an *ex vivo* eye model; scale bar: 1.5 cm. (c) Photograph of the contact lens sensor inside the readout device during a sustained artificial tear fluid flow on an *ex vivo* model; scale bar: 2.5 mm. (d-k) Smartphone readouts; (d) The welcome page of the app; (e) The name of the patient is entered; (f) showing the App menu; (g) The take measurements section where the patient is asked to take or to upload a photo of the sensor; (h) The region of interest (ROI) and the corresponding analyte to be measured are selected; (i) The App outputs the concentration value associated with the analyte's color in the ROI; (j) Medical record section of the app, where the previous measurements may be saved; (k) Reference values section of the App. The healthy ranges of biomarkers were displayed and were compared to measurements. The response could be sent to a clinician or healthcare provider such as a General Practitioner (GP).

5.4. Conclusions

Colorimetric sensors were synthetized before being deposited on paper, and then embedded as a paper microfluidic sensor within a commercial laser-inscribed acrylate contact lens. The microfluidic chip was sealed by chemically bonding a laboratory-made poly-HEMA contact lens. The paper sensors detected changes in the concentration of hydrogen ions (pH), ascorbic acid, glucose, proteins, and nitrite ions in 2 µL of artificial tear fluid within 35 s. The microfluidic chip could be filled in 1-2 s. All dye based colorimetric sensors showed good stability when investigated through UV exposure for up to 30 minutes. The smartphone application (App) was optimized for the multiplexed detection of pH, glucose, ascorbic acid, proteins, and nitrites concentrations by comparing the chromatic variations of the biosensors to its calibration points in a model tear fluid. The advantage of using paper-based sensors relied on the feasibility to operate the device without calibration, based on the eye color. The readout device acted as a *black box* in which the smartphone light acted as the only light source, standardizing the measurements by removing the noise and background contributions arising from the variation of saturation and brightness of colors under different lighting conditions. Sensors used in this study are not associated with toxicity concerns, due to their low concentrations and the fact that they are retained in a paper matrix, sealed in the lens. In future, the sensor feasibility should be assessed in *in vivo* samples and in *in vitro* animal models to understand the immunogenicity and foreign body response. In addition, we will explore

the applications of the sensors to the detection of electrolytes, cytokines, pathogenic microorganisms, and other biomarkers, which may have possible applications in medical diagnostics to monitor a broad range of ocular conditions.

5.5. References

1. D. C. Christodouleas, B. Kaur and P. Chorti, *ACS Cent Sci*, 2018, **4**, 1600-1616.
2. M. Elsherif, R. Moreddu, M. U. Hassan, A. K. Yetisen and H. Butt, *Lab Chip*, 2019, **19**, 2060-2070.
3. R. Moreddu, M. Elsherif, H. Butt, D. Vigolo and A. K. Yetisen, *RSC Advances*, 2019, **9**, 11433-11442.
4. A. K. Yetisen, R. Moreddu, S. Seifi, N. Jiang, K. Vega, X. Dong, J. Dong, H. Butt, M. Jakobi, M. Elsner and A. W. Koch, *Angew Chem Int Ed Engl*, 2019, DOI: 10.1002/anie.201904416.
5. X. Yang, X. Pan, J. Blyth and C. R. Lowe, *Biosens Bioelectron*, 2008, **23**, 899-905.
6. M. E. Stern, R. W. Beuerman, R. I. Fox, J. Gao, A. K. Mircheff and S. C. Pflugfelder, *Cornea*, 1998, **17**, 584-589.
7. R. Moreddu, D. Vigolo and A. K. Yetisen, *Adv Healthc Mater*, 2019, DOI: 10.1002/adhm.201900368, e1900368.
8. R. Ihnatko, U. Eden, N. Lagali, A. Dellby and P. Fagerholm, *J Proteomics*, 2013, **94**, 78-88.
9. J. Soria, J. A. Duran, J. Etxebarria, J. Merayo, N. Gonzalez, R. Reigada, I. Garcia, A. Acera and T. Suarez, *J Proteomics*, 2013, **78**, 94-112.
10. S. J. Venkata, A. Narayanasamy, V. Srinivasan, G. K. Iyer, R. Sivaramakrishnan, M. Subramanian and R. Mahadevan, *Indian J Ophthalmol*, 2009, **57**, 289-292.
11. N. A. Delamere, *Subcell Biochem*, 1996, **25**, 313-329.
12. R. N. Williams and C. A. Paterson, *Exp Eye Res*, 1986, **42**, 211-218.
13. S. Saika, K. Uenoyama, K. Hiroi, H. Tanioka, K. Takase and M. Hikita, *Graefes Arch Clin Exp Ophthalmol*, 1993, **231**, 221-227.
14. N. Kasetsuwan, F. M. Wu, F. Hsieh, D. Sanchez and P. J. McDonnell, *Arch Ophthalmol*, 1999, **117**, 649-652.
15. M. B. Abelson, I. J. Udell and J. H. Weston, *Arch Ophthalmol-Chic*, 1981, **99**, 301-301.
16. L. G. Carney, T. F. Mauger and R. M. Hill, *Acta Ophthalmologica*, 1990, **68**, 75-79.
17. M. B. Abelson, A. A. Sadun, I. J. Udell and J. H. Weston, *American Journal of Ophthalmology*, 1980, **90**, 866-869.
18. J. E. M. Thygesen and O. L. Jensen, *Acta Ophthalmologica*, 1987, **65**, 134-136.
19. G. E. K. Mirza, S.; Er, M.; Güngörmüs, N.; Karaküçükb, I.; Saraymen, R., *Ophthalmic research*, 2001, **33**, 48-51.
20. J. D. Lane, D. M. Krumholz, R. A. Sack and C. Morris, *Current Eye Research*, 2006, **31**, 895-901.
21. J. Zhang, W. Hodge, C. Hutnick and X. Wang, *J Diabetes Sci Technol*, 2011, **5**, 166-172.
22. C. Chen, Z.-Q. Dong, J.-H. Shen, H.-W. Chen, Y.-H. Zhu and Z.-G. Zhu, *ACS Omega*, 2018, **3**, 3211-3217.
23. J. L. Ruan, C. Chen, J. H. Shen, X. L. Zhao, S. H. Qian and Z. G. Zhu, *Polymers (Basel)*, 2017, **9**, 125.
24. V. L. Alexeev, S. Das, D. N. Finegold and S. A. Asher, *Clin Chem*, 2004, **50**, 2353-2360.
25. S. Manju, P. R. Hari and K. Sreenivasan, *Biosens Bioelectron*, 2010, **26**, 894-897.
26. M. Elsherif, M. U. Hassan, A. K. Yetisen and H. Butt, *ACS Nano*, 2018, **12**, 5452-5462.
27. H. Yao, A. J. Shum, M. Cowan, I. Lahdesmaki and B. A. Parviz, *Biosens Bioelectron*, 2011, **26**, 3290-3296.
28. H. Y. Yu-Te Liao, Andrew Lingley, Babak Parviz, Brian P. Otis, *IEEE Journal of Solid-State Circuits* 2012, **47**.
29. H. Yao, Y. Liao, A. R. Lingley, A. Afanasiev, I. Lahdesmaki, B. P. Otis and B. A. Parviz, *Journal of Micromechanics and Microengineering*, 2012, **22**.
30. S. Iguchi, H. Kudo, T. Saito, M. Ogawa, H. Saito, K. Otsuka, A. Funakubo and K. Mitsubayashi, *Biomedical Microdevices*, 2007, **9**, 603-609.
31. R. S. Riaz, M. Elsherif, R. Moreddu, I. Rashid, M. U. Hassan, A. K. Yetisen and H. Butt, *ACS Omega*, 2019, DOI: 10.1021/acsomega.9b02638.

32. J. Park, J. Kim, S. Y. Kim, W. H. Cheong, J. Jang, Y. G. Park, K. Na, Y. T. Kim, J. H. Heo, C. Y. Lee, J. H. Lee, F. Bien and J. U. Park, *Sci Adv*, 2018, **4**, eaap9841.
33. S. Lee, I. Jo, S. Kang, B. Jang, J. Moon, J. B. Park, S. Lee, S. Rho, Y. Kim and B. H. Hong, *ACS Nano*, 2017, **11**, 5318-5324.
34. S. Kaur, Y. J. Kim, H. Milton, D. Mistry, I. M. Syed, J. Bailey, K. S. Novoselov, J. C. Jones, P. B. Morgan, J. Clamp and H. F. Gleeson, *Opt Express*, 2016, **24**, 8782-8787.
35. C. M. Haggerty and J. R. Larke, *Ophthal Physl Opt*, 1982, **2**, 187-191.

Chapter 6

Conclusions and future work

Contact lenses are potential low-cost platforms which may be used either to replace or to aid existing ophthalmic technologies. Techniques for their development were proposed in this thesis, and some of their applications were demonstrated.

Laser inscription is a facile and potentially scalable method to engrave microstructures into commercial contact lenses. Femtosecond lasers allow to achieve higher resolutions compared with long pulse lasers. Microstructures were inscribed in the form of sensing cavities to embed surface sensors, and as microfluidic element to build more complex, organized fluid processing networks. Cholesteric, thermochromic liquid crystals were integrated into sensing cavities for ocular temperature monitoring via rigid contact lenses. Further work may be focused on improving the resolution of the contact lens sensing medium. The cholesteric material used in this thesis has been reported to have a sensitivity of 0.1 °C, which can be further increased by acting on the readout method. For example, a machine learning algorithm may be included to discriminate between nearly identical color shades. Simplifying ocular temperature measurement may help detecting and monitoring ocular infections.

Microfluidic networks were utilized to demonstrate multiple proof-of-concept sensors. An alternative method for tear fluid sampling and tear volume measurement was proposed, based on a contact lens featuring a spiral microfluidic channel. This technique may overcome the limitations encountered with current technologies, primarily contamination risks and sensitivity. The tear volume sensor configuration may be improved and modelled based on the needs by tuning its geometrical features. For example, a microfluidic valve may be added to delay or speed up tear fluid sampling based on the blink rate. The channel may be kept hydrophobic, by skipping the hydrophilization step, and the eye blink may be used as the fluid pump. Reservoirs may be added to the geometry to allow tear sampling at different times of

the day. Microfluidic elements were also employed to build sensing networks comprising a micro-splitter and multiple cavities, where liquid or paper colorimetric sensors were embedded. This approach allowed to detect and semi-quantify uric acid, glucose, proteins, nitrites, ascorbic acid, and hydrogen ions concentrations in model tears, both in capillary flow within hydrophilic polymeric channels and in paper channels integrated into laser-ablated lenses. Such devices may be used to aid the diagnosis of ocular conditions, including keratopathies, uveitis, and dry eye, as well as for general ocular health screening.

The possibility of integrating sensing functionalities into flexible, soft lenses, was demonstrated with PDMS surface nanopatterning *via* electron beam lithography and replica molding. Stretchable nanobuttons were characterized as tunable diffraction gratings under applied stimuli in the ocular pressure physiological range. Continuous ocular pressure monitoring is desirable in glaucomatous patients with ocular hypertension.

Table 12. Key future improvements for the proposed devices.

Device	Future Improvements
Tear volume sensor	• Evaluation of the mechanical stability of laser-inscribed contact lenses before and after wearing; • Standardizing the correlation between Schirmer's test and tear volume sensor; • Comparing different channel geometries to select the best trade-off between accuracy and efficiency.
Ocular temperature monitoring	• Reducing the size of the microcavities whilst preserving a high-quality signal; • Evaluating the in vitro cytotoxicity of the sensing materials; • Standardize the readout method under different environmental lighting.
Ocular pressure monitoring	• Incorporating the nanostructures within the commercial contact lens mould to reduce inter-device variability and shorten the fabrication process to a single step; • Evaluating the repeatability of the color change of the diffraction grating; • Evaluating the impact of the iris color variation on the readout.
Tear fluid screening	• Testing the biocompatibility of the sensing materials and, if needed, developing novel detection media; • Optimize the functionality of the devices by introducing the methods described in Chapter 2 (e.g. fluidic valves and reservoirs). • Evaluating the impact of roughness on ocular impairment.

More generally, contact lens medical technology presents some limitations:

- Smart contact lenses may be a comfortable solution for contact lens wearers. However, they require an effort from the part of the population which does not use them. In those cases, continuous monitoring may be difficult to exploit, although they could still be employed by ophthalmologists for one-off measurements. Some of the technologies proposed in this work were based on the use of rigid contact lenses, which as of today are reserved to a niche of ophthalmic patients and are not used for vision correction. However, enhanced contact lenses for futuristic applications are predicted to be rigid lenses in other fields, such as lenses that can integrate displays and antennas.
- Contact lenses are wearable devices used in direct contact with the corneal tissue. This implies that their go-to-market route is more complex than it is for other wearables, such as fitness trackers. They require years of testing, *in vitro* and *in vivo*, before being authorized. As a result, the choice of materials would be limited to non-toxic and highly biocompatible sensing compounds. In the context of this thesis, the devices which would be more suitable for a real-case scenario are the pressure-sensitive contact lens and the microfluidic lens for tear volume measurement. Both approaches are (or can be developed as) of a subtractive nature, taking out the limitation of introducing external materials into the eye.

The microfluidic approach, despite being further from being applied in medical settings, has substantial potential for different applications. Future work in that regard may be focused on the optimization of microfluidic geometries for the purpose of:

- Limiting reflow and backflow along microfluidic networks, to avoid possible leakage of sensing media;
- Being suitable to target continuous monitoring of tear analytes, by considering external perturbations of the system, such as eye blinking, tear film production rate, viscosity, waste handing, and re-usability of the sensing materials;

- Achieving a scalable manufacturing roadmap to produce enclosed microfluidic networks. This could be accomplished by incorporating a laser inscription and a bonding step into the rigid contact lens manufacture process.

Further investigations are needed in the biological front to assess the reliability of tear fluid-based diagnostics, to investigate on the correlations between tear fluid biomarkers concentrations and their presence in other body fluids, and to evaluate the consistency in the significance of tear biomarkers in healthy and unhealthy individuals.

Appendix I

MATLAB Code for Computational Femtosecond Laser Ablation

The algorithm for laser ablation simulation is included below.

```
close all
%Constants
%Specific heat of PMMA: 1418 J/kg/K
%Thermal diffusivity of PMMA: 0.115e-6 m2/s
%Absorbance of PMMA: 50200 1/m
%Density PMMA: 1180 Kg/m3
%Width beam output: 1 mm
%focal point: 3-5 cm
%Power: 5W
%Speed: 10 mm/s
%Frequency of delivering pulses: 50 Khz
%Beam diameter: 35 um
%Pulse duration: 390 fs
%Wavelength: 1030 nm
%Hatch distance: 20 um

%thermal diffusivity hydrogel SI
diffcoefh=1e-5;

%window size in SI
wsx=3e-4;
wsy=3e-4;
wsz=wsx;

%Absorbance in SI
alfah=30000;
alfah=10000;
alfaa=0;

%Air interface
interface=0.5e-4; %top offset from laser beam

%Specific heat
%PMMA specific heat
cp=1400;

%Ambient temperature
temp0=25;

%Ablation temperature in celcius
tempab=200;

%Density SI Kg/m3
densityh=1180; %PMMA density
```

```
%Speed SI m/s
speed=10e-3;

%beam intensity (W)
intb=2.5;

%resolution in pixels x and y
nx=201;
ny=round(nx*wsy/wsx);
nz=round(nx*wsz/wsx);

[meshx,meshy]=meshgrid(linspace(-wsx/2,wsx/2,nx),linspace(0,-wsy,ny)+interface);

%full width half maximum beam in SI
pe2=35e-6; %beam spot size
fwhm=pe2/1.7;

%beamwaist
sigmab=fwhm/2*sqrt(2*log(2));

%pixel size x and y
psx=wsx/(nx-1);
psy=wsy/(ny-1);
psz=wsz/(nz-1);

%time step (this defines the chart: black area + beam area)
pt=psz/speed;

maskm=zeros(ny,nx);

pm=interface/wsx;

maskm(floor(pm*ny)+1:end,1:end)=1+maskm(floor(pm*ny)+1:end,1:end);

[meshx,meshz]=meshgrid(linspace(-wsx/2,wsx/2,nx),linspace(-wsz/2,wsz/2,nx));
intgauss2=intb/100*exp(-(meshx.^2+meshz.^2)/(2*sigmab^2))/(2*pi()*sigmab^2);

heatmc=0;

tempc=temp0;
maskmt=maskm;

for zp=-wsz/2:psx:wsz/2

    if round(1+zp/psz+(nz-1)/2)>=1 && round(1+zp/psz+(nz-1)/2)<=nz
        intgaussy=intgauss2(round(1+zp/psz+(nz-1)/2),:);
    else
        intgaussy=0*intgauss2(1,:);
    end

    intgaussy2=repmat(intgaussy,ny,1);

    alfam=(alfah*maskmt)+(alfaa*(1-maskmt));
    topti=10.^(-alfam.*psy);
    intm=cumprod(topti).*intgaussy2;
    heatipt=log(10)*alfam.*intm;
```

```
    heatmi=heatipt*pt;
    heatmc=heatmc+heatmi;


    dtempc=heatmc/ch/densityh;
    dtempi=heatmi/ch/densityh;
    dtemp=dtempc;
    tempc=temp0+dtemp;
    maskmt=maskmt.*double(tempc<tempab);
    heatmc=heatmc.*maskmt;

end

    dtemp=heatmc/ch/densityh;
    tempc=temp0+dtemp;

%Plot
figure(1)
surf(meshx*1e6,meshy*1e6,tempc,'edgecolor','none') %this defines plot area +
parameter
colormap(bone);
view(2)
axis equal

% ablated mass in kg
abmass=densityh*sum(sum(maskm-maskmt))*psx*psy*psz
```

Appendix II

Supplementary Information on Femtosecond Laser Ablation of Contact Lenses

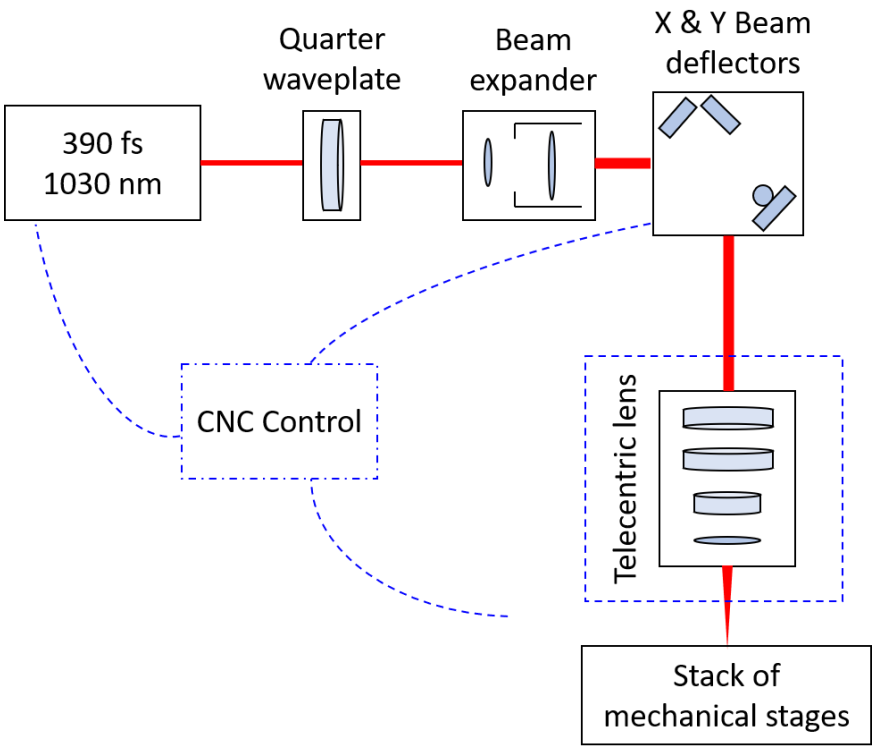

Figure A1. 2D schematic of the laser setup with components.

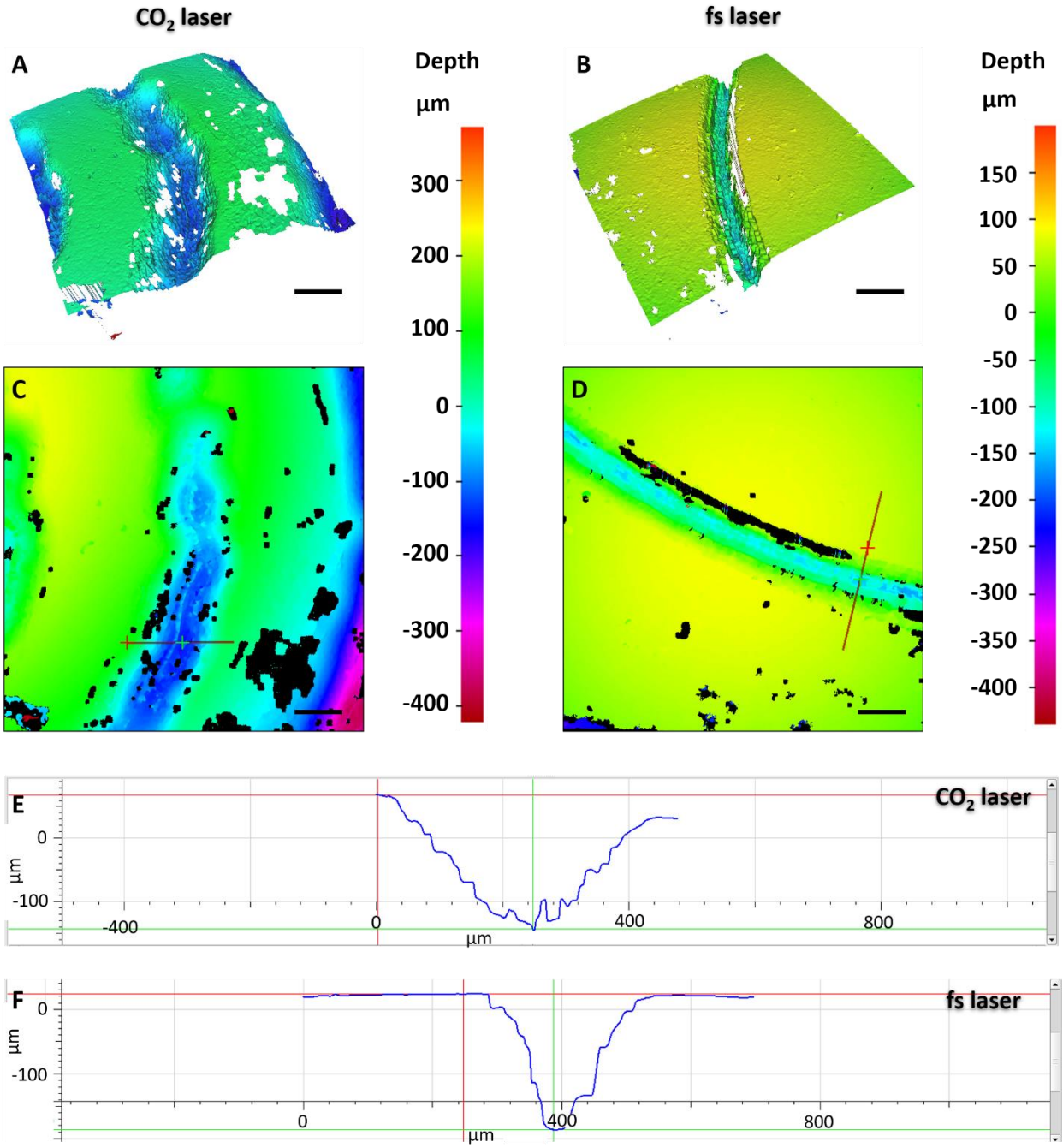

Figure A2. Roughness of contact lens microchannels obtained by CO_2 laser or femtosecond laser writing. Surface topography: A) CO_2 laser-inscribed material, B) Femtosecond laser-inscribed material. Scale bars: 250 µm. Surface roughness visualization: C) CO_2 laser, D) femtosecond laser. Surface roughness profile: E) CO_2 laser, F) Femtosecond laser.

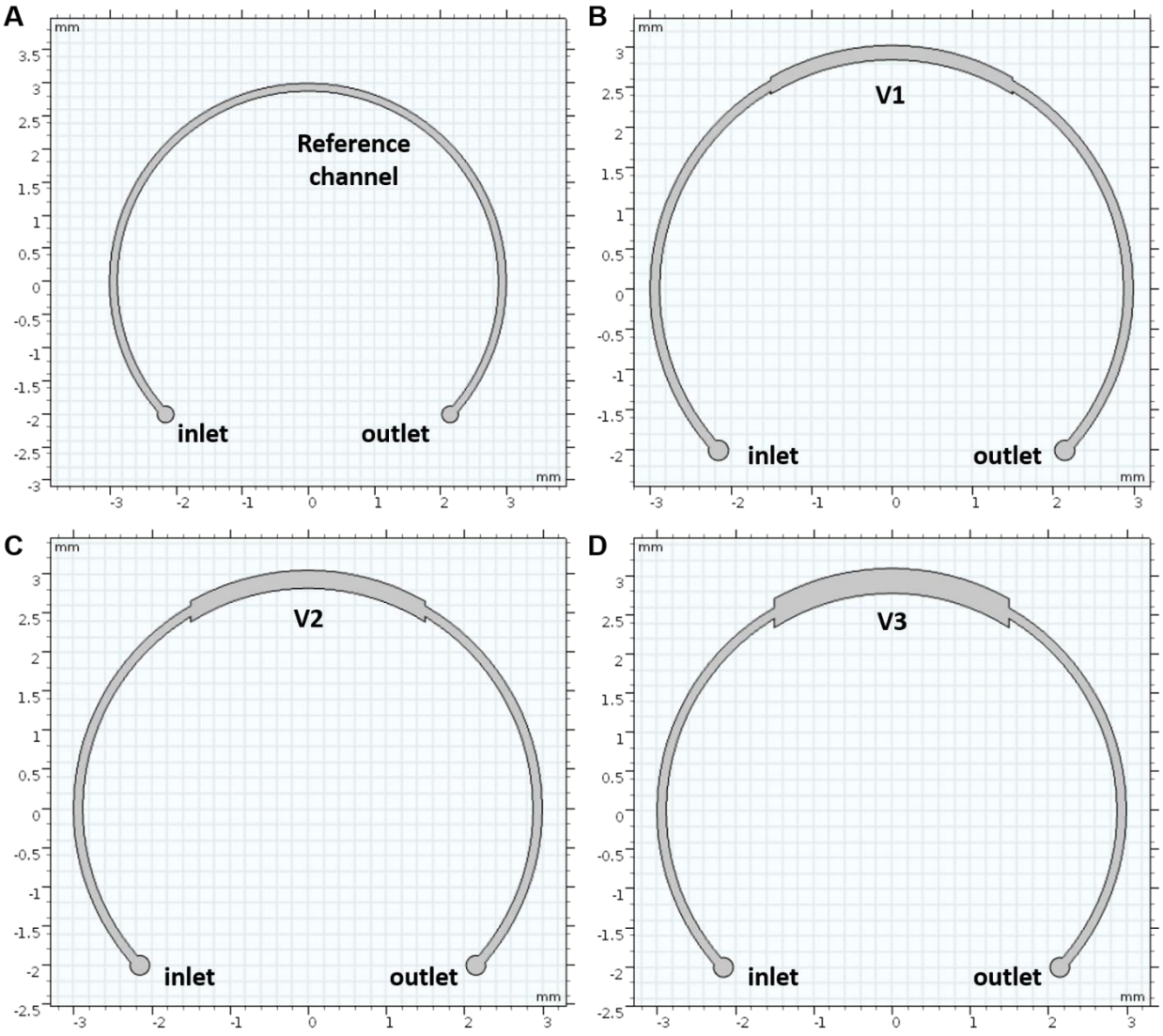

Figure A2. Valve geometries. A) Base channel, 120 µm thin. B) Valve, 100% enlargement (V1). C) Valve, 200% enlargement (V2). D) Valve, 300% enlargement (V3).

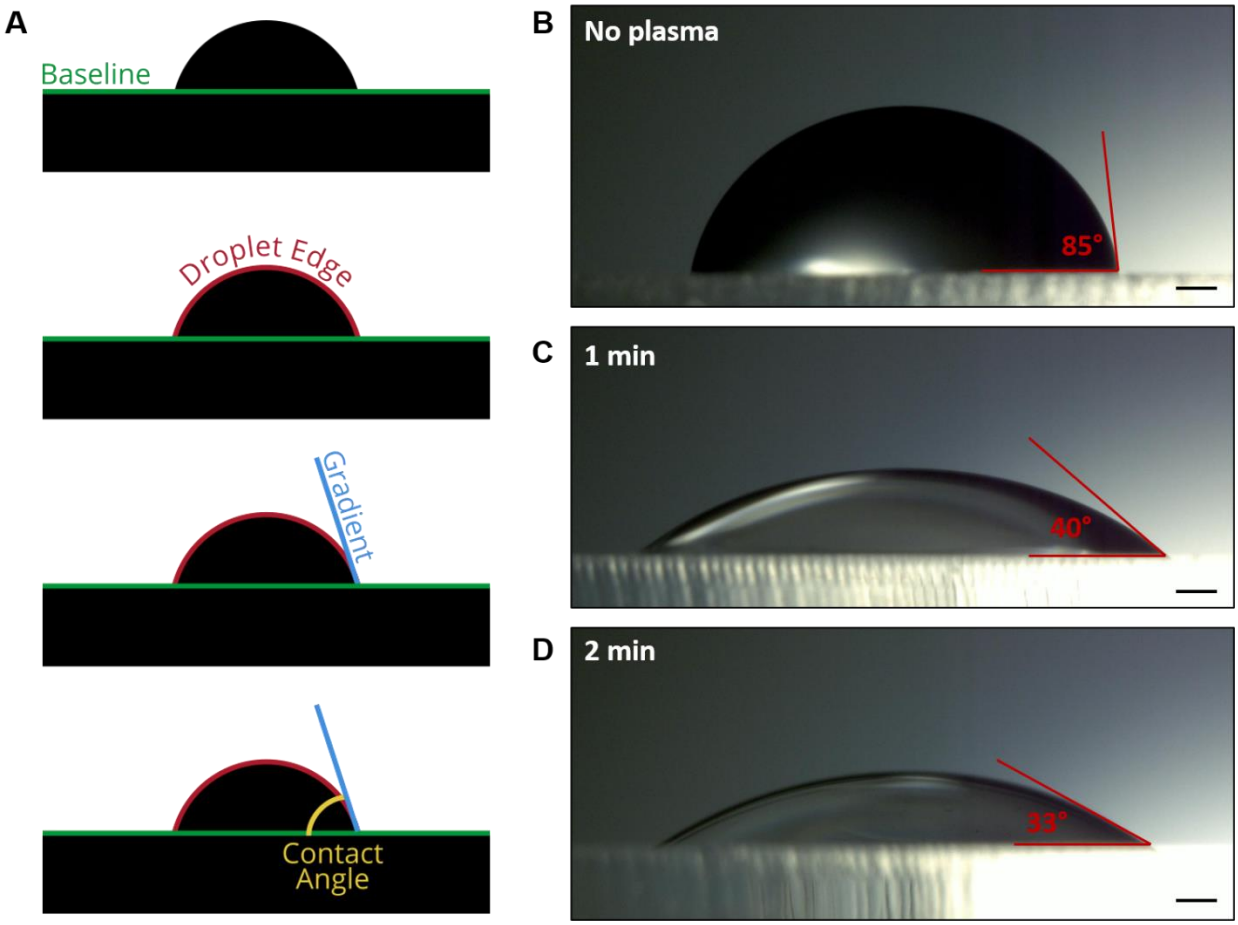

Figure A3. PMMA contact angle before and after oxygen plasma treatment. A) Schematic of contact angle measurement. B-D) Experimentally measured contact angle of PMMA without (B), after 1 minute (C) and after 2 minutes (D) of plasma treatment.

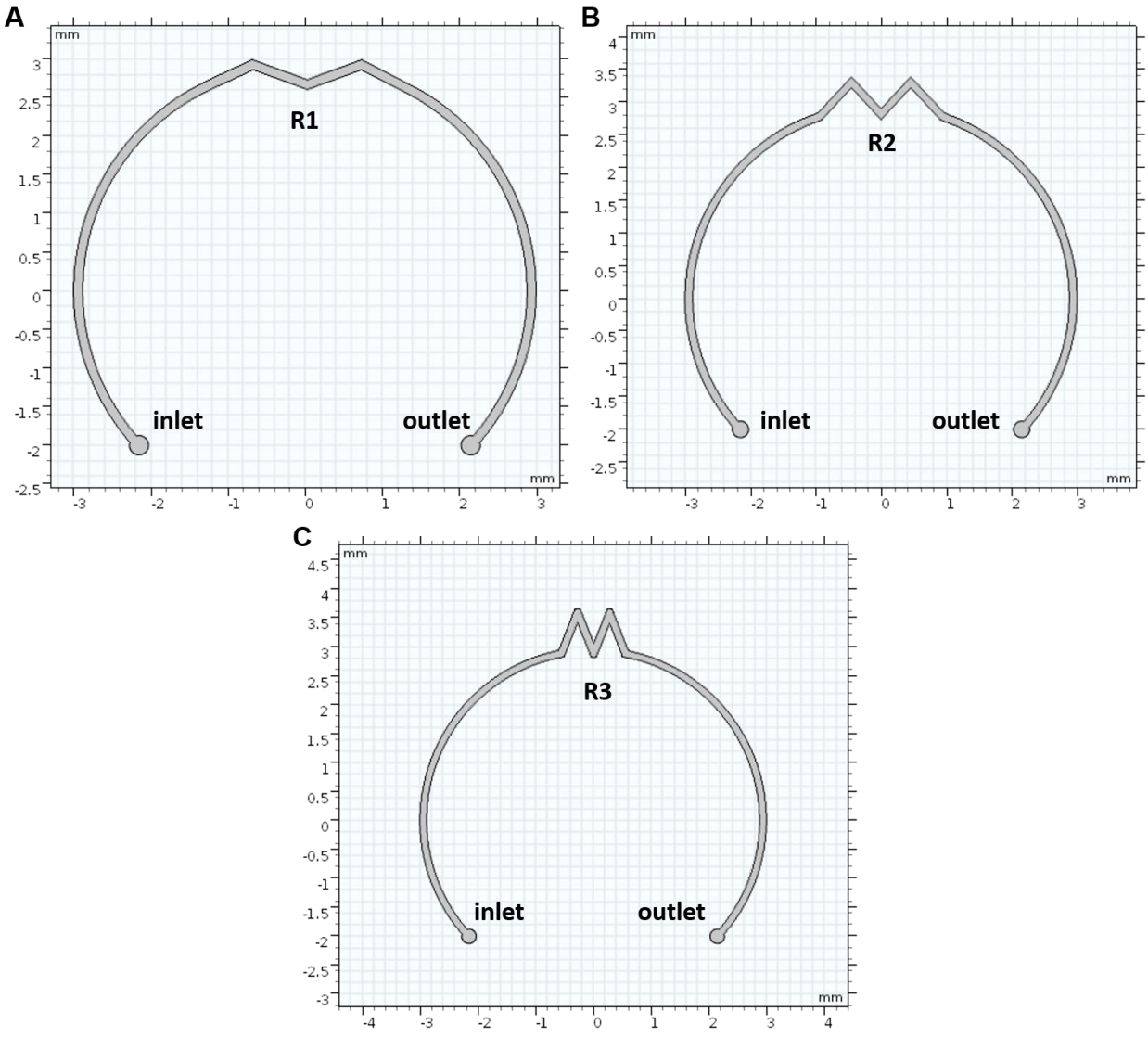

Figure A4. Resistors geometries. A) Wide resistor (R1). B) Standard resistor (R2). C) Narrow resistor (R3).

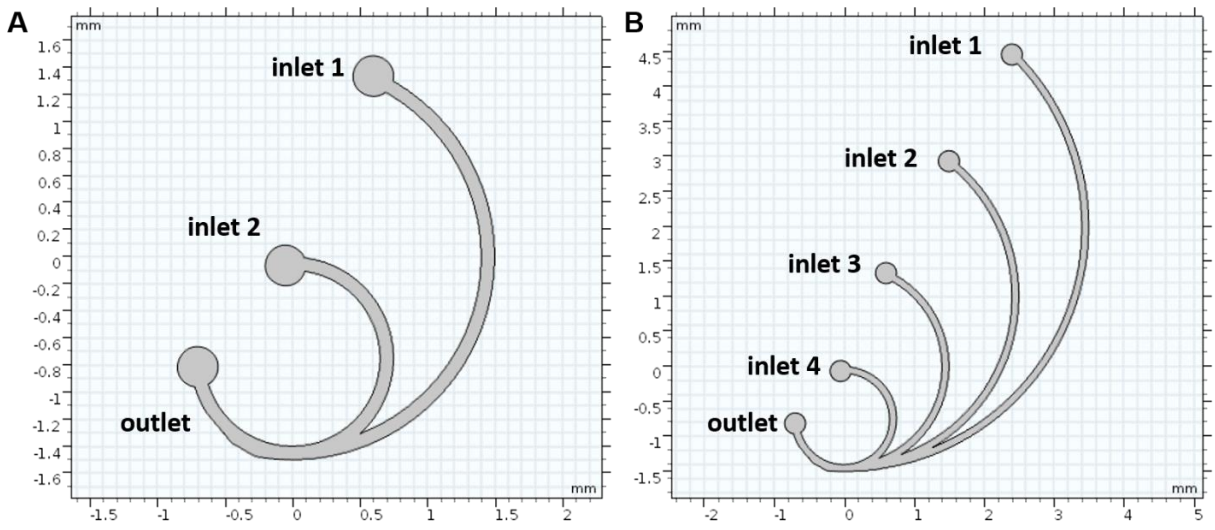

Figure A5. Multi-inlet geometries. A) Two-inlet network (M1). B) Four-inlet network (M2).

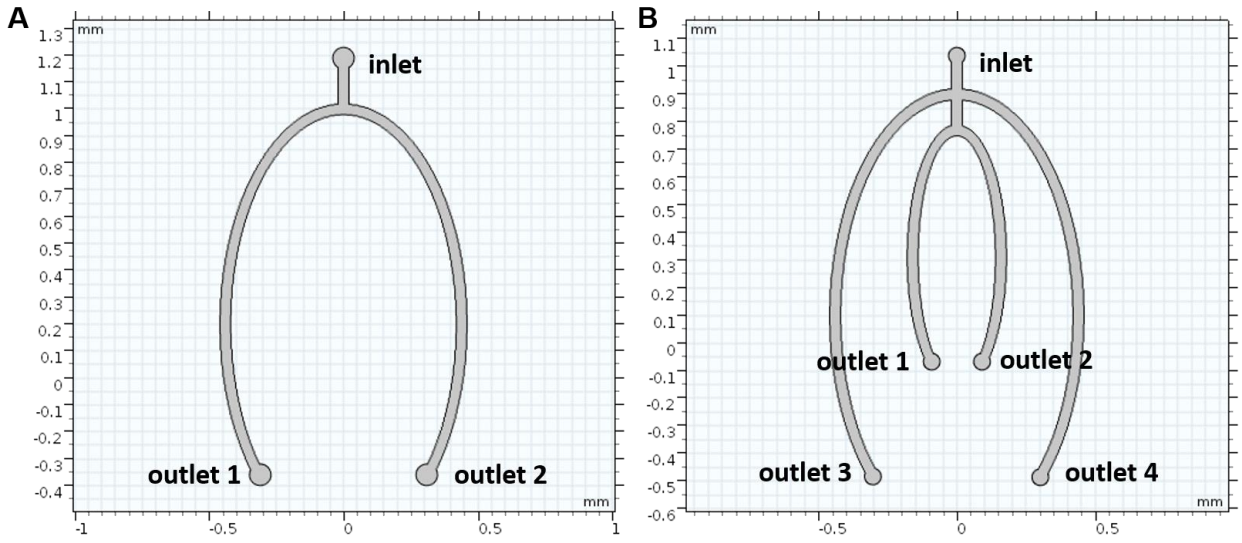

Figure A6. Splitter geometries. A) Two-branched splitter (S1). B) Four-branched splitter (S2).

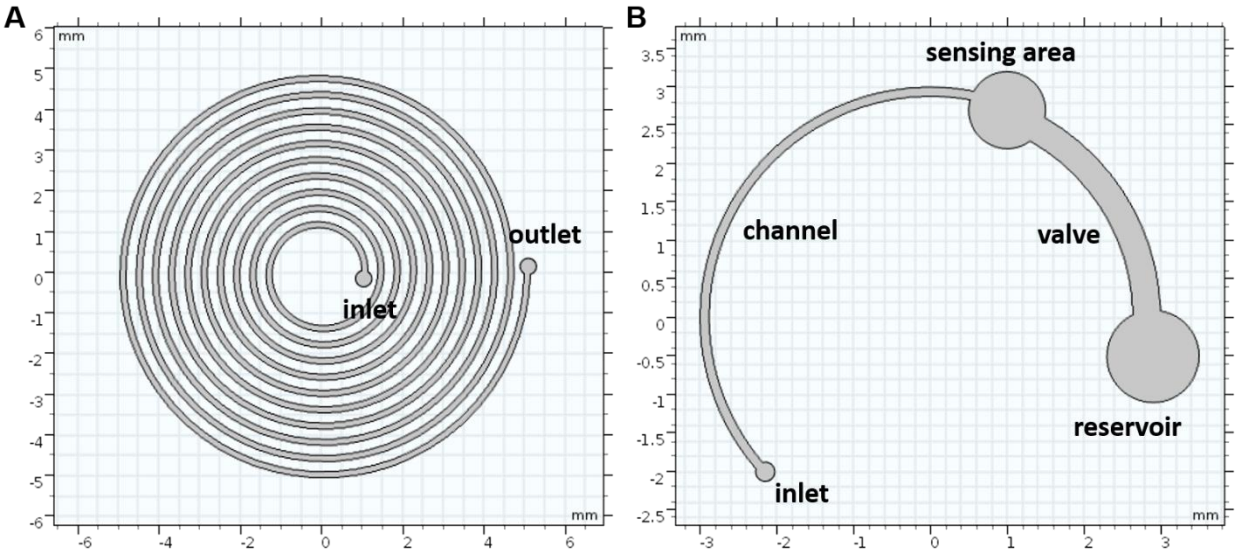

Figure A7. Contact lens sensor geometries. A) Spiral-shaped tear volume sensor. B) Uric acid sensor featuring inlet, sensing area, valve and reservoir.

Appendix III

Nanobuttons Design

Nanobuttons were designed as circular patters grouped into squares, using CleWin 5 software (**Figure A8**). The design was drawn within a 5 inches shape, corresponding to the area of the silicon wafer, in four sections (**Figure A8, A**) and three layers, comprising wafer area, nanobuttons, and inner areas (**Figure A8, B**). The sections of interest in the context of this thesis are the ones located at the center (**Figure A8, C**). Each square featured a different geometry, for a total of 16. Only three of them were used.

Figure A8, D displays the zoom on the geometries of interest: pattern 1, 2, and 3, employed as stretchable pressure sensors for ocular pressure monitoring. A photograph of a nanopatterned PDMS sample is presented in **Figure A8, E**. The geometrical details of the 16 nanopatterns are included in **Figure A8, F**, where the pattern number recalls its position indicated in Figure A8, C. Micrographs of each pattern are displayed in **Figure A9**.

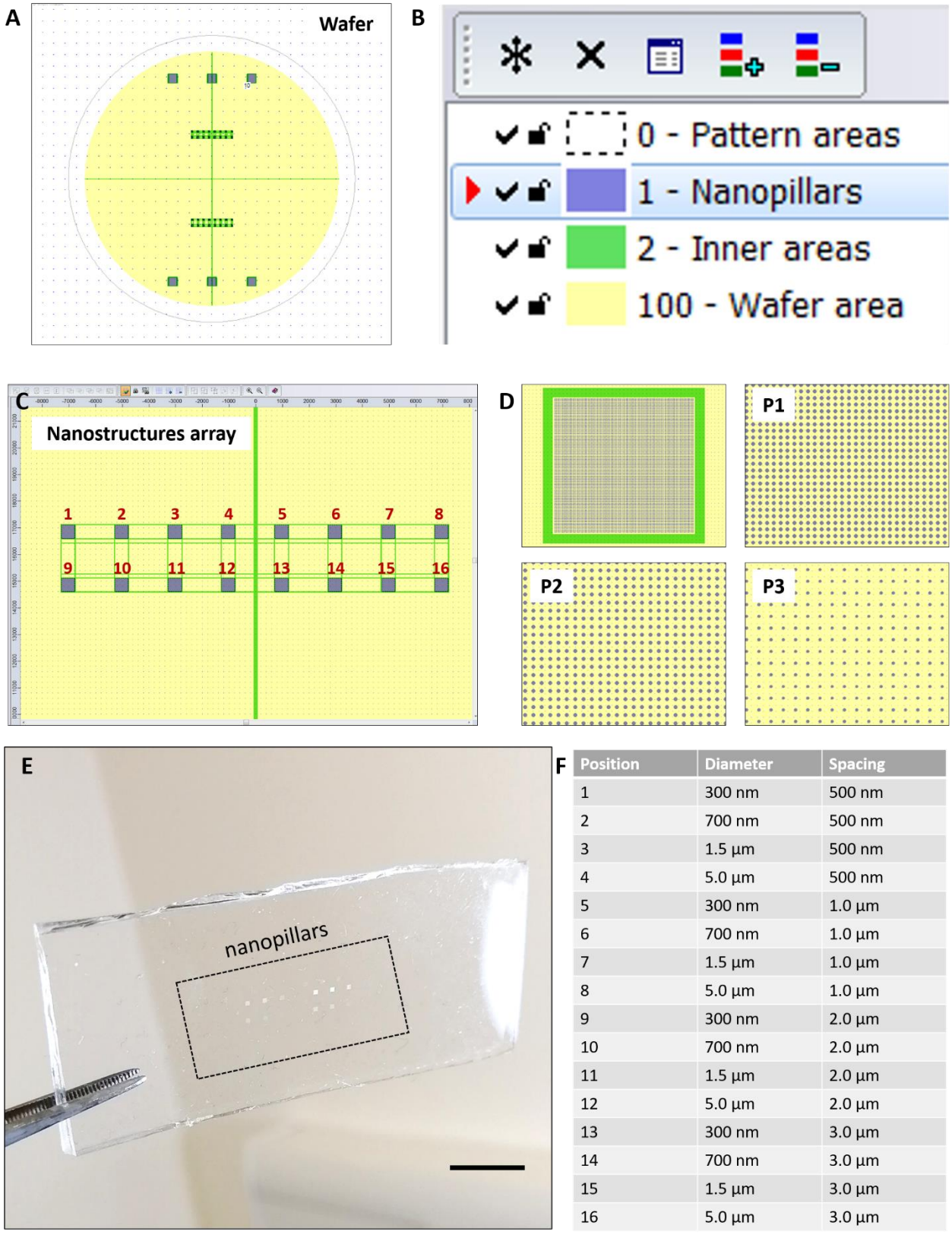

F

Position	Diameter	Spacing
1	300 nm	500 nm
2	700 nm	500 nm
3	1.5 µm	500 nm
4	5.0 µm	500 nm
5	300 nm	1.0 µm
6	700 nm	1.0 µm
7	1.5 µm	1.0 µm
8	5.0 µm	1.0 µm
9	300 nm	2.0 µm
10	700 nm	2.0 µm
11	1.5 µm	2.0 µm
12	5.0 µm	2.0 µm
13	300 nm	3.0 µm
14	700 nm	3.0 µm
15	1.5 µm	3.0 µm
16	5.0 µm	3.0 µm

Figure A8. Design of nanobuttons. A) 4-inch wafer featuring four main areas. The nanostructures further used in this work are the two arrays located around the center of the wafer. B) Legend of the layers. Three areas were identified to allow an easier visualization: actual nanostructures (purple), nanostructures contours (green), wafer area (light yellow). Only the purple layer

was transferred on silicon. C) Zoom on the nanostructures array. The array contains 16 patterns. D) Zoom on the nanopatterns used in this work. Top left: design of a single nanostructures square; top-right: P1 (spacing d = 500 nm); bottom-left: P2 (spacing d = 1 µm); bottom-right: P3 (spacing d = 2 µm). E) Photograph of PDMS nanobuttons. Scale bar: 1 cm. F) Geometrical features of the 16 nanopatterns.

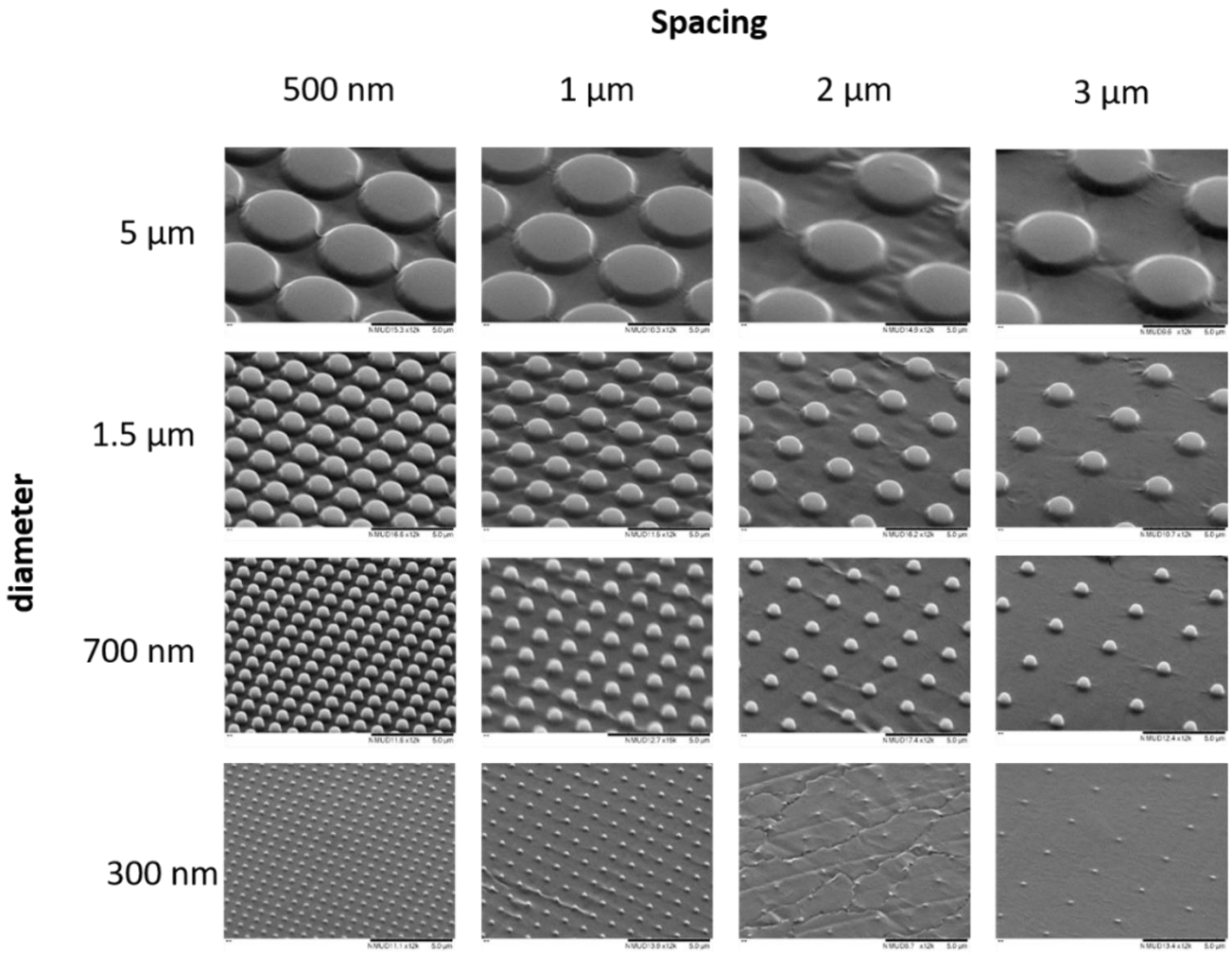

Figure A9. SEM micrographs of the 16 sets of nanostructures contained in each array. Diameters and spacings were varied in the ranges 300 nm - 5 µm and 500 nm – 3 µm, respectively. Scale bars: 5 µm.

Appendix IV

Colorimetric Sensors Readout

Colorimetric sensors were readout using a MATLAB algorithm further implemented into a smartphone app prototype, based on the nearest neighbor model. The code is included below.

```
function [] = readout()

disp('Please type in analyte to be measured:')
comment=input('ph/glucose/protein/nitrites/ascorbic acid: ', 's');

x=  zeros(1,5);
y=  zeros(1,5);

if (strcmp(comment, 'ph'))


          var1_1= imread('pH_5.1.png');
          var1_2= imread('pH_5.2.png');
          var1_3= imread('pH_5.3.png');

          var2_1= imread('pH_6.1.png');
          var2_2= imread('pH_6.2.png');
          var2_3= imread('pH_6.3.png');

          var3_1=imread('pH_7.1.png');
          var3_2=imread('pH_7.2.png');
          var3_3=imread('pH_7.3.png');

          var4_1=imread('pH_8.1.png');
          var4_2=imread('pH_8.2.png');
          var4_3=imread('pH_8.3.png');

          var5_1=imread('pH_9.1.png');
          var5_2=imread('pH_9.2.png');
          var5_3=imread('pH_9.3.png');

elseif (strcmp(comment, 'glucose'))


        var1_1=  imread('gl_0.1.png');
        var1_2=  imread('gl_0.2.png');
        var1_3=  imread('gl_0.3.png');

        var2_1=  imread('gl_2.1.png');
        var2_2=  imread('gl_2.2.png');
        var2_3=  imread('gl_2.3.png');

        var3_1=  imread('gl_6.1.png');
        var3_2=  imread('gl_6.2.png');
        var3_3=  imread('gl_6.3.png');

        var4_1= imread('gl_14.1.png');
        var4_2= imread('gl_14.2.png');
        var4_3= imread('gl_14.3.png');

        var5_1= imread('gl_55.1.png');
        var5_2= imread('gl_55.2.png');
```

```
        var5_3= imread('gl_55.3.png');

elseif (strcmp(comment, 'albumin'))


        var1_1=  imread('al_0.1.png');
        var1_2=  imread('al_0.2.png');
        var1_3=  imread('al_0.3.png');

        var2_1= imread('al_03.1.png');
        var2_2= imread('al_03.2.png');
        var2_3= imread('al_03.3.png');

        var3_1=  imread('al_1.1.png');
        var3_2=  imread('al_1.2.png');
        var3_3=  imread('al_1.3.png');

        var4_1=  imread('al_5.1.png');
        var4_2=  imread('al_5.2.png');
        var4_3=  imread('al_5.3.png');

elseif (strcmp(comment, 'nitrites'))


        var1_1=  imread('nl_0.1.png');
        var1_2=  imread('nl_0.2.png');
        var1_3=  imread('nl_0.3.png');

        var2_1=  imread('nl_2.1.png');
        var2_2=  imread('nl_2.2.png');
        var2_3=  imread('nl_2.3.png');

        var3_1=  imread('nl_6.1.png');
        var3_2=  imread('nl_6.2.png');
        var3_3=  imread('nl_6.3.png');

        var4_1= imread('nl_14.1.png');
        var4_2= imread('nl_14.2.png');
        var4_3= imread('nl_14.3.png');

        var5_1= imread('nl_55.1.png');
        var5_2= imread('nl_55.2.png');
        var5_3= imread('nl_55.3.png');

elseif (strcmp(comment, 'ascorbic acid'))


        var1_1=  imread('aal_0.1.png');
        var1_2=  imread('aal_0.2.png');
        var1_3=  imread('aal_0.3.png');

        var2_1=  imread('aal_2.1.png');
        var2_2=  imread('aal_2.2.png');
        var2_3=  imread('aal_2.3.png');

        var3_1=  imread('aal_6.1.png');
        var3_2=  imread('aal_6.2.png');
        var3_3=  imread('aal_6.3.png');

        var4_1= imread('aal_14.1.png');
        var4_2= imread('aal_14.2.png');
        var4_3= imread('aal_14.3.png');

        var5_1= imread('aal_55.1.png');
        var5_2= imread('aal_55.2.png');
        var5_3= imread('aal_55.3.png');


else
      disp('Input invalid! Please try again.')
      return
end
```

```
%--------------Calculation--------------------------

        R_1_1 = var1_1(:,:,1);
        G_1_1 = var1_1(:,:,2);
        B_1_1 = var1_1(:,:,3);

        %red
        meanR_1_1= sum(sum(R_1_1))/numel(R_1_1(:,:));
        mR_1_1l=((0.55+meanR_1_1/1.055))^2.4;

        %green
        meanG_1_1= sum(sum(G_1_1))/numel(G_1_1(:,:));
        mG_1_1l=((0.55+meanG_1_1/1.055))^2.4;

        %blue
        meanB_1_1= sum(sum(B_1_1))/numel(B_1_1(:,:));
        mB_1_1l=((0.55+meanB_1_1/1.055))^2.4;

        %Plot RGB coordinates in the chromaticity diagram
        X_1_1 = 0.1805*mB_1_1l + 0.3576*mG_1_1l + 0.4124*mR_1_1l;
        Y_1_1 = 0.0722*mB_1_1l + 0.7152*mG_1_1l + 0.2126*mR_1_1l;
        Z_1_1 = 0.9505*mB_1_1l + 0.1192*mG_1_1l+ 0.0193*mR_1_1l;

        x1(:,1) = X_1_1/(X_1_1+Y_1_1+Z_1_1);
        y1(:,1) = Y_1_1/(X_1_1+Y_1_1+Z_1_1);

 %-----------------var1_2-----------------
        R_1_2 = var1_2(:,:,1);
        G_1_2 = var1_2(:,:,2);
        B_1_2 = var1_2(:,:,3);

        %red
        meanR_1_2= sum(sum(R_1_2))/numel(R_1_2(:,:));
        mR_1_2l=  ((0.55+meanR_1_2/1.055))^2.4;

        %green
        meanG_1_2= sum(sum(G_1_2))/numel(G_1_2(:,:));
        mG_1_2l=   ((0.55+meanG_1_2/1.055))^2.4;

        %blue
        meanB_1_2= sum(sum(B_1_2))/numel(B_1_2(:,:));
        mB_1_2l=   ((0.55+meanB_1_2/1.055))^2.4;

        % Plot RGB coordinates in the chromaticity diagram
        X_1_2 = 0.1805*mB_1_2l + 0.3576*mG_1_2l + 0.4124*mR_1_2l;
        Y_1_2 = 0.0722*mB_1_2l + 0.7152*mG_1_2l + 0.2126*mR_1_2l;
        Z_1_2 = 0.9505*mB_1_2l + 0.1192*mG_1_2l+ 0.0193*mR_1_2l;

        x1(:,2) = X_1_2/(X_1_2+Y_1_2+Z_1_2);
        y1(:,2) = Y_1_2/(X_1_2+Y_1_2+Z_1_2);


%----------------var1_3----------------------
        R_1_3 = var1_3(:,:,1);
        G_1_3 = var1_3(:,:,2);
        B_1_3 = var1_3(:,:,3);

        %red
        meanR_1_3= sum(sum(R_1_3))/numel(R_1_3(:,:));
        mR_1_3l=((0.55+meanR_1_3/1.055))^2.4;

        %green
        meanG_1_3= sum(sum(G_1_3))/numel(G_1_3(:,:));
        mG_1_3l=((0.55+meanG_1_3/1.055))^2.4;

        %blue
        meanB_1_3= sum(sum(B_1_3))/numel(B_1_3(:,:));
        mB_1_3l=((0.55+meanB_1_3/1.055))^2.4;

        % Plot RGB coordinates in the chromaticity diagram
        X_1_3 = 0.1805*mB_1_3l + 0.3576*mG_1_3l + 0.4124*mR_1_3l;
        Y_1_3 = 0.0722*mB_1_3l + 0.7152*mG_1_3l + 0.2126*mR_1_3l;
        Z_1_3 = 0.9505*mB_1_3l + 0.1192*mG_1_3l+ 0.0193*mR_1_3l;
```

```
    x1(:,3) = X_1_3/(X_1_3+Y_1_3+Z_1_3);
    y1(:,3) = Y_1_3/(X_1_3+Y_1_3+Z_1_3);

    x(:,1)=sum(x1)/3;
    y(:,1)=sum(y1)/3;

 %-----------------var2_1--------------------

    R_2_1=  var2_1(:,:,1);
    G_2_1 = var2_1(:,:,2);
    B_2_1 = var2_1(:,:,3);

    meanR_2_1= sum(sum(R_2_1))/numel(R_2_1(:,:));
    mR_2_1l=((0.55+meanR_2_1/1.055))^2.4;

    meanG_2_1= sum(sum(G_2_1))/numel(G_2_1(:,:));
    mG_2_1l=((0.55+meanG_2_1/1.055))^2.4;

    meanB_2_1= sum(sum(B_2_1))/numel(B_2_1(:,:));
    mB_2_1l=((0.55+meanB_2_1/1.055))^2.4;

    X_2_1 = 0.1805*mB_2_1l + 0.3576*mG_2_1l + 0.4124*mR_2_1l;
    Y_2_1 = 0.0722*mB_2_1l + 0.7152*mG_2_1l + 0.2126*mR_2_1l;
    Z_2_1 = 0.9505*mB_2_1l + 0.1192*mG_2_1l+ 0.0193*mR_2_1l;

    x2(:,1) = X_2_1/(X_2_1+Y_2_1+Z_2_1);
    y2(:,1) = Y_2_1/(X_2_1+Y_2_1+Z_2_1);

%-----------------var2_2-------------------------

    R_2_2=  var2_2(:,:,1);
    G_2_2 = var2_2(:,:,2);
    B_2_2 = var2_2(:,:,3);

    meanR_2_2= sum(sum(R_2_2))/numel(R_2_2(:,:));
    mR_2_2l=((0.55+meanR_2_2/1.055))^2.4;

    meanG_2_2= sum(sum(G_2_2))/numel(G_2_2(:,:));
    mG_2_2l=((0.55+meanG_2_2/1.055))^2.4;

    meanB_2_2= sum(sum(B_2_2))/numel(B_2_2(:,:));
    mB_2_2l=((0.55+meanB_2_2/1.055))^2.4;

    X_2_2 = 0.1805*mB_2_2l + 0.3576*mG_2_2l + 0.4124*mR_2_2l;
    Y_2_2 = 0.0722*mB_2_2l + 0.7152*mG_2_2l + 0.2126*mR_2_2l;
    Z_2_2 = 0.9505*mB_2_2l + 0.1192*mG_2_2l+ 0.0193*mR_2_2l;

    x2(:,2) = X_2_2/(X_2_2+Y_2_2+Z_2_2);
    y2(:,2) = Y_2_2/(X_2_2+Y_2_2+Z_2_2);


%-------------------var2_3-----------------------------

    R_2_3= var2_3(:,:,1);
    G_2_3= var2_3(:,:,2);
    B_2_3= var2_3(:,:,3);

    meanR_2_3= sum(sum(R_2_3))/numel(R_2_3(:,:));
    mR_2_3l=((0.55+meanR_2_3/1.055))^2.4;

    meanG_2_3= sum(sum(G_2_3))/numel(G_2_3(:,:));
    mG_2_3l=   ((0.55+meanG_2_3/1.055))^2.4;

    meanB_2_3= sum(sum(B_2_3))/numel(B_2_3(:,:));
    mB_2_3l=   ((0.55+meanB_2_3/1.055))^2.4;

    X_2_3 = 0.1805*mB_2_3l + 0.3576*mG_2_3l + 0.4124*mR_2_3l;
    Y_2_3 = 0.0722*mB_2_3l + 0.7152*mG_2_3l + 0.2126*mR_2_3l;
    Z_2_3 = 0.9505*mB_2_3l + 0.1192*mG_2_3l+ 0.0193*mR_2_3l;

    x2(:,3) = X_2_3/(X_2_3+Y_2_3+Z_2_3);
    y2(:,3) = Y_2_3/(X_2_3+Y_2_3+Z_2_3);
```

```
        x(:,2)=sum(x2)/3;
        y(:,2)=sum(y2)/3;

%------------var3_1-----------------------------

        R_3_1=  var3_1(:,:,1);
        G_3_1 = var3_1(:,:,2);
        B_3_1 = var3_1(:,:,3);

        meanR_3_1= sum(sum(R_3_1))/numel(R_3_1(:,:));
        mR_3_1l=((0.55+meanR_3_1/1.055))^2.4;

        meanG_3_1= sum(sum(G_3_1))/numel(G_3_1(:,:));
        mG_3_1l=((0.55+meanG_3_1/1.055))^2.4;

        meanB_3_1= sum(sum(B_3_1))/numel(B_3_1(:,:));
        mB_3_1l=((0.55+meanB_3_1/1.055))^2.4;

        X_3_1 = 0.1805*mB_3_1l + 0.3576*mG_3_1l + 0.4124*mR_3_1l;
        Y_3_1 = 0.0722*mB_3_1l + 0.7152*mG_3_1l + 0.2126*mR_3_1l;
        Z_3_1 = 0.9505*mB_3_1l + 0.1192*mG_3_1l+ 0.0193*mR_3_1l;

        x3(:,1) = X_3_1/(X_3_1+Y_3_1+Z_3_1);
        y3(:,1) = Y_3_1/(X_3_1+Y_3_1+Z_3_1);

%----------var3_2-----------------------------

        R_3_2=  var3_2(:,:,1);
        G_3_2 = var3_2(:,:,2);
        B_3_2 = var3_2(:,:,3);

        meanR_3_2= sum(sum(R_3_2))/numel(R_3_2(:,:));
        mR_3_2l=((0.55+meanR_3_2/1.055))^2.4;

        meanG_3_2= sum(sum(G_3_2))/numel(G_3_2(:,:));
        mG_3_2l=((0.55+meanG_3_2/1.055))^2.4;

        meanB_3_2= sum(sum(B_3_2))/numel(B_3_2(:,:));
        mB_3_2l=((0.55+meanB_3_2/1.055))^2.4;

        X_3_2 = 0.1805*mB_3_2l + 0.3576*mG_3_2l + 0.4124*mR_3_2l;
        Y_3_2 = 0.0722*mB_3_2l + 0.7152*mG_3_2l + 0.2126*mR_3_2l;
        Z_3_2 = 0.9505*mB_3_2l + 0.1192*mG_3_2l+ 0.0193*mR_3_2l;

        x3(:,2) = X_3_2/(X_3_2+Y_3_2+Z_3_2);
        y3(:,2) = Y_3_2/(X_3_2+Y_3_2+Z_3_2);

%------------------var3_3-------------------------------

        R_3_3=  var3_3(:,:,1);
        G_3_3 = var3_3(:,:,2);
        B_3_3 = var3_3(:,:,3);

        meanR_3_3= sum(sum(R_3_3))/numel(R_3_3(:,:));
        mR_3_3l=((0.55+meanR_3_3/1.055))^2.4;

        meanG_3_3= sum(sum(G_3_3))/numel(G_3_3(:,:));
        mG_3_3l=((0.55+meanG_3_3/1.055))^2.4;

        meanB_3_3= sum(sum(B_3_3))/numel(B_3_3(:,:));
        mB_3_3l=((0.55+meanB_3_3/1.055))^2.4;

        X_3_3 = 0.1805*mB_3_3l + 0.3576*mG_3_3l + 0.4124*mR_3_3l;
        Y_3_3 = 0.0722*mB_3_3l + 0.7152*mG_3_3l + 0.2126*mR_3_3l;
        Z_3_3 = 0.9505*mB_3_3l + 0.1192*mG_3_3l+ 0.0193*mR_3_3l;

        x3(:,3) = X_3_3/(X_3_3+Y_3_3+Z_3_3);
        y3(:,3) = Y_3_3/(X_3_3+Y_3_3+Z_3_3);

        x(:,3)=sum(x3)/3;
        y(:,3)=sum(y3)/3;

%---------------gl_14_1---------------------
```

```
        R_4_1=  var4_1(:,:,1);
        G_4_1 = var4_1(:,:,2);
        B_4_1 = var4_1(:,:,3);

        meanR_4_1= sum(sum(R_4_1))/numel(R_4_1(:,:));
        mR_4_1l=((0.55+meanR_4_1/1.055))^2.4;

        meanG_4_1= sum(sum(G_4_1))/numel(G_4_1(:,:));
        mG_4_1l=((0.55+meanG_4_1/1.055))^2.4;

        meanB_4_1= sum(sum(B_4_1))/numel(B_4_1(:,:));
        mB_4_1l=((0.55+meanB_4_1/1.055))^2.4;

        X_4_1 = 0.1805*mB_4_1l + 0.3576*mG_4_1l + 0.4124*mR_4_1l;
        Y_4_1 = 0.0722*mB_4_1l + 0.7152*mG_4_1l + 0.2126*mR_4_1l;
        Z_4_1 = 0.9505*mB_4_1l + 0.1192*mG_4_1l + 0.0193*mR_4_1l;

        x4(:,1) = X_4_1/(X_4_1+Y_4_1+Z_4_1);
        y4(:,1) = Y_4_1/(X_4_1+Y_4_1+Z_4_1);


%---------------var4_2----------------------

        R_4_2=  var4_2(:,:,1);
        G_4_2=  var4_2(:,:,2);
        B_4_2=  var4_2(:,:,3);

        meanR_4_2= sum(sum(R_4_2))/numel(R_4_2(:,:));
        mR_4_2l=((0.55+meanR_4_2/1.055))^2.4;

        meanG_4_2= sum(sum(G_4_2))/numel(G_4_2(:,:));
        mG_4_2l=((0.55+meanG_4_2/1.055))^2.4;

        meanB_4_2= sum(sum(B_4_2))/numel(B_4_2(:,:));
        mB_4_2l=((0.55+meanB_4_2/1.055))^2.4;

        X_4_2 = 0.1805*mB_4_2l + 0.3576*mG_4_2l + 0.4124*mR_4_2l;
        Y_4_2 = 0.0722*mB_4_2l + 0.7152*mG_4_2l + 0.2126*mR_4_2l;
        Z_4_2 = 0.9505*mB_4_2l + 0.1192*mG_4_2l+ 0.0193*mR_4_2l;

        x4(:,2) = X_4_2/(X_4_2+Y_4_2+Z_4_2);
        y4(:,2) = Y_4_2/(X_4_2+Y_4_2+Z_4_2);


  %----------------var4_3----------------------

        R_4_3=  var4_3(:,:,1);
        G_4_3=  var4_3(:,:,2);
        B_4_3=  var4_3(:,:,3);

        meanR_4_3= sum(sum(R_4_3))/numel(R_4_3(:,:));
        mR_4_3l=((0.55+meanR_4_3/1.055))^2.4;

        meanG_4_3= sum(sum(G_4_3))/numel(G_4_3(:,:));
        mG_4_3l=((0.55+meanG_4_3/1.055))^2.4;

        meanB_4_3= sum(sum(B_4_3))/numel(B_4_3(:,:));
        mB_4_3l=((0.55+meanB_4_3/1.055))^2.4;

        X_4_3 = 0.1805*mB_4_3l + 0.3576*mG_4_3l + 0.4124*mR_4_3l;
        Y_4_3 = 0.0722*mB_4_3l + 0.7152*mG_4_3l + 0.2126*mR_4_3l;
        Z_4_3 = 0.9505*mB_4_3l + 0.1192*mG_4_3l+ 0.0193*mR_4_3l;

        x4(:,3) = X_4_3/(X_4_3+Y_4_3+Z_4_3);
        y4(:,3) = Y_4_3/(X_4_3+Y_4_3+Z_4_3);

        x(:,4)=sum(x4)/3;
        y(:,4)=sum(y4)/3;

  %------------var5_1--------------------------

if (strcmp(comment, 'ph'))|| (strcmp (comment, 'glucose'))
        R_5_1=  var5_1(:,:,1);
```

```
        G_5_1 = var5_1(:,:,2);
        B_5_1 = var5_1(:,:,3);

        meanR_5_1= sum(sum(R_5_1))/numel(R_5_1(:,:));
        mR_5_1l=((0.55+meanR_5_1/1.055))^2.4;

        meanG_5_1= sum(sum(G_5_1))/numel(G_5_1(:,:));
        mG_5_1l=((0.55+meanG_5_1/1.055))^2.4;

        meanB_5_1= sum(sum(B_5_1))/numel(B_5_1(:,:));
        mB_5_1l=((0.55+meanB_5_1/1.055))^2.4;

        X_5_1 = 0.1805*mB_5_1l + 0.3576*mG_5_1l + 0.4124*mR_5_1l;
        Y_5_1 = 0.0722*mB_5_1l + 0.7152*mG_5_1l + 0.2126*mR_5_1l;
        Z_5_1 = 0.9505*mB_5_1l + 0.1192*mG_5_1l+ 0.0193*mR_5_1l;

        x5(:,1) = X_5_1/(X_5_1+Y_5_1+Z_5_1);
        y5(:,1) = Y_5_1/(X_5_1+Y_5_1+Z_5_1);


    %------------------var5_2---------------------------

        R_5_2=  var5_2(:,:,1);
        G_5_2 = var5_2(:,:,2);
        B_5_2 = var5_2(:,:,3);

        meanR_5_2= sum(sum(R_5_2))/numel(R_5_2(:,:));
        mR_5_2l=((0.55+meanR_5_2/1.055))^2.4;

        meanG_5_2= sum(sum(G_5_2))/numel(G_5_2(:,:));
        mG_5_2l=((0.55+meanG_5_2/1.055))^2.4;

        meanB_5_2= sum(sum(B_5_2))/numel(B_5_2(:,:));
        mB_5_2l=((0.55+meanB_5_2/1.055))^2.4;

        X_5_2 = 0.1805*mB_5_2l + 0.3576*mG_5_2l + 0.4124*mR_5_2l;
        Y_5_2 = 0.0722*mB_5_2l + 0.7152*mG_5_2l + 0.2126*mR_5_2l;
        Z_5_2 = 0.9505*mB_5_2l + 0.1192*mG_5_2l+ 0.0193*mR_5_2l;

        x5(:,2) = X_5_2/(X_5_2+Y_5_2+Z_5_2);
        y5(:,2) = Y_5_2/(X_5_2+Y_5_2+Z_5_2);

    %----------------var5_3-----------------

        R_5_3=  var5_3(:,:,1);
        G_5_3 = var5_3(:,:,2);
        B_5_3 = var5_3(:,:,3);

        meanR_5_3= sum(sum(R_5_3))/numel(R_5_3(:,:));
        mR_5_3=((0.55+meanR_5_3/1.055))^2.4;

        meanG_5_3= sum(sum(G_5_3))/numel(G_5_3(:,:));
        mG_5_3=((0.55+meanG_5_3/1.055))^2.4;

        meanB_5_3= sum(sum(B_5_3))/numel(B_5_3(:,:));
        mB_5_3=((0.55+meanB_5_3/1.055))^2.4;

        X_5_3 = 0.1805*mB_5_3 + 0.3576*mG_5_3 + 0.4124*mR_5_3;
        Y_5_3 = 0.0722*mB_5_3 + 0.7152*mG_5_3 + 0.2126*mR_5_3;
        Z_5_3 = 0.9505*mB_5_3 + 0.1192*mG_5_3+ 0.0193*mR_5_3;

        x5(:,3) = X_5_3/(X_5_3+Y_5_3+Z_5_3);
        y5(:,3) = Y_5_3/(X_5_3+Y_5_3+Z_5_3);


        x(:,5)=sum(x5)/3;
        y(:,5)=sum(y5)/3;

    elseif (strcmp(comment, 'albumin'))


        x(:,5)=0;
        y(:,5)=0;
```

```
 end

%----------Readout unknown concentration-----------------

        [unknown, ~]=uigetfile('*.jpg','Select Image for Measurement');
        figure('name','Crop Image for Measurement');
        title('Mark area to be analyzed and double-click in the crop rectangle:');
        hold on;
        new= imread(unknown);
        imshow(unknown, 'InitialMagnification', 'fit')
        [new, ~]= imcrop(new);
        close(gcf);

        R_n = new(:,:,1);
        G_n = new(:,:,2);
        B_n = new(:,:,3);

        meanR_n= sum(sum(R_n))/numel(R_n(:,:));
        mR_nl=((0.55+meanR_n/1.055))^2.4;

        meanG_n= sum(sum(G_n))/numel(G_n(:,:));
        mG_nl=((0.55+meanG_n/1.055))^2.4;

        meanB_n= sum(sum(B_n))/numel(B_n(:,:));
        mB_nl=((0.55+meanB_n/1.055))^2.4;

        X_n = 0.1805*mB_nl + 0.3576*mG_nl + 0.4124*mR_nl;
        Y_n = 0.0722*mB_nl + 0.7152*mG_nl + 0.2126*mR_nl;
        Z_n = 0.9505*mB_nl + 0.1192*mG_nl + 0.0193*mR_nl;

        x_n = X_n/(X_n+Y_n+Z_n);
        y_n = Y_n/(X_n+Y_n+Z_n);

        figure('name', 'CIE 1931 chromaticity space');
        hold on;
        cieplot( );
        title('CIE 1931 chromaticity space');
        hold on;

            if (strcmp(comment, 'ph'))|| (strcmp(comment, 'glucose'))
                for i=1:5
                    plot(x(:,i),y(i), 'ko');
                end
            elseif (strcmp(comment, 'albumin'))
                for i=1:4
                    plot(x(:,i),y(i), 'ko');
               end
             elseif (strcmp(comment, 'nitrites'))
                for i=1:4
                    plot(x(:,i),y(i), 'ko');
              end

             elseif (strcmp(comment, 'ascorbic acid'))
                for i=1:4
                    plot(x(:,i),y(i), 'ko');

       end

        hold on;
        plot(x_n,y_n, 'wo')
        disp('The according calibration points and the measured value are marked in the CIE
1931 chromaticity space.');


%--------Measurement of shortest path

             if (strcmp(comment, 'ph'))
                    dk=zeros(1,5);
                    ck=[5, 6, 7, 8, 9];
                    for i=1:5
                    dk(i)= sqrt((x(:,i)-x_n).^2 + (y(:,i)-y_n).^2);
                    end
```

```
                dks = min(dk(dk<1));

%---------Measurement of concentration range----------

                    for i=1:5
                        if dks== dk(:, i)
                            cm = ck(:,i);
                        end
                    end
               str=['The measured ph value is ' num2str(cm) '.'];
               disp(str)


            elseif (strcmp(comment, 'glucose'))
                   dk=zeros(1,5);
                   ck=[0, 2, 6, 14, 55];
                   for i=1:5
                   dk(i)= sqrt((x(:,i)-x_n).^2 + (y(:,i)-y_n).^2);
                   end
                   dks = min(dk(dk<1));

                    for i=1:5
                        if dks== dk(:, i)
                            cm = ck(:,i);
                        end
                    end
               str=['The measured glucose value is ' num2str(cm) '.'];
               disp(str)


            elseif (strcmp(comment, 'albumin'))
             dk=zeros(1,4);
                   ck=[0, 0.3, 1, 5];
                   for i=1:4
                   dk(i)= sqrt((x(:,i)-x_n).^2 + (y(:,i)-y_n).^2);
                   end
                   dks = min(dk(dk<1));

                    for i=1:4
                        if dks== dk(:, i)
                            cm = ck(:,i);
                        end
                    end
               str=['The measured albumin value is ' num2str(cm) '.'];
               disp(str)

            elseif (strcmp(comment, 'nitrites'))
                   dk=zeros(1,5);
                   ck=[0, 2, 6, 14, 55];
                   for i=1:5
                   dk(i)= sqrt((x(:,i)-x_n).^2 + (y(:,i)-y_n).^2);
                   end
                   dks = min(dk(dk<1));

                    for i=1:5
                        if dks== dk(:, i)
                            cm = ck(:,i);
                        end
                    end
               str=['The measured nitrites value is ' num2str(cm) '.'];
               disp(str)

            elseif (strcmp(comment, 'ascorbic acid'))
                   dk=zeros(1,5);
                   ck=[0, 2, 6, 14, 55];
                   for i=1:5
                   dk(i)= sqrt((x(:,i)-x_n).^2 + (y(:,i)-y_n).^2);
                   end
                   dks = min(dk(dk<1));
```

```
                for i=1:5
                    if dks== dk(:, i)
                        cm = ck(:,i);
                    end
                end
            str=['The measured ascorbic acid value is ' num2str(cm) '.'];
            disp(str)

    end

end
```

Appendix V

Additional Applications: Tattoo Sensors

Tattooing is a ubiquitous body modification involving the injection of ink and/or dye pigments into the dermis. Biosensors in the form of tattoos can be used to monitor metabolites in interstitial fluid. Here, minimally invasive, injectable dermal biosensors were developed for measuring pH, glucose, and albumin concentrations. The dermal pH sensor was based on methyl red, bromothymol blue, and phenolphthalein, which responded to a pH range from 5.0 to 9.0. The dermal glucose sensor consisted of glucose oxidase, 3,3′,5,5′-tetramethylbenzidine, and peroxidase that detected concentrations up to 50.0 mmol L^{-1}. The dermal albumin sensor consisted of 3′,3″,5′,5″-tetrachlorophenol-3,4,5,6-tetrabromosulfophthalein to measure concentrations up to 5.0 g L^{-1}. The sensors were multiplexed in *ex vivo* skin tissue and quantitative readouts were obtained using a smartphone camera. These sensors can be used to manage of acid–base homeostasis, diabetes, and liver failure in point-of-care settings. **Figure A10, A** displays a schematic of the tattoo needle interfacing the dermis. To assess the feasibility of injecting biosensors in skin tissues with controlled ink density, depth, and injection angles, a phantom tissue structure was tattooed using black ink. **Figure A10, C** illustrates the top-view micrographs of tattooed phantom tissue with 14.0, 8.3, 1.5, and 1.3 injections mm^{-2}. **Figure A10, D** shows the density of the tattooed area in phantom tissue samples for the indicated regions of interest. The overall tattooed surface area decreased as the number of injections was reduced. 14.0, 8.3, 1.5, and 1.3 injections mm^{-2} yielded up to 91%, 80%, 52%, and 32% of tattooed area over the total surface area, respectively. **Figure A10, E** illustrates cross-section micrographs of the tattoos obtained with different injection densities. The overall tattooed cross-sectional area decreased as the number of injections was reduced within the highlighted regions of interest. Up to 86%, 58%, 36%, and 28% tattooed cross-sectional areas over the total surface area were measured in the cases of 14.0, 8.3, 1.5, and 1.3 injections mm^{-2}, respectively (**Figure A10, F**). The tattooing angle

was evaluated based on the conventional tattooing practice, where a variation in angle between the needle and the phantom tissue surface produced a different aesthetic result (**Figure A10, G**). Ink was injected in phantom samples at 90° (lining tattooing), 80°, 70°, 60°, 50°, and 45° (shading tattooing). **Figure A10, H** shows the expected angle over the measured angle. Average percentage errors for 90°, 80°, 70°, 60°, 50°, and 45° tattooing angles were 0.7%, 1.2%, 0.2%, 2.2%, 7.6%, and 6.8%, respectively. Hence, the density, position, depth, and angle of the inks could be accurately controlled for biosensor injections.

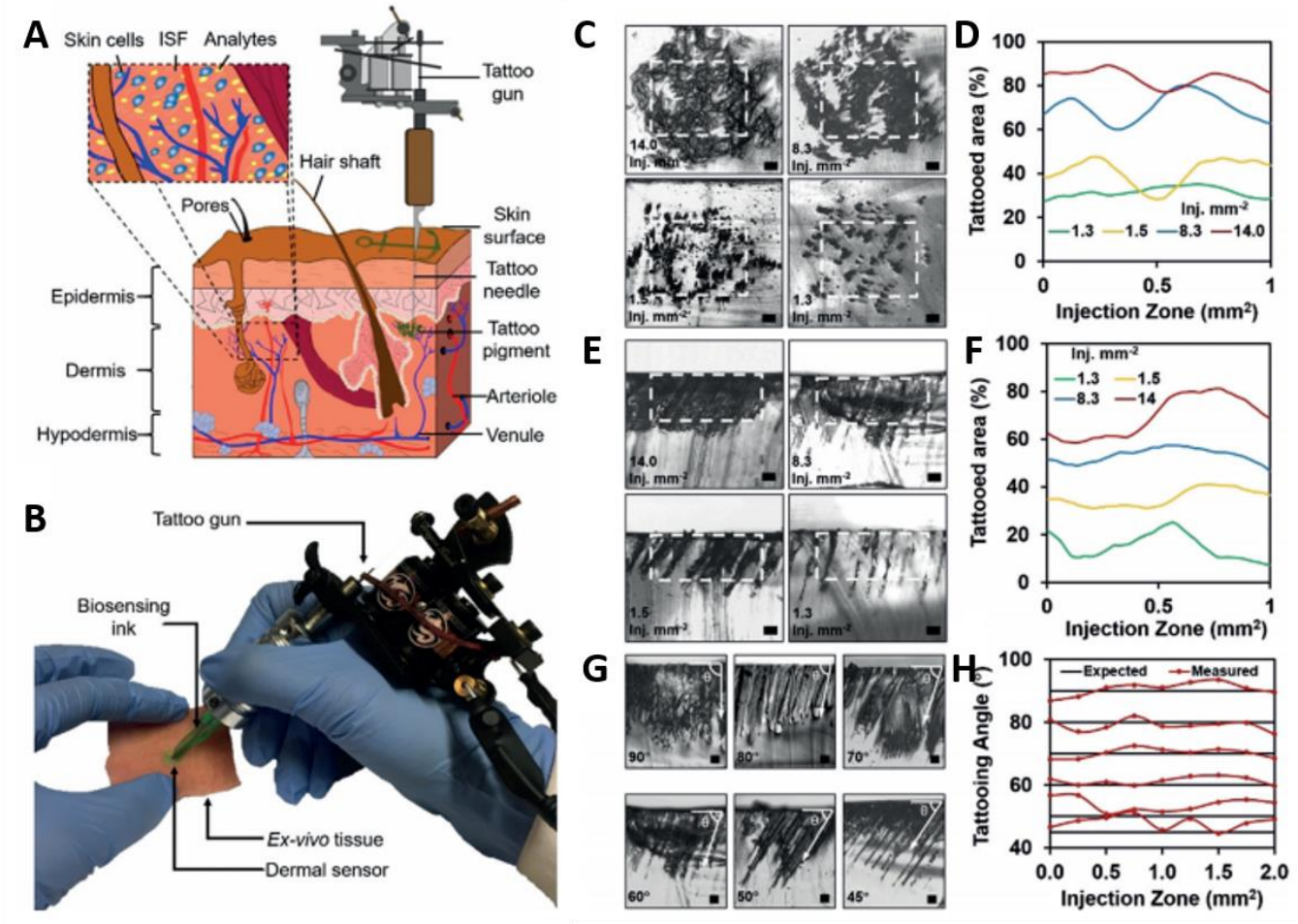

Figure A10. Injection of colorimetric biosensors within the dermis. A) Schematic of human skin cross-section. The tattoo needle (Ø=350 mm) reaches the dermis, where it accesses the ISF. B) Injection of biosensors in ex vivo porcine skin tissue. The biosensor is loaded into a commercial tattoo gun to create visible assay areas in the derma that colorimetrically display the concentration of analytes. Characterization of tattoo inks injected in phantom skin tissues. C) Micrographs of phantom substrates (top view) tattooed with 14.0, 8.3, 1.5, and 1.3 injections mm^{-2}. Scale bars=200 mm. D) Tattooed area over the total surface area with 14.0, 8.3, 1.5, and 1.3 injections mm^{-2} measured over the surface of the phantom tissue. E) Micrographs of phantom substrates (cross-section view) tattooed with 14.0, 8.3, 1.5, and 1.3 injections mm^{-2}. Scale bars=200 mm. F) Tattooed

area over the total cross-section area with 14.0, 8.3, 1.5, and 1.3 injections mm^{-2} measured over cross sections of the phantom tissue. G) Micrographs of phantom substrates tattooed at angles of 908, 808, 708, 608, 508, and 458 between the needle of the tattoo gun and the skin surface. Scale bars=150 mm. H) Measured tattooing angles compared with the expected tattooing angles.

The pH sensor combination (**Figure A11, A**) was tested in aqueous solutions, yielding a color change from yellow to blue in the pH range from 5.0 to 9.0 with increments of 1.0 pH value. **Figure A11, B** shows the absorbance spectra of pH sensors in aqueous solutions at different pH values. The absorbance intensity peak at 620 nm decreased by 85% as the pH decreased from 9.0 to 5.0. The pH sensors were imaged with a smartphone camera and red, green, and blue (RGB) values were analyzed with a MATLAB algorithm (**Figure A11, C**). In response to buffered pH 8.0 solution, the absorbance value of the pH sensor in aqueous solution increased two-fold to saturate within 5 s (**Figure A11, D**). No obvious variation in the absorbance of the pH sensor (pH 8.0) was measured in aqueous solution and in the ex vivo skin tissue after exposure to UV light (2 W) for 30 min, showing stability for long-term use (**Figure A11, E**). The diffusion of the pH sensor (pH 8.0) in the ex vivo porcine skin tissue was evaluated (**Figure A11, F**). By measuring tattooed sensor diameters and RGB triplets of the sensor, no obvious sensor-area changes were observed over 5 h, indicating the stability of the sensors in the skin tissue. Buffered pH solutions (pH 5.0–9.0, 200 mL) were introduced to the pH-sensor-functionalized ex vivo skin tissues to measure the colorimetric changes. **Figure A11, G** shows the RGB values of pH-sensitive biosensors in ex vivo porcine skin tissue at pH values from 5.0 to 9.0. The inset in Figure 3 g shows the photographs of the pH-dependent color variation of the sensors. Video S1 in the Supporting Information shows the pH-sensor color changes (pH 8.0 to 5.0) and reversibility. **Figure A11, H** shows the CIE 1931 chromaticity diagram of the calibration points of the colors obtained in ex vivo porcine tissues (white) and their mean values (black). **Figure A11, I** shows the correlation of the biosensors in aqueous solutions and ex vivo skin samples compared to the actual pH values measured by an ion-selective electrode (gold standard). Despite the subtle variations in the RGB triplets in ex vivo tissues compared to aqueous solutions, the measurements yielded a standard error of 0.3 pH value in aqueous solutions and 0.2 pH value in the ex vivo tissues.

The glucose sensor was based on the chemistry illustrated in **Figure A11, A**. The absorbance spectra of glucose biosensors in aqueous solutions at different glucose concentrations (2.0 to 50.0 $mmolL^{-1}$) is displayed in **Figure A11, B**. An absorbance peak intensity at 680 nm increased when the glucose concentration in aqueous solutions increased to 50.0 $mmolL^{-1}$. **Figure A11, C** shows RGB readouts of glucose sensors with a smartphone camera in aqueous solutions. The glucose sensor in aqueous solution exhibited a color change from yellow to dark green when the glucose concentration was increased from 2.0 to 50.0 $mmolL^{-1}$ (Figure A11, C inset). The response time of the glucose sensor was 30 s for a concentration of 5 $mmolL^{-1}$ (**Figure A11, D**). No obvious variations were measured in the absorbance peak of the glucose sensor in aqueous solutions and ex vivo skin samples in response to a glucose concentration of 5 mmolL-1 after 30 min UV (2 W) exposure, showing stability for long-term use (**Figure A11, E**). The diffusion test showed the high stability of the tattooed glucose sensor after 5 h in the ex vivo skin tissue in 5 $mmolL^{-1}$ glucose solution (**Figure A11, F**). **Figure A11, G** shows the RGB values of glucose-sensitive biosensors injected in an ex vivo porcine skin tissue. The inset in Figure A11, G shows the glucose-concentration-dependent color variation of the sensors. **Figure A11, H** shows the CIE 1931 chromaticity diagram of the calibration points of the glucose-sensor colors obtained in ex vivo tissues (white) and their mean values (black). **Figure A11, I** illustrates the glucose concentrations measured with a smartphone camera in aqueous solutions and in ex vivo skin tissue samples. The measurements yielded a standard error of 0.3 $mmolL^{-1}$ in aqueous solutions and 0.2 $mmolL^{-1}$ in ex vivo tissue samples.

Figure A12, A shows the chemistry of the sensor. **Figure A12, B** displays the absorbance spectra of albumin sensors in aqueous solutions at different concentrations (0.0–5.0 gL^{-1}). The absorbance peak intensity at 620 nm increased as the albumin concentration increased from 0.0 to 5.0 gL^{-1}. **Figure A12, C** shows the RGB triplets of the sensor in the presence of albumin imaged with a smartphone camera in aqueous solutions.

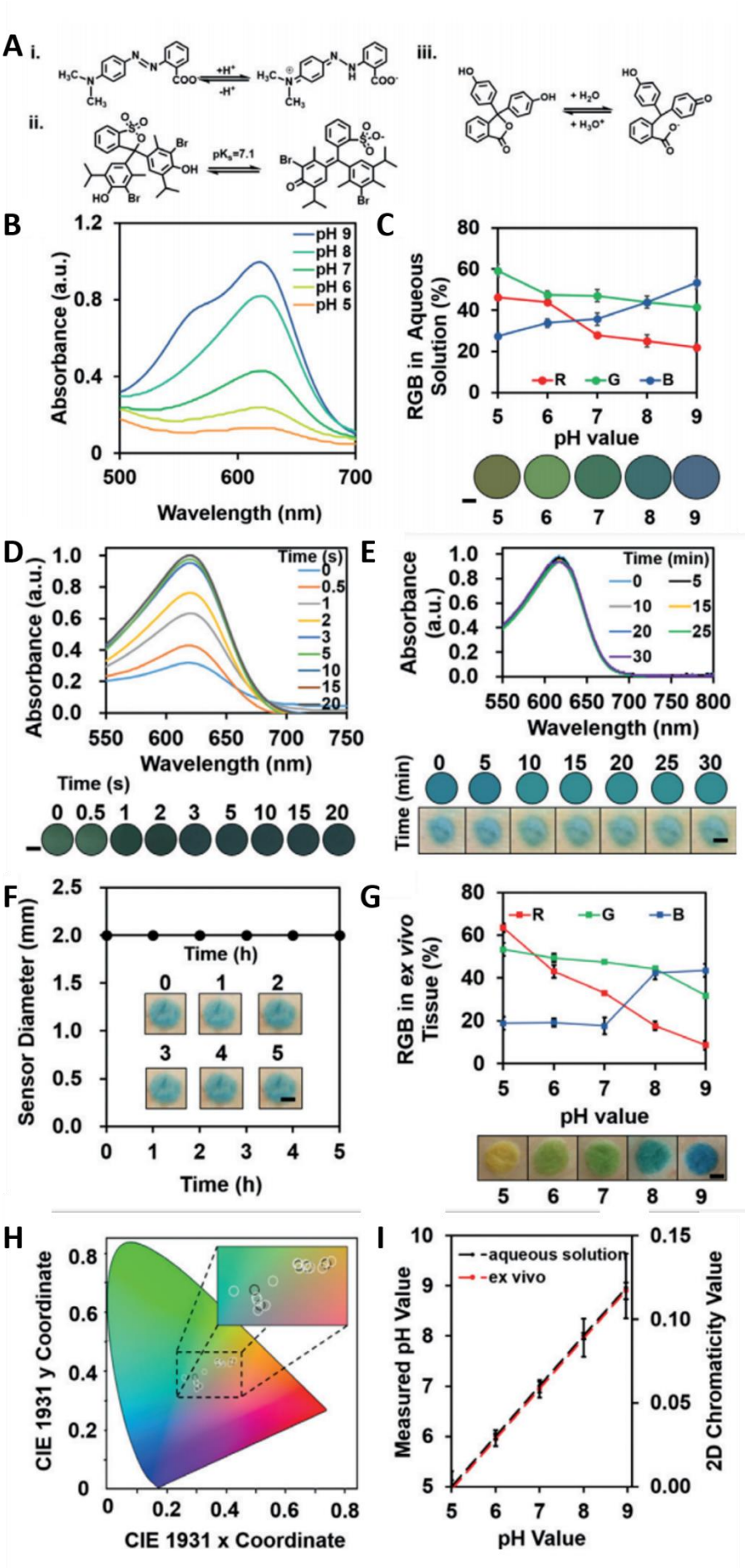
A
i.
ii.
iii.
pKa=7.1
+ H2O
+ H3O+
B
Absorbance (a.u.)
Wavelength (nm)
pH 9
pH 8
pH 7
pH 6
pH 5
C
RGB in Aqueous Solution (%)
pH value
R
G
B
D
Absorbance (a.u.)
Wavelength (nm)
Time (s)
0
0.5
1
2
3
5
10
15
20
E
Absorbance (a.u.)
Wavelength (nm)
Time (min)
0
5
10
15
20
25
30
F
Sensor Diameter (mm)
Time (h)
G
RGB in ex vivo Tissue (%)
pH value
H
CIE 1931 y Coordinate
CIE 1931 x Coordinate
I
Measured pH Value
2D Chromaticity Value
pH Value
aqueous solution
ex vivo

Figure A11. Dermal pH sensors. a) Chemical structures of the pH-sensing compounds: methyl red, bromothymol blue, and phenolphthalein. i) Methyl red exhibits a color change from red (pH 4.3) to yellow (pH 6.2). ii) Bromothymol blue shows a variation from yellow (pH 6.0) to blue (pH 7.6). iii) Phenolphthalein changes color from pink (pH 8.2) to fuchsia (pH 12.0). The net result is a color change from orange–red to blue, via yellow and green. b) Absorbance spectra of the sensors in the pH range 5.0 to 9.0 with steps of 1.0 in aqueous solutions. c) RGB triplet of the sensors at pH values from 5.0 to 9.0 at steps of 1.0 in aqueous solutions. Inset shows colors of the different solutions. Scale bar=1.0 mm. d) Absorbance spectra and images (inset) of the pH sensor in buffered aqueous solutions as a function of response time. Scale bar=1.0 mm. e) Stability of pH sensor under UV exposure (2 W) for 30 min. Absorbance spectra and images (inset) of the pH sensor in aqueous solutions (top) and in ex vivo porcine skin (bottom). Scale bar=1.0 mm. f) Diffusion test of pH sensor in ex vivo porcine skin tissue (pH 8.0). Insets show images of pH sensor tattooed in the porcine skin. Scale bar=1.0 mm. g) RGB triplets of tattooed pH sensor at pH values from 5.0 to 9.0 at steps of 1.0. Insets show colors of the dermal sensors in ex vivo porcine skin tissues at different pH values. Scale bar=1.0 mm. h) CIE 1931 chromaticity diagram obtained from the readout algorithm in ex vivo measurements. White circles highlight calibration points, black circles represent their respective mean value. i) Comparison of algorithm readouts in aqueous solution (black) and in ex vivo tissues (red) with an ion-selective pH electrode. The error bars (n=3) represent the standard deviation of the mean, representing the distance from the measurement points 2D (xj, yj) in CIE 1931 chromaticity space.

The albumin sensor changed color from gray to blue in the concentration range from 0.0 to 5.0 gL-1 (Figure A12, C inset). The response time of the colorimetric biosensor to albumin (4.0 $mmolL^{-1}$) was 30 s (**Figure A12, D**). No obvious variations were observed in the absorbance peak of the biosensor in response to albumin (0.3 gL^{-1}) in aqueous solutions and in the ex vivo tissue samples after 30 min UV exposure (2 W), showing stability for long-term use (**Figure A12, E**). The diffusion test showed high stability of the tattooed albumin sensor in the ex vivo porcine skin tissue in albumin solutions (0.3 $mmolL^{-1}$, **Figure A12, F**). **Figure A12, G** illustrates the albumin concentration dependent RGB triplet variation of the sensors in *ex vivo* tissue samples and their respective photographs. **Figure A12, H** shows the CIE 1931 chromaticity diagram of the calibration points of the albumin sensor colors measured in *ex vivo* tissues (white) and their mean values (black).

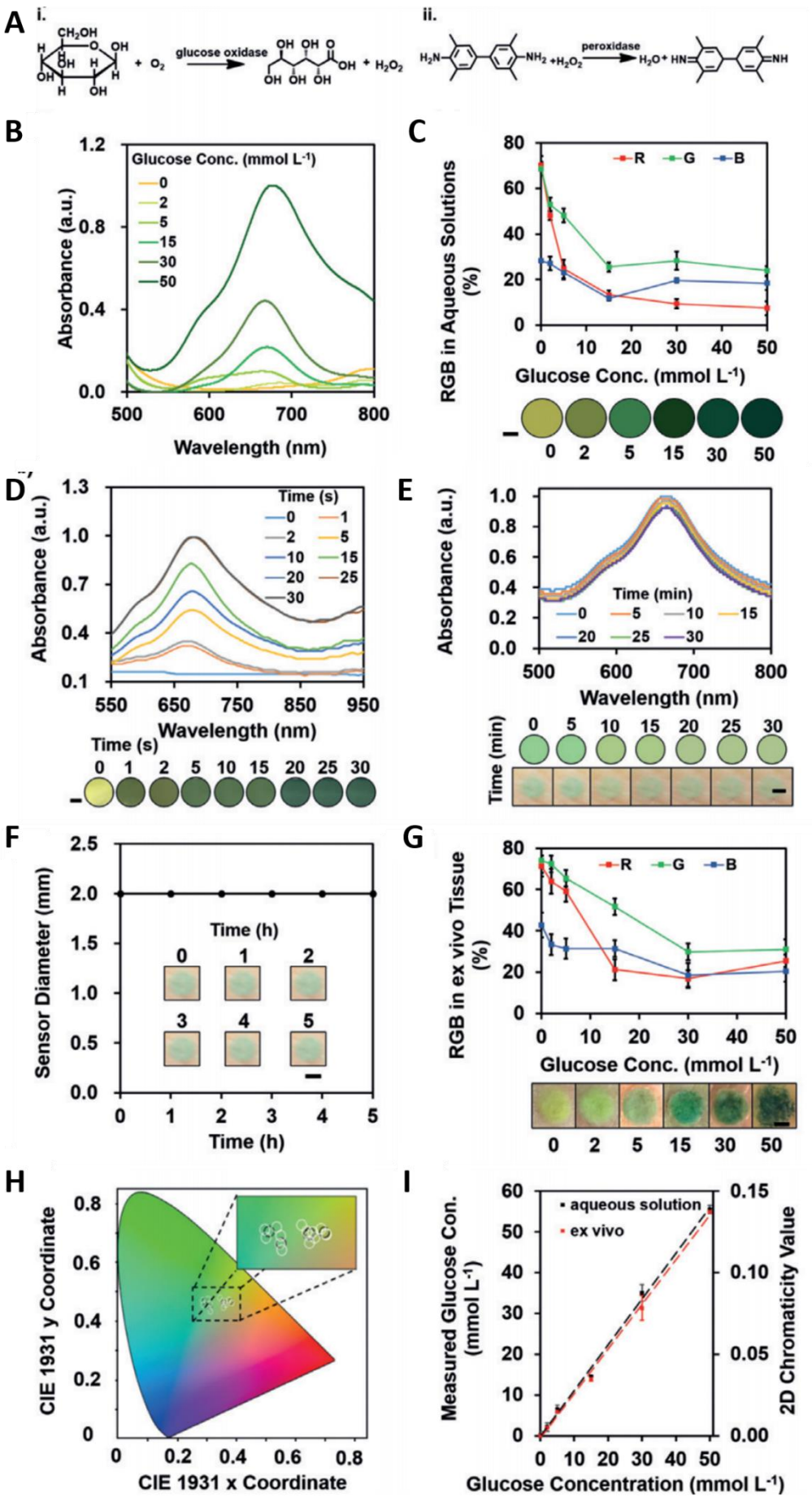
A
i.
glucose oxidase
ii.
peroxidase
B
Glucose Conc. (mmol L-1)
0
2
5
15
30
50
Absorbance (a.u.)
Wavelength (nm)
C
R
G
B
RGB in Aqueous Solutions (%)
Glucose Conc. (mmol L-1)
D
Time (s)
Absorbance (a.u.)
Wavelength (nm)
E
Time (min)
Absorbance (a.u.)
Wavelength (nm)
Time (min)
F
Sensor Diameter (mm)
Time (h)
G
RGB in ex vivo Tissue (%)
Glucose Conc. (mmol L-1)
H
CIE 1931 y Coordinate
CIE 1931 x Coordinate
I
aqueous solution
ex vivo
Measured Glucose Con. (mmol L-1)
2D Chromaticity Value
Glucose Concentration (mmol L-1)

Figure A12. Dermal glucose sensors. a) Chemical structures of the glucose-sensing compounds: glucose oxidase (GOD), peroxidase (POD), and 3,3',5,5'-tetramethylbenzidine (TMB); i) d-glucose is oxidized to d-gluconolactone and hydrogen peroxide is produced. ii) Under peroxidase catalysis, hydrogen peroxide oxidizes TMB to form a blue–green dye. b) Absorbance spectra of the sensors in aqueous solutions in the range of 0–50 $mmolL^{-1}$ glucose. c) RGB triplets of sensors in aqueous solutions at glucose concentrations of 0, 2, 5, 15, 30, and 50 $mmolL^{-1}$. The inset shows the photographs of the sensor colors at different glucose concentrations (0–50 $mmolL^{-1}$). Scale bar=1.0 mm. d) Absorbance spectra and images (inset) of the glucose sensor in aqueous solution containing glucose (5 $mmolL^{-1}$) as a function of response time. Scale bar=1.0 mm. e) Absorbance spectra of glucose sensor exposed to UV light (2 W) for 30 min. Inset images show sensors in aqueous solutions (top) and in ex vivo porcine skin samples (bottom). Scale bar=1.0 mm. f) Diffusion test of glucose sensor in an ex vivo porcine skin sample. Insets show images of glucose sensor in the porcine skin in the presence of glucose (5 $mmolL^{-1}$). Scale bar=1.0 mm. g) RGB triplets of dermal biosensors at different glucose concentrations (0–50 $mmolL^{-1}$). Insets show colors of the dermal glucose sensors in ex vivo tissues at different glucose concentrations (0–50 $mmolL^{-1}$). Scale bar=1.0 mm. h) CIE 1931 chromaticity diagram obtained from the smartphone camera in ex vivo measurements, showing calibration points (white) and their respective mean values (black). i) Smartphone readouts of glucose sensors in aqueous solutions (black) and in ex vivo tissues (red) in response to glucose concentrations (0–50 $mmolL^{-1}$). The error bars (n=3) represent the standard deviation of the mean representing the mean distance from the measurement points 2D (xj, yj) in CIE 1931 chromaticity space.

Figure A12, I shows the correlation of the albumin biosensors in aqueous solutions and *ex vivo* skin samples compared with the actual albumin values. The measurements yielded a standard error of 0.2 gL^{-1} in aqueous solutions and 0.1 gL^{-1} in *ex vivo* tissue samples.

Dermal sensors were multiplexed in ex vivo porcine skin tissues to provide quantitative imaging of pH, glucose, and albumin assays using a smartphone camera. **Figure A13, A** shows the smartphone readout process performed at 200 lux at ambient light conditions. The smartphone camera was placed at 5 mm normal distance to the multiplexed dermal sensors. **Figure A13, B** illustrates multiplexed pH, glucose, and albumin dermal sensors in the form of aesthetic tattoos.

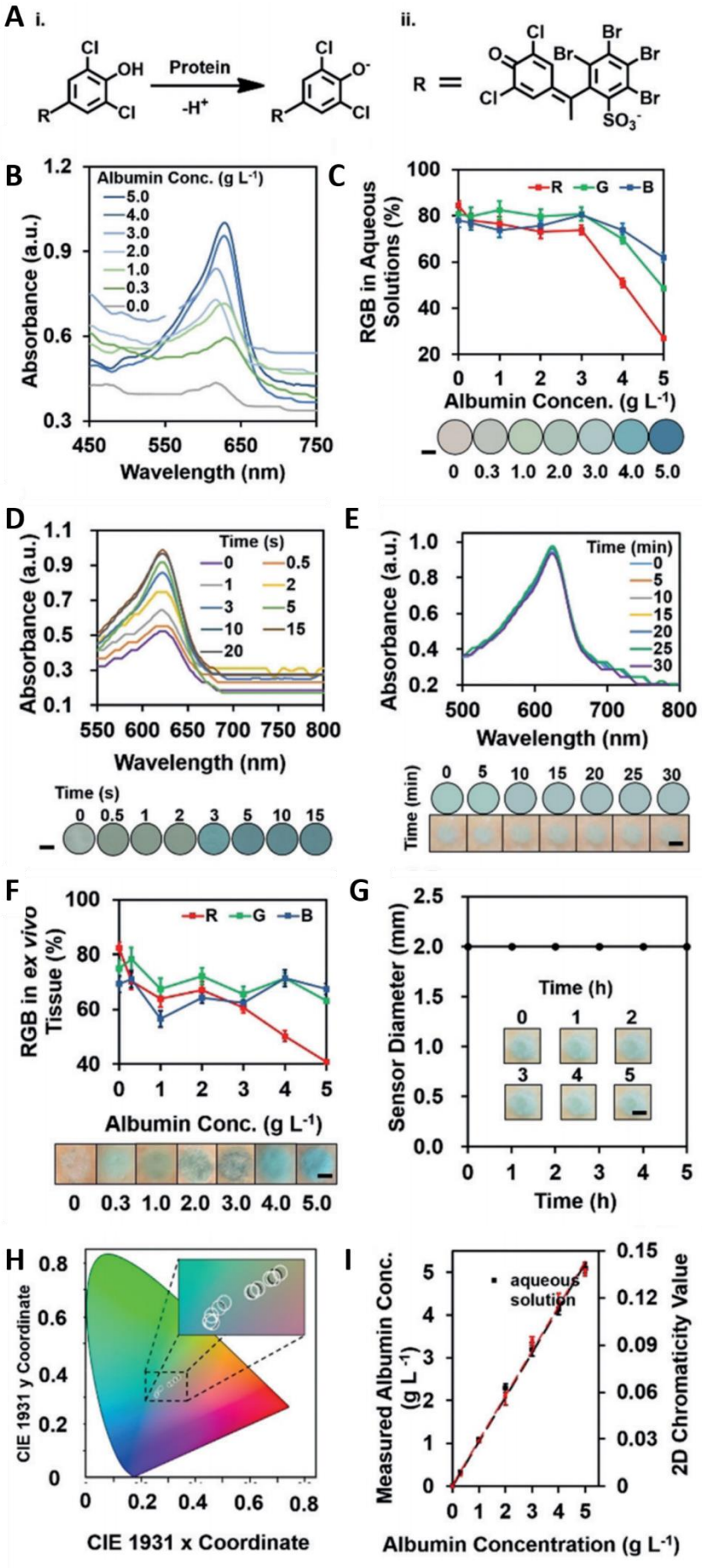
A
i.
Cl
OH
Protein
-H+
Cl
R
Cl
O-
Cl
R
Cl
ii.
R =
Cl
Br
Br
Br
O
Cl
Br
SO3-
B
Albumin Conc. (g L-1)
5.0
4.0
3.0
2.0
1.0
0.3
0.0
Absorbance (a.u.)
Wavelength (nm)
C
R
G
B
RGB in Aqueous Solutions (%)
Albumin Concen. (g L-1)
0 0.3 1.0 2.0 3.0 4.0 5.0
D
Time (s)
0
0.5
1
2
3
5
10
15
20
Absorbance (a.u.)
Wavelength (nm)
Time (s)
0 0.5 1 2 3 5 10 15
E
Time (min)
0
5
10
15
20
25
30
Absorbance (a.u.)
Wavelength (nm)
Time (min)
0 5 10 15 20 25 30
F
R
G
B
RGB in ex vivo Tissue (%)
Albumin Conc. (g L-1)
0 0.3 1.0 2.0 3.0 4.0 5.0
G
Sensor Diameter (mm)
Time (h)
0
1
2
3
4
5
Time (h)
H
CIE 1931 y Coordinate
CIE 1931 x Coordinate
I
aqueous solution
Measured Albumin Conc. (g L-1)
2D Chromaticity Value
Albumin Concentration (g L-1)

Figure A13. Dermal albumin sensors. a) Chemical structure of albumin sensor containing 3',3'',5',5''-tetrachlorophenol-3,4,5,6-tetrabromosulfophthalein. b) Absorbance spectra of the sensors in the albumin range 0.0 g L^{-1} to 5.0 g L^{-1} in aqueous solutions. c) RGB triplets of the sensors at albumin concentrations from 0.0 to 5.0 g L^{-1} in aqueous solutions. Inset shows sensor colors in different albumin concentrations. Scale bar=1.0 mm. d) Absorbance spectra and images (inset) of the biosensor to albumin (4.0 mmolL^{-1}) as a function of response time in aqueous solutions. Scale bar=1.0 mm. e) Stability test of the albumin sensor exposed to UV light (2 W) for 30 min. i) Absorbance spectra; ii) images of aqueous solution (top) and ex vivo porcine skin (bottom). Scale bar=1.0 mm. f) Diffusion test of albumin sensor in the ex vivo porcine skin for 5 h. Inset shows images of albumin sensor tattooed in the ex vivo porcine skin. Scale bar=1.0 mm. g) RGB triplets of the sensors in albumin (0.3 to 5.0 g L^{-1}) in aqueous solutions. Inset shows colors of the dermal sensors in ex vivo tissues at different albumin concentration values. Scale bar=1.0 mm. h) CIE 1931 chromaticity diagram obtained using a smartphone camera in ex vivo measurements, showing calibration points (white) and their respective mean values (black). i) Quantitative readouts of albumin biosensors in aqueous solutions (black) and in ex vivo tissues (red). The error bars (n=3) represent the standard deviation of the mean representing the mean distance from the measurement points 2D (xj,yj) in CIE 1931 chromaticity space.

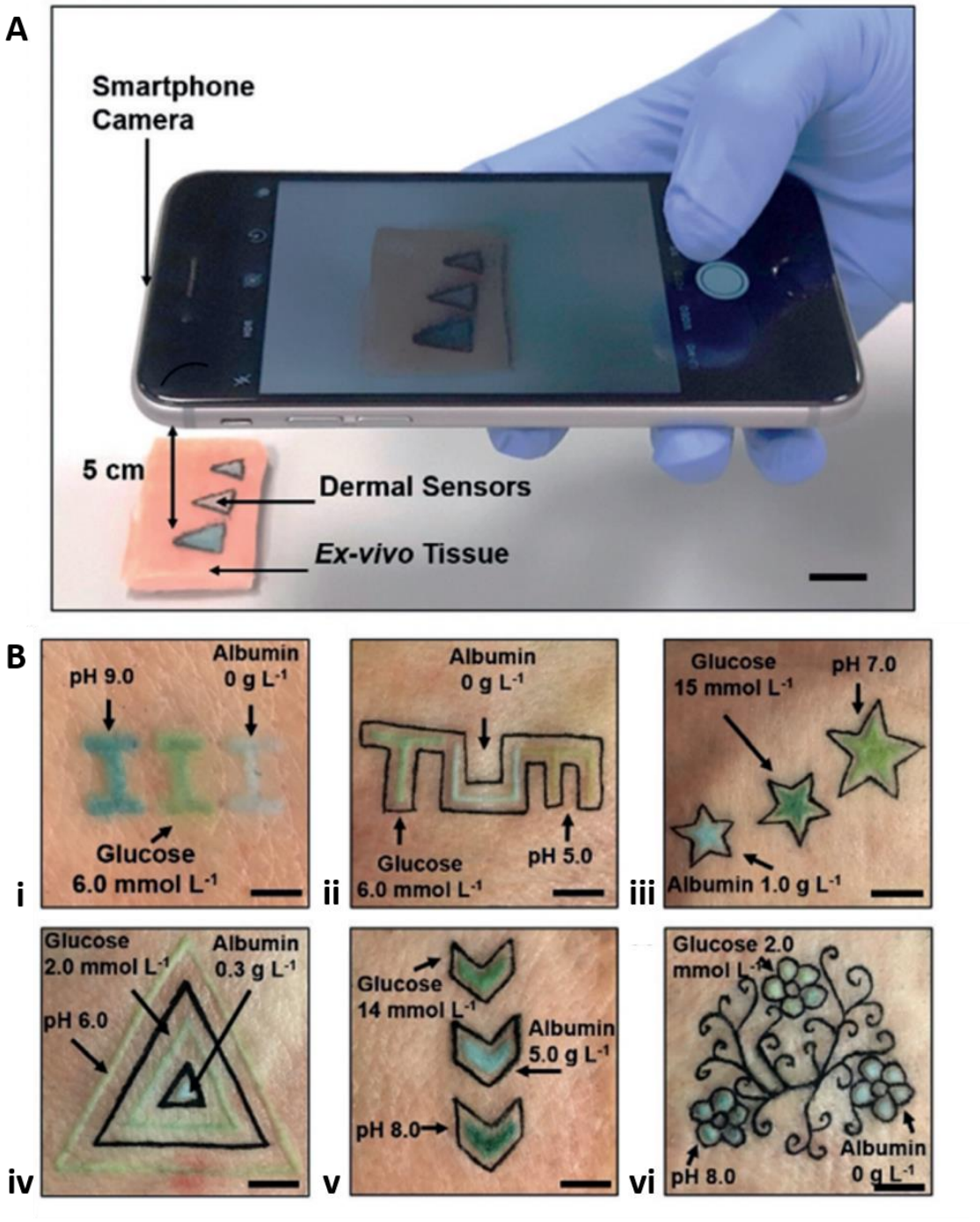

Figure A14. Multiplex dermal sensors. a) The assay is imaged using a smartphone camera at 5.0 mm of distance and at normal incidence to the detection area. Scale bar=1.0 cm. b) Multiplexed dermal biosensors with individual areas devoted to the sensing of a different analyte, yielding different colors based on the concentrations of pH, glucose, and albumin. Colorimetric readouts in i) alkalosis, ii) metabolic acidosis, iii) hyperglycemia, iv) hypoglycemia, v) hypoalbuminemia, and vi) co-developed hypoglycemia and respiratory alkalosis. Scale bars=1.0 cm.

Appendix VI

Additional Methods: Soaking

Chapter 2 and *Chapter 5* of the thesis were focused on the inscription of microfluidic networks within contact lenses for the purpose of integrating sensors into them. As an alternative, preliminary tests of whole-colored contact lenses were performed with anthocyanin biocompatible, pH-sensitive dye.

Commercial soft contact lenses were soaked into anthocyanin aqueous solution at concentrations of 0.35, 0.5, 0.75, 1.00, and 1.50 $mmolL^{-1}$ for 24 hours (**Figure A15, A**) and tested under physiological pH values, yielding a color change from pink (pH 6.5) to purple (7.0) and water green (pH 7.5) (**Figure A15, B**).

Transmission spectra of pH-sensitive contact lenses were acquired with the setup illustrated in **Figure A15, C**. The influence of anthocyanin concentration in aqueous solution on the coloring of the contact lens was evaluated at pH 6.5, 7.0, and 7.5, resulting in increasingly darker colors, more visible with the naked eye, at higher concentrations (**Figure A15, D**). The colors were readout using a color grab smartphone application and the variation in the red, green, and blue composition over anthocyanin concentration was plotted (**Figure A15, E**).

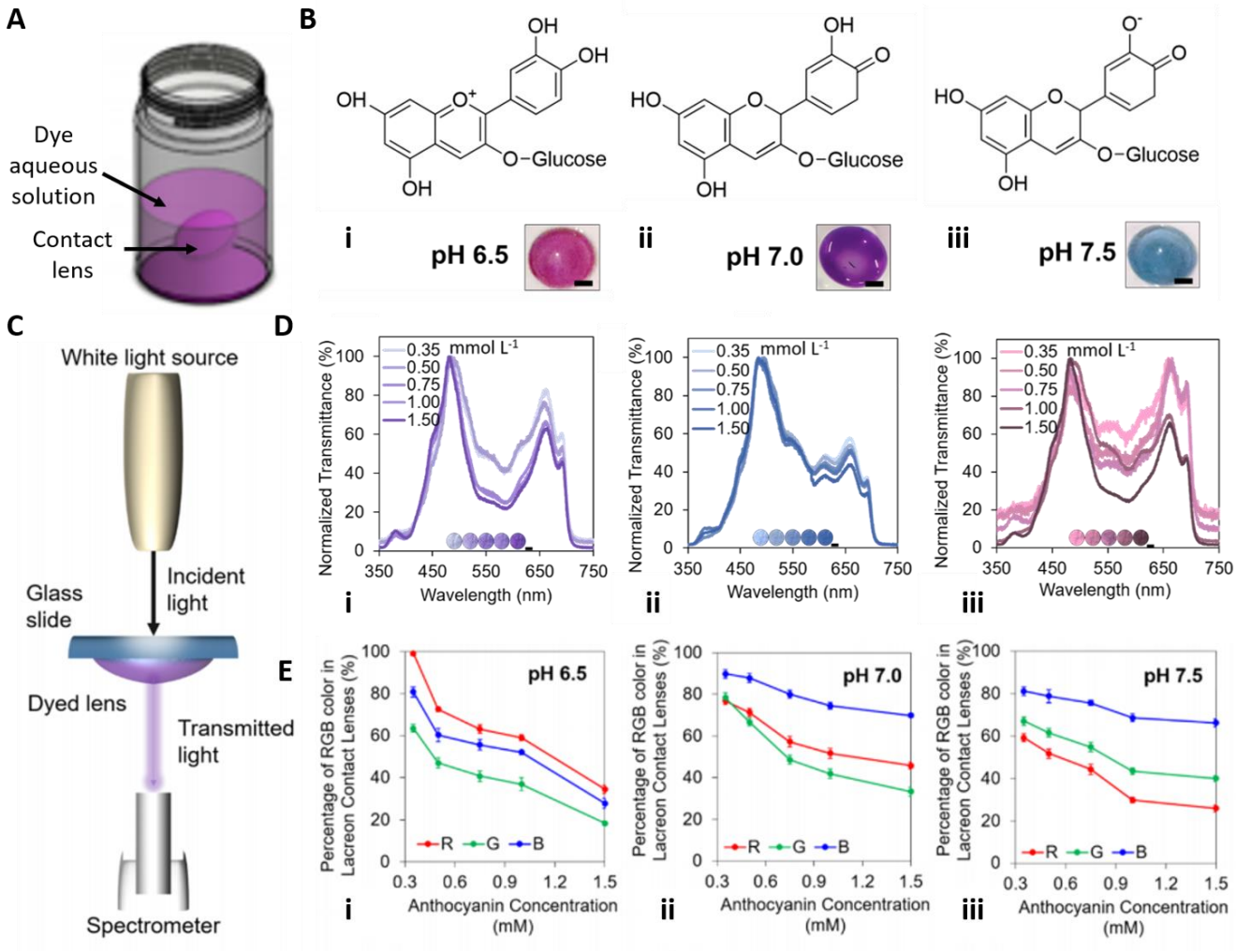

Figure A15. Anthocyanin-functionalized soft contact lenses for ocular pH sensing. and its optimization for dying soft contact lenses. A) Schematic of the soaking method. B) Anthocyanin chemical formulas at pH physiological levels. (i) pH 6.5, (ii) pH 7.0, (iii), and pH 7.5. Inset photographs show tinted contact lenses at different pH values. Scale bars: 5.0 mm. C) Transmittance measurement setup. A white light source (450-1100 nm) irradiates the sample at normal incidence, and the transmitted light is recorded at the opposite side with a spectrometer. D) Normalized transmission spectra at different anthocyanin concentrations in solution at pH 6.5 (i), 7.0 (ii), and 7.5 (iii). E) Percentage of the RGB color of contact lenses at pH 6.5 (i), 7.0 (ii), and 7.5 (iii) as a function of the dye concentration in solution. Inset micrographs show the color of the contact lens and the normalized color acquired with the smartphone application. Scale bars: 2.0 mm.

Appendix VII

Supplementary Information on Ocular Pressure Monitoring

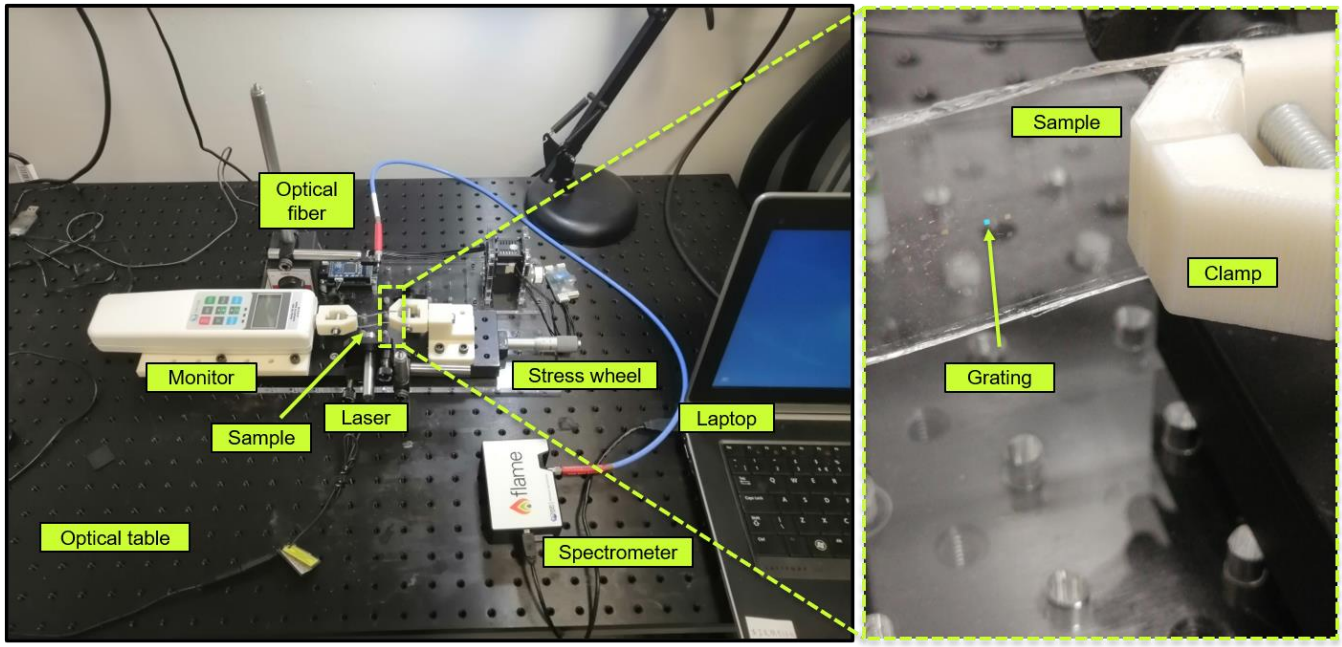

Figure A16. Setup for stress/strain characterization of diffraction gratings. The figure on the left shows the whole setup, build on an optical table. The sample is held firm by two clamps, from where the applied force is regulated manually via the stress wheel and the value (resolution 0.1 N) is visualized on the monitor. A portable laser shines the beam on the grating. The optical fiber underneath collects the spectra, and the spectrometer displays them in the laptop. On the right a zoom on the sample area is displayed.

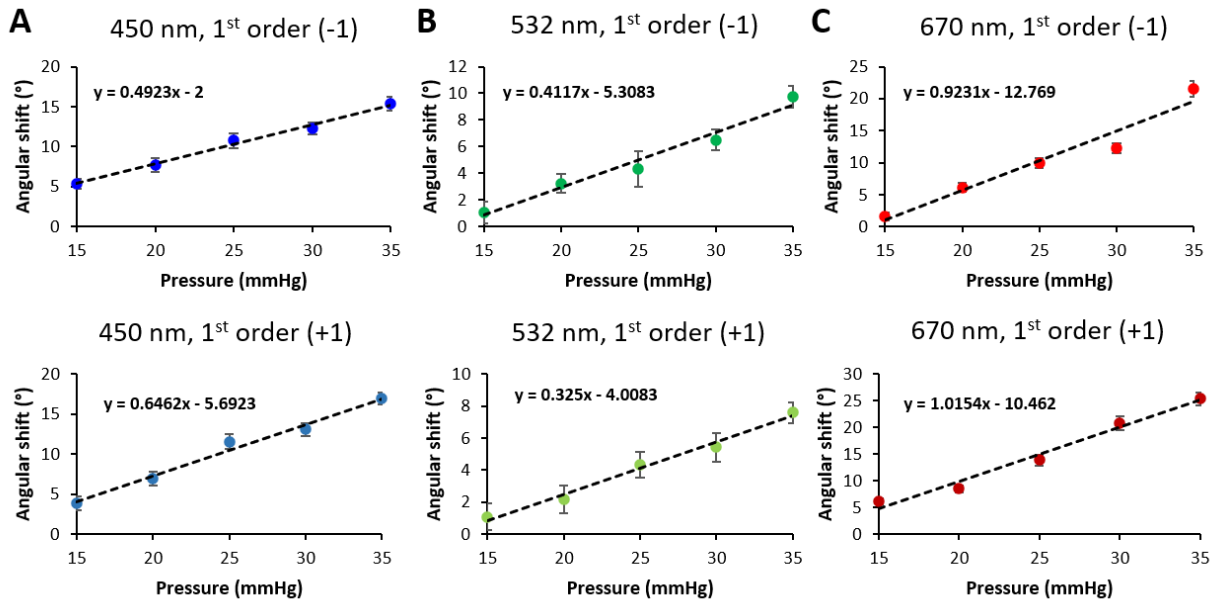

Figure A17. Pressure-dependent individual angular shifts in Pattern 1. A) First order diffraction shift at 450 nm. B) First order diffraction shift at 532 nm. C) First order diffraction shift at 670 nm.

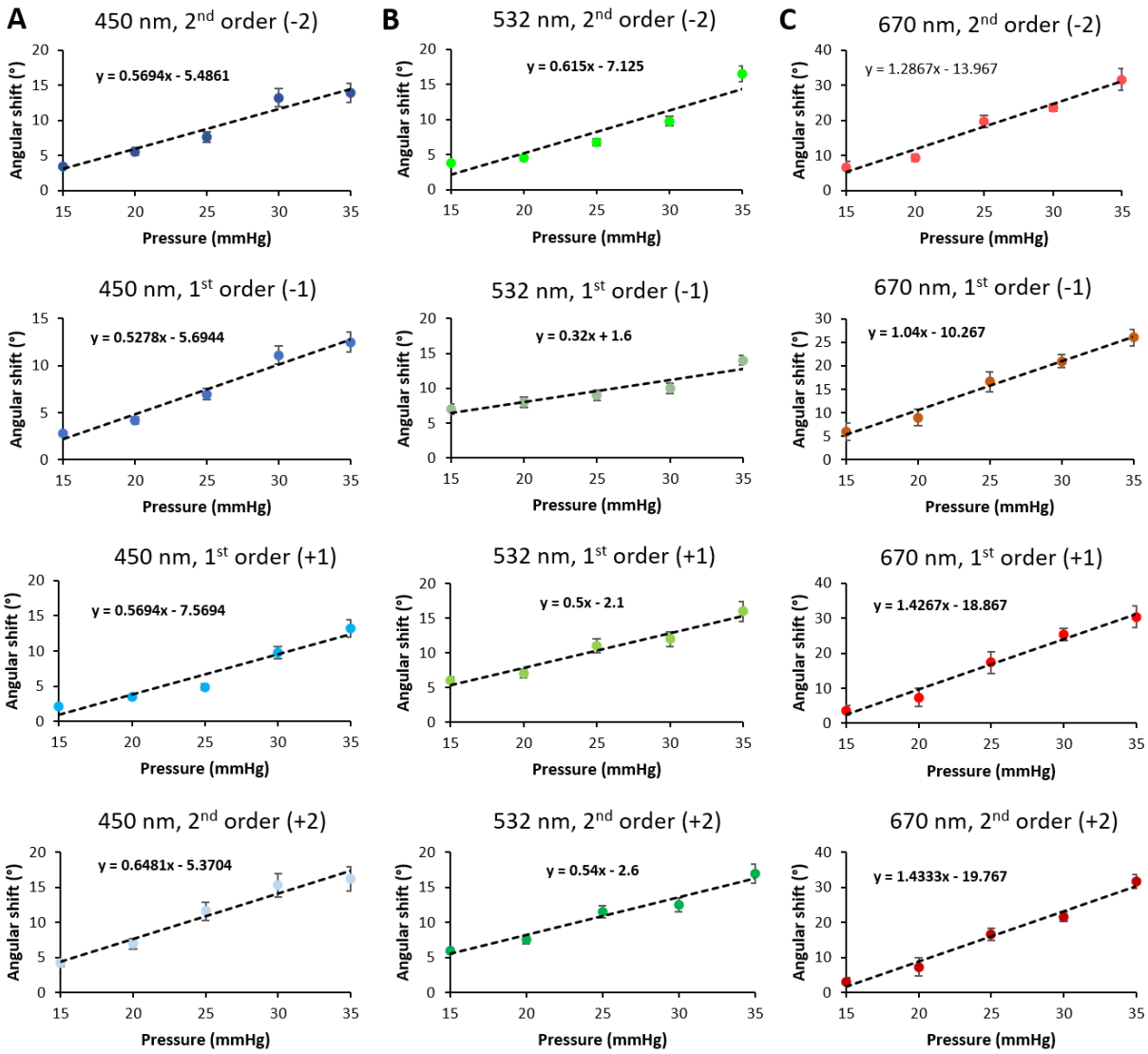

Figure A18. Pressure-dependent individual angular shifts in Pattern 2. A) First and second order diffraction shift at 450 nm. B) First and second order diffraction shift at 532 nm. C) First and second order diffraction shift at 670 nm.

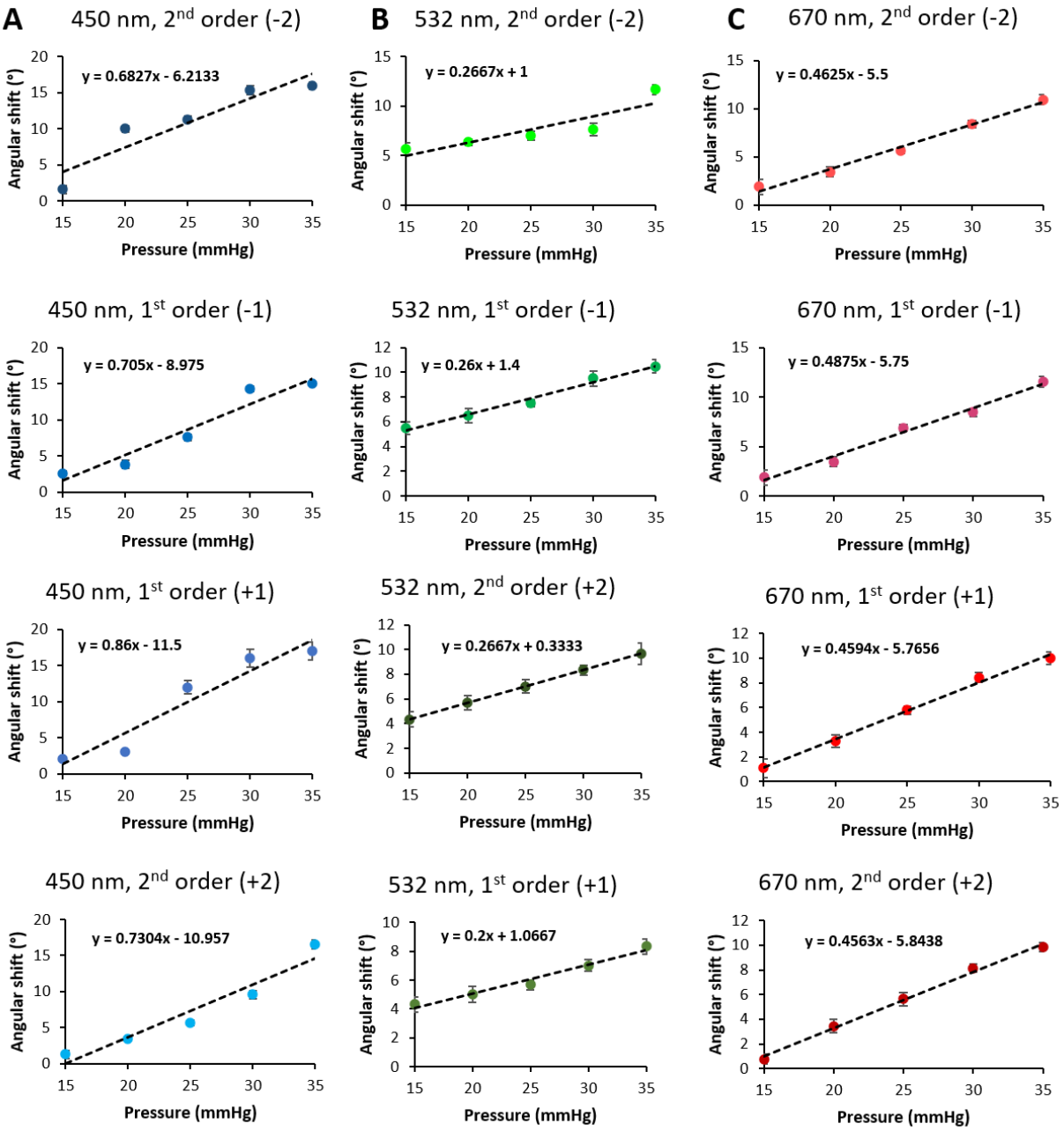

Figure A19. Pressure-dependent individual angular shifts in Pattern 3. A) First and second order diffraction shift at 450 nm. B) First and second order diffraction shift at 532 nm. C) First and second order diffraction shift at 670 nm.

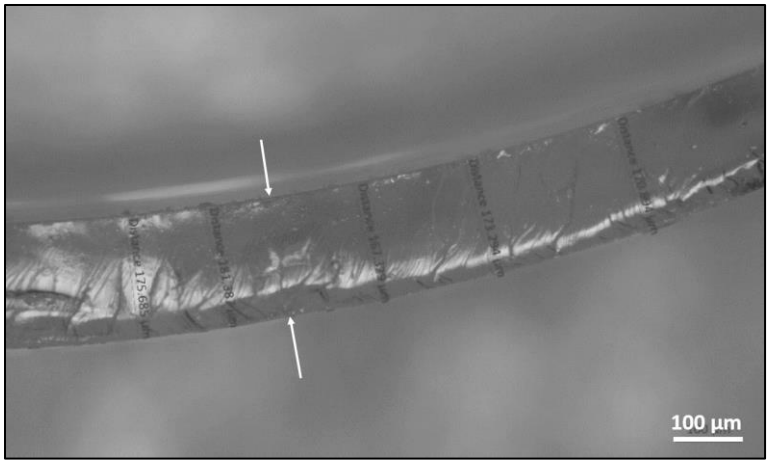

Figure A20. Cross section of a PDMS lab-made contact lens imaged with an optical microscope.

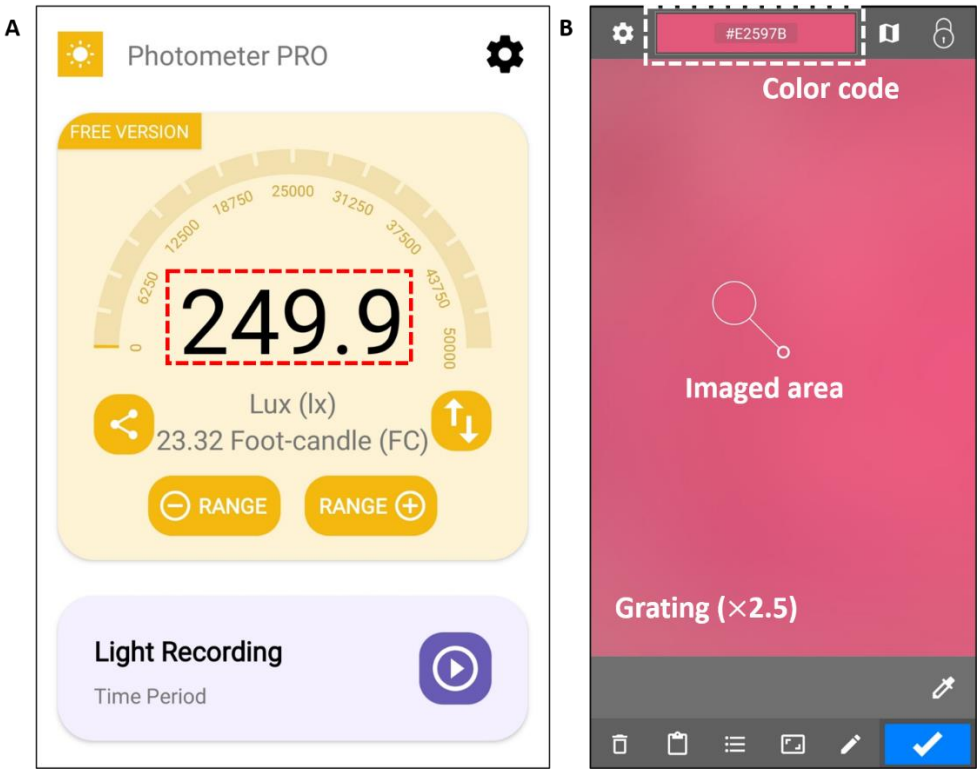

Figure A21. Screenshots of the smartphone apps. A) Photometer PRO, the ambient light level is continuously recorded. B) Color Grab, example of color readout of a grating. The value is further converted in RGB coordinates.

Appendix VIII

Supplementary Information on Paper-assisted Microfluidics

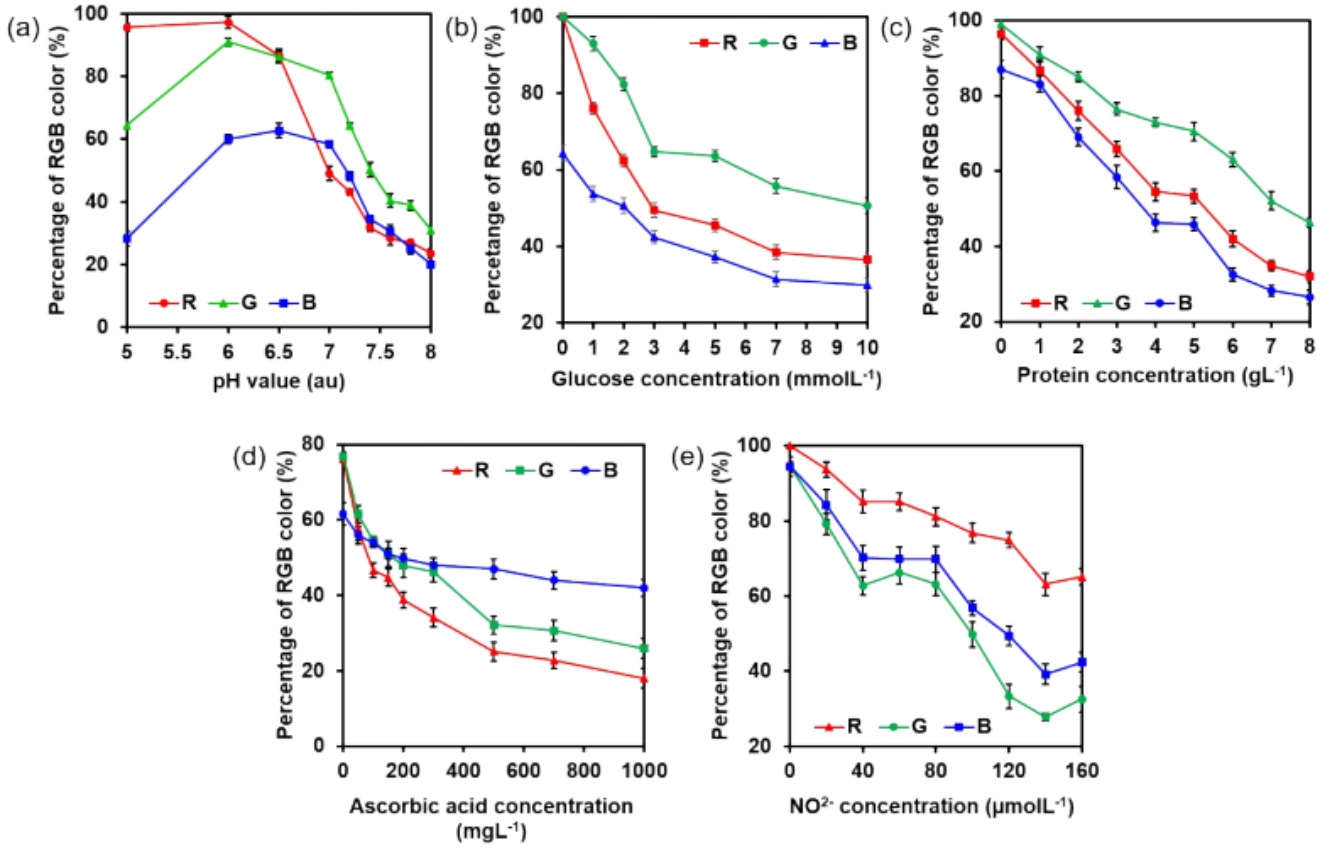

Figure A22. Percentage of RGB color at different concentration of analytes. (a) Hydrogen ions; (b) glucose; (c) proteins; (d) ascorbic acid; (e) nitrite ions.

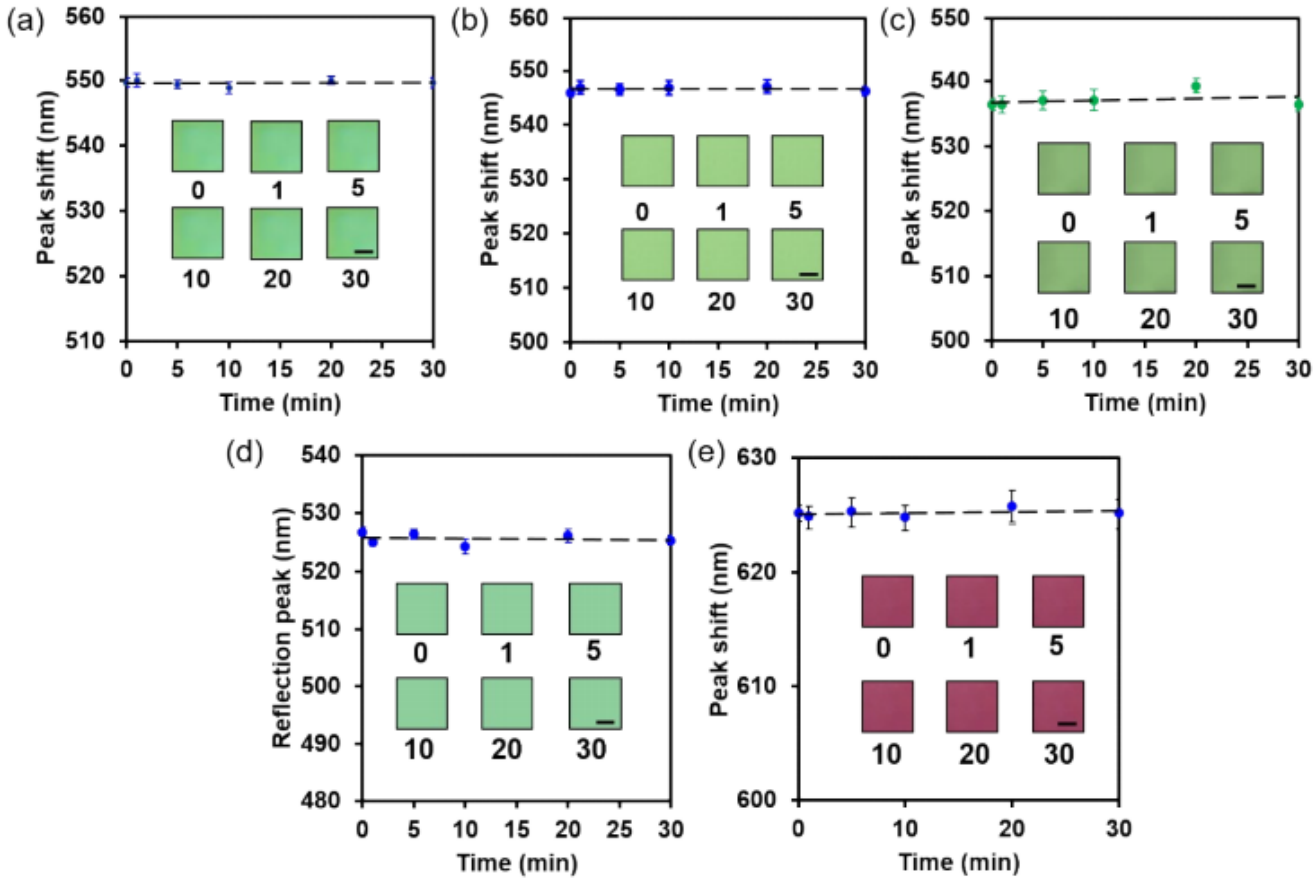

Figure A23. UV-dependent reflection peak trend when exposing the sensors to UV light at 355 nm for 0, 1, 5, 10, 20 and 30 minutes. (a) pH sensor, (b) glucose sensor), (c) protein sensor, (d) L-ascorbic acid sensor, (e) nitrite sensor.

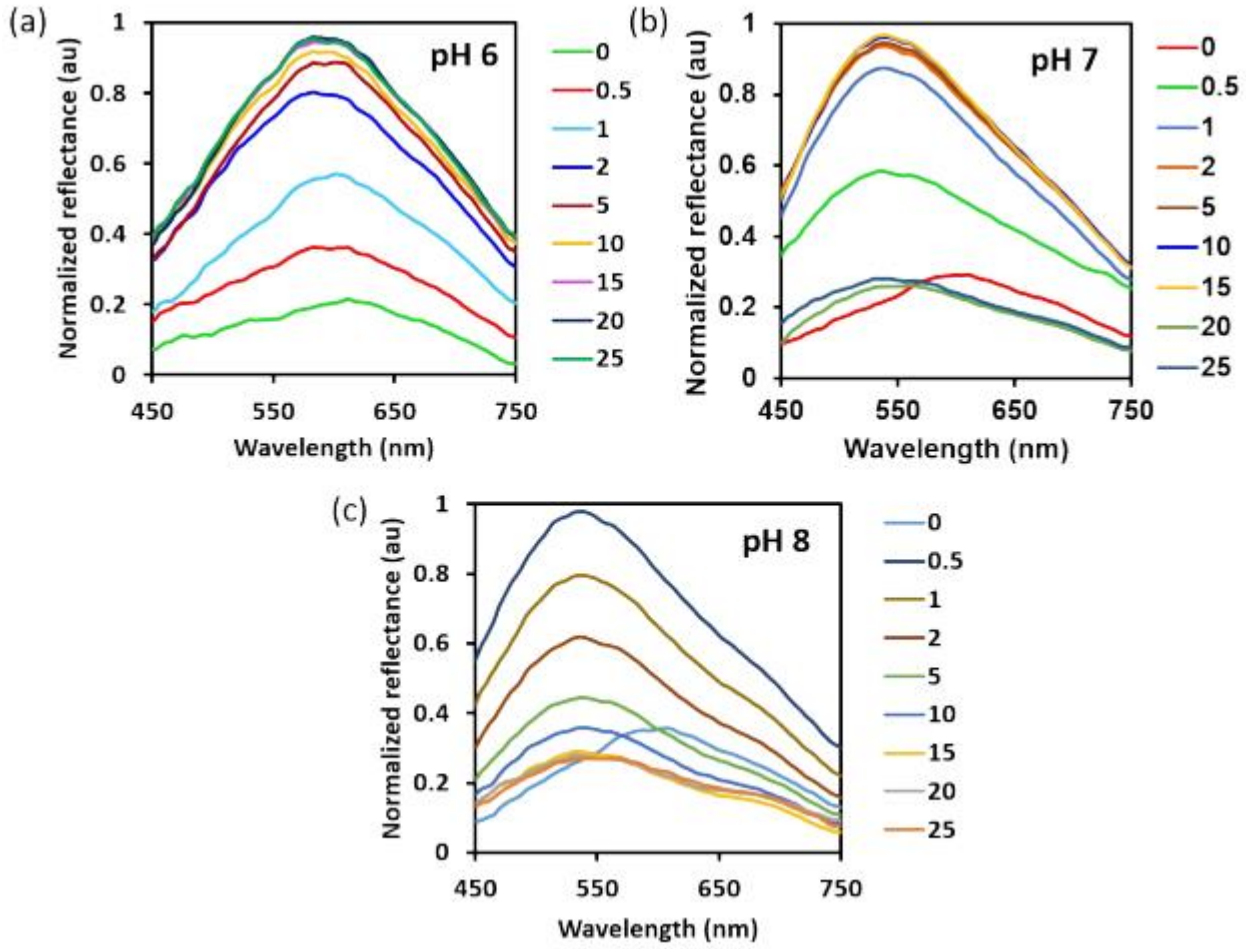

Figure A24. Time response of the pH sensor at different pH values. (a) pH 6.0: (i) Reflection spectra; (ii) reflection peak shift over time; (iii) Photographs of the sensor at discrete times: (b) pH 8.0: (i) Reflection spectra; (ii) reflection peak shift over time; (iii) Photographs of the sensor at discrete times; scale bar: 1.5 mm.

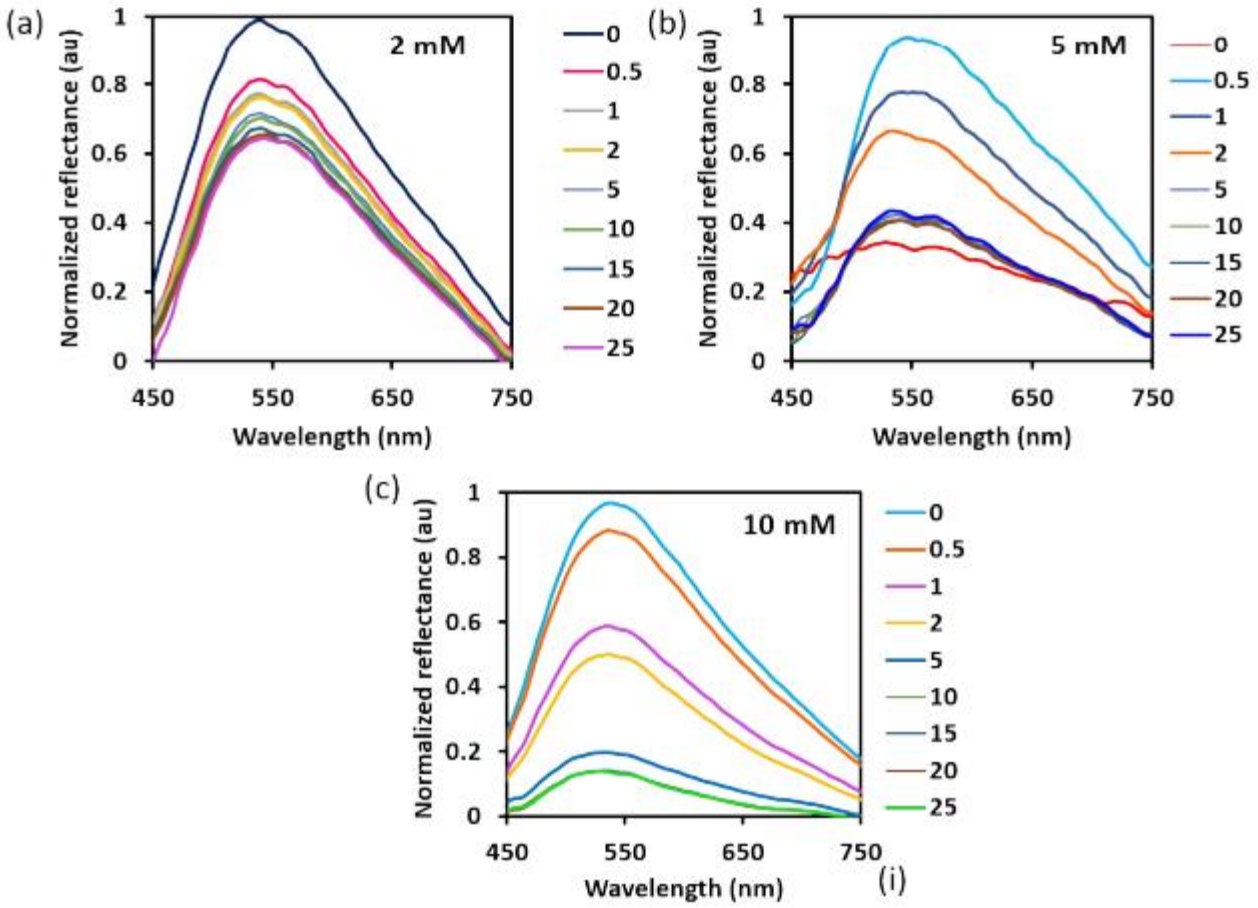

Figure A25. Time response of the glucose sensor at different glucose concentrations. (a) Time response when exposed to artificial tear fluid containing 5 mmol L^{-1} of D-glucose: (i) Reflection spectra; (ii) reflection peak shift over time; (iii) Photographs of the sensor at discrete times; (b) Sensor exposed to a D-glucose concentration of 10 mmol L^{-1}: (i) Reflection spectra; (ii) reflection peak shift over time; (iii) Photographs of the sensor at discrete times; scale bar: 1.5 mm.

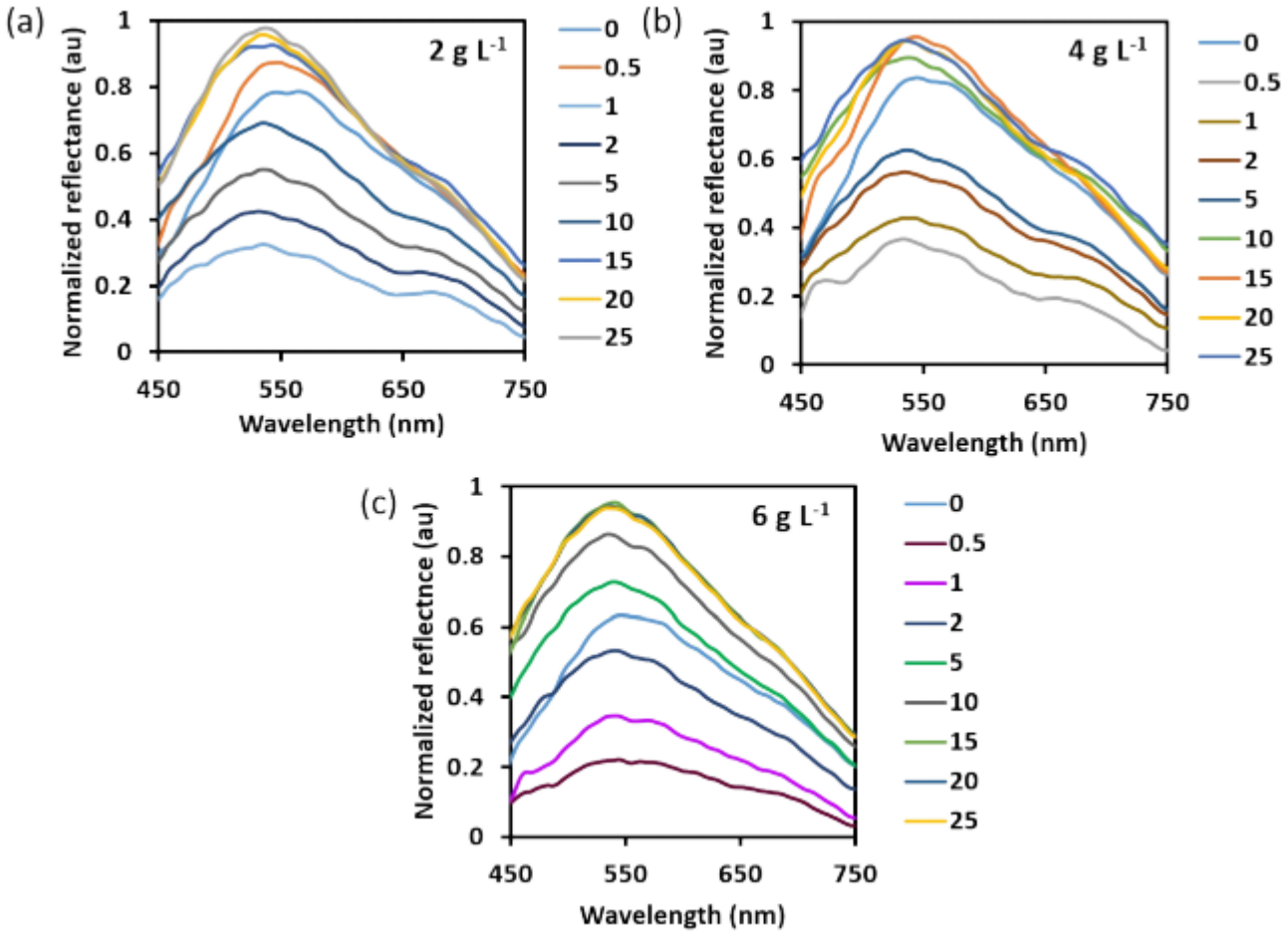

Figure A26. Time response of the protein sensor at different protein concentrations. (a) Protein concentration 2 g L^{-1}: (i) Reflection spectra; (ii) reflection peak shift over time; (iii) Photographs of the sensor at discrete times: (b) Protein concentration 4 g L^{-1}: (i) Reflection spectra; (ii) reflection peak shift over time; (iii) Photographs of the sensor at discrete times; scale bar: 1.5 mm.

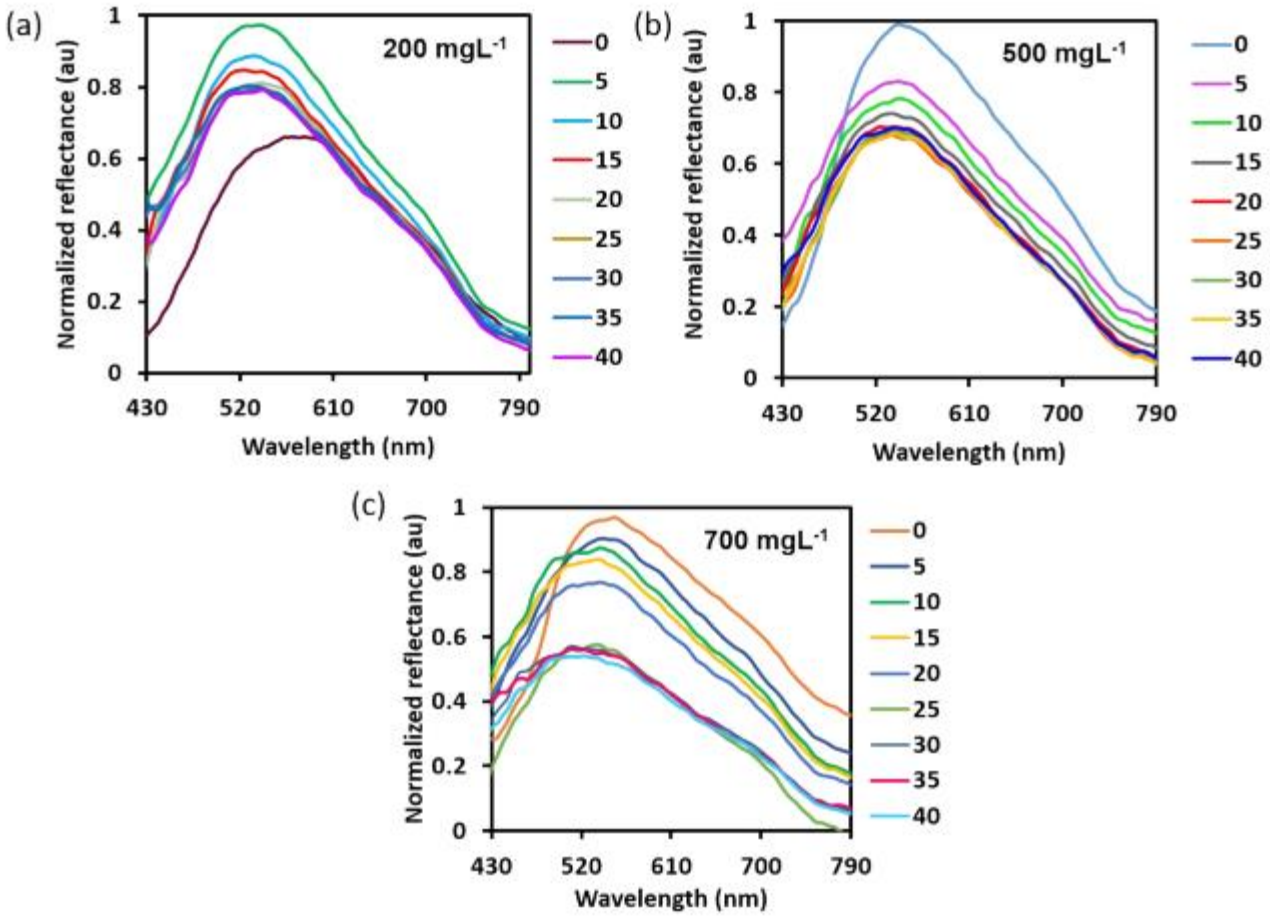

Figure A27. Time response of the L-ascorbic acid sensor at different concentrations. (a) Ascorbic acid concentration 500 mg L^{-1}. (i) Reflection spectra; (ii) reflection peak shift over time; (iii) Photographs of the sensor at discrete times: (b) Ascorbic acid concentration 700 mg L^{-1}: (i) Reflection spectra; (ii) reflection peak shift over time; (iii) Photographs of the sensor at discrete times; scale bar: 1.5 mm.

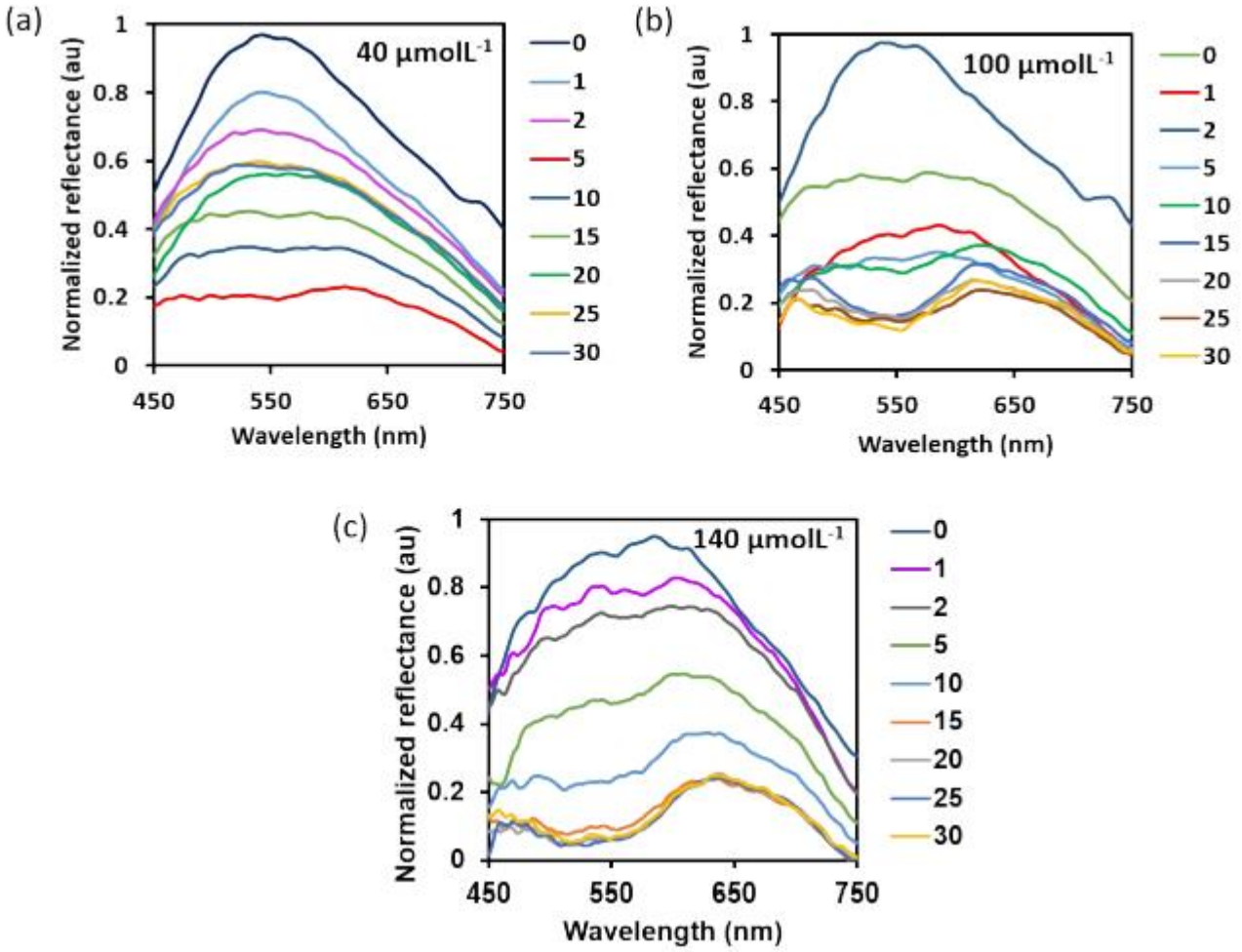

Figure A28. Time response of the nitrite sensor at different concentrations. (a) Nitrite concentration 40 µmol L^{-1}. (i) Reflection spectra; (ii) reflection peak shift over time; (iii) Photographs of the sensor at discrete times: (b) Nitrite concentration 100 µmol L^{-1}: (i) Reflection spectra; (ii) reflection peak shift over time; (iii) Photographs of the sensor at discrete times; scale bar: 1.5 mm.